Exploiting the properties of boron doped diamond for electrochemical sensing applications

Zoë Joanna Ayres

A thesis submitted for the degree of Doctor of Philosophy

Department of Physics

March 2017

The present is theirs; the future, for which I really worked, is mine.

Nikola Tesla

Table of Contents

Acknowledgements

I wish to extend my deepest thanks to my supervisor Professor Julie Macpherson for all your help and guidance. Thank you for helping me to grow both personally and as a scientist over the past few years. Many thanks to Professor Mark Newton and Professor Patrick Unwin. I can only hope that I have picked up a modicum of your knowledge of diamond and electrochemistry along the way. Thank you to all the members of the Electrochemistry and Interfaces group, past and present, for making my time at Warwick so enjoyable. It has been my pleasure to work alongside such a mix of personalities and learn from the wealth of knowledge you have had to offer.

I am indebted to the fantastic electronic and mechanical technicians at Warwick, particularly Rod Wesson, Lee Butcher and Marcus Grant. I am also extremely grateful to both the EPSRC and Element Six for funding me to do my PhD, as well as providing me with the opportunity to get experience of industry. Dr. Tim Mollart and Nikki Palmer, thank you for your very useful input throughout the past few years. Tony Bristow, Andy Ray and Andy Poulton thank you for your insight into industry.

To my office friends – thank you for keeping my spirits high on the darker days and sharing in my joy on the brighter ones. You know who you are.

Jonathan Duncan, my husband, confidant and best friend, for your continual support, love and belief in me, I thank you and love you with all my heart. Mum and Dad, thank you for everything you have done for me. I could not have asked for better parents. Thank you for always pushing me to be the best I can be.

Declaration

This thesis is submitted to the University of Warwick in support of my application for the degree of Doctor of Philosophy. It has been composed by myself and has not been submitted in any previous application for any degree.

The work presented (including data generated and data analysis) was carried out by the author except in the cases outlined below: The electrochemical data in Chapter 4 and Chapter 7 was collected in conjunction with Samuel Cobb. Laser micromachining throughout the thesis was conducted by Dr Jonathan Newland, Samuel Cobb and Mareike Herrmann. The scanning electron microscopy (SEM) image in Chapter 6 was collected by Dr Lingcong Meng, with elevated temperature data collected by Lucy Holt. White Light Interferometry data was collected by both Jonathan Newland and Samuel Cobb. The 2D finite element modelling in Chapter 6 was conducted by Dr. Maxim Joseph and SEM images in Chapter 5 were collected by Haytham Hussein.

Parts of this thesis have been published by the author:

Chapter 3:

Z. J. Ayres, M. E. Newton, and J. V. Macpherson, *Quantitative analysis of trace palladium contamination in solution using electrochemical X-ray fluorescence (EC-XRF)*, *Analyst*, **2016**, *141*, 3349–3357.

Chapter 4:

Z. J. Ayres, S. J. Cobb, M. E. Newton and J. V. Macpherson, *Quinone electrochemistry for the comparative assessment of sp^2 surface content of boron doped diamond electrodes*, *Electrochem. Comm.*, **2016**, *72*, 59–63.

Chapter 6:

Z. J. Ayres, A. J. Borrill, J. C. Newland, M. E. Newton and J. V. Macpherson, *Controlled sp^2 functionalization of boron doped diamond as a route for the fabrication of robust and Nernstian pH electrodes, Anal. Chem*., **2016**, *88* (1), 974–980.

And Chapter 5, recently accepted for publication:

Z. J. Ayres, J. C. Newland, M. E. Newton, S. Mandal, O. A. Williams and J. V. Macpherson, *Impact of multimode chemical vapour deposition growth under low pressure conditions on the spatial variation of sp^2 carbon in boron doped diamond electrodes*, *Carbon*, accepted May 2017.

Abstract

This thesis explores utilising the advantageous electrochemical properties of polycrystalline boron doped diamond (BDD), including low background currents and a wide potential window, for a range of different electroanalytical applications.

The newly developed technique Electrochemical X-ray Fluorescence is employed for the quantitative detection of palladium (Pd^{2+}) in the presence of electroactive species relevant to the pharmaceutical industry. Significant improvements on analysis times are achieved by EC-XRF parameter optimisation and consideration of the detection limits required for the end application.

Given that the quality of BDD utilised (the amount of sp^2 content present) can directly impact on the electrochemical response observed, a new BDD characterisation technique is developed. This involves the electrochemical determination of the surface coverage of quinone groups only present on sp^2 carbon. This technique is then applied for the characterisation of diamond films grown via chemical vapour deposition under low pressure conditions, identifying regions across BDD wafers with distinctly different electrochemical properties.

A Nernstian BDD pH sensor is also successfully fabricated, capable of operating in both buffered and unbuffered solutions. This is achieved by controllably laser micromachining the BDD surface introducing pH sensitive quinone groups. The resulting sensor is found to be stable in a variety of extreme environments.

List of Figures

List of Tables

Abbreviations

ACM	Acetaminophen
API	Active Pharmaceutical Ingredient
ASV	Anodic stripping voltammetry
BDD	Boron-doped diamond
CE	Counter electrode
CV	Cyclic Voltammetry
CVD	Chemical Vapour Deposition
DOS	Density of states
EC-XRF	Electrochemical X-ray Fluorescence
ED	Energy dispersive
EMA	European Medicines Agency
EPPG	Edge-Plane Pyrolytic Graphite
ET	Electron transfer
$FcTMA^+$	Ferrocenylmethyltrimethylammonium hexafluorophosphate
FE-SEM	Field Emission Scanning Electron Microscopy
FWHM	Full width half maximum
GC	Glassy Carbon
HPHT	High Pressure High Temperature
HFCVD	Hot Filament Chemical Vapour Deposition
HMDE	Hanging Mercury Drop Electrode
ICP-MS	Inductively Coupled Plasma Mass Spectrometry
IrOx	Iridium oxide
IS	Inner sphere
ISE	Ion Selective Electrode
ISFET	Ion-Selective Field Effect Transistor
LOD	Limit of detection
MWCVD	Microwave Chemical Vapour Deposition
OES	Optical Emission Spectroscopy

ORR	Oxygen reduction reaction
OS	Outer sphere
PCET	Proton coupled electron transfer
ppb	Parts per billion
ppm	Parts per million
RDE	Rotating Disc Electrode
RE	Reference electrode
$Ru(NH_3)_6^{3+}$	Hexaaminеruthenium (III) chloride
SCE	Saturated Calomel Electrode
SPE	Screen printed electrode
SW	Solvent window
SWV	Square Wave Voltammetry
TR	Total reflection
UHV	Ultra-high vacuum
UME	Ultramicroelectrode
UNC	Ultrananocrystalline
WD	Wavelength dispersive
WE	Working electrode
WLI	white light interferometry
XPS	X-ray Photoelectron Spectroscopy
XRF	X-ray Fluorescence

Glossary of symbols

A	Electrode area
a	Activity
C	Capacitance
c^*	Concentration
ΔE_p	Peak-to-peak separation
Δi	Differential current
E	Potential
E_F	Fermi level
E^o	Standard electrode potential
F	Faraday's constant
f	Angular rotation rate
F	Fluence
Hz	Frequency
Γ	Quinone surface coverage
i	Current
i_{lim}	Limiting current
i_p	Maximum current
j	Flux
K	Kelvin
Ω	Ohms
R	Molar gas constant
Rs	Solution resistance
T	Temperature
t	time
n	number of electrons transferred
η	Overpotential
V	Volts

Chapter 1

Introduction

1.1 Overview

Diamond has long been recognised as much more than just a gemstone due to its range of extraordinary chemical and physical properties. These include, but are not limited to, a broad wavelength transparency (from deep ultraviolet to far infrared); being the hardest known material (~90 GPa); having a high thermal conductivity (2600 W m $^{-1}$ K^{-1}) and exhibiting resistance to chemical corrosion.[1] It is through advancements in artificial synthesis of diamond, particularly that of Chemical Vapour Deposition (CVD),[2] that these favourable properties have been exploited for a range of scientific technologies, from radiation detectors[3] and high-power lasers[4] to bionic eyes.[5,6] Furthermore, by controllably introducing impurities into diamond during CVD growth, the characteristics of the material produced can be tailored for specific applications. For example, by simply incorporating boron into the lattice, diamond can be made electrically conductive, denoted as boron-doped diamond (BDD).

The use of BDD as an electrode material has increased rapidly over the last 20 years due to the material having many of the useful properties of diamond,[1] as well as a wide potential window in both aqueous and organic solvents,[7,8] low background (capacitive) currents and higher resistance to fouling compared to other traditional electrode surfaces.[9] Furthermore, diamond is capable of surviving in extreme environments.[10] Work in this thesis explores utilising the beneficial properties of BDD for the advancement of electrochemical-based sensor technologies in two key areas: (1) heavy metal detection and (2) pH sensing.

1.2 Diamond Synthesis

Diamond was first successfully grown in the laboratory in 1955 by General Electric using the technique high pressure, high temperature (HPHT).[11] This process involves compressing graphitic carbon at extreme pressures (5 GPa) at elevated temperatures, ranging from 1800–2300 K in the presence of a metallic solvent, in order to thermodynamically drive the formation of diamond.[12] HPHT diamonds are primarily utilised as abrasives for tools, due to their small size (from microns to millimetres). The technique is also used to produce single crystal diamonds, although quality often suffers, particularly when growing large (> 1 carat) diamonds, due to unintentional impurity incorporation (typically nitrogen).[13] In order to achieve large, high-purity diamonds exceptional process control is required. It is not until recently that consistently large, colourless (grades D to F) HPHT diamonds have been synthesised by the Russian company New Diamond Technology.[14]

First demonstrated by Eversole *et al* in 1962, CVD offers a viable alternative for diamond synthesis, conducted at temperatures and pressures where diamond is metastable compared to graphite.[15,16] The technique offers the possibility of growing diamond material tens of centimetres across, at relatively low cost due to the low pressures required (20–30 Torr).[17] There has been over 40 years of research into a variety of different CVD techniques to grow diamond.[18] The process involves a gas phase which contains carbon-containing precursor molecules (typically CH_4) which must undergo activation in order to initiate growth. This can be achieved by several methods including hot filament CVD (HFCVD) and microwave plasma CVD (MWCVD).[19] HFCVD utilises a metal filament such as tungsten typically heated to > 1400 K, with the substrate heated separately to ~1000 K.[19] HFCVD is a popular choice

for diamond growth as the method is relatively cheap, easy to use and can produce reasonably high quality (low sp^2 content) diamond films at a rate of up to 10 µm h^{-1}.[20] The method however often results in contamination of the diamond film with metal from the filament. Furthermore, the filament itself can be damaged by corrosive and oxidising gases, limiting the gas mixtures utilised.[20] These issues are removed when using MWCVD. Other advantages of MWCVD include faster growth rates due to the higher powers that can be employed, as well as large deposition areas (up to 20 cm).[20] All diamond material used in this thesis has been grown using MWCVD, with a typical reactor shown in **Figure 1.1**. In order to make BDD, a boron source such as B_2H_6 is added to the gas-phase feedstock.

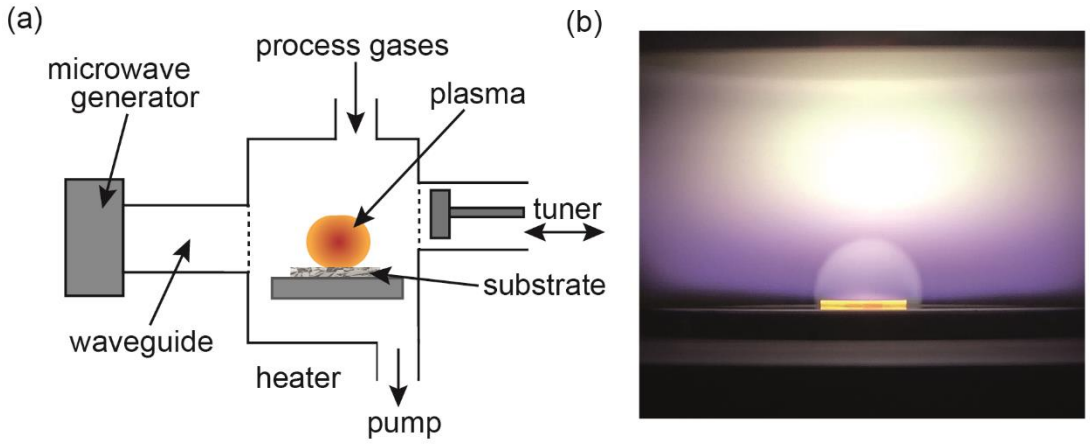

***Figure 1.1**: (a) Schematic of a commercial Applied Science and Technology Inc (ASTeX) MWCVD plasma reactor[19] and (b) an optical image taken through the window of a MWCVD reactor, showing the plasma and diamond growth onto a glowing Si wafer (50 mm in diameter). Image courtesy of Professor Oliver Williams.*

CVD involves the atom-by-atom 'building' of the diamond tetrahedral lattice with carbon atoms (introduced via a carbon source such as CH_4).[21] This can occur by homoepitaxial growth, where the precursor diamond seed crystals are dispersed onto a substrate or by heteroepitaxial growth using a non-diamond substrate.[22] Typical

substrates include Si, W, Ti, Mo or diamond, with the prerequisite that they must be capable of withstanding high temperatures.[21]

The exact mechanism of diamond growth is complex and has therefore been subject to a vast amount of research.[23,24] The diamond produced is affected by several factors including the CH_4 concentration and the presence of hydrogen in the reactor, with ratios of ~99.5% H_2 and 0.5% CH_4/B_2H_6 typically required to produce high-quality material.[25,26] Note, high-quality diamond throughout this thesis is defined as diamond with negligible sp^2 carbon content. The presence of atomic hydrogen during growth is essential in order to produce high-quality diamond material, with the hydrogen stabilising the lattice during growth by terminating any dangling bonds to form C-H groups, thus preventing the formation of the sp^2 carbon.[27] Atomic hydrogen present in excess also etches both sp and sp^2 carbon at a faster rate than sp^3 carbon.[25] This results in slow growth rates (~0.1–10 μm hr^{-1}) but typically results in higher quality (lower sp^2 carbon) diamond growth than that produced by HPHT.[28] Furthermore, atomic hydrogen is necessary for diamond synthesis, reacting with both the CH_4 molecules present in the gas phase and C-H groups at the diamond substrate surface, producing the radical $CH_3^{\bullet}$.[19] Any gas phase $CH_3^{\bullet}$ can then react with other carbon-containing radicals at the substrate surface, adding to the diamond lattice, as illustrated in **Figure 1.2**.[19]

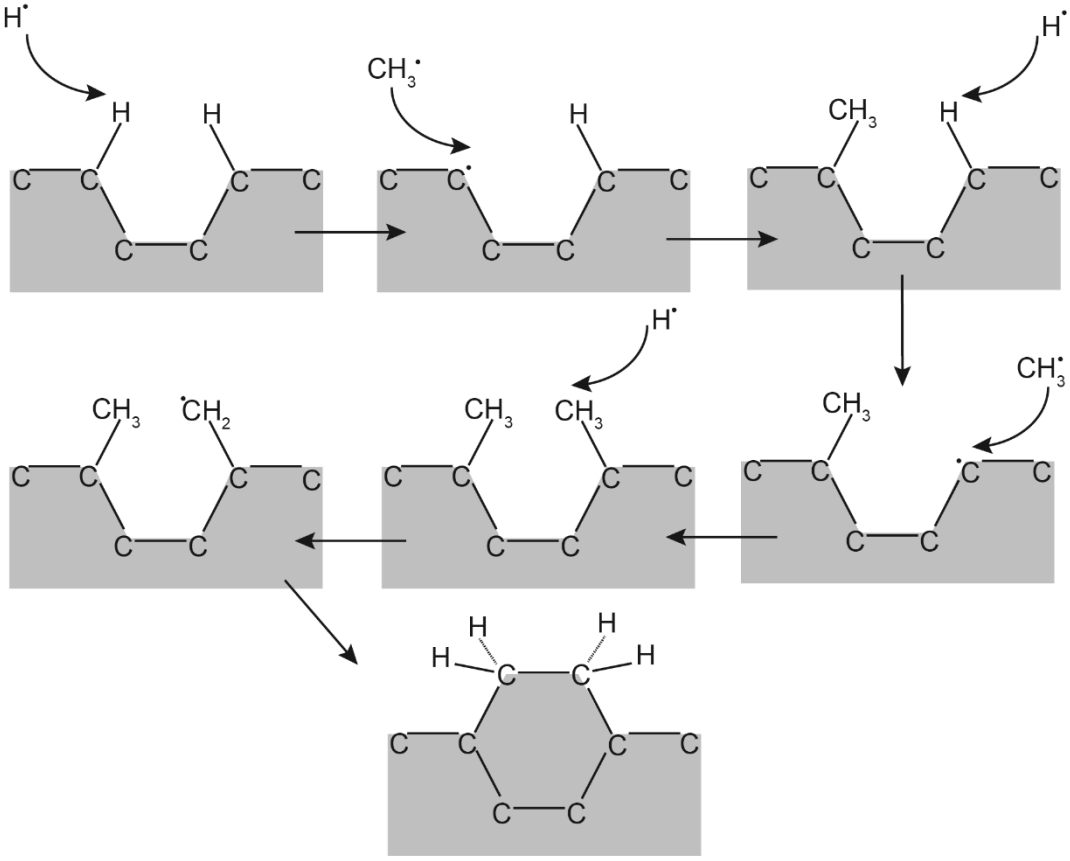

Figure 1.2*: *Illustration of the growth of diamond at a [110] trough site by CVD reproduced from reference 19.

Dependent on growth conditions, BDD can be grown as thin film ultrananocrystalline (UNC) or as microcrystalline material, with grain sizes of < 10 nm and up to several μm's respectively.[29] UNC BDD is typically left on the growth substrate for support and is left with an as-grown surface, whilst microcrystalline material can be grown thick enough to be removed from the growth substrate. However, the surface is now markedly rougher than UNC and therefore for electrochemical studies is often polished to ~ nm roughness (see **Figure 1.3a**).[30] This allows the production of freestanding BDD as shown in **Figure 1.3b**.

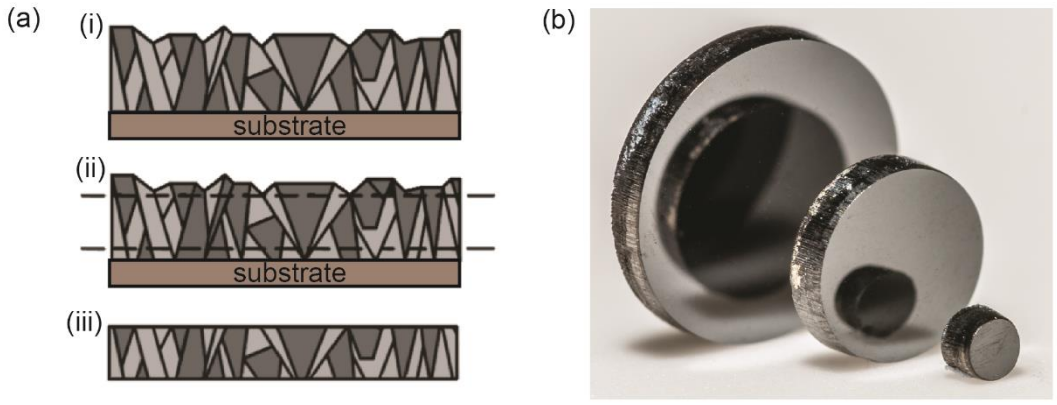

***Figure 1.3**: (a) Illustration showing (i) as-grown surface, (ii) polish lines and (iii) the resulting freestanding structure of a microcrystalline BDD wafer.[31] (b) Photograph of freestanding, 470 µm thick BDD rounds (photo credit: Dr Jonathan Newland).*

1.3 Diamond structure and doping

Diamond is an allotrope of carbon, with atoms fully hybridised forming a sp^3 tetrahedral lattice, as shown in **Figure 1.4a**.

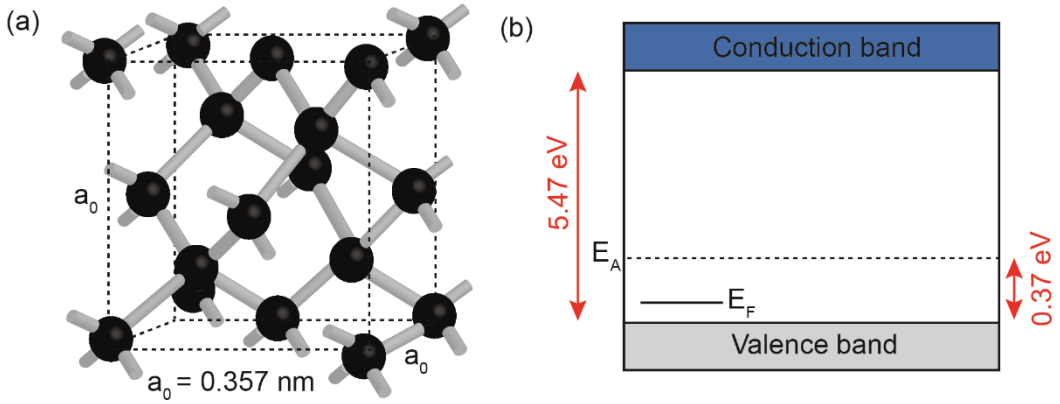

***Figure 1.4**: (a) the tetrahedral carbon structure of diamond and (b) band structure for semi-conducting diamond (p-type), where E_F denotes the fermi level potential and E_A the acceptor level.*

Each carbon atom is connected to the next with a single σ bond, which gives rise to many of the fundamental properties of diamond (summarised in **Table 1.1**), including extreme hardness and high thermal conductivity.[18,22]

***Table 1.1**: Physical properties of diamond.* [32]

Property	Value
Broad transmission spectra	226 nm to 500 µm
High resistance to thermal shock	1000 MW m^{-1}
High thermal conductivity	2200 W m^{-1} K^{-1}
Good electrical insulator	10^{15} to 10^{16} Ω cm
Low thermal expansion	0.9 ppm K^{-1}
High electronic mobility	4500 cm^2 V^{-1} s^{-1} (electron), 3800 cm^2 V^{-1} s^{-1}
Low dielectric constant	5.68 ± 0.15

In its intrinsic (undoped) form, diamond is a semi-conductor with a wide band gap of 5.47 eV (at T=300 K), making it electrically insulating.[33] However, by introducing dopant impurities diamond can be made electrically conductive. Common dopants include nitrogen (n-type) and boron (p-type), which sit either side of carbon in the periodic table, and thus can be substituted readily into the diamond lattice. Doping with nitrogen (~1.7 eV) however does not provide appreciable electrical conductivity for electrochemistry therefore boron is the preferred choice, providing an acceptor level 0.37 eV above the valence band (illustrated in **Figure 1.4b**).[34] The boron doping density dictates the behaviour of the BDD, with a dopant level of 10^{16} – 10^{19} B atoms cm^{-3} giving the diamond p-type semi-conductor properties.[35] At boron dopant levels of ≥ 10^{20} B atoms cm^{-3} the material becomes "metal-like" in regards to electrical conductivity, due to the fact that the acceptor density is high enough that there is a significant wave function overlap of acceptor atoms.[29] BDD can thus be utilised for electroanalytical applications. The change in dopant density can be observed by eye as an increased density of states (DOS) results in increase visible light absorption, with semi-conducting material exhibiting a blue colour and BDD near the metallic transition appearing black (opaque).[36]

1.4 Electroanalysis

Electrochemistry is often considered for analytical applications due to its simplicity, relatively low cost compared to other analytical techniques and the fact it is amenable to in-situ analysis.[37] For this reason, electrochemical measurements have been applied to wide range of fields including energy generation,[38] environmental monitoring,[39] healthcare diagnostics,[40,41] biosensors[42] and waste management[43,44] to name but a few. Electrochemical measurements are typically either voltammetric (where a potential is applied and a current is measured) or potentiometric (where an equilibrium voltage is measured).[45]

1.4.1 Dynamic electrochemistry

A simple electrochemical reaction can be represented by **Equation 1.1**:

$$O + ne^- \underset{k_f}{\overset{k_b}{\rightleftharpoons}} R \qquad (1.1)$$

where O and R represent the oxidised and reduced form of an electroactive species respectively.[37] The position of equilibrium is linked to the standard electrode potential, E^o. Applying an overpotential η (where $\eta = E - E^o$, with E denoting the electrode potential) perturbs the position of equilibrium and drives either the reduction of oxidation of species in solution at the electrode/electrolyte interface. This exchange of electrons results in current flow. As η increases, the rate of electron transfer (ET) increases resulting in the current (i) increasing approximately exponentially with increasing η, predicted by the Butler-Volmer model.[37]

i is also directly proportional to the rate of reaction, or flux (*j*), shown in **Equation 1.2**:

$$i = nAFj \qquad (1.2)$$

where *i* = the faradaic current; *n* = the number of electrons transferred during the redox event; *F* = Faraday's constant (96485 C mol^{-1}) and *j* = the flux of electroactive species (mol cm^{-2} s^{-1}).

Figure 1.5 shows the processes that control *j*. These include: (1) mass transport of O from bulk solution to the electrode surface region; (2) chemical reactions, such as protonation; (3) surface reactions (adsorption/desorption) and (4) electron transfer at the electrode surface.[46] The slowest step in the process controls the rate of the reaction; reactions are typically either mass transport or electron transfer controlled.

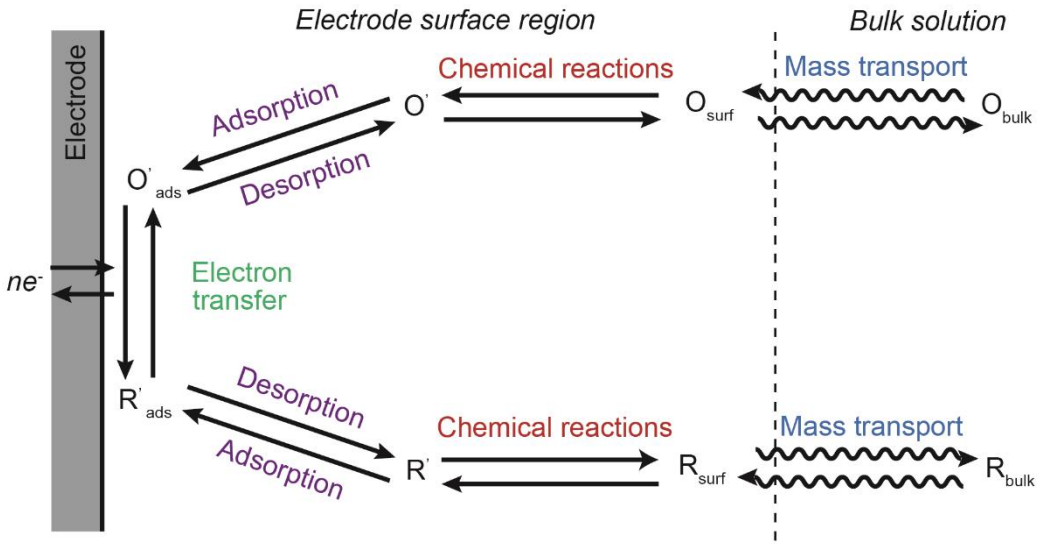

***Figure 1.5**: Typical electrode reaction pathway.*[37]

Mass transfer can be broken down into three contributions: migration, convection and diffusion. For electrochemical measurements migration effects are mitigated by the

addition of a high concentration of non-electroactive supporting electrolyte to solution. Adding a high concentration of salt also reduces the solution resistance, therefore compensates for ohmic drop between the electrodes as well as ensuring that the double layer remains small (~ nm) compared to the diffusion layer.[37] Coupled with the careful control of temperature (to prevent thermal convection), for most electrochemical experiments diffusion is the only mass transfer contribution. Thus in order to access ET kinetics the diffusional flux is increased by either moving to microelectrodes (radial diffusion over linear diffusion) or by introducing a convective contribution, e.g. deliberately stirring, flowing or heating the solution of interest.[37]

Note, compared to a metal (~10^{23} cm^{-3} eV^{-1}), BDD exhibits a much lower DOS – determined to vary between 2×10^{20} cm^{-3} eV^{-1} and 6×10^{20} cm^{-3} eV^{-1} at 0.0 V versus Ag|AgCl for a BDD electrode with an average B dopant density of 5×10^{20} B atoms cm^{-3}.[47] It has been observed that ET rates are ~ two orders slower on BDD (for $Ru(NH_3)_6^{3+}$ and $FcTMA^+$) compared to metal electrodes.[29,48] This is thought to be due to a combination of both the lower DOS, which indicates the number of available energy states at a particular energy and the probability of them being occupied (the Fermi function).[11,47] This however does not impact the electrochemical response for fast outer sphere electron transfer redox species such as $FcTMA^+$ or $Ru(NH_3)_6^{3+}$ observed at BDD macroelectrodes in quiescent solutions, using cyclic voltammetry at typical scan rates of 0.1 V s^{-1}, as ET is still faster than diffusion under these conditions.[29]

1.4.2 Cell setup

The majority of electroanalysis is conducted using a three-electrode cell, as shown in **Figure 1.6a** and **Figure 1.6b**, containing a working electrode (WE), reference electrode (RE) and a counter electrode (CE). In order to facilitate an electrochemical reaction, an external potential is applied between the WE and RE using a potentiostat, resulting in a current response. The electrochemical reaction occurs at the WE/solution interface.

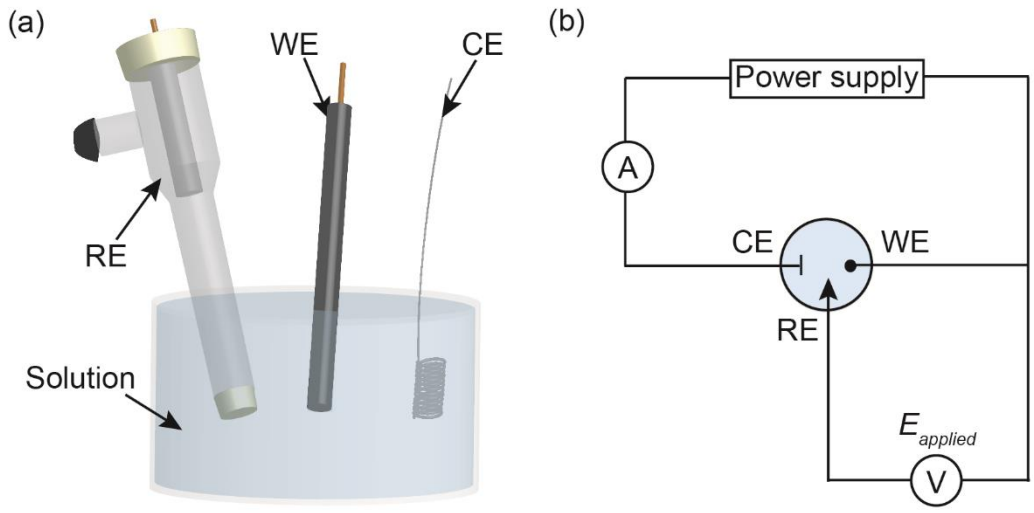

***Figure 1.6**: Illustration of 3-electrode cell (a) experimental setup and (b) corresponding circuit diagram.*[37]

When current is passed between the WE and RE only (i.e. 2 electrode set-up), ohmic drop can occur, especially for resistive solutions and high currents. To mitigate this, high concentrations of inert salt (supporting electrolyte) are added to the analyte solution as well as placing the WE and RE in close proximity to each other, but most importantly a third electrode is added to the system; the counter.[37] As the RE potential must remain constant, current in a 3 electrode set-up flows between the WE and the CE. For this reason, it is also important to consider the electrochemical reaction taking

place at the CE and whether the products of such reaction will interfere detrimentally with the WE reaction under study. For this reason, in some experiments the CE is separated by a frit from the WE and RE.[37]

The RE must maintain a constant potential irrespective of solution conditions, and hence the concentration (or activity) of the potential determining ions must remain constant. A common reference electrode and one used throughout this thesis is the saturated calomel electrode (SCE), which can be denoted using the cell notation:

$$Cl^{-}(aq) \mid Hg_2Cl_2(s) \mid Hg(l) \mid Pt\ (s) \qquad (1.3)$$

where | indicates a phase boundary. The SCE constitutes a Pt wire, coated in mercury, covered by a layer of mercury (II) chloride, or calomel, contained within a glass vial,[49] which is filled with a saturated potassium chloride solution (4 M). A porous frit serves as the junction between the RE solution and the sample solution.[50]

The overall cell reaction is shown in **Equation 1.4**:

$$Hg_2Cl_2(s) + 2e^{-} \rightleftharpoons 2Hg(l) + 2Cl^{-}\ (aq) \qquad (1.4)$$

Which can be substituted into the Nernst equation, **Equation 1.5**:

$$E = E^{o} + \frac{RT}{2F}\ln\frac{1}{a_{Cl^-}^{2}} \qquad (1.5)$$

where E=the electrode potential, E^{o} = the standard electrode potential and a = the activity of the species, defined in **Equation 1.6** as:

$$a = \gamma\,[c^*] \qquad (1.6)$$

where γ is the activity and c* = the concentration of the species.

Therefore as the potential of the SCE is dependent only the activity of Cl^- ions present, placement of the electrode in concentrated KCl solution acts to ensure a constant potential is maintained.

1.4.3 Cyclic Voltammetry (CV)

CV is the most common electrochemical technique.[37] A potential is applied to the electrochemical cell from a potential where no reaction occurs (the open circuit potential, OCP) then linearly swept in both the anodic (oxidative) and cathodic (reductive) directions, resulting in ET. The CV waveform is shown in **Figure 1.7a**.[51,52]

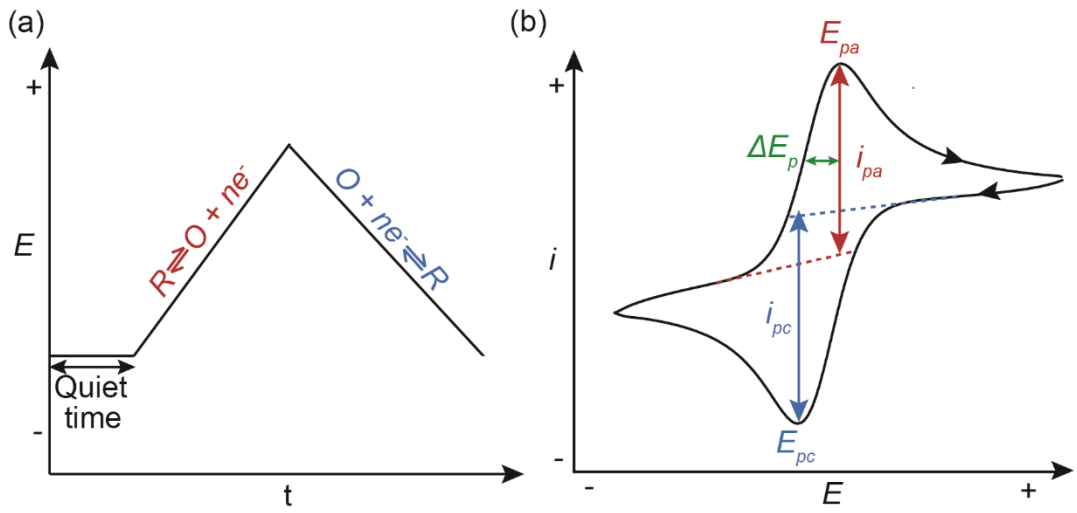

***Figure 1.7**: (a) A CV waveform and (b) a CV for a simple one-electron transfer reaction at a macroelectrode.*

A typical CV is shown in **Figure 1.7b**. The CV scan starts at the OCP, then as the potential is driven negatively, the rate of reductive ET increases, resulting in an exponential increase in current flow. A maximum current (i_p) is reached (i_{pa} and i_{pc} for the anodic and cathodic sweep respectively), forming a peak in the CV. The peak-to-

peak separation, ΔE_p, is 59 mV / n (at T=298 K) dictated by the Nernst equation.[37] Under kinetic controlled conditions, ΔE_p increases for slower and slower ET reactions compared to the rate of mass transfer.

For a macroelectrode, after reaching i_p, a subsequent drop in current is observed, as the rate of mass transfer of the redox species to the interface is not sufficient to replace that being consumed at the electrode surface (shown in **Figure 1.7b)**. Under diffusion controlled conditions, the Randles-Sevcik equation, **Equation 1.7** states:[53]

$$i_p = 0.4463nFAc^*\left(\frac{nF\nu D}{RT}\right)^{\frac{1}{2}} \qquad (1.7)$$

where n = the number of electrons transferred; A = the total electrode surface area (cm^2); c^* = the bulk concentration of the electroactive species (mol cm^{-3}); D = the diffusion coefficient of the electroactive species ($cm^2\ s^{-1}$) and ν = the potential scan rate ($V\ s^{-1}$).

The current observed is a combination of two processes that occur at the electrode surface, faradaic and non-faradaic.[37] Faradic processes involve the reduction and oxidation of chemical species in solution by the exchange of electrons across the electrode interface. Non-faradic current involves no charge transfer across the interface, instead arising from changes in the electrode/solution interface.[37] Examples of non-faradic processes include capacitance of the electrode material and the electrical double layer (*vide infra*).[37]

1.4.4 Increasing mass transport

Increasing mass transport is advantageous for electrochemistry as analysis times can be greatly reduced, but it also offers a means to explore fast electron transfer reactions.[37] Two main methods exist in order to increase mass transfer of electroactive species to the electrode surface: (1) reducing the size of the WE, from macro to micro and nano, which results predominantly in radial diffusion compared to linear diffusion (although the currents measured are smaller) and (2) introducing forced convection.[54,55] Any convection introduced into the system must result in well-defined laminar flow in order to obtain quantitative information. Several hydrodynamic electrodes have been developed which include the: Rotating Disc Electrode (RDE);[56] Channel Electrode[57] and Wall-jet electrodes.[57]

In Chapter 3, a RDE is utilised (illustrated in **Figure 1.8a** along with a typical CV in **Figure 1.8b**), allowing analysis times to be substantially reduced compared to measurements made in quiescent solution by the introduction of forced convection.

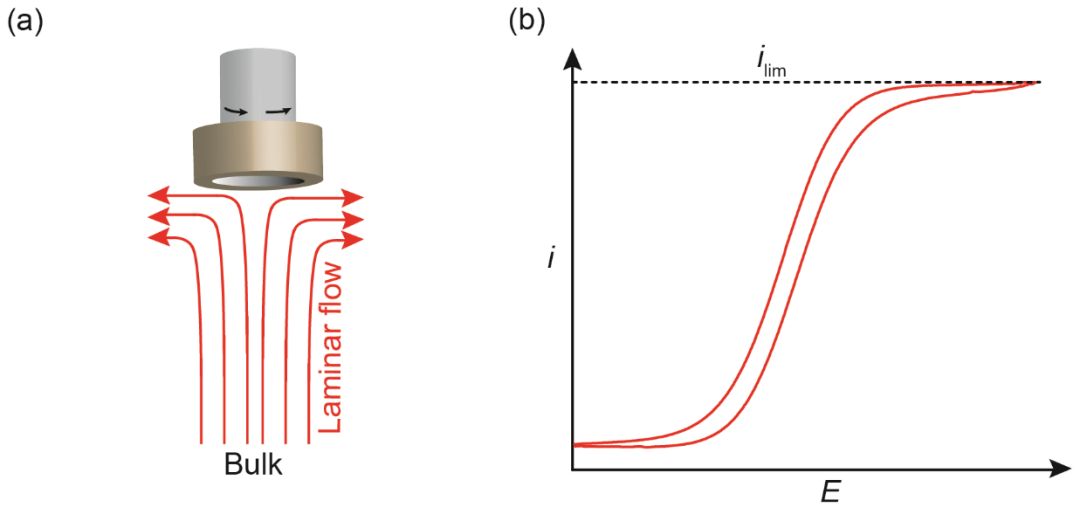

***Figure 1.8**: (a) Illustration of solution flow to a RDE and (b) a typical CV response under hydrodynamic control.*

A sigmoidal CV shape is observed as the increased mass transport (due to the forced convection) is now able to compete with the rate at which the redox species are removed at the electrode, resulting is a steady state limiting current, i_{lim}. The i_{lim} is predicted using the Levich equation, **Equation 1.8**:[58]

$$i_{lim} = 0.620nFAD^{2/3}f^{1/2}v^{-1/6}c* \qquad (1.8)$$

where f = the angular rotation rate of the electrode (Hz) and v = the kinematic viscosity of the bulk solution ($cm^2\ s^{-1}$).

1.4.5 Square Wave Voltammetry (SWV)

Often used for electroanalysis, SWV is a pulse voltammetry technique which results in excellent detection sensitivities with a typical SWV waveform is shown in **Figure 1.9a**.

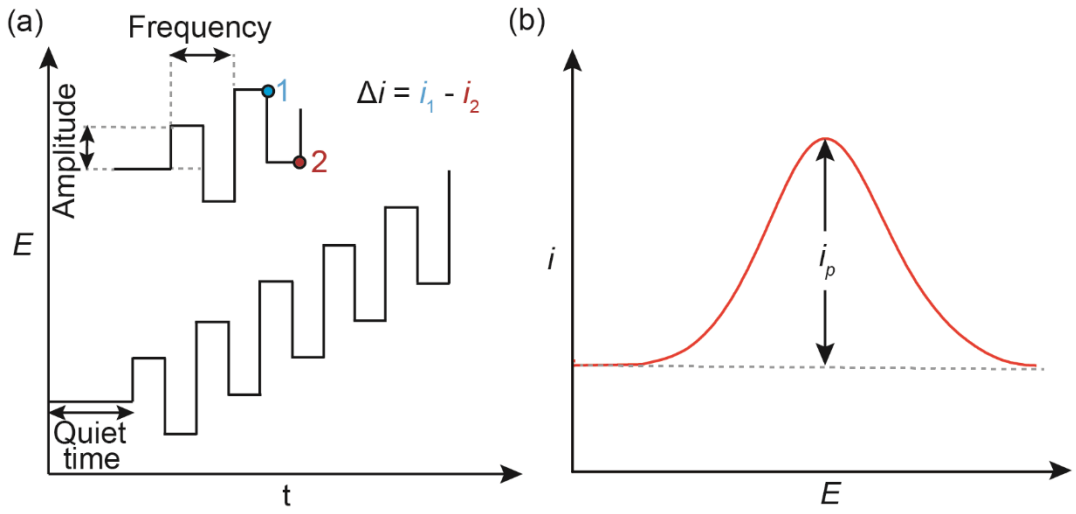

***Figure 1.9**: (a) SWV waveform, including i sampling positions and (b) typical SWV response.*[59]

Given that the non-faradic current is proportional to $e^{-t/RsC}$, where t = time, R_s is the solution resistance and C is the double layer capacitance, and the faradaic current is proportional to $t^{-1/2}$ the non-faradic current decays much faster than the faradic contribution.[60] Taking this into account, in SWV the current is sampled at two time intervals (i_1 and i_2) and the differential (Δi) plotted against the applied E (shown in **Figure 1.9b**).[59,60] This results in a negligible contribution from the charging (non-faradic) current in the final voltammogram. For this reason, much lower detection limits can be achieved using SWV compared to conventional CV techniques.[59,61]

1.5 BDD Electrochemistry

BDD exhibits many advantageous properties over other common electrode materials, such as Au, Pt and glassy carbon (GC) including: wide solvent window (SW); low background currents and reduced fouling.[7,29] **Figure 1.10** shows the comparison of a typical BDD SW with other common electrode materials.

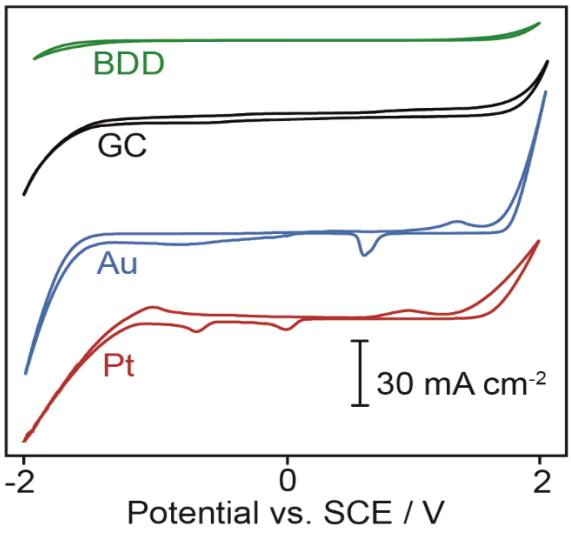

***Figure 1.10**: Comparison of SWs for BDD, GC, Au and Pt, ran in 0.1 M KNO_3 at 0.1 V s^{-1}.*

To understand why BDD exhibits such a large solvent window (> 3 V in 0.1 M KNO_3, within a ± 0.4 mA cm^{-2} threshold)[62] it is important to note that the sp^3 structure results in the BDD surface being electrocatalytically inactive.[63] As water electrolysis is an inner-sphere (IS) redox species, the water molecules must adsorb to the electrode surface in order for a redox event to occur.[37] This contrasts to outer-sphere (OS) redox reactions that only require proximity to the electrode surface for interactions to occur.[37] This is illustrated in **Figure 1.11.** Note, **Figure 1.10** also demonstrates the electrical double layer which contributes to capacitance (*vide supra*).[37] This occurs as if an electrode holds charge, unsolvated ions (inner Helmholtz plane, IHP) and solvated ions (outer Helmholtz plane, OHP) assemble at the electrode-solution interface in order to balance the charge.[11] Subsequently, when a potential is applied to the electrode, the charge distribution on the electrode surface adapts to the change, giving rise to non-faradaic current.[23]

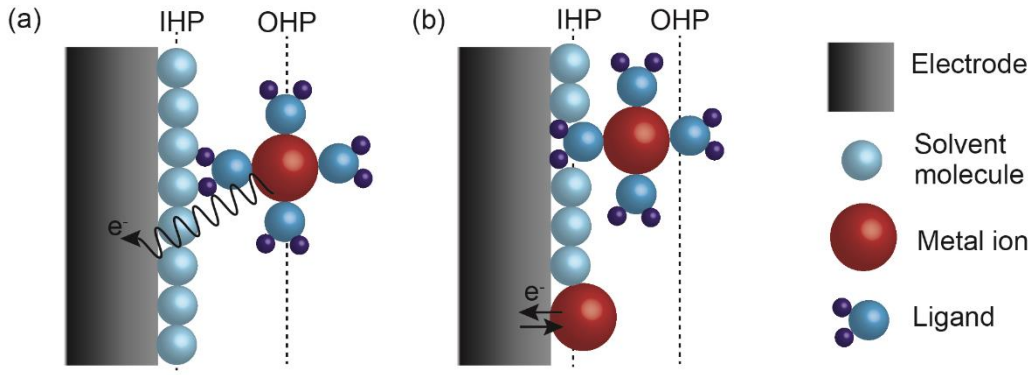

***Figure 1.11**: Illustration of (a) outer sphere and (b) inner sphere electron transfer processes, as well as the IHP and OHP.*[37]

As BDD lacks catalytic sites for water electrolysis to occur, water oxidation and reduction is retarded. It should also be noted that compared to the other electrode

materials in **Figure 1.10**, there is no oxygen reduction signature on BDD, as this is also an IS reaction, requiring catalytic binding sites. Other than being electrocatalytically inactive, there are several key factors that influence the electrochemical performance of BDD: (1) boron dopant concentration; (2) surface termination; (3) sp^2 incorporation and (4) surface morphology and finish.[29] It should be noted that these factors are intrinsically related to one another, with one directly impacting the other.[29]

1.5.1 Boron Dopant Concentration

As discussed in **Chapter 1.3** adding boron during diamond growth imparts metal-like electrical conductivity at boron dopant concentrations $\geq 10^{20}$ B atoms cm^{-3}. It has been noted that heavily doped BDD ([B] $>10^{21}$ cm^{-3}) shows an increase in sp^2 carbon, compared to lower doped material, due to strains on the structure from the boron impurities.[64]

BDD can be probed electrochemically to determine if it is suitably doped for electroanalysis by running a CV of the OS redox couple, $Ru(NH_3)_6^{3+/2+}$.[62] For an electrode doped over the metallic threshold, the peak current observed will be reversible and can be predicted by the Randles-Sevcik equation (**Equation 1.7**).[37] However, for BDD doped below the metallic threshold, as the formal potential (E_0') of $Ru(NH_3)_6^{3+/2+}$ lies within the bandgap of BDD, the CV response is affected by boron dopant concentrations, shown in **Figure 1.12**.[29] These measurements can be complemented with other methods of assessing boron dopant concentration including secondary ion mass spectrometry (SIMS, which is quantitative) and Raman spectroscopy (the Raman 500 cm^{-1} peak is associated with boron, and downshifts with

increasing boron content), which is also thought to be quantitative.[65] Furthermore, the different facets of polycrystalline BDD incorporate boron at different rates, producing grains with varying conductivity.[66]

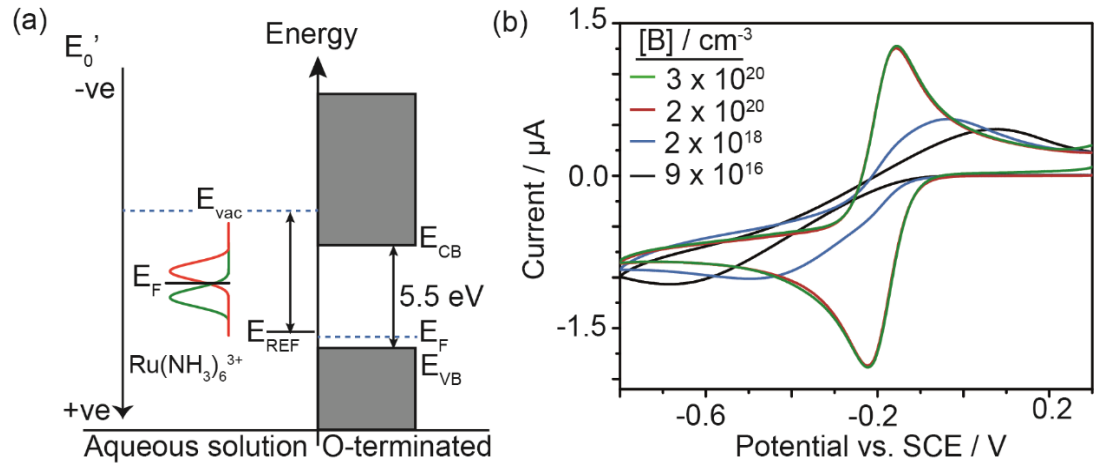

Figure 1.12*: *(a) Schematic showing the approximate position of the OS redox couple $Ru(NH_3)_6^{3+}$ (−0.16 V vs. SCE) with respect to EVB and ECB for semi-conducting O-terminated BDD and (b) 1 mM $Ru(NH_3)_6^{3+/2+}$ CV response for different boron dopant densities in 0.1 M KNO_3 run at 0.1 V s^{-1}. Adapted from references 29 and 62 with permission.

1.5.2 Surface termination

BDD can be either oxygen (O-) or hydrogen (H-) terminated, imparting vastly different properties. For example, an O-terminated surface is hydrophilic, whist H-termination is hydrophobic.[7] This can be measured using contact angle measurements (shown in **Figure 1.13**), where contact angles are typically < 65° for O-termination, compared to closer to 90° for H-termination.[67] Research has also shown that the functional groups on each surface (shown in **Figure 1.13**) also depend on crystallographic orientation, with hydroxyl groups (C-OH) most abundant on the (111) diamond surface and ether (C-O-C) and carbonyl (C=O) groups on the (100) facet.[68]

After CVD growth, BDD leaves the chamber H-terminated. O-termination can be achieved by a variety of different methods including: leaving to air oxidise for a prolonged period; acid treatment (boiling in concentrated acid);[69] alumina polishing;[62] oxygen plasma exposure;[70] photochemical oxidation;[71] exposure to chemical oxidants[72] and electrochemically by anodic polarisation.[73] To convert O-termination back to H-termination, the BDD can be re-exposed to hydrogen plasma. For electroanalysis, O-terminated BDD is typically preferred as the surface is inherently more stable than its counterpart. H-termination does however have advantages, with recent studies showing that the surface diamond can be photochemically amine terminated,[74] and thus used to add a range of biomolecules on the surface.[75,76]

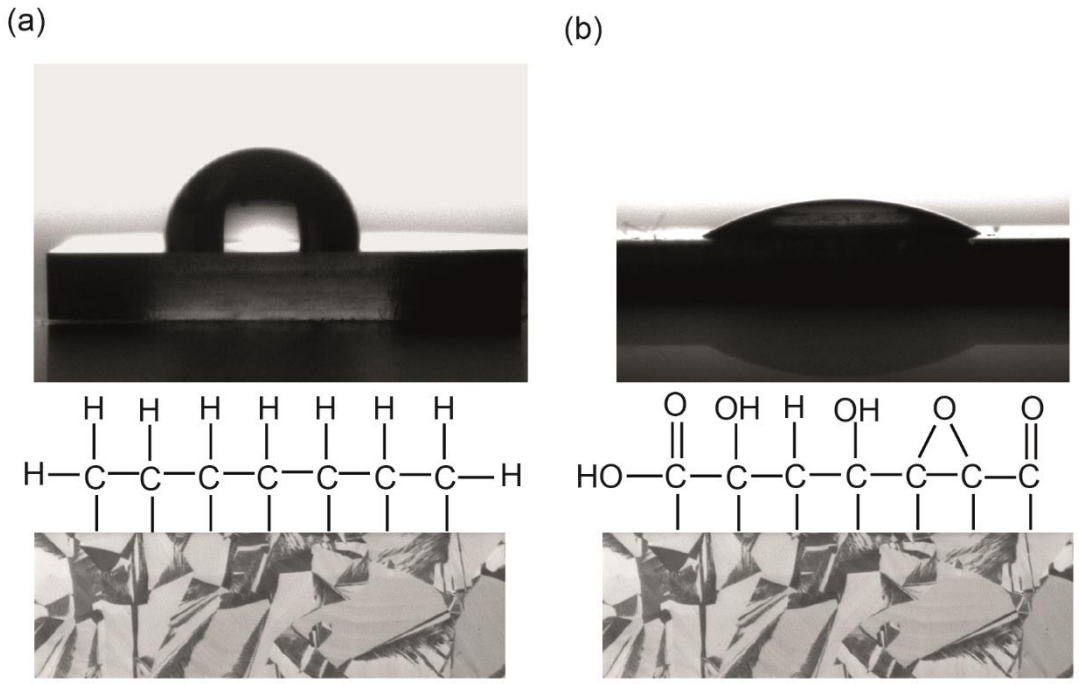

***Figure 1.13**: optical images of contact angle measurements present on (a) H-terminated and (b) O-terminated BDD surface and corresponding illustrations of the possible functional groups.*

It has also been noted that H-termination can impart additional surface conductivity onto diamond surfaces (surface transfer doping),[77] particularly for BDD films with

dopant densities below the metallic threshold. This phenomenon results in the observation of faster electron transfer (ET) kinetics than can be attributed to the bulk film due to subsurface hole accumulation giving rise to two-dimensional conductivity[77,78,79] This was also shown by electrochemically patterning semi-conducting BDD to create regions of H-termination alongside regions of O-termination (by electrochemical oxidation).[80] Significant increases in the rate of ET for $Ru(NH_3)_6^{3+/2+}$ reduction was observed (increased current) in the H-terminated areas compared to the O-terminated regions.

1.5.3 sp^2 incorporation

As the amount of sp^2 carbon increases in BDD films, the catalytic activity of the surface increases,[64] which is reflected in the electrochemical signatures observed. The SW range is reduced with increased sp^2 content as water hydrolysis is facilitated more favourably at catalytic sp^2 sites.[81] Furthermore, peaks (i) and (ii) associated with sp^2, shown on **Figure 1.14**, are attributed to oxygen reduction and sp^2 oxidation respectively.[29] The background capacitance also increases for BDD containing sp^2 impurities.[21]

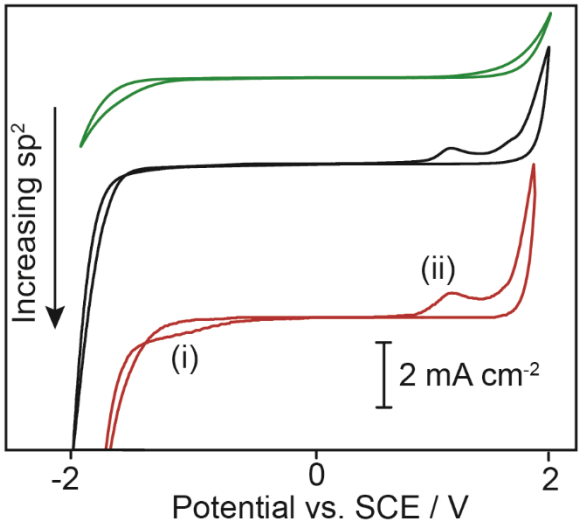

Figure 1.14*: *SW measurements of BDD electrodes with increasing sp^2 carbon content.

The presence of sp^2 in BDD has long been considered by the community as an inherent issue for the majority of electrochemical applications, due to the reduced SW range and increased background currents.[7] It is, however, not until more recently that work has explored the impact that sp^2 content may have on specific electroanalytical applications.[29,64,82] Interestingly, the presence of sp^2 and the additional catalytic activity that it imparts, has been found to be beneficial for certain applications. Swain and coworkers have noted that the ET rates of IS redox mediators such as $Fe^{3+/2+}$ and 4-*tert*-butylcatechol are significantly increased when employing BDD with a higher sp^2 content.[83] Research has also shown that for electrochemical breakdown of organic pollutants sp^2 facilitates more efficient mineralisation, due to ozone production.[84,82] Work in this thesis also explores the advantages of BDD with intentional sp^2 incorporation.

Previous studies typically utilised changing growth conditions to qualitatively vary sp^2 content, specifically by altering the C to H ratios in the growth reactor,[19] discussed in

detail in **Chapter 1.2**. However, the sp^2 content cannot be spatially controlled using this approach. Furthermore, by changing the growth conditions other factors such as surface roughness and boron dopant density may be affected, making it difficult to deconvolute whether the observed response is due solely to the change is sp^2 content or a combination of factors.[85] In this thesis, laser ablation is utilised as an alternative methodology to overcome these issues for the controlled introduction of sp^2 into high-quality BDD. The laser ablation process is discussed in more detail in the experimental **Chapter 2.3.3**.

1.5.4 **Surface** morphology and finish

The vast difference in morphology between microcrystalline and nanocrystalline material is shown in **Figure 1.15**. Studies have noted that sp^2 carbon resides primarily at grain boundaries, thus UNC material typically contains more sp^2, which is evident in the electrochemical response observed.[86,87]

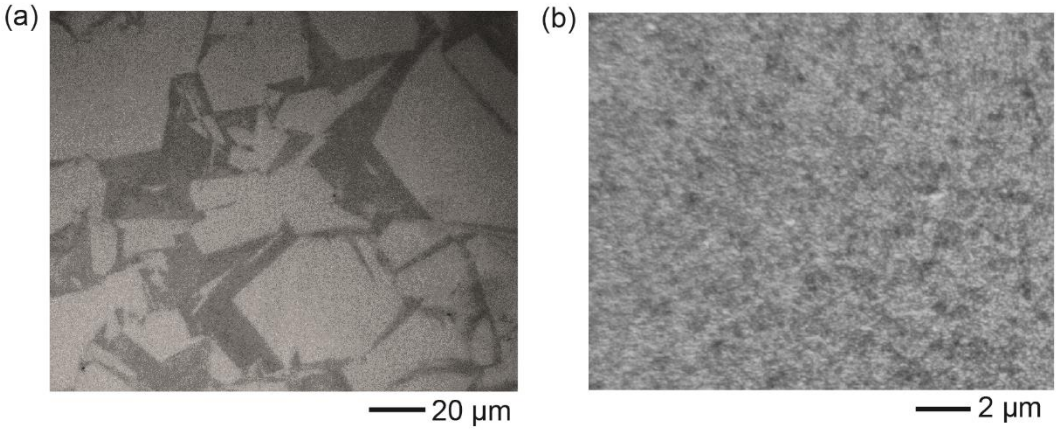

***Figure 1.15**: Optical images for (a) microcrystalline BDD (×50 objective) and (b) nanocrystalline BDD (×100 objective).*

Furthermore, as-grown surfaces are typically rougher than polished BDD. Care must therefore be taken to correctly determine the surface area of the BDD material to ensure comparable capacitance values. It has also been noted that poor polishing of BDD material may cause sub-surface damage, creating defect sites that can trap charge carriers.[29] The polishing process must therefore be carefully controlled in order to not adversely impact on the electrochemical properties of the BDD.[62]

1.6 sp^2 characterisation techniques

Characterisation of BDD material is essential for electroanalytical applications. As discussed in **Chapter 1.5.3** both the SW and capacitance values can be used as an indicator of sp^2 content.

1.6.1 Raman Spectroscopy

Laser Raman spectroscopy is a widely used analytical technique as it is non-destructive and requires minimal sample preparation.[88] The technique involves shining monochromatic light perpendicular to the sample of interest. A small fraction (approximately 1 in 10 million photons) of the incident beam is affected by inelastic scattering, where a photon interacts with the rotational and vibrational modes of a molecule, exciting it from the ground state to a virtual energy state.[89] Relaxation then occurs, with the molecule returning to an energy state different to the original, resulting in the emission of a photon. The change in frequency of the photon emitted is then measured, with a decrease and increase in photon energy described as Stokes and anti-

Stokes respectively.[90] Typically a range of laser wavelengths (from visible to ultraviolet) are employed.

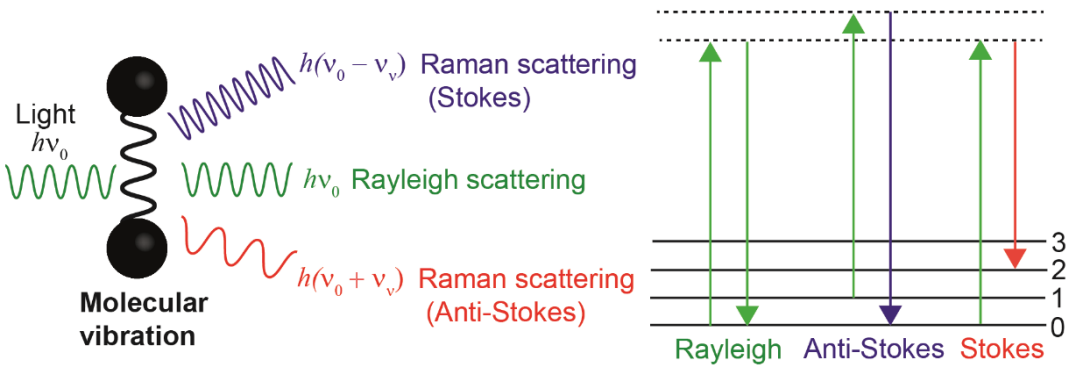

***Figure 1.16*: *Energy level diagram showing the elastic Raleigh scattering, and the in elastic scattering, Stokes and Anti-stokes scattering which give rise to the Raman signal.*[90]**

Raman spectroscopy is a useful analytical technique for the characterisation of diamond materials as it (1) can qualitatively assess the quality of the film; (2) provides information of the various different types of carbon present, such as diamond, amorphous carbon and graphite; (3) provide insight to the B dopant density and (4) is non-destructive.[91] Diamond has as single zone centre optical phonon line occurring at 1332 cm^{-1}, shown in **Figure 1.17**. Throughout this thesis, this peak is referred as the sp^3 peak. Looking at the intensity and full width half maximum (FWHM) of the 1332 cm^{-1} peak provides an indication of the quality of the film. High quality diamond exhibits a sharp sp^3 peak (FWHM is approximately 1.9 cm^{-1}), with peak broadening indicative of defects (sp^2 phases, point defects) due to a shorter phonon lifetime.[92] Thus quality of been shown that diamond films with a higher boron dopant level are typically more defective, thus exhibit a wider FWHM.[93] The incorporation of sp^2 during the growth process is indicated by the occurrence of further Raman signals at

1550 cm^{-1} (G peak) and 1355 cm^{-1} (D peak).[94] To assess BDD quality it is common for the sp^3/G peak ratio to be calculated.[95]

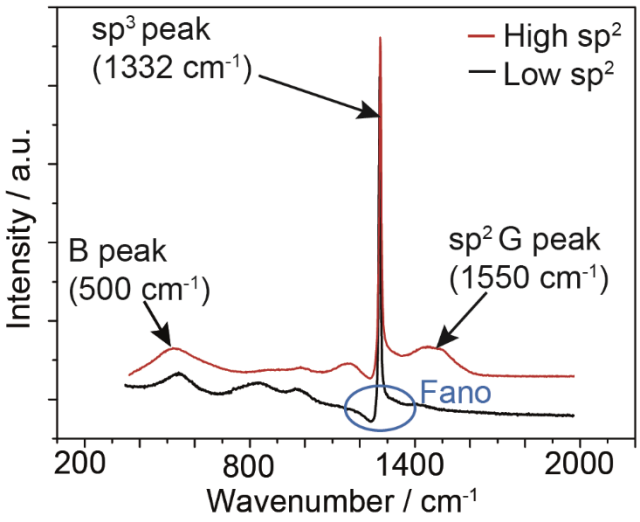

Figure 1.17*: *Visible (514 nm) Raman spectra for BDD with high and low sp^2 content, showing the peaks for diamond, sp^2 carbon and boron, along with sp^3 peak and the asymmetry associated with Fano resonance.

The Raman spectrum of diamond can also be used to qualitatively evaluate the B dopant density of BDD. Heavily doped BDD ($\geq 10^{20}$ B cm^{-3}) results in asymmetry of the 1332 cm^{-1} peak (Fano effect), which occurs due to interference between the zone-centre diamond phonons and the continuum of electronic excitations induced due to the presence of the dopant. It has been shown a peak at 500 cm^{-1} occurs for BDD (shown in **Figure 1.17**) corresponding to boron.[96] This peak can be used to quantitatively assess the B dopant concentration with the peak downshifting with increasing B concentration.[65] Different laser wavelengths have also been shown to exacerbate different features. For example, using a 785 nm line a peak at 1087 cm^{-1} is observed if diamond nanocrystallites are present and trans-polyacetylene (1076 cm^{-1}) at grain boundaries can be observed at 632 nm.[97]

Whilst Raman is considered a 'gold standard' for diamond characterisation, whether Raman as truly a reliable assessment of the quality of BDD for electrochemical applications is discussed in this thesis. The fact that Raman penetration depth is typically several microns is not ideal for the electrochemist, where only the surface of the BDD is important.[98] Furthermore, Raman is a one spot technique (limited by the resolution of the laser – typically μm's). As BDD polycrystalline material is spatially heterogeneous this can result in vastly different Raman spectra across the same sample.[80] Additionally, the sp^3 peak is affected by boron dopant concentration, with high [B] resulting in reduced peak intensities.[95] This makes comparison of sp^3/G peak ratios for samples with differing [B] not possible.

1.7 Issues with current sensing technologies

It has been discussed that BDD exhibits many properties that make it an ideal material for electroanalysis. Work in this thesis explores utilising these beneficial properties for the advancement in sensor technologies in two key areas: (1) heavy metal detection and (2) pH sensing. It is therefore important to understand the current measurement techniques available.

1.7.1 Heavy metal detection

The detection of heavy metals is extremely important due their toxicity even at trace concentrations.[99] For this reason, tight legislation is in place to ensure public health, with wide-scale monitoring of heavy metal contamination required. The presence of heavy metals in the environment can arise from both natural and anthropogenic

sources, with common contaminants including the 'big four': mercury (Hg), lead (Pb), cadmium (Cd) and arsenic (As). Taking Hg as an example, the maximum permitted concentration of Hg in the drinking water is 2 parts-per-billion (ppb).[100]

1.7.1.1 Inductively coupled plasma mass spectrometry (ICP-MS)

The main analytical method for heavy metal analysis is ICP-MS due to its low detection limit capability (parts per trillion), high sample throughput and the isotopic information that it provides.[101] The method involves an ICP torch, consisting of a plasma tube and a radio frequency (RF) coil, shown in **Figure 1.18**.[102]

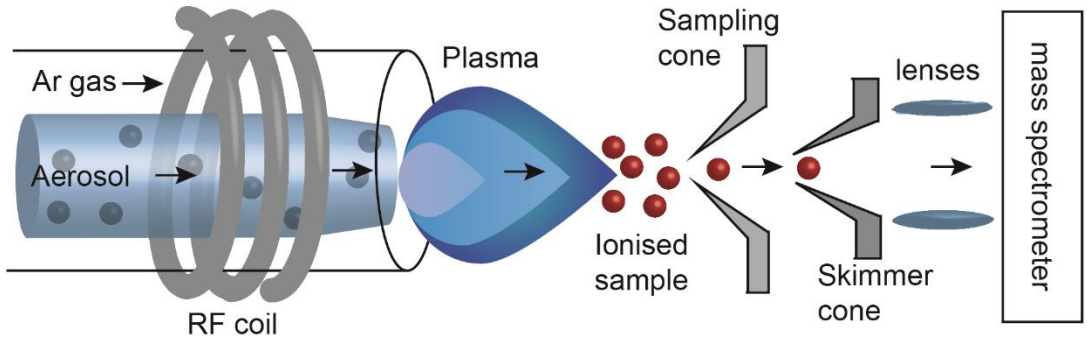

***Figure 1.18*: *Schematic of the ICP torch and sampling setup in an ICP-MS.*[103]**

Argon gas is flowed into the system and seeded with a spark, ionising the argon. The generated ions are accelerated towards the RF coil, colliding with other argon molecules, creating high temperatures (~6000 °C).[103] The sample of interest is turned into an aerosol by introduction to a nebuliser and undergoes atomisation in the high temperature plasma. This acts to break down the sample into its constituent ions. The ionised sample is then analysed in the mass spectrometer through sampling and skimmer cones, designed to refine the ion beam, where ions are separated based on

their mass to charge (m/z) ratio, providing a fully quantitative breakdown of the elemental composition of the sample.[103] Unfortunately, ICP-MS is relatively expensive and bulky, meaning it is not easily amenable to in-situ analysis. Samples must also be (i) filtered before analysis, with any particulates capable of blocking the nebuliser and (ii) acidified to ensure a stable plasma, and polyatomic interferences can occur.[104]

1.7.1.2 Electrochemistry

Electrochemistry presents a simple, portable alternative to ICP-MS and is capable of achieving low detection limits in the ppb range.[37] The most prevalent electrochemical method for heavy metal detection is anodic stripping voltammetry (ASV), illustrated in **Figure 1.19**.[105] The method involves applying a reduction potential to an electrode, resulting in the electroplating of metal ions from solution onto an electrode surface. After a defined deposition time, a suitable oxidative potential is applied resulting in the subsequent stripping of the metal off the electrode surface, resulting in a faradic current response.[106]

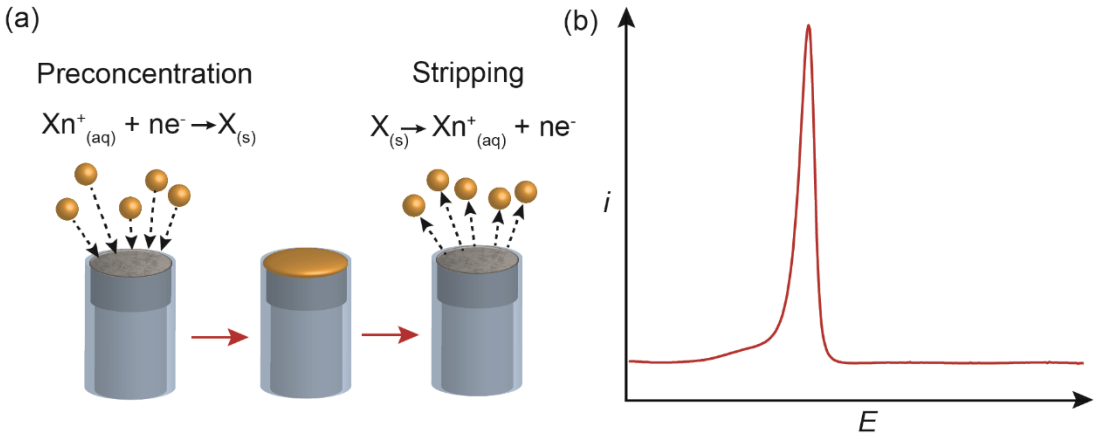

***Figure 1.19**: (a) Illustration of ASV preconcentration of metal ions and subsequent stripping step and (b) typical stripping peak for an electroactive species.*

Historically, the hanging mercury drop electrode (HMDE) was the electrode of choice due to the formation of a liquid amalgam, during metal preconcentration, and enabling the attainment of excellent detection sensitivities (ppb). However, due to the toxicity of the HMDE, a variety of electrode materials have been used including Au, Pt and GC and iridium oxide.[107] Research has shown that BDD is a viable alternative for HDME, achieving ppb detection limits due to the inherently low background currents of the material.[108] To this end, modification of BDD with Au nanoparticles has also been conducted to enable ASV detection of metals that do not readily deposit onto the BDD surface whilst utilising the low capacitance of diamond.[109]

ASV is reliant on the current magnitude or area (charge transferred) scaling with the concentration of the analyte of interest. Unfortunately, this can be affected by factors such as co-deposition and perturbation of the deposited metal layer during the preconcentration step.[110] Furthermore, whilst the position of the stripping peaks is used to identify the heavy metals present in solution, changes in matrix can shift the peak positions.[111] Multiple peaks have also been associated with just one analyte, relating

to the morphology of the deposited metal and peak overlap often occurs, making it difficult to identify all metals present.[112,113]

1.7.1.3 X-ray fluorescence (XRF)

XRF analysis provides several significant advantages over ICP-MS. These include: (1) the development of handheld portable devices, ideal for in situ analysis; (2) simple (if any) sample preparation and (3) the possibility to perform non-destructive analysis.[114] Furthermore, commercial XRF instruments typically can measure any element from Na and U in the periodic table.[115] XRF has therefore been used to study a large variety of elemental species in a wide range of applications including analysis of archaeological sites[116] and artefacts,[117] environmental monitoring,[118] pharmaceuticals[119] and foodstuffs.[120,121]

The technique works by irradiating a sample of interest, in solid, liquid or powder form. When the sample is irradiated with X-ray photons of sufficient energy (higher than the electron binding energy), an electron will be ejected from one of the orbitals, creating a 'hole' or initial vacancy.[115] In an attempt to restore the original electron configuration and stability of the atom, an electron from one of the outer orbitals is transferred to the inner orbital to fill the initial vacancy. The excess energy from this transition is emitted as an X-ray photon (fluorescence), illustrated in **Figure 1.20a**.[122] This emitted energy (or line) can then be recorded, giving rise to an XRF spectrum (**Figure 1.20b**).

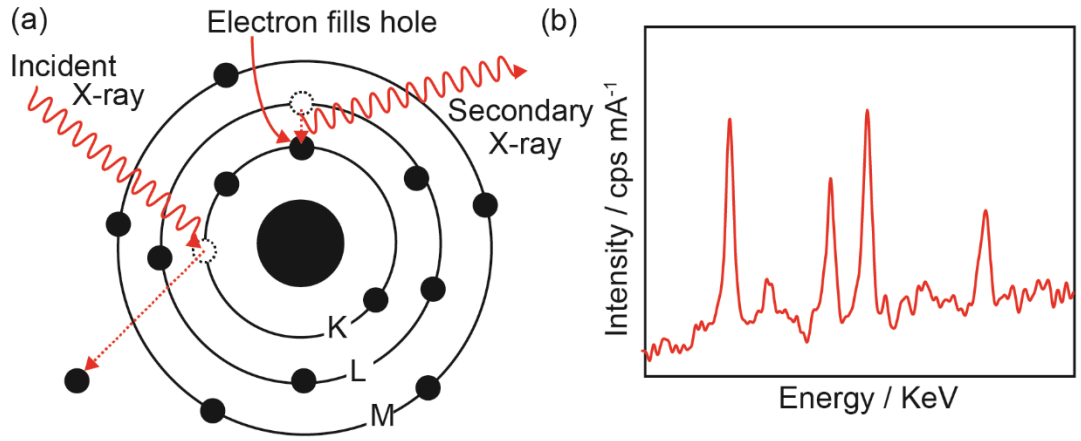

Figure 1.20: *(a) schematic showing the irradiation of an atom, generating fluorescence. (b) Illustrative example of an XRF spectrum, with each peak indicative of unique elemental fluorescence.*[122]

In reality, when an element is exposed to a beam of X-ray photons multiple electron ejections can occur, creating many 'holes' in different orbitals. As different electrons from within the atom can be transferred to these holes and each atom has specific energy levels, the lines emitted (e.g. Kα, Lα, Lβ) are characteristic of that particular element.[122] This creates a characteristic XRF 'fingerprint' of each element which can be used for identification. Furthermore, these lines typically scale with concentration making XRF a quantitative technique.[115] Typical XRF methods include Energy Dispersive (ED) and Wavelength Dispersive (WD). For samples with an unknown composition ED-XRF is used as the entire spectrum is acquired simultaneously.[115] However, compared to WD-XRF the resolution is significantly reduced (150 eV compared to 20 eV for WD) which can lead to element line overlap.[123] For this reason, for routine analysis (where specific analytes are being assessed) WD-XRF is often preferred, where a particular wavelength is detected.[123]

Despite the advantages of XRF, the technique suffers from poor limits of detection (LODs) in the parts per million (ppm) range for both ED and WD compared to that of ICP-MS (sub-ppb) and is therefore not capable of reaching sensitivities required for many applications.[124,125] Several methods to improve XRF LODs have thus emerged. Improvements to the technique has led to the development of total-reflection XRF (TR-XRF), which utilises an angle of incident radiation below the critical angle, resulting only the surface of the sample being irradiated (~ top 10 nm, depending on the material).[126] This reduces instrumental background noise typically arising from scattered radiation, thus measurement sensitivity is improved. Furthermore, the detector can be position much closer to the sample, resulting in the emitted fluorescence being detected with high efficiency.[127,128] Preconcentration methods such as ion exchange,[129] evaporation, precipitation[130] and liquid-liquid extraction[131] techniques have also been explored, with the aim to concentrate the analyte of interest before conducting XRF analysis. For some species, the LOD is notably improved (to ppb) using the Rigaku evaporative technology, the UltraCarry®, however the method is time-consuming, typically taking over 1 hour to complete.[132]

Researchers at Warwick have recently developed electrochemical XRF (EC-XRF) to improve XRF detection limits.[132] The technique works by electrochemically preconcentrating (by electrochemical deposition) the species of interest onto a BDD surface, similar to that ASV. However, unlike in ASV, where identification and quantification of the species in solution is conducted by electrochemically stripping after deposition, XRF is instead used to identify and quantify the analyte. BDD is the ideal substrate for EC-XRF, not only due to its exceptional electrochemical properties, but also due to the fact that both boron and carbon atoms are not detectable by XRF

due to their low Z number. Using EC-XRF detection limits have been shown to be improved by over four orders of magnitude to sub-ppb levels and an in-situ device has been demonstrated.[132,133]

1.7.2 pH sensing

The concept of the pH scale was first introduced in 1909 by Danish Chemist Søren Peder Lauritz Sørensen, working at the Carlsberg laboratory in Copenhagen.[134] His real innovation was to quantify acidity as the negative logarithmic function of proton activity (aH^+), thereby defining pH as in **Equation 1.9**:[135]

$$pH = -\log_{10} aH^+ \qquad (1.9)$$

pH measurements are made in a wide range of industries, including the manufacture of biomedicine,[136] food production, waste management and environmental monitoring.[137] Even the slightest change in pH can affect a whole chemical process, therefore a wide range of pH sensors have been developed.

1.7.2.1 Optical

The majority of optical pH sensors comprise of colorimetric reagents immobilised on a porous membrane, utilising techniques such as absorbance, fluorescence and reflectance for pH determination.[138,139] Example dyes include phenol red, which changes from red at high pH to yellow at low pH and fluorescein isothiocyanate. The sensors are low-cost, can easily be miniaturised, offer high selectivity and are not subject to electromagnetic interference.[140] However, unfortunately the typical pH response of dye-based pH sensors is sigmoidal, with only a very small dynamic range

(five pH units maximum) and is suited to only measure the pH of near neutral solutions.[141] Furthermore, the sensors are typically one use, often suffer from photodegradation of the dye, limiting the long term stability and are subject to ionic strength errors.[142]

1.7.2.2 Glass pH probe

The most prevalent electrochemical pH sensor is the glass pH probe (shown in **Figure 1.21**) due to its wide dynamic range from pH 2 –12, high sensitivity and relatively fast response time.[143,144]

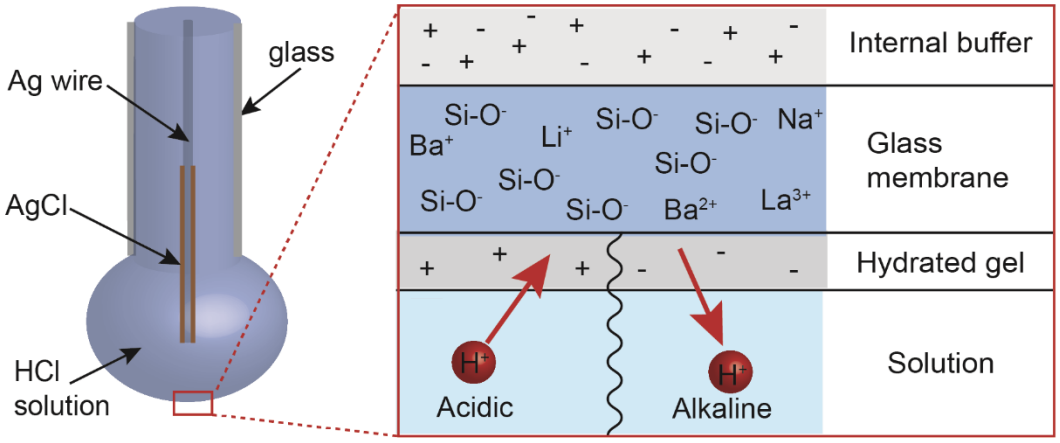

Figure 1.21: Illustration of the glass pH electrode and the glass membrane interface.

The sensor is fundamentally a hydrogen ion selective electrode (ISE), comprised of a RE (typically an Ag|AgCl RE) held at a constant potential and a thin glass membrane (ca 0.1 mm thick), coupled with an external RE.[145] The glass membrane consists mainly of amorphous silicon dioxide, with additional alkali metal ions embedded within its matrix. The pH sensing capability arises from ion exchange that occurs at this glass membrane, with the silicon oxide groups becoming protonated when

submerged in solution. An equilibrium is established, with the degree of protonation dictated by the solution pH, creating a potential difference at the glass membrane/solution interface.

The measured potential can be related mathematically to the solution pH via the Nernst equation:

$$E = E^{o} - \frac{2.303\ RT}{nF}\text{pH} \qquad (1.10)$$

Thus at T=298 K a Nernstian dependence on proton activity is predicted to be 59 mV per pH unit. The glass pH electrode is however subject to several issues. The glass is inherently fragile, making the sensor often not suitable for in-situ measurements or high-pressure, high-temperature applications. It also must be stored hydrated to maintain its functionality. Furthermore, at high pH values, the sensor is subject to 'alkali' errors where alkali cations of similar charge and size to protons, such as Li^{+}, Na^{+}, K^{+} and Ca^{2+} can bind to the glass membrane resulting in erroneous pH measurements.[146,147] Strong alkali solutions can also etch and permanently damage the glass pH probe.

1.7.2.3 Solid state pH sensors

Ion-Selective Field Effect Transistors (ISFET) devices have become increasingly popular in recent years due to the technology addressing the fragility of the glass pH electrode and the fact the sensors can be stored dry.[148,149] ISFET pH measurements work by controlling the current between two semiconductor electrodes. To do this, the two electrodes are separated by a third electrode (the gate) that is in direct contact with

the solution of interest integrated into a silicon chip.[150] The gate is made of a proton sensitive chemical layer such as silicon oxide, silicon nitride and aluminium oxide, which when exposed to solution becomes hydrated.[151] This layer then acts as a surface charge transfer layer, enabling current to flow from one of the semiconducting electrodes to the other. The degree of protonation of the gate (thus the solution pH) dictates the voltage observed, which exhibits a Nernstian dependence. The technology however still has inherent issues, with ISFET devices often having drift issues and experiencing blockages when placed in real-world solutions such as wastewater.[152] Exposure to certain chemicals such as chlorine and other aggressive media also permanently damages ISFET devices.

A variety of hydrogen sensitive metal oxide probes have also emerged, such as ruthenium oxide, manganese oxide and tin oxide.[153] Unfortunately they are subject to drift issues and are subject to redox interferences.[154] It has also been found that with increasing sensitivity, the response time increases dramatically and the stability is greatly reduced.[155] Iridium oxide (IrOx) is a popular choice for pH sensing, particularly as it can be miniaturised and is biocompatible.[156,157] Unfortunately, in order to provide stable potentials the IrOx film must stay hydrated.[158]

Limited studies have also been conducted with BDD. For example, as BDD exhibits an extended SW, chronopotentiometry was employed to assess the potential dependent pH response for a fixed current threshold.[159,160] Unfortunately, this method can suffer from redox interferences. Potentiometric methods have also been explored, with BDD O-terminated by oxygen plasma treatment.[161] The pH response was however reported as sub-Nernstian and the sensor was stable for only two days.[161]

1.7.2.4 Quinone electrochemistry

Voltammetric pH sensing with carbon electrodes has been explored in great detail due to their low cost and robust nature.[162] Typically, the electrode surface is chemically functionalized with pH sensitive molecules, with quinone moieties a popular choice.[162,163] Quinone electrochemistry has been widely studied, with the possible reaction mechanisms summarised in the generalised scheme of squares in **Figure 1.22**.[164]

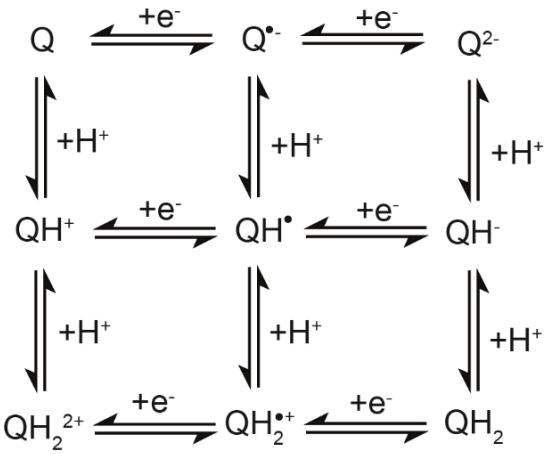

Figure 1.22: Generalised quinone scheme of squares.[164]

The simplest and most studied quinone mechanism is the $2e^-$ reaction ($Q + 2e^- \rightleftharpoons Q^{2-}$) that occurs in buffered aprotic solution.[165] The voltammetric response typically has two well defined redox peaks and is pH independent.[165] In buffered aqueous media, quinone species are considered to operate under a proton coupled electron transfer (PCET) regime ($2e^-$, $2H^+$), summarised in **Equation 1.11**. It is widely accepted that this happens via a *stepwise* pathway, where both the electron and proton are transferred in a single kinetic step.[166] Due to potential inversion, where the transfer of the second electron is more favourable that the first, only one redox peak is observed.[166]

$$Q + 2H^+ + 2e^- \rightleftharpoons QH_2 \qquad (1.11)$$

By substituting this into the Nernst equation (**Equation 1.12**) it is apparent that the voltammetric response changes by 59 mV per pH unit at 298 K:

$$E = E^{o} + \frac{0.0592}{2}\text{pH}\,\frac{[Q]}{[QH_2]} - 0.0592\ \text{pH} \qquad (1.12)$$

As the pH of the solution is increased and the pK_{a1} of the quinone is reached (shown in **Figure 1.23**), a 2e$^-$, H$^+$ reaction proceeds, equating to a 30 mV / pH unit change. By increasing the pH further, once pK_{a2} is reached (see **Figure 1.23**), a proton independent electron transfer (ET) reaction (2e$^-$) occurs.[164] Often pK_{a1} and pK_{a2} are coincident.[163]

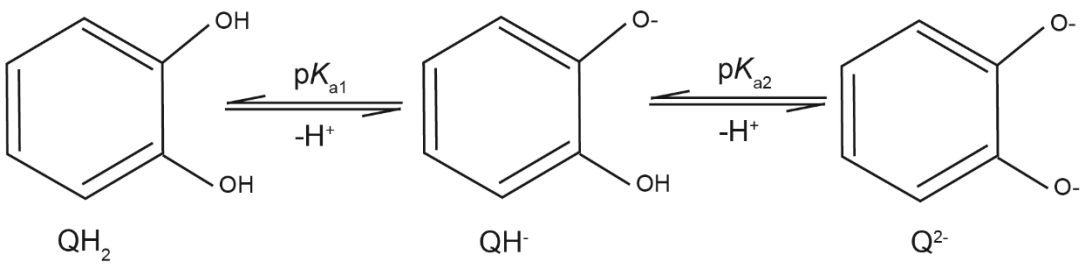

***Figure 1.23**: Schematic of the deprotonation of the quinone catechol showing pK_{a1} and pK_{a2}.[167]*

It is thus evident that for a reliable pH sensor, the reaction outlined in **Equation 1.11** is preferable, providing the highest sensitivity for protons.

Unfortunately, the quinone based electrodes are not without their disadvantages. Functionalisation procedures are often complex and time-consuming, requiring a number of reagents.[162] The stability of the quinone moieties on the surface of the electrode is also a problem, particularly at elevated temperatures and pressures, and mechanical abrasion to clean the surface is not suitable. Work utilising inherent quinone groups on the surface of sp^2 containing carbon electrodes such as GC, EPPG

and SPE has emerged to mitigate these problems.[168,169,170] However, due to the catalytic nature of these electrodes oxygen reduction interference is an issue. Degassing of the solution of interest is therefore required to get measurable signals, which makes in-situ measurements problematic.[168]

Furthermore, quinone based pH technologies show deviation from 59 mV/pH unit in unbuffered aqueous media.[164] Theories behind this deviation are mixed, with some researchers suggesting that by conducting the electrochemical reduction of quinones in unbuffered solution, a localised change in pH at the electrode surface results due to the consumption of protons, resulting in the pH that is measured to be more alkaline than the bulk.[164,171] This effect is mirrored for quinone oxidation, resulting in a more acidic "effective pH" at the interface.[164] Others suggest that quinone moieties will respond similarly to that of buffered solution if $[H^+] > [Q]$.[164] It is thought that if $[H^+] < [Q]$ deviation occurs, where the quinone instead undergoes a $2e^-$ reduction to make the strongly hydrogen-bonded quinone dianion ($Q_2^-(H_2O)_{2n}$), resulting in pH independence.[164] Thus far, this still presents a major scientific challenge for quinone-based pH sensing technologies as many of commercial pH measurements are made in unbuffered media.[164]

1.8 Aims and objectives

This thesis aims to utilise the advantageous properties of BDD for the development of robust sensors for operation in extreme environments and complex matrices for both heavy metal detection and pH sensing. **Chapter 3** explores the use of EC-XRF by investigating the detection of palladium contamination in electroactive pharmaceutical products. Analysis is optimised to reduce EC-XRF analysis times in order to improve the techniques commercial viability.

In order to employ BDD for particular applications, the quality of the material must be fully understood, with sp^2 content affecting the mechanical, chemical and electrochemical performance. **Chapter 4** therefore focuses on the development of a new electrochemical characterisation technique of BDD to assess sp^2 content. To do this, the natural presence of electroactive quinone groups that exist on sp^2 carbon, but are absent on sp^3 carbon, are exploited advantageously. **Chapter 5** proceeds to demonstrate the newly developed electrochemical characterisation technique on thin film microcrystalline material, providing a detailed insight into changes in reactor growth conditions across BDD wafers in low-pressure, overmoded systems.

Chapter 6 details the development of a BDD pH sensor, created by the intentional introduction of sp^2 regions containing pH sensitive quinone groups onto the electrode surface using laser micromachining. The BDD pH electrodes are fully characterised and their pH performance is assessed in buffered solutions ranging from pH 2–12, as well as inter-sensor performance. Long term stability is also explored and the effect of possible redox interferences is explored as well as the effect of temperature on the pH response.

In **Chapter 7**, the complications of measuring pH of unbuffered solutions using quinone-like moieties is explored, with redesigns of the initial pH sensor conducted to obtain a linear, Nernstian pH response in unbuffered pH solutions across the pH range 1–14.

Finally, **Chapter 8** concludes the work presented in this thesis and discusses possible future directions of this work.

1.9 References

(1) Kraft, A. *Int. J. Electrochem. Sci*, **2007**, *2*, 355–385.
(2) Gicquel, A.;Hassouni, K.;Silva, F.;Achard, J. *Current Applied Physics*, **2001**, *1*, 479–496.
(3) Kozlov, S. F.;Belcarz, E.;Hage-Ali, M.;Stuck, R.;Siffert, P. *Nuclear Instruments and Methods*, **1974**, *117*, 277–283.
(4) Schein, J.;Campbell, K. M.;Prasad, R. R.;Binder, R.;Krishnan, M. *Review of Scientific Instruments*, **2002**, *73*, 18–22.
(5) Ganesan, K.;Garrett, D. J.;Ahnood, A.;Shivdasani, M. N.;Tong, W.;Turnley, A. M.;Fox, K.;Meffin, H.;Prawer, S. *Biomaterials*, **2014**, *35*, 908–915.
(6) Byrappa, K.;Ohachi, T. *Crystal growth technology*;Elsevier, **2003**, 99–101.
(7) Fujishima, A. *Diamond electrochemistry*;Elsevier, **2005**,12–32.
(8) Yoshimura, M.;Honda, K.;Kondo, T.;Uchikado, R.;Einaga, Y.;Rao, T. N.;Tryk, D. A.;Fujishima, A. *Diamond. Relat. Mater.*, **2002**, *11*, 67–74.
(9) Shin, D.;Tryk, D. A.;Fujishima, A.;Merkoçi, A.;Wang, J. *Electroanalysis*, **2005**, *17*, 305–311.
(10) Samudrala, G. K.;Moore, S. L.;Vohra, Y. K. *Materials*, **2015**, *8*, 2054–2061.
(11) Bundy, F.;Hall, H.;Strong, H. *Nature*, **1955**, *176*, 51–55.
(12) F G Celii, a.;Butler, J. E. *Annual Review of Physical Chemistry*, **1991**, *42*, 643–684.
(13) Davies, G. *Physica B: Condensed Matter*, **1999**, *273*, 15–23.
(14) D'Haenens-Johansson, U. F.;Katrusha, A.;Moe, K. S.;Johnson, P.;Wang, W. *Gems & Gemology*, **2015**, *51*, 3–15.
(15) Angus, J. C. *Diamond. Relat. Mater.*, **2014**, *49*, 77–86.
(16) Luong, J. H. T.;Male, K. B.;Glennon, J. D. *Analyst*, **2009**, *134*, 1965–1979.
(17) Angus, J. C.;Hayman, C. C. *Science*, **1988**, *241*, 913–921.
(18) Spear, K. E.;Dismukes, J. P. *Synthetic diamond: emerging CVD science and technology*;John Wiley & Sons, **1994**, 2–34.
(19) May, P. W. *Philosophical Transactions: Mathematical, Physical and Engineering Sciences*, **2000**, *358*, 473–495.
(20) Menon, P. M.;Edwards, A.;Feigerle, C.;Shaw, R.;Coffey, D.;Heatherly, L.;Clausing, R.;Robinson, L.;Glasgow, D. *Diamond. Relat. Mater.*, **1999**, *8*, 101–109.
(21) Pleskov, Y. V. *Russian Journal of Electrochemistry*, **2002**, *38*, 1275–1291.
(22) Lee, S. T.;Lin, Z.;Jiang, X. *Materials Science and Engineering: R: Reports*, **1999**, *25*, 123–154.
(23) Van Enckevort, W.;Janssen, G.;Vollenberg, W.;Schermer, J.;Giling, L.;Seal, M. *Diamond. Relat. Mater.*, **1993**, *2*, 997–1003.
(24) Lee, S.-T.;Lin, Z.;Jiang, X. *Materials Science and Engineering: R: Reports*, **1999**, *25*, 123–154.
(25) Angus, J. C.;Argoitia, A.;Gat, R.;Li, Z.;Sunkara, M.;Wang, L.;Wang, Y. *Philosophical Transactions of the Royal Society of London. Series A: Physical and Engineering Sciences*, **1993**, *342*, 195–208.
(26) Butler, J.;Mankelevich, Y. A.;Cheesman, A.;Ma, J.;Ashfold, M. *Journal of Physics: Condensed Matter*, **2009**, *21*, 364–386.
(27) Anthony, T. R. *The Physics and Chemistry of Carbides, Nitrides and Borides*; Springer Netherlands. 1990, 122–126.
(28) Ashfold, M. N. R.;May, P. W.;Rego, C. A.;Everitt, N. M. *Chemical Society Reviews*, **1994**, *23*, 21–30.

(29) Macpherson, J. V. *Phys. Chem. Chem. Phys.*, **2015**, *17*, 2935–2949.
(30) Williams, O. A. *Diamond. Relat. Mater.*, **2011**, *20*, 621–640.
(31) Wilson, N. R.;Clewes, S. L.;Newton, M. E.;Unwin, P. R.;Macpherson, J. V. *The Journal of Physical Chemistry B*, **2006**, *110*, 5639–5646.
(32) Balmer, R.;Brandon, J.;Clewes, S.;Dhillon, H.;Dodson, J.;Friel, I.;Inglis, P.;Madgwick, T.;Markham, M.;Mollart, T. *Journal of Physics: Condensed Matter*, **2009**, *21*, 364221.
(33) Wort, C. J. H.;Balmer, R. S. *Materials Today*, **2008**, *11*, 22–28.
(34) Wang, S.;ProQuest, **2008**. 34–37.
(35) Lagrange, J.-P.;Deneuville, A.;Gheeraert, E. *Diamond. Relat. Mater.*, **1998**, *7*, 1390–1393.
(36) Kuech, T. *Handbook of Crystal Growth: Thin Films and Epitaxy*;Elsevier, **2014**. 626–632.
(37) Bard, A. J.;Faulkner, L. R.;Leddy, J.;Zoski, C. G. *Electrochemical methods: fundamentals and applications*;Wiley New York, **1980**.
(38) Hagfeldt, A.;Boschloo, G.;Sun, L.;Kloo, L.;Pettersson, H. *Chemical Reviews*, **2010**, *110*, 6595–6663.
(39) Hanrahan, G.;Patil, D. G.;Wang, J. *J. Environ. Monitor.*, **2004**, *6*, 657–664.
(40) Heller, A.;Feldman, B. *Accounts of Chemical Research*, **2010**, *43*, 963–973.
(41) Chin, C. D.;Linder, V.;Sia, S. K. *Lab on a Chip*, **2007**, *7*, 41–57.
(42) Frew, J. E.;Hill, H. A. O. *Anal. Chem.*, **1987**, *59*, 933–944.
(43) Chen, G. *Separation and Purification Technology*, **2004**, *38*, 11–41.
(44) Martinez-Huitle, C. A.;Ferro, S. *Chemical Society Reviews*, **2006**, *35*, 1324–1340.
(45) Wang, J. *Analytical electrochemistry*;John Wiley & Sons, **2006**.
(46) Zoski, C. G. *Handbook of electrochemistry*;Elsevier, **2006**.
(47) Patten, H. V.;Meadows, K. E.;Hutton, L. A.;Iacobini, J. G.;Battistel, D.;McKelvey, K.;Colburn, A. W.;Newton, M. E.;Macpherson, J. V.;Unwin, P. R. *Angewandte Chemie International Edition*, **2012**, *51*, 7002–7006.
(48) Tan, S.-y.;Unwin, P. Macpherson, J. V.;Zhang, J.;Bond, A. M. *Anal. Chem.*, **2017**, 2830–2837.
(49) Banus, M. G. *Science*, **1941**, *93*, 601–602.
(50) Bott, A. *Current Separations*, **1995**, *14*, 64–69.
(51) Kissinger, P. T.;Heineman, W. R. *Journal of Chemical Education*, **1983**, *60*, 702.
(52) Compton, R. G.;Banks, C. E. *Understanding voltammetry*;World Scientific, **2007**.
(53) Monk, P. M. *Fundamentals of electro-analytical chemistry*;John Wiley & Sons, **2008**. 162–163.
(54) Forster, R. J. *Chemical Society Reviews*, **1994**, *23*, 289–297.
(55) Jahn, D.;Vielstich, W. *J. Electrochem. Soc.*, **1962**, *109*, 849–852.
(56) Opekar, F.;Beran, P. *Journal of Electroanalytical Chemistry and Interfacial Electrochemistry*, **1976**, *69*, 1–105.
(57) Cooper, J. A.;Compton, R. G. *Electroanalysis*, **1998**, *10*, 141–155.
(58) Nikolic, J.;Expósito, E.;Iniesta, J.;González-Garcia, J.;Montiel, V. *Journal of Chemical Education*, **2000**, *77*, 1191.
(59) Osteryoung, J. G.;Osteryoung, R. A. *Anal. Chem.*, **1985**, *57*, 101–110.
(60) Ramaley, L.;Krause, M. S. *Anal. Chem.*, **1969**, *41*, 1362–1365.
(61) Dogan-Topal, B.;Ozkan, S. A.;Uslu, B. *The Open Chemical and Biomedical Methods Journal*, **2010**, *3*, 56–73.
(62) Hutton, L. A.;Iacobini, J. G.;Bitziou, E.;Channon, R. B.;Newton, M. E.;Macpherson, J. V. *Anal. Chem.*, **2013**, *85*, 7230–7240.

(63) Patten, H. V.;Lai, S. C. S.;Macpherson, J. V.;Unwin, P. R. *Anal. Chem.*, **2012**, *84*, 5427–5432.
(64) Watanabe, T.;Honda, Y.;Kanda, K.;Einaga, Y. *physica status solidi (a)*, **2014**, *211*, 2709–2717.
(65) Bernard, M.;Deneuville, A.;Muret, P. *Diamond. Relat. Mater.*, **2004**, *13*, 282–286.
(66) Visser, E. P.;Bauhuis, G.;Janssen, G.;Vollenberg, W.;van Enckevort, J.;Giling, L. *Journal of Physics: Condensed Matter*, **1992**, *4*, 7365.
(67) Yagi, I.;Notsu, H.;Kondo, T.;Tryk, D. A.;Fujishima, A. *J. Electroanal. Chem.*, **1999**, *473*, 173–178.
(68) Thomas, R. E.;Rudder, R. A.;Markunas, R. J. *Journal of Vacuum Science & Technology A*, **1992**, *10*, 2451–2457.
(69) Liu, F. B.;Wang, J. D.;Liu, B.;Li, X. M.;Chen, D. R. *Diamond. Relat. Mater.*, **2007**, *16*, 454–460.
(70) Kondo, T.;Ito, H.;Kusakabe, K.;Ohkawa, K.;Einaga, Y.;Fujishima, A.;Kawai, T. *Electrochim. Acta.*, **2007**, *52*, 3841–3848.
(71) Boukherroub, R.;Wallart, X.;Szunerits, S.;Marcus, B.;Bouvier, P.;Mermoux, M. *Electrochem. Commun.*, **2005**, *7*, 937–940.
(72) Charrier, G.;Lévy, S.;Vigneron, J.;Etcheberry, A.;Simon, N. *Diamond. Relat. Mater.*, **2011**, *20*, 944–950.
(73) Girard, H.;Simon, N.;Ballutaud, D.;Herlem, M.;Etcheberry, A. *Diamond. Relat. Mater.*, **2007**, *16*, 316–325.
(74) Szunerits, S.;Jama, C.;Coffinier, Y.;Marcus, B.;Delabouglise, D.;Boukherroub, R. *Electrochem. Commun.*, **2006**, *8*, 1185–1190.
(75) Szunerits, S.;Boukherroub, R. *J. Solid. State. Electr.*, **2008**, *12*, 1205–1218.
(76) Yang, W.;Baker, S. E.;Butler, J. E.;Lee, C.-s.;Russell, J. N.;Shang, L.;Sun, B.;Hamers, R. J. *Chemistry of Materials*, **2005**, *17*, 938–940.
(77) Strobel, P.;Riedel, M.;Ristein, J.;Ley, L. *Nature*, **2004**, *430*, 439–441.
(78) Jürgen, R. *Journal of Physics D: Applied Physics*, **2006**, *39*, 71.
(79) Holt, K. B.;Bard, A. J.;Show, Y.;Swain, G. M. *The Journal of Physical Chemistry B*, **2004**, *108*, 15117–15127.
(80) Patten, H. V.;Hutton, L. A.;Webb, J. R.;Newton, M. E.;Unwin, P. R.;Macpherson, J. V. *Chemical Communications*, **2015**, *51*, 164–167.
(81) Martin, H. B.;Argoitia, A.;Landau, U.;Anderson, A. B.;Angus, J. C. *J. Electrochem. Soc.*, **1996**, *143*, 133–136.
(82) Garcia-Segura, S.;Vieira dos Santos, E.;Martínez-Huitle, C. A. *Electrochem. Commun.*, **2015**, *59*, 52–55.
(83) Bennett, J. A.;Wang, J.;Show, Y.;Swain, G. M. *J. Electrochem. Soc.*, **2004**, *151*, 306–313.
(84) Watanabe, T.;Honda, Y.;Kanda, K.;Einaga, Y. *physica status solidi (a)*, **2014**, *211*, 2709–2717.
(85) Wang, X. H.;Ma, G. H. M.;Zhu, W.;Glass, J. T.;Bergman, L.;Turner, K. F.;Nemanich, R. J. *Diamond. Relat. Mater.*, **1992**, *1*, 828–835.
(86) Carlisle, J. A.;Auciello, O. *Interface-Electrochemical Society*, **2003**, *12*, 28–32.
(87) Cleri, F.;Keblinski, P.;Colombo, L.;Wolf, D.;Phillpot, S. *EPL (Europhysics Letters)*, **1999**, *46*, 671.
(88) Filik, J. *Spectroscopy Europe*, **2005**, *17*, 10.
(89) Ferraro, J. R.;Nakamoto, K.;Brown, C. W. *Introductory Raman Spectroscopy (Second Edition)*; Academic Press. 2003.

(90) Szymanski, H. A. *Raman spectroscopy: theory and practice*;Springer Science & Business Media, **2012**.
(91) Ferrari, A. C.;Robertson, J. *Philosophical Transactions of the Royal Society of London A: Mathematical, Physical and Engineering Sciences*, **2004**, *362*, 2477–2512.
(92) Pickard, C. D. O.;Davis, T. J.;Wang, W. N.;Steeds, J. W. *Diamond. Relat. Mater.*, **1998**, *7*, 238–242.
(93) Wang, W.;Polo, M.;Sanchez, G.;Cifre, J.;Esteve, J. *Journal of applied physics*, **1996**, *80*, 1846–1850.
(94) Prawer, S.;Nemanich, R. J. *Philosophical Transactions of the Royal Society of London A: Mathematical, Physical and Engineering Sciences*, **2004**, *362*, 2537–2565.
(95) Zaitsev, A. M. *Optical properties of diamond: a data handbook*;Springer Science & Business Media, **2013**. 98–120.
(96) Ushizawa, K.;Watanabe, K.;Ando, T.;Sakaguchi, I.;Nishitani-Gamo, M.;Sato, Y.;Kanda, H. *Diamond. Relat. Mater.*, **1998**, *7*, 1719–1722.
(97) Niaura, G.;Ragauskas, R.;Dikčius, A.;Šebeka, B.;Kuodis, Z. *chemija*, **2009**, *20*, 78–83.
(98) Ferreira, N. G.;Abramof, E.;Corat, E. J.;Trava-Airoldi, V. J. *Carbon*, **2003**, *41*, 1301–1308.
(99) Bremner, I. *Quarterly Reviews of Biophysics*, **1974**, *7*, 75–124.
(100) Duruibe, J.;Ogwuegbu, M.;Egwurugwu, J. *International Journal of Physical Sciences*, **2007**, *2*, 112–118.
(101) Skoog, D. A. *Fundamentals of analytical chemistry*;Grupo Editorial Norma, **2004**.
(102) Thomas, R. *Practical guide to ICP-MS: a tutorial for beginners*;CRC press, **2013**.
(103) Skoog, D. A.;West, D. M. *Principles of instrumental analysis*;Saunders College Philadelphia, **1980**.
(104) May, T. W.;Wiedmeyer, R. H. *Atomic Spectroscopy* **1998**, *19*, 150–155.
(105) Ellis, William D. *J. Chem. Educ* ,**1973**, *50*, 131–153.
(106) Copeland, T. R.;Skogerboe, R. K. *Anal. Chem.*, **1974**, *46*, 1257–1268.
(107) Hull, E.;Piech, R.;Kubiak, W. W. *Electroanalysis*, **2008**, *20*, 2070–2075.
(108) McGaw, E. A.;Swain, G. M. *Anal. Chim. Acta.*, **2006**, *575*, 180–189.
(109) Luong, J. H. T.;Lam, E.;Male, K. B. *Analytical Methods*, **2014**, *6*, 6157–6169.
(110) Prado, C.;Wilkins, S. J.;Marken, F.;Compton, R. G. *Electroanalysis*, **2002**, *14*, 262–272.
(111) Schonberger, E. A.;Pickering, W. F. *Talanta*, **1980**, *27*, 11–18.
(112) Hutton, L. A.;Newton, M. E.;Unwin, P. R.;Macpherson, J. V. *Anal. Chem.*, **2011**, *83*, 735–745.
(113) Fierro, S.;Watanabe, T.;Akai, K.;Yamanuki, M.;Einaga, Y. *International Journal of Electrochemistry*, **2012**, *2012*, 5.
(114) Thomsen, V.;Schatzlein, D. *Spectroscopy Europe*, **2002**, *17*, 14–21.
(115) Brouwer, P. *Almelo, Netherlands: PANalytical BV*, **2006**,
(116) Vittiglio, G.;Janssens, K.;Vekemans, B.;Adams, F.;Oost, A. *Spectrochimica Acta Part B: Atomic Spectroscopy*, **1999**, *54*, 1697–1710.
(117) Shackley, M. S. *Encyclopedia of Global Archaeology*; Springer New York. 2014.
(118) Kalnicky, D. J.;Singhvi, R. *Journal of Hazardous Materials*, **2001**, *83*, 93–122.
(119) Marguí, E.;Van Meel, K.;Van Grieken, R.;Buendía, A.;Fontàs, C.;Hidalgo, M.;Queralt, I. *Anal. Chem.*, **2009**, *81*, 1404–1410.

(120) Perring, L.;Andrey, D.;Basic-Dvorzak, M.;Hammer, D. *Journal of Food Composition and Analysis*, **2005**, *18*, 655–663.
(121) Reames, G.;Valerie Charlton MPH, M. *Journal of environmental health*, **2013**, *75*, 16.
(122) Beckhoff, B.;Kanngießer, B.;Langhoff, N.;Wedell, R.;Wolff, H. *Handbook of practical X-ray fluorescence analysis*;Springer Science & Business Media, **2007**.
(123) Zhan, X. *X-Ray Spectrometry*, **2005**, *34*, 207–212.
(124) Metz, U.;Hoffmann, P.;Weinbruch, S.;Ortner, H. M. *Microchimica Acta*, **1994**, *117*, 95–108.
(125) Kadachi, A. N.;Al-Eshaikh, M. A. *X-Ray Spectrometry*, **2012**, *41*, 350–354.
(126) Klockenkämper, R.;von Bohlen, A. *Total-reflection X-ray fluorescence analysis and related methods*;John Wiley & Sons, **2014**.
(127) Aiginger, H. *Spectrochimica Acta Part B: Atomic Spectroscopy*, **1991**, *46*, 1313–1321.
(128) Streli, C. *Applied Spectroscopy Reviews*, **2006**, *41*, 473–489.
(129) Blount, C. W.;Leyden, D. E.;Thomas, T. L.;Guill, S. M. *Anal. Chem.*, **1973**, *45*, 1045–1050.
(130) Panayappan, R.;Venezky, D. L.;Gilfrich, J. V.;Birks, L. S. *Anal. Chem.*, **1978**, *50*, 1125–1126.
(131) Igarashi, S.;Takahashi, A.;Ueki, Y.;Yamaguchi, H. *Analyst*, **2000**, *125*, 797–798.
(132) Hutton, L. A.;O'Neil, G. D.;Read, T. L.;Ayres, Z. J.;Newton, M. E.;Macpherson, J. V. *Anal. Chem.*, **2014**, *86*, 4566–4572.
(133) O'Neil, G. D.;Newton, M. E.;Macpherson, J. V. *Anal. Chem.*, **2015**, *87*, 4933–4940.
(134) Feldman, I. *Anal. Chem.*, **1956**, *28*, 1859–1866.
(135) Harris, D. C. *Quantitative Chemical Analysis*;W. H. Freeman, **2010**.
(136) Kurkdjian, A;Guern, J. *Annual Review of Plant Physiology and Plant Molecular Biology*, **1989**, *40*, 271–303.
(137) Banna, M. H.;Najjaran, H.;Sadiq, R.;Imran, S. A.;Rodriguez, M. J.;Hoorfar, M. *Sensor. Actuat. B-Chem.*, **2014**, *193*, 434–441.
(138) Leiner, M. J.;Hartmann, P. *Sensor. Actuat. B-Chem.*, **1993**, *11*, 281–289.
(139) Lin, J. *TrAC Trends in Analytical Chemistry*, **2000**, *19*, 541–552.
(140) Wencel, D.;Abel, T.;McDonagh, C. *Anal. Chem.*, **2014**, *86*, 15–29.
(141) Safavi, A.;Bagheri, M. *Sensor. Actuat. B-Chem.*, **2003**, *90*, 143–150.
(142) Narayanaswamy, R.;Wolfbeis, O. S. *Optical sensors: industrial environmental and diagnostic applications*;Springer Science & Business Media, **2003**. 285–286
(143) Boyes, W. *Instrumentation Reference Book* ;Butterworth-Heinemann: Boston, **2010**. 374–395.
(144) Pungor, E.;Toth, K. *Analyst*, **1970**, *95*, 625–648.
(145) Vanysek, P. *Electrochemical Society Interface*, **2004**, 19.
(146) Licht, S. *Anal. Chem.*, **1985**, *57*, 514–519.
(147) Sharma, B. *Instrumental methods of chemical analysis*;Krishna Prakashan Media, **2000**. 90–102.
(148) Duroux, P.;Emde, C.;Bauerfeind, P.;Francis, C.;Grisel, A.;Thybaud, L.;Arstrong, D.;Depeursinge, C.;Blum, A. *Gut*, **1991**, *32*, 240–245.
(149) Yuqing, M.;Jianrong, C.;Keming, F. *Journal of biochemical and biophysical methods*, **2005**, *63*, 1–9.
(150) Moretto, L. M.;Kalcher, K. *Environmental analysis by electrochemical sensors and biosensors*;Springer, **2014**. 745–755.

(151) Matsuo, T.;Esashi, M. *Sensors and Actuators*, **1981**, *1*, 77–96.
(152) Khanna, V. K. *Sensor Review*, **2007**, *27*, 233–238.
(153) Głab, S.;Hulanicki, A.;Edwall, G.;Ingman, F. *Critical Reviews in Analytical Chemistry*, **1989**, *21*, 29–47.
(154) da Silva, G. M.;Lemos, S. G.;Pocrifka, L. A.;Marreto, P. D.;Rosario, A. V.;Pereira, E. C. *Anal. Chim. Acta.*, **2008**, *616*, 36–41.
(155) Gill, E.;Arshak, K.;Arshak, A.;Korostynska, O. *Microsystem Technologies*, **2008**, *14*, 499–507.
(156) Wang, M.;Yao, S.;Madou, M. *Sensor. Actuat. B-Chem.*, **2002**, *81*, 313–315.
(157) VanHoudt, P.;Lewandowski, Z.;Little, B. *Biotechnology and bioengineering*, **1992**, *40*, 601–608.
(158) Nguyen, C. M.;Rao, S.;Yang, X.;Dubey, S.;Mays, J.;Cao, H.;Chiao, J.-C. *Sensors (Basel, Switzerland)*, **2015**, *15*, 4212-4228.
(159) Fierro, S.;Seishima, R.;Nagano, O.;Saya, H.;Einaga, Y. *Sci. Rep.*, **2013**, *3*, 1–10.
(160) Fierro, S.;Mitani, N.;Comninellis, C.;Einaga, Y. *Phys. Chem. Chem. Phys.*, **2011**, *13*, 16795–16799.
(161) Silva, E. L.;Bastos, A. C.;Neto, M. A.;Silva, R. F.;Ferreira, M. G. S.;Zheludkevich, M. L.;Oliveira, F. J. *Electrochem. Commun.*, **2014**, *40*, 31–34.
(162) Kahlert, H. *J. Solid. State. Electr.*, **2008**, *12*, 1255–1266.
(163) Xiong, L.;Batchelor-McAuley, C.;Compton, R. G. *Sensor. Actuat. B-Chem.*, **2011**, *159*, 251–255.
(164) Quan, M.;Sanchez, D.;Wasylkiw, M. F.;Smith, D. K. *J. Am. Chem. Soc.*, **2007**, *129*, 12847–12856.
(165) Guin, P. S.;Das, S.;Mandal, P. C. *International Journal of Electrochemistry*, **2011**, *1*, 22.
(166) Kim, R. S.;Chung, T. D. *Bulletin of the Korean Chemical Society*, **2014**, *35*, 3143–3155.
(167) Lee, P. T.;Harfield, J. C.;Crossley, A.;Pilgrim, B. S.;Compton, R. G. *RSC Advances*, **2013**, *3*, 7347–7354.
(168) Lu, M.;Compton, R. G. *Analyst*, **2014**, *139*, 4599–4605.
(169) Lu, M.;Compton, R. G. *Analyst*, **2014**, *139*, 2397–2403.
(170) Galdino, F. E.;Smith, J. P.;Kwamou, S. I.;Kampouris, D. K.;Iniesta, J.;Smith, G. C.;Bonacin, J. A.;Banks, C. E. *Anal. Chem.*, **2015**, 14–17.
(171) Dai, C.;Song, P.;Wadhawan, J. D.;Fisher, A. C.;Lawrence, N. S. *Electroanalysis*, **2015**, *27*, 917–923.

Chapter 2

Experimental

This chapter details the materials, chemicals, instrumentation and apparatus used throughout this thesis.

2.1 Materials

The freestanding BDD materials (i.e. removed from the growth wafer) used throughout this thesis, were supplied by Element Six Ltd., Harwell, UK, and manufactured using microwave CVD (described in Chapter 1). The average boron dopant concentration was determined to be 5×10^{20} atoms cm^{-3}, confirmed by secondary ion mass spectrometry (SIMS).[1] For the majority of studies the BDD was 470 µm thick. For EC-XRF measurements in Chapter 3 the BDD was polished to a thickness of 250 µm to minimise X-ray scattering.[2]

The ultrananocrystalline BDD thin-film material (2 µm thick) used in Chapter 4, was supplied by the Advanced Diamond Technologies (ADT) Inc., Illinois, USA, grown on a Nb substrate, with a boron dopant concentration of 1.6×10^{21} atoms cm^{-3}.[1] The 1 µm thin-film BDD used in Chapter 5, was grown by Dr. Soumen Mandel and Prof. Oliver Williams at Cardiff University, Department of Physics, using a Seki 6500 series Microwave Plasma reactor, run under multi-moded conditions, onto 500 µm thick 2-inch diameter silicon (100) p-type wafers.

2.2 Chemicals

***Table 2.1**: List of chemicals used throughout this thesis.*

Chemicals	Supplier	Details
Acetominophen, $C_8H_9NO_3$	≥99%	Sigma-Aldrich
Boric acid, H_3BO_3	99.97%	Sigma-Aldrich
Cadmium (II) nitrate, $Cd(NO_3)_2$	99.99%	Sigma-Aldrich
Caffeine, $C_8H_{10}N_4O_2$	99%	Sigma-Aldrich
Citric acid, $C_6H_8O_7$	≥99.5%	Sigma-Aldrich
Copper (II) nitrate, $Cu(NO_3)_2$	99.99%	Sigma-Aldrich
Hexaaminеruthenium (III) chloride, $Ru(NH_3)_6^{3+}$	99%	Strem Chemicals Ltd., U.K.
Hydrochloric acid, HCl	>37%	Sigma-Aldrich
Iron (III) chloride, $FeCl_3$	99.99%	Sigma-Aldrich
L-ascorbic acid, $C_6H_8O_6$	99%	Sigma-Aldrich
Lead (II) nitrate, $Pb(NO_3)_2$	99.99%	Sigma-Aldrich
Nitric acid, HNO_3	70%	Sigma-Aldrich
Palladium chloride, $PdCl_2$	99.0%	Sigma-Aldrich
Potassium hydroxide, KOH	≥99.97%	Sigma-Aldrich
Potassium nitrate, KNO_3	99.9%	Puratronic
Riboflavin, $C_{17}H_{20}N_4O_6$	99.9%	Sigma-Aldrich
Sulfuric acid, H_2SO_4	99.99%	Sigma-Aldrich
Tertiary sodium phosphate, Na_3PO_4	≥95%	Sigma-Aldrich
Zinc (II) chloride	≥98%	Sigma-Aldrich

2.3 Fabrication

2.3.1 BDD electrodes

Throughout this thesis 1 mm diameter BDD macroelectrodes were used, illustrated in in **Figure 2.1a** and **Figure 2.1b**. These were fabricated using an optimised in-house method.[3]

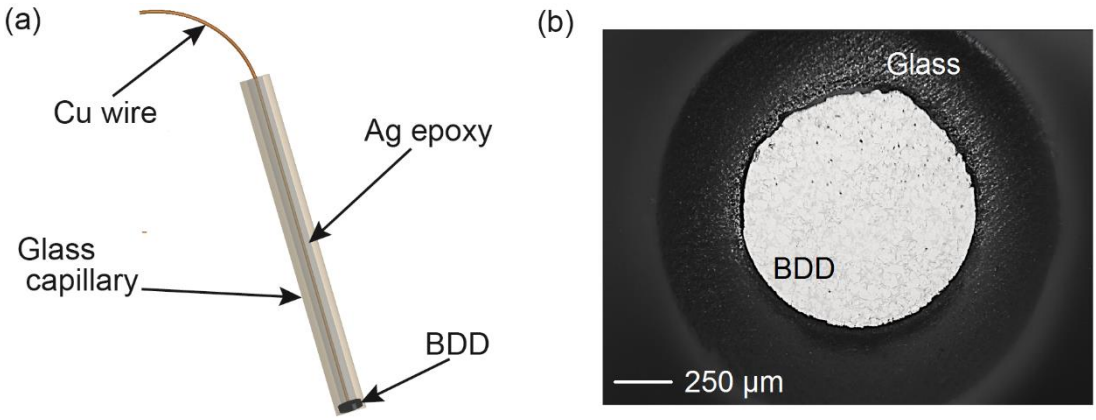

Figure 2.1*: *(a) Schematic of a BDD macroelectrode and (b) an optical image of a 1 mm BDD macroelectrode showing the glass/BDD seal.

BDD discs with a diameter of 1 mm were cut from a BDD wafer using a laser micromachiner (E-355H-3-ATHI-O system, Oxford Lasers). A kerfing program was incorporated into the lasering process to produce uniform disks. Several laser passes are required to cut through the wafer using the following laser parameters: 100% laser power, 20 kHz, machining speed of 1 mm s^{-1}.

2.3.1.1 Acid cleaning

The laser cut BDD discs were acid cleaned to remove any loose sp^2 and oxygen-terminate the BDD surface. The diamond disks were placed in concentrated H_2SO_4 (Fisher Scientific, 95%) which had been supersaturated with KNO_3 (Sigma Aldrich,

≥99.0%) for 30 minutes and heated (ca 200 °C) until the brown fumes produced became white (NO_2).[1] The disks were then removed from the solution, washed multiple times with ultra-pure water and then left to air dry on lint-free cloth.

2.3.1.2 Formation of an ohmic contact

A reliable ohmic connection was established (confirmed electrochemically – see **Chapter 2.5.3**) using by sputtering (Moorfield Minibox E606) layers of Ti and Au (10 nm and 400 nm respectively) onto the nucleation face of the diamond discs and subsequently annealing in a tube furnace for 5 hours at 400 ^{o}C. A carbide-based tunnelling contact between the carbon and titanium layer forms with a resistivity lower than 1 Ω cm.[4] The diamond disks were then placed into pulled borosilicate glass capillaries (2 mm outer diameter (OD), 1.16 mm inner diameter (ID), GC 200-10, Harvard Apparatus Ltd., Kent, U.K.) with the Au sputtered side facing the open capillary end. A vacuum was then applied and the diamond disks were heat sealed (Narishige PB-7) within the capillaries to seal the sides of the electrode. An external electrical contact was established by filling the glass capillary with silver epoxy (RS Components Ltd, Northants, U.K.) and inserting a tinned copper wire (OD = 0.5 mm).[3]

2.3.1.3 Polishing

The BDD discs were then exposed by polishing away the glass from the tip using carbimet abrasive discs (Buehler Ltd, Germany), incrementally moving from discs with grit sizes P120, P180 and P240 then finally exposing the BDD round out of the glass surround with a P1000 carbimet disc. Note, care must be taken to ensure that the

glass capillary is held perpendicular to the abrasive disks. Failure to do so, results in the exposure of the laser ablated edges of the BDD discs, which contains significant sp^2 carbon (*vide infra*). The electrodes were imaged (Olympus BH-2-HLSH) to check that all glass remnants had been removed from the electrode surface, exposing the full electrode area.

2.3.2 All Diamond Devices

Due to the robust nature of diamond, failure of a BDD sensor is most likely to arise due to the degradation of the insulating seal around the edge of the electrode. Typical materials for sealing include glass (used for the BDD electrodes in **Chapter 2.3.1**) and epoxy resin.[3] Furthermore, as the BDD material is laser micromachined to the required geometry, sp^2 carbon contamination down the sidewalls, arising from the ablation process, can occur if the sidewalls of the BDD round are exposed to solution. To overcome these problems, all-diamond devices have been fabricated where BDD electrodes are encased in insulating BDD (shown in **Figure 2.2**).[5] The devices are fabricated by laser micromachining the desired electrode geometry into an insulating diamond substrate, then overgrowing with a layer of BDD. The BDD layer is then polished back to reveal the coplanar all-diamond structure.[5] A variety of different electrode structures have been produced including band electrodes for conductivity measurements and ring-disc arrangements for heavy metal detection, as well as 1 mm macroelectrodes.[6,7]

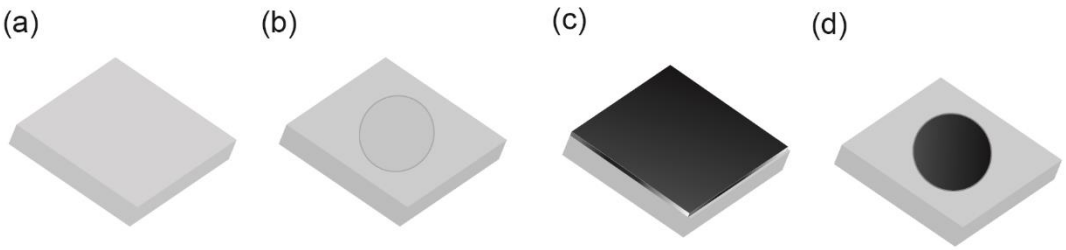

Figure 2.2: The all-diamond device manufacturing process including (1) the growth of insulating diamond; (2) the laser ablation of the insulating diamond in the pattern of the electrode required; (3) overgrowth of BDD and (4) the subsequent polish back of the material to reveal a BDD electrode coplanar with the intrinsic diamond surround.

2.3.3 Laser Micromachining

Laser micromachining has been utilised throughout this thesis in order to (1) machine BDD of appropriate sizes from larger CVD wafers, as well as to (2) create sp^2 containing features for electroanalytical and electrocatalytic applications. To do this, an incident laser pulse (a source of heat energy) is directed at the BDD, shown in **Figure 2.3a**.

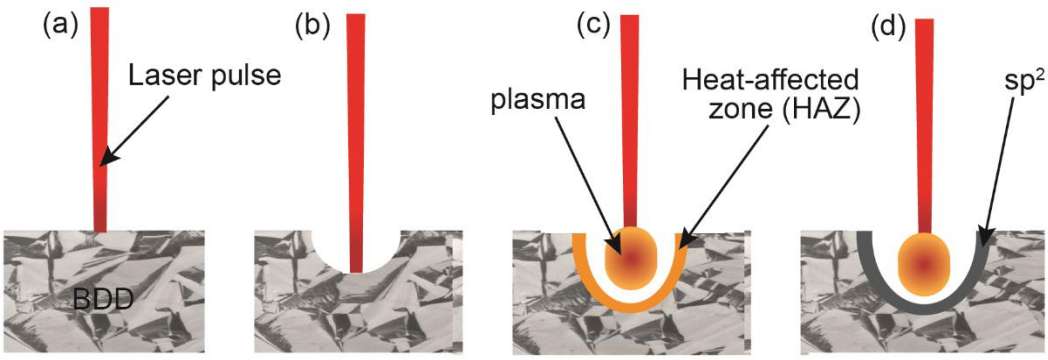

Figure 2.3: The laser micromachining process of BDD: (a) laser pulse hitting the BDD surface; (b) ablation (c) generation of a plasma and HAZ and (d) the generation of surface bound sp^2.

The heat energy is absorbed by the surface layers, resulting in subsequent ablation of the material (**Figure 2.3b**). This ablated material forms a highly energetic plasma, which is stabilised due to further laser pulses being delivered to the sample, resulting in an increase in temperature. The generated plasma further ablates the BDD surface and results in the generation of a heat-affected zone (HAZ), shown in **Figure 2.3c**. The energy generated in the HAZ is enough to induce a change in the bonding of the material (oxidisation of sp^3 to sp^2), graphitising the BDD surface (**Figure 2.3d**). Note, it is typically the size of the HAZ that dictates the resolution of the laser micromachining process (10 µm).

Laser micromachining was performed using an E-355H-3-ATHI-O system (Oxford Lasers Ltd.) operating a fully diode pumped solid state Nd:YAG laser (355 nm). The system average output power is 6 W (at 10 kHz), with a pulse duration of 34 ns and a laser pulse frequency range of 1–250 kHz.

2.4 Characterisation

2.4.1 Raman Spectroscopy

Raman spectroscopy was utilised to provide qualitative information on the quality (sp^2 content) of the BDD employed (see Chapter 1.6.1), as well as to verify that the boron dopant concentrations were above the metallic threshold in all samples. Note, Raman microscopy is not truly surface sensitive and this must be taken into account when interpreting the data. A Renishaw inVia Raman microscope was used for all measurements at room temperature (25 °C). A green Ar^+ laser of wavelength of 514.5

nm was primarily used for analysis, operating at a power of 10 mW, in conjunction with a × 50 objective, resulting in a spot size of ~10 µm.

2.4.2 Field Emission Scanning Electron Microscopy (FE-SEM)

FE-SEM is a microscopy technique that utilises an electron beam to produce high resolution images. Electrons are accelerated towards the sample of interest under vacuum by applying a potential difference between a field-emission cathode and anode, ranging from 0.1–50 kV.[8] The resolution is typically ~10 nm, limited by both the electron beam width and the volume of primary excitation of electrons in a solid (shown in **Figure 2.4a**).[9] When electrons strike the sample, several interactions may occur, shown in **Figure 2.4a**. Both secondary electron and backscattered electron emissions are used to create FE-SEM images.

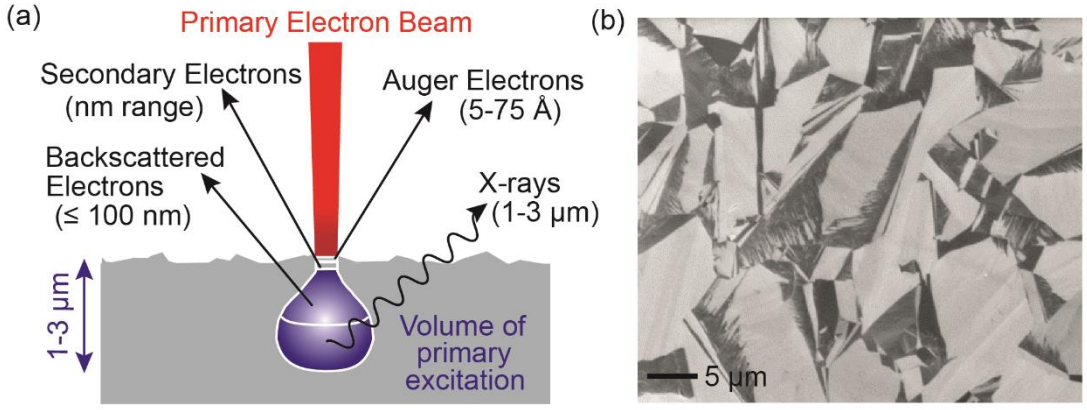

***Figure 2.4*: *(a) Schematic of FE-SEM interactions with a sample surface and (b) an in-lens backscattered electron image of high quality BDD.*[9]**

FE-SEM of BDD allows detailed observation of grain boundaries, morphologies, defects and variations in boron concentration across the polycrystalline material. A typical backscattered electron FE-SEM image of high quality BDD is shown in **Figure**

2.4b. Vast contrast between BDD grains is observed due to different facets having varying conductivities, with more highly doped grains appearing darker, whilst less doped grains appearing lighter.[10] Higher energy backscattered electrons provide information about sample composition.

For all FE-SEM images in this thesis, a high resolution Zeiss Supra 55 VP was utilised an in-lens detector. Accelerating voltages between 2 and 15 kV were used, with a working distance of 4 mm.

2.4.3 X-ray Fluorescence (XRF)

XRF analysis detailed in this thesis was conducting using an energy dispersive XRF system, illustrated in **Figure 2.5**.

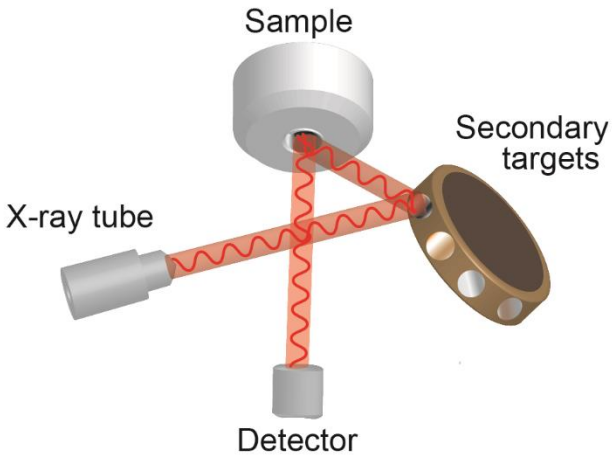

***Figure 2.5**: Schematic of an energy dispersive XRF system with secondary targets.*[11]

The X-ray tube (Pd anode) was run at 50 kV with a 1 mA tube current. Several secondary targets were used dependent on the analyte of interest including the Mo target (17.45 keV) and the polychromatic Al_2O_3 Barkla secondary target (> 10 keV).[12]

All spectra were measured under moderate vacuum (12 Pa) for a sampling time of 150 s. The interrogation area of the X-Ray source was determined to be elliptical and ~1.2 cm in diameter.

2.4.4 X-ray Photoelectron Spectroscopy (XPS)

Based on the photoelectric effect, XPS, otherwise known as Electron Spectroscopy for Chemical Analysis (ESCA), allows the elemental composition of up to the top 10 nm of a surface to be investigated.[13] Monochromatic incident photons (energies ranging from 200–2000 eV) bombard the sample surface and are absorbed by atoms, causing them to emit electrons from core atomic orbitals.[14] This is illustrated in **Figure 2.6a**.

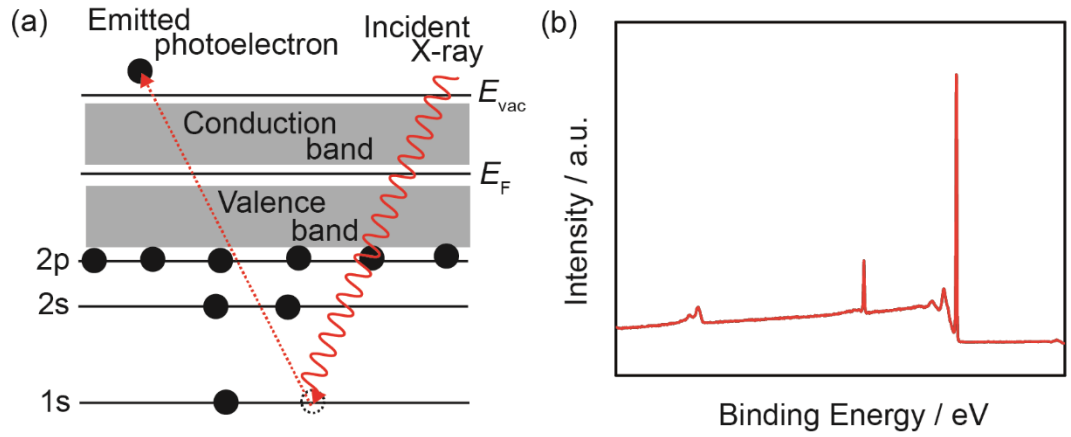

***Figure 2.6*: *(a) Illustration of the ejection of a photoelectron by x-ray excitation and (b) an example XPS spectrum, showing orbital lines.*[13]**

The kinetic energy of the emitted electrons is then measured, allowing the binding energy of the emitted electron to be calculated and thus the element present as each element has specific electron binding energies, shown in **Equation 2.1**:[15]

$$E_{binding} = E_{photon} - (E_{kinetic} + \Phi) \quad (2.1)$$

where $E_{binding}$ = the binding energy of the electron, E_{photon} = the energy of the X-ray photons being used, $E_{kinetic}$ = the kinetic energy measured by the XPS analyser and Φ = the work function of the material. An XPS spectrum can then be created, with each line indicative of a unique electron arrangement, shown in **Figure 2.6b**.

XPS is a particularly powerful technique as it provides quantitative analysis of surface composition.[16] Furthermore, changes to $E_{binding}$ occur not only on the level from which the photoelectron is emitted from, but also due to changes to the local chemical and physical environments. Subtle shifts in line position can provide information such as the oxidation state of an atom and the functional groups present.[13]

XPS analysis was performed using a Kratos Axis Ultra DLD photoelectron spectrometer, with a monochromated $Al_{K\alpha}$ X-ray source (1486.69 eV) operating at 150 V, operating under ultrahigh vacuum (UHV) conditions with a spectrometer base pressure of 2×10^{-10} mbar.

2.4.5 White Light Interferometry (WLI)

WLI is a non-contact optical method used to measure the topography of a surface through the application of optical interference.[17] The interferometer uses a broad spectrum light source that is collimated using a condenser lens. The light is then split into two beams, one that is reflected from a reference mirror and the other that is scattered by the sample of interest. The reflected beams are then relayed to a CCD, forming an interference pattern.[18] This allows topographical information of a sample

to be collected with sub-nm resolution. In this thesis, WLI images were collected using a Bruker ContourGT (Bruker Nano Inc., USA).

2.5 Electrochemical Characterisation

2.5.1 Capacitance (*C*)

Using a three electrode setup, CVs were collected in 0.1 M KNO_3 at a scan rate of 0.1 V s^{-1}, sweeping the potential between −0.1 V and 0.1 V, starting at 0 V for 7 cycles. The second full CV was then utilised to calculate *C* according to **Equation 2.2**:

$$C = i_{average}/vA_{geometric} \qquad (2.2)$$

where $i_{average}$ is the current average from the forward and reverse sweep at 0 V versus SCE, v is the scan rate (V s^{-1}), and $A_{geometric}$ the geometric electrode area (cm^2). Note: no significant change in the *C* measurement is observed from the second CV onwards, with the additional scans recorded for statistical purposes.

2.5.2 Solvent Window (SW)

The potentiostat is used to sweep the potential from 0 V, down to −2 V then to + 2 V before returning to 0 V for three full cycles. The second full CV is then converted to current density (mA cm^{-2}) by dividing by the electrode area. The SW is defined as the potential range in which a current of no more than of ±0.4 mA cm^{-2} is passed.[1]

2.5.3 Reversibility

CVs of the outer sphere redox mediator $Ru(NH_3)_6^{3+}$ (1 mM) are conducted in 0.1 M KNO_3 at a scan rate of 0.1 V s^{-1} selected as its formal potential is sufficiently in the band gap of BDD (see Chapter 1.5.1). The potential is swept from + 0.2 V and −0.5 V for 3 cycles. The second CV is assessed with a peak-to-peak separation (discussed in detail in Chapter 1.4.3) of < 70 mV indicative of BDD with metal-like conductivity and good ohmic contact.[ss] Using $Ru(NH_3)_6^{3+}$ as a mediator also allows identification of electrodes that are doped below the metallic threshold as there are not enough available charge carriers, resulting electron transfer being the rate determining step. As a result, the peak-to-peak separation (ΔE_p) of $Ru(NH_3)_6^{3+}$ becomes larger (≥ 70 mV) – shown to be > 300 mV for BDD doped at 2×10^{18} B atoms cm^{-3}.[1]

2.6 References

(1) Hutton, L. A.;Iacobini, J. G.;Bitziou, E.;Channon, R. B.;Newton, M. E.;Macpherson, J. V. *Anal. Chem.*, **2013**, *85*, 7230–7240.
(2) Hutton, L. A.;O'Neil, G. D.;Read, T. L.;Ayres, Z. J.;Newton, M. E.;Macpherson, J. V. *Anal. Chem.*, **2014**, *86*, 4566–4572.
(3) Hutton, L.;Newton, M. E.;Unwin, P. R.;Macpherson, J. V. *Anal. Chem.*, **2009**, *81*, 1023–1032.
(4) Tachibana, T.;Williams, B. E.;Glass, J. T. *Physical Review B*, **1992**, *45*, 11975–11981.
(5) Joseph, M. B.;Bitziou, E.;Read, T. L.;Meng, L.;Palmer, N. L.;Mollart, T. P.;Newton, M. E.;Macpherson, J. V. *Anal. Chem.*, **2014**, *86*, 5238–5244.
(6) Joseph, M. B.;Colburn, A.;Mollart, T. P.;Palmer, N.;Newton, M. E.;Macpherson, J. V. *Sensor. Actuat. B-Chem.*, **2017**, *238*, 1128–1135.
(7) Read, T. L.;Bitziou, E.;Joseph, M. B.;Macpherson, J. V. *Anal. Chem.*, **2014**, *86*, 367–371.
(8) Oatley, C.;Nixon, W.;Pease, R. *Advances in Electronics and Electron Physics*, **1966**, *21*, 181–247.
(9) Watt, I. M. *The principles and practice of electron microscopy*;Cambridge University Press, **1997**.
(10) Miller, J. B.;Brandes, G. R. *Journal of Applied Physics*, **1997**, *82*, 4538–4545.
(11) Brouwer, P. *Almelo, Netherlands: PANalytical BV*, **2006**.
(12) Van Grieken, R.;Markowicz, A. *Handbook of X-ray Spectrometry*;CRC Press, **2001**.
(13) Siegbahn, K. *Atomic Physics 3*; Springer. 1973.
(14) Wang, J.;Wu, W.;Feng, D. *National Defense Industry Press, Beijing*, **1992**, 249–260.
(15) Acocella, A.;de Simone, M.;Evangelista, F.;Coreno, M.;Rudolf, P.;Zerbetto, F. *Phys. Chem. Chem. Phys.*, **2016**, *18*, 13604–13615.
(16) Penn, D. R. *Journal of Electron Spectroscopy and Related Phenomena*, **1976**, *9*, 29–40.
(17) Hariharan, P.;Hariharan, P. *Basics of Interferometry (Second edition)*; Academic Press. 2007.
(18) Hariharan, P. *Basics of interferometry*;Academic Press, **2010**.

Chapter 3

Quantitative analysis of trace palladium contamination in aqueous solution using Electrochemical X-Ray Fluorescence (EC-XRF)

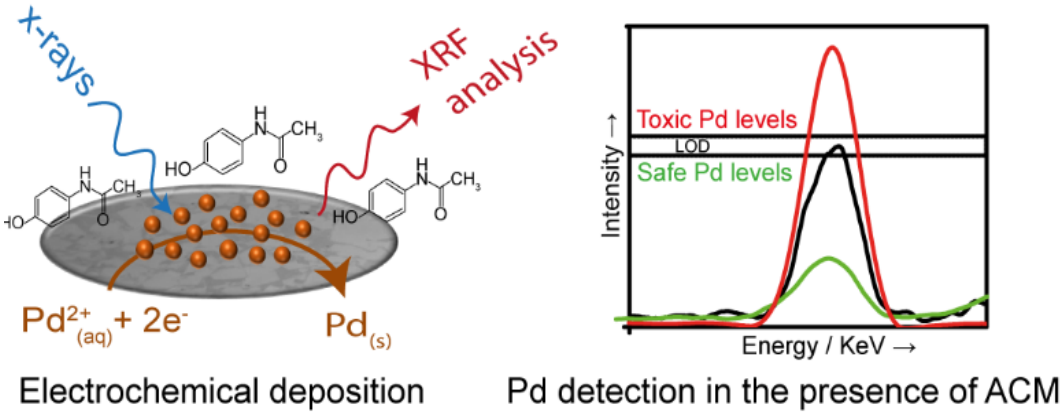

The application of Electrochemical X-ray Fluorescence (EC-XRF), for the detection of palladium (Pd) contamination in a range of aqueous solutions containing electrochemically active compounds, present in excess and relevant to the pharmaceutical and food industries, is reported. In EC-XRF, EC is used to electrochemically pre-concentrate metal onto an electrode surface under forced convection conditions, whilst XRF is employed to spectroscopically quantify the amount of metal deposited, which quantitatively correlates with the original metal concentration in solution. Boron doped diamond is used as the electrode due to its very wide cathodic window and the fact that B and C are non-interfering elements for XRF analysis. The effect of several parameters on the Pd XRF signal intensity are explored including: deposition potential (E_{dep}), deposition time (t_{dep}) and Pd^{2+} concentration, [Pd^{2+}]. Under high deposition potentials (E_{dep} = −1.5 V), the Pd XRF peak intensity (XRF_{max}) varies linearly with both t_{dep} and [Pd^{2+}]. Quantification of [Pd^{2+}] is

demonstrated in the presence of excess acetaminophen (ACM), L-ascorbic acid, caffeine and riboflavin. We show the same Pd XRF signal intensity (for $[Pd^{2+}]$ = 1.1 μM and t_{dep} = 325 s) is observed, *i.e.* same amount of Pd is deposited on the electrode surface, irrespective of whether these redox active molecules are present or absent. For t_{dep} = 900 s we report a limit of detection for $[Pd^{2+}]$ of 3.6 ppb (34 nM). Even lower LODs are possible by increasing t_{dep} or by optimising the X-ray source specifically for Pd. The work presented for Pd detection in the presence of ACM, achieves the required detection sensitivity stipulated by international pharmacopeia guidelines.

3.1 Introduction

Heavy metal contamination (HMC) is prevalent in many industries including: wastewater treatment,[1] environmental monitoring,[2] pharmaceutical manufacturing and food production.[3] HMC raises significant health concerns due to the inherent toxicity of heavy metals even when present at trace concentrations.[4] As a result, government bodies such as the World Health Organisation[5] and the European Medicines Agency (EMA)[6] have stringent guidelines on quantification of heavy metal impurities to ensure that they do not exceed safe concentration limits. Currently, the analytical techniques recommended for quantitative heavy metal detection are laboratory based inductively coupled plasma optical emission spectroscopy (ICP-OES) and ICP-mass spectrometry (ICP-MS).[7] For ICP (MS or OES) prior to analysis complex matrices such as soil, pharmaceutical products and foodstuffs must first be broken down into solution form, typically by microwave digestion in concentrated acid.[8] The solution is then diluted prior to ICP ionisation.

In the electrochemical field, anodic stripping voltammetry (ASV) has long been used as a means to detect heavy metals in aqueous environments[9] due to its rapid analysis time, ease of use, inexpensive instrumentation, the potential for on-line (on-site) analysis, unlike ICP-MS (-OES), as well as the ability to reach ppb detection limits.[10] As discussed in **Chapter 1.7.1.2**, in ASV, dissolved and labile heavy metals are electrochemically reduced onto an electrode and then oxidatively stripped from the surface, with the stripping peak(s) analysed. With liquid mercury functioning as the detection electrode, the position of the stripping peak can be used to inform on metal chemical identity, with peak area or height providing quantitative information on metal ion concentration.[11] However, as mercury can no longer be employed, due to its own

toxicity concerns,[12] wide cathodic window solid electrodes such as boron doped diamond (BDD)[13] and iridium oxide[14] are required as an alternative. Interpretation of stripping peaks from metal deposition/dissolution on solid electrodes is complex as the deposit morphology, peak suppression and the appearance of intermetallic peaks can all affect the number, position and magnitude of peaks observed.[15] This makes chemical identification and quantification of metal concentrations in solution challenging.

Furthermore, this approach ideally requires that no other redox active species (interferents) are present which can negatively impact on the metal deposition and stripping process. This is to avoid fouling of the surface with electrochemical intermediates/products of the redox process and interferent electrochemistry masking the analytical stripping signal. This is likely to be especially problematic when investigating solutions which contain high parts-per-million (ppm) concentrations of electroactive species, for example, in dissolved foodstuffs, e.g. L-ascorbic acid (vitamin C),[16] riboflavin (vitamin B2)[17] and in dissolved pharmaceutical tablets where the majority of active pharmaceutical ingredients (APIs) i.e. the drug molecule themselves,[18] show a redox electrochemical signature.

Stand-alone XRF provides a simple, non-destructive alternative for heavy metal detection, requiring little, if any sample preparation.[19] Typically, the sample of interest, usually in solid form, is excited with an X-ray beam of a chosen energy resulting in the emission of a unique fluorescent signature, allowing unequivocal elemental identification from Na^{11} to U^{92}. In conventional energy dispersive-XRF, ppm detection limits are found.[20] Unfortunately these are not appropriate for trace level metal

detection studies, which typically require detection sensitivities at the ppb level.[21] To improve detection limits, pre-concentration procedures can be employed, such as precipitation, liquid-solid extraction and evaporation, however they still do not enable many of the required detection sensitivities to be achieved using XRF alone.[22]

EC-XRF capitalises on the advantages of both electrochemistry and XRF, overcoming the aforementioned disadvantages associated with each independent technique.[23] "Preconcentration" of metal ions on the surface of the electrode is achieved using electrodeposition. However, no oxidative stripping step is employed for analysis, unlike ASV. Unequivocal chemical identification and subsequent quantification is instead made using the XRF component of the technique. Boron doped diamond (BDD) is utilised as the electrode substrate, to take advantage of its excellent electrochemical properties suitable for both electrodeposition and XRF including: a wide cathodic solvent window; low background currents and high resistance to fouling.[24] Furthermore, the thin BDD substrate (250 μm) is freestanding i.e. is unsupported, and constitutes only B and C atoms, which are noninterfering elements in the XRF spectra.[25] Previous EC-XRF ex-situ studies, which focused on determining detection sensitivities, employed model solutions containing only inert background electrolyte (0.1 M KNO_3, pH 6) and the labile metal ions Cu^{2+} and Pb^{2+}.[23]

In this work the ability of EC-XRF to provide the required detection sensitivities for more challenging solutions appropriate to both the pharmaceutical and food industry is investigated. Initial focus is placed on the ability of EC-XRF to monitor heavy metal contamination in a pharmaceutical API, acetaminophen (ACM). Note the API is always present at significantly higher concentrations than the contaminant, and the

vast majority of APIs show oxidative signatures.[26] Contamination of drug intermediates and drug products with heavy metals can arise from many sources[27] including raw materials, equipment, solvents, reagents and catalysts,[28,29] with the latter being a key cause for concern. Palladium (Pd) contamination in the pharmaceutical industry is very common[30] as Pd-derived catalysts are routinely used in API synthesis.[31,32] Pd is of particular concern not only due to its toxicity, but also its ability to catalyse drug decomposition. For these reasons levels of Pd must not be greater than 10 ppm with respect to the API.[6] The widespread applicability of the EC-XRF technique is further demonstrated by investigating the detection of our target metal (Pd) in the presence of high concentrations of other complex electroactive species appropriate to the food industry, including L-ascorbic acid, caffeine and riboflavin. Finally, the applicability of the technique to the detection of other metals contaminants present in solution is demonstrated.

3.2 Experimental

3.2.1 EC-XRF measurements

EC-XRF measurements involve first an electrochemical deposition (pre-concentration) step (**Figure 3.1a**). The BDD electrode is then removed from solution and the metal plated surface analysed using XRF (**Figure 3.1b**). The resulting spectrum (**Figure 3.1c**) provides information on the chemical identity of the electrodeposited metal (from the peak position) and the quantity of metal deposited (peak height). Provided the metal has been electrodeposited under known mass transport conditions the amount of metal deposited on the surface can be related back to the original concentration of metal ions in solution.

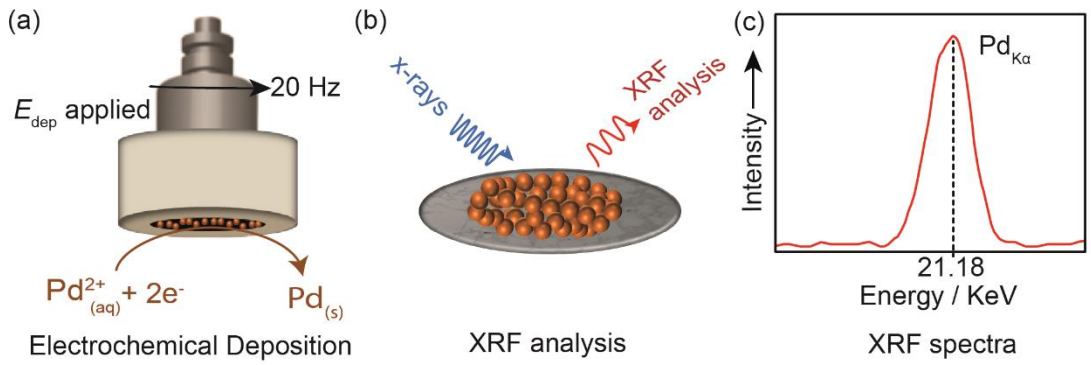

***Figure 3.1**: The EC-XRF technique: (a) the electrochemical deposition step; (b) XRF analysis and (c) the XRF spectra obtained for Pd (Kα line).*

3.2.2 Electrochemical setup

For electrochemical deposition a rotating disc electrode (RDE) setup was employed due to the well-defined hydrodynamic mass transport characteristics.[33] A three-electrode configuration was utilised with the BDD RDE functioning as the working electrode, a platinum gauze as the counter electrode and a saturated calomel electrode (SCE) as the reference electrode. Note, all potentials are quoted versus SCE, unless otherwise stated. To provide an ohmic contact to the BDD electrode, 10 nm Ti / 400 nm Au was sputtered onto the back of the BDD electrode, followed by annealing at 400 °C for 5 h. To avoid any metallic interference from the Ti/Au contacts in XRF analysis, the ohmic contact was sputtered as a ring with an inner diameter of 2.2 cm (the interrogation area of the XRF is 1.2 cm in diameter).

To form the RDE, the BDD was screwed into a polyether ether ketone (PEEK) cap (shown in **Figure 3.2**). The backside of the Ti/Au sputtered BDD contacted a metal rod that was connected to a rotating disc set-up, fabricated in-house. The PEEK cap

acts to reduce the electrode area to 1.5 cm^2 (1.4 cm diameter) with an O-ring positioned behind the cap, to provide a watertight seal.

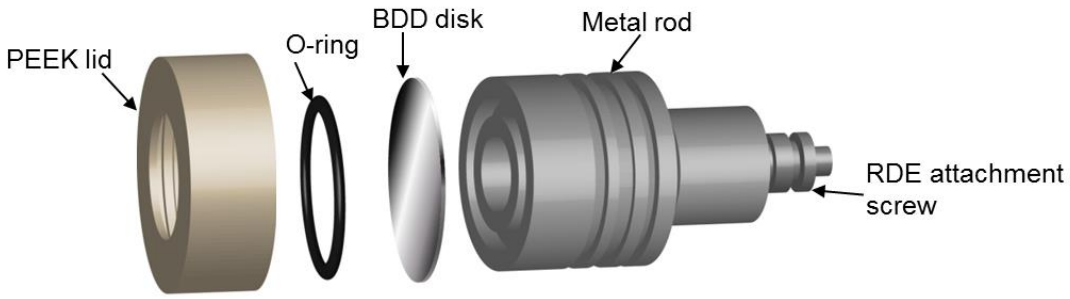

Figure 3.2: *Deconstructed schematic of the RDE.*

In between measurements the BDD disc was mechanically polished with alumina particles (~0.05 µm particle size, Micropolish, Buehler, Germany) on a deionised water saturated polishing pad (Microcloth, Buehler, Germany) and then rinsed with deionised water to ensure removal of any remaining alumina particles.

For cyclic voltammetry (CV) measurements of ACM, L-ascorbic acid, caffeine, and riboflavin, a 1 mm diameter BDD disc macroelectrode[34] (glass-sealed) was utilised as the working electrode. In order to create a Pd-coated BDD electrode, the electrode was held at −1 V for 30 minutes in 1 mM $PdCl_2$ in 0.2 M KNO_3, acidified with 0.1 M HCl.[35]

3.2.3 XRF Instrumentation

XRF analysis was conducted using an energy dispersive-XRF (NEX CG, Rigaku, Japan). The X-ray tube with Pd anode was run at 50 kV with a 1 mA current and utilised an Al secondary target (the polychromatic Barkla target, Al_2O_3 > 10 keV).[36]

This secondary target was selected to provide the maximum excitation for Pd, using the NEX CG system.[37] For comparison of the excitation efficiency of the secondary source with respect to the metal detected, the Mo secondary target (17.45 keV) was also used for data collection. All spectra shown are smoothed using a Savitsky-Golay filter.[38] After electrodeposition, the BDD disc was removed from the RDE set-up, air-dried with nitrogen and then placed in the XRF chamber for analysis. All spectra were measured under moderate vacuum (12 Pa) for a sampling time of 150 s. The interrogation area of the X-Ray source on the sample is elliptical and ~1.2 cm in diameter. All spectra are presented to show the $Pd_{K\alpha}$ peak at 21.18 keV. For any XRF measurement involving Cu or Fe, XRF spectra were background corrected using a representative blank sample. This was due to the presence of background Cu and Fe peaks, attributed to residual scattered X-rays from the brass shutter and the steel body of the sample chamber fluorescing close to the optical path.

3.2.4 Energy Dispersive-XRF evaporation techniques

EC-XRF was compared against conventional energy dispersive-XRF, in order to explore the differences in detection sensitivity. The Rigaku patented solution evaporation methodology for analyte pre-concentration (Ultra Carry^{TM}) in combination with XRF, was utilised which consists of a plastic sample plate containing a hydrophobic Mylar film, and a central hydrophilic, X-ray transmissive pad. 200 µL of the sample of interest was pipetted onto the hydrophilic region of the absorbent pad and heated on a hot plate (IKA RCT Basic) at 45 $^{\circ}$C for ~60 minutes, until all solution had evaporated.

3.3 Results and Discussion

3.3.1 Cell Characterisation

The electrochemical response of the 1.4 mm diameter BDD disc electrode was initially investigated to ensure that the BDD was doped sufficiently to behave as a metal-like electrode. Figure 3.3 shows the CV response for 1 mM $Ru(NH_3)_6^{3+}$ (half wave potential, $E_{1/2}$ = −0.11 V versus SCE) electrolysis in 0.2 M KNO_3, under quiescent conditions, at a scan rate of 0.1 V s^{-1} (black) and under forced convection conditions (red). In stationary solution, near reversible electron transfer kinetics were observed (peak-to-peak, ΔE_p, separation of 65 mV) indicative of highly doped diamond material. This value also indicates that ohmic drop is minimal and that there is a good electrical connection to the BDD. Furthermore, the observed peak current (i_p) of 0.40 mA, is close to that predicted by Randles Sevcik theory[33] of 0.39 mA, described previously in Equation 1.7, with n = 1; A = 1.54 cm^2; D, for $Ru(NH_3)_6^{3+}$ = 8.65 × 10^{-6} cm^2 s^{-1} (determined using a 14.5 µm radius Pt ultramicroelectrode in a solution containing 1 mM $Ru(NH_3)_6^{3+}$ and 0.2 M KNO_3).; v is the scan rate (0.1 V s^{-1}) and c* is the concentration of the analyte (1 mM) at 298 K.

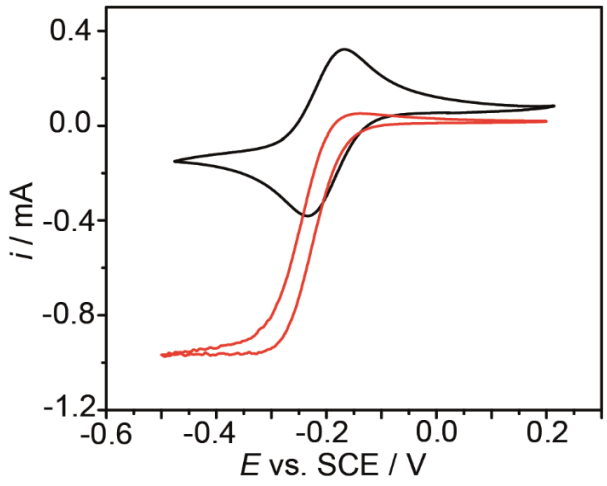

Figure 3.3**:** *CV response for the reduction of 1 mM $Ru(NH_3)_6^{3+}$ in 0.1 M KNO_3 at a scan rate of 0.1 V^{-1}, in stationary (black) solution and with the electrode rotated at 20 Hz (red).*

To ensure rapid analysis times, forced convection was implemented to increase mass transport to the electrode surface, with steady state currents (i_{lim}) obtained at 20 Hz (red) of 0.97 ± 0.01 mA, similar to those as predicted by Levich theory[33] (0.95 mA), calculated using **Equation 1.8**, assuming the kinematic viscosity of water to be 0.01 $cm^2\ s^{-1}$.

Deviation from Levich theory was observed at f > 20 Hz. This could be due to the fact the electrode is recessed (1 mm) from the top surface of the PEEK holder (**Figure 3.2)**; the effect on mass transport is seen most prominently at higher f values. Therefore, all subsequent EC-XRF measurements were conducted at f = 20 Hz.

3.3.2 The effect of API on the EC-XRF signal

The maximum amount of Pd allowed in pharmaceutical products for oral consumption was considered in order to select an appropriate concentration range for analysis. The

EMA define a limit of 10 ppm for Pd with respect to the amount of API present,[6] as shown in **Equation 3.1**. Concentrations above this value are considered unsafe for human consumption:

$$\text{maximum safe limit} = \frac{10 \text{ mg of Pd}}{1 \text{ kg of API}} 10 \text{ ppm} \qquad (3.1)$$

The amount of Pd that must be detectable is therefore directly dependent on the concentration of API in solution. ACM was employed as the model API, as it is a well-known, widely used pharmaceutical drug molecule. High concentrations of ACM (12 g/L) were added to solution, close to the solubility of ACM (14.9 g/L at 25°C),[39] as the API is always present in excess within pharmaceutical preparations compared to any heavy metal contamination that may be present.[40] This also acted to maximise any possible electrochemical interferences observed from the API. Based on **Equation 3.1** it was determined that at least 1.1 µM of Pd^{2+} must be quantifiable in the presence of 12 g/L of ACM, to achieve the EMA 10 ppm detection limit.[6]

The electrochemical signature of ACM was first investigated in order to explore possible interferences. CVs for the first (red) and second (black) scan of 12 g/L ACM at a 1 mm BDD electrode are shown in **Figure 3.4** in an aqueous, quiescent solution containing 0.2 M KNO_3 (pH 3), recorded at 0.1 V s^{-1}. When oxidised, in aqueous solution, ACM undergoes a quasi-reversible two-electron, two-proton oxidation to N-acetyl-p-benzoquinone-imine (NAPQI).[41] During the first CV scan (cycled from 0 V negative to −1.5 V, then positive to 0.5 V then back to 0 V) no reduction signature is observed, whilst a reduction peak is apparent in the second scan ACM ($E_{1/2}$ = −0.18 vs. SCE). This is due to the fact that ACM must first be oxidised to NAPQI before reduction can occur. As only a reductive deposition E_{dep} is applied during EC-XRF

preconcentration, ACM electrolysis should therefore not compete with deposition of Pd on the BDD electrode. The CV response recorded on the EC-XRF electrode in the reductive window (0 V to −2 V and back) in 0.2 M KNO_3 only at a scan rate of 0.1 V s^{-1} (pH 3) at f = 20 Hz (red line) is also almost identical to that recorded with the addition of 12 g/L ACM 0.2 M KNO_3 (black line: **Figure 3.4**, inset).

As the presence of ACM did not adversely affect the cathodic electrochemical response, experiments were conducted first, in the absence of ACM, to determine the effect of various EC-XRF parameters on the electrodeposition of Pd^{2+} including: (i) the applied deposition potential, E_{dep}; (ii) the dependence of the XRF signal intensity on the solution concentration of Pd^{2+} and (iii) the deposition time, t_{dep}.

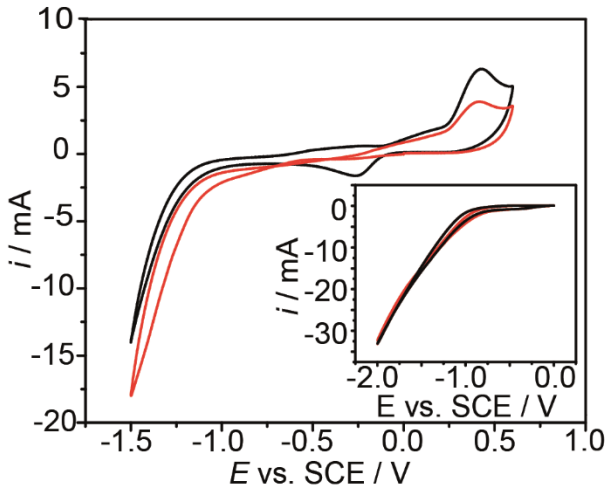

Figure 3.4*: *CVs of 12 g/L ACM in 0.2 M KNO_3 (pH 3) using a 1 mm BDD electrode in stationary solution for the first scan (red) and second scan (black) at a scan rate of 0.1 V s^{-1}. Start potential 0 V scanning to -2 V and then back. Inset: Reductive window potential scan using the EC-XRF electrode in the presence of 0.2 M KNO_3 at a scan rate of 0.1 V s^{-1} (pH 3) with (red) and without (black) 12 g/L ACM present.

A 1 mm BDD electrode glass sealed electrode (see **Chapter 2.3.1**)[34] was held at −1.5 V for 300 s in 1.1 µM Pd^{2+} (palladium (II) chloride ($PdCl_2$: 99.0 %, Sigma Aldrich) in 0.2 M KNO_3 (pH 3), under stationary conditions, then subsequently stripped from the

surface by scanning from 0 V to 0. 65 V, at a scan rate of 0.1 V s^{-1} in 0.2 M KNO_3 solution. The ASV is shown in **Figure 3.5**. A Pd^{2+} stripping peak is observed at 0.56 V vs. SCE.

Note, the ASV stripping peak for Pd, shown in **Figure 3.5**, occurs in a very similar potential region to that of the ACM oxidation peak, but with much smaller currents (dependent on concentration), making ASV analysis of Pd in the presence of ACM problematic.

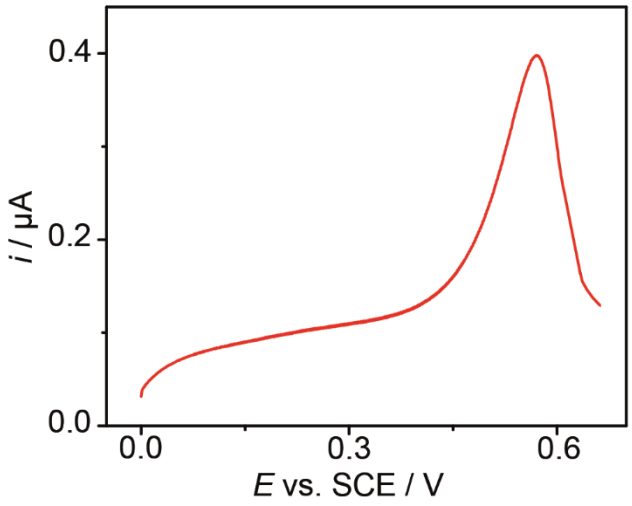

Figure 3.5*: *ASV of 1.1 µM Pd^{2+} in 0.2 M KNO_3 (pH 3), at a scan rate of 0.1 V s^{-1} after deposition for 300 s at −1.5 V, swept from 0 V to + 0.65 V.

3.3.3 Deposition potential (E_{dep}) optimisation

The CV characteristics for Pd^{2+} electrodeposition on the BDD EC-XRF electrode (diameter = 1.4 cm), were recorded at 0.1 V s^{-1} in a stationary solution containing 1.1 µM Pd^{2+} (palladium (II) chloride ($PdCl_2$: 99.0 %, Sigma Aldrich), as depicted in **Figure 3.6**. The CV shows the reduction currents associated with Pd electrodeposition on the surface of the BDD, along with hydrogen adsorption and desorption peaks.[42]

From **Figure 3.6** the half wave reduction potential ($E_{1/2}$) for Pd^{2+} was determined to be + 0.16 V (vs. SCE).

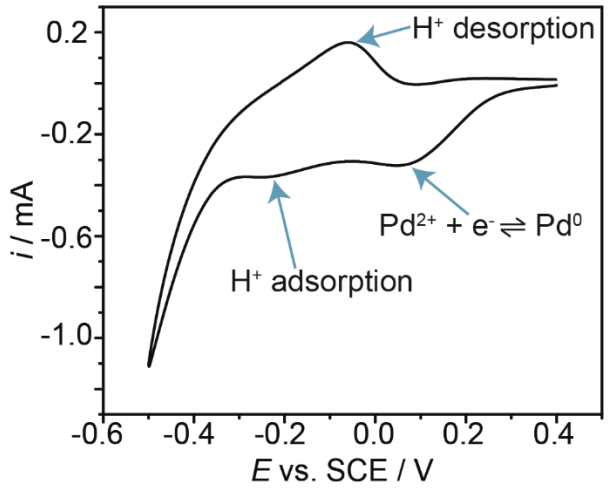

Figure 3.6*: *CV of 1.1 µM Pd^{2+} in 0.2 M KNO_3 (pH 3) under stationary conditions, using the EC-XRF BDD electrode at a scan rate of 0.1 V s^{-1}.

A range of E_{dep} were then employed > $E_{1/2}$ to investigate the electrodeposition characteristics of Pd^{2+} on the BDD electrode, interrogated by XRF. **Figure 3.7a** shows the XRF signals obtained for E_{dep} values of −0.25 V, −0.5 V, −0.75 V, −1.0 V, −1.25 V, −1.5 V and −1.75 V, using 1.1 µM Pd^{2+} in 0.2 M KNO_3, acidified to pH 3, at f = 20 Hz. A fixed t_{dep} of 900 s was employed, in order to obtain an appreciable XRF signal for all measurements.

Figure 3.7b shows the maximum XRF signal intensity (XRF_{max}) i.e. the peak intensity, corresponding to $Pd_{K\alpha}$ (21.18 keV) as a function of E_{dep} for n = 3 measurements per applied potential. As the overpotential for electrodeposition increases, it is apparent that an increasing amount of Pd is deposited onto the BDD electrode, evidenced by the increasing Pd XRF_{max}. However, at an E_{dep} of −1.75 V the amount of Pd deposited

onto the electrode drops significantly from an XRF_{max} of 0.028 ± 0.006 cps mA^{-1} (at E_{dep} = −1.5 V) to 0.012 ± 0.005 cps mA^{-1} (at E_{dep} = −1.75 V). Furthermore a significant increase in the variability of the XRF signal is observed. At E_{dep} = −1.75 V bubble formation (most likely hydrogen formation due to water reduction) on the electrode surface was visible, which is the likely cause of the reduced and variable XRF signals, reducing the efficacy of Pd^{2+} deposition on BDD. E_{dep} = −1.5 V was therefore deemed to be optimal as it returned both the highest XRF_{max} (over a fixed time) and reproducible results.

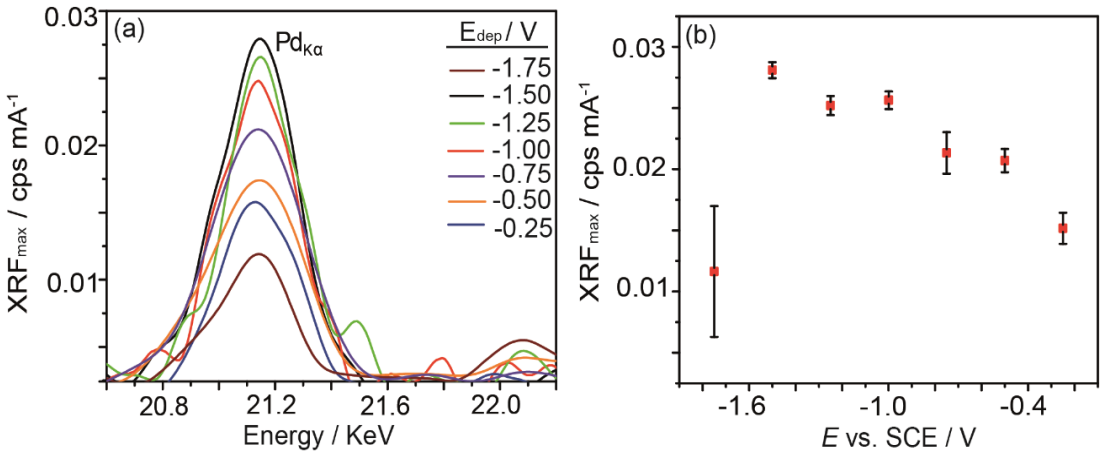

Figure 3.7: *(a) EC-XRF signal for 1.1 µM Pd^{2+} in 0.2 M KNO_3 (acidified to pH 3) for a range of E_{dep} values from -0.25 V to −1.75 V, at a scan rate of 0.1 V s^{-1} at f = 20 Hz and (b) XRF_{max} vs. E_{dep} for t_{dep} = 900 s.*

3.3.4 Quantitative detection of Pd^{2+} in the presence of ACM

The XRF signal dependence on Pd^{2+} concentration in the absence and presence of ACM (12 g/L) was investigated to ensure that EC-XRF could be used quantitatively and to determine the limit of detection for Pd (LOD; 3σ, where σ = the standard deviation of the background noise).[19] The concentration range 0.08 µM to 1.1 µM Pd^{2+} (equating to 0.7–10 ppm Pd^{2+} with respect to ACM) was explored, using the optimised

E_{dep} of −1.5 V for a t_{dep} = 900 s in 0.2 M KNO_3, acidified to pH 3 and rotated at f = 20 Hz. **Figure 3.8a** illustrates the XRF signal response for Pd in the absence of ACM across the concentration range investigated, showing clear peaks (XRF_{max} at 21.18 KeV) which decrease in peak intensity with decreasing Pd^{2+} concentration, [Pd^{2+}]. **Figure 3.8b** shows a strong linear correlation between [Pd^{2+}] and XRF_{max} (n=3) both with (red) and without (black) ACM present, with gradients of 0.029 cps mA^{-1} s^{-1} (R^2 = 0.998) and 0.030 cps mA^{-1} s^{-1} (R^2 = 0.999) respectively. It is thus clear that the EC-XRF signal is unaffected by the presence of a large excess of ACM, as evidenced also by the data in **Figure 3.4**, with high accuracy observed (all values obtained (red) fall within the standard error of the regression line (black) of ± 0.001 cps mA^{-1}). A LOD of 34 nM was calculated (3σ), both with and without ACM, equating to 0.36 ppm with respect to 12 g/L ACM, significantly lower than the required detection limit of 10 ppm, by over an order of magnitude.

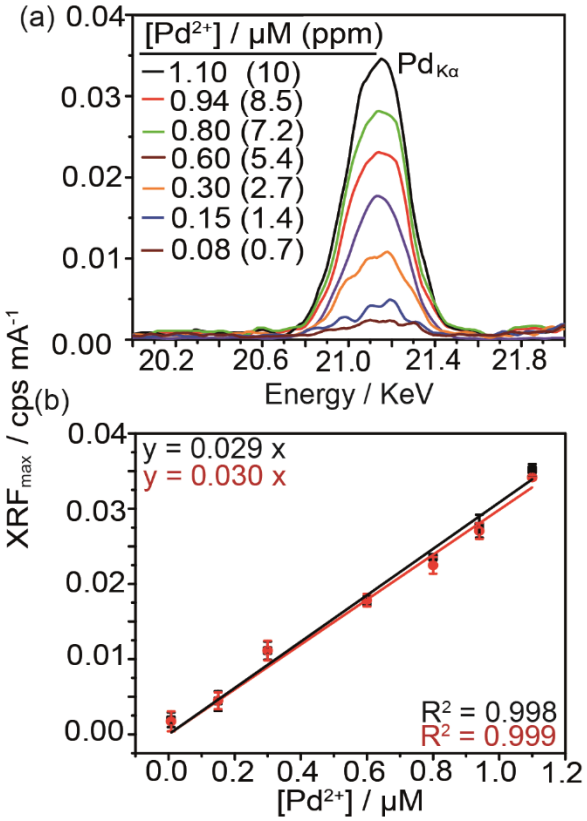

Figure 3.8**:** *(a) EC-XRF spectra for [Pd^{2+}] in the range 0.08 µM - 1.1 µM at t_{dep} = 900s and E_{dep} = −1.5 V and (b) plots of EC-XRF_{max} versus [Pd^{2+}] in the absence (black) and presence of 12 g/L ACM (red).*

3.3.5 Deposition time (t_{dep})

With a view to decreasing deposition times - t_{dep} represents the rate determining step in an EC-XRF measurement - the relationship between t_{dep} and XRF_{max} was further explored to investigate the shortest t_{dep} required to accurately detect Pd^{2+} at 10 ppm. **Figure 3.9a** demonstrates the effect of t_{dep} over the time period 100–1500 s, on XRF_{max} for a fixed E_{dep} = −1.5 V and Pd^{2+} concentration of 1.1 µM in 0.2 M KNO_3 (pH = 3), n = 3 and f = 20 Hz, with a magnified view of the 100 s signal shown in **Figure 3.9b**. **Figure 3.9c** shows the plot of XRF_{max} versus t_{dep}. The plot is linear with an R^2 = 0.999 and gradient of 3.3 × 10^{-5} ± 2.0 x10^{-6} cps $mA^{-1}s^{-1}$ clearly demonstrating that the

amount of Pd deposited on the electrode surface scales linearly with t_{dep} under these conditions. It is thus evident that t_{dep} can be reduced significantly if the aim is to be able to detect at most 10 ppm of Pd in the solution. The linearity of the XRF_{max} signal for Pd deposition with t_{dep} permits calculation of a limit of t_{dep} (3σ) = 42 ± 1 s, for 10 ppm detection. The smallest t_{dep} employed experimentally in the collection of data for **Figure 3.9a** is 100 s (zoomed view in **Figure 3.9b**) and, as shown, a clear peak is observed. The shorter analysis times employed here are on a par with the analysis times of conventional ICP-MS or -OES (~60 s).[7]

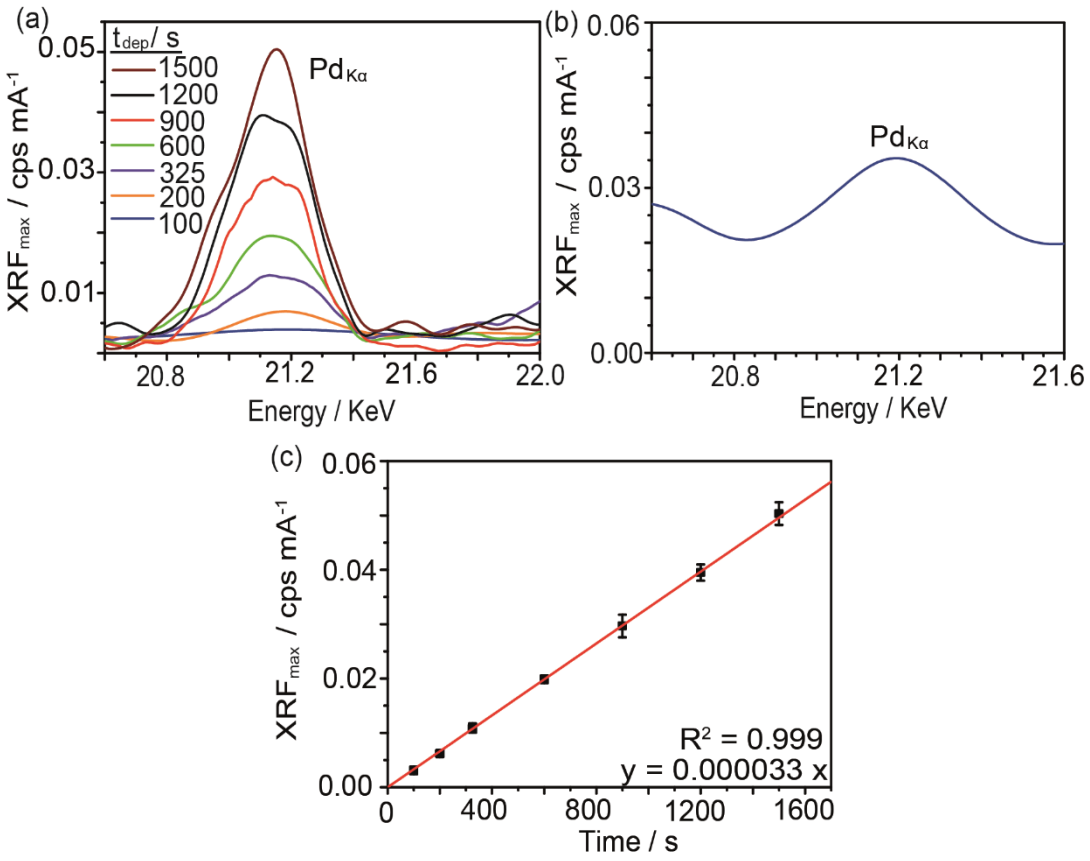

***Figure 3.9**: (a) EC-XRF spectra for 1.1 µM Pd^{2+} in 0.2 M KNO_3 for t_{dep} in the range 100 –1500 s at E_{dep} = −1.5 V, in pH 3 solution, f = 20 Hz. (b) zoom into the t_{dep} = 100 s data, to visualise the $Pd_{K\alpha}$ peak. (c) Plot of EC-XRF peak intensities versus t_{dep} for 1.1 µM Pd^{2+} at an E_{dep} = −1.5 V in 0.2 M KNO_3 (pH 3, f = 20 Hz) for t_{dep} in the range 100 s to 1500 s.*

3.3.6 Pd^{2+} Screening in the presence of ACM

Figure 3.10 demonstrates the use of EC-XRF to positively discriminate between samples containing both safe i.e. less than 10 ppm (here, 4 ppm) and toxic i.e. greater than ppm (here, 16 ppm), Pd^{2+} levels in the presence of ACM (12 g/L).

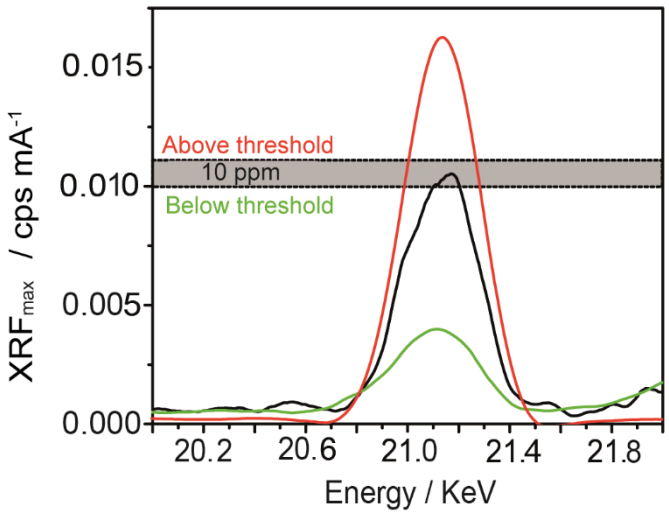

***Figure 3.10**: EC-XRF spectra for 10 ppm (black), 16 ppm (red) and 4 ppm (green) Pd^{2+} in the presence of excess ACM (12 g/L). E_{dep} = −1.5 V, t_{dep} = 325 s and f = 20 Hz. Grey band indicates the 10 ppm threshold signal range (n=3).*

t_{dep} was fixed at 325 s (to ensure a signal was observed for Pd concentrations below 10 ppm). An E_{dep} of −1.5 V was utilised for all experiments. The threshold EC-XRF signals for 10 ppm (grey band) were determined by the signal intensities recorded (n=3) for 1.1 µM Pd^{2+} (10 ppm) at t_{dep} = 325 s (black), **Figure 3.9**. As shown in **Figure 3.10**, the sample containing 4 ppm of Pd^{2+} (green), clearly falls below the toxicity safety limit, whilst the signal for the sample containing 16 ppm Pd^{2+}, falls above this limit.

From the three points for the three different concentrations, at a fixed t_{dep} and E_{dep} a linear relationship is observed between XRF_{max} and $[Pd^{2+}]$ (y=0.001 cps mA^{-1}, R^2 = 0.999), shown in **Figure 3.11** as expected, at reduced deposition times. As shown, a high correlation R^2 value of 0.999 is obtained.

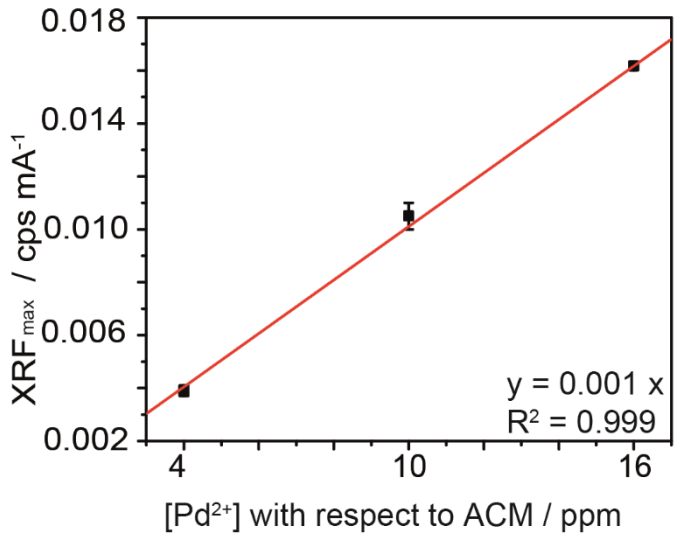

***Figure 3.11**: Plot of EC-XRF_{max} versus $[Pd^{2+}]$ concentration at an E_{dep} = −1.5 V and t_{dep} of 325 s in 0.2 M KNO_3 (pH 3, f = 20 Hz).*

3.3.7 EC-XRF in alternative complex matrices

Detecting toxic metal contamination is also important in foodstuffs[3b] and drinks and therefore the use of EC-XRF to detect Pd in the presence of other relevant electrochemically active molecules was investigated, in particular: (i) L-ascorbic acid (vitamin C); (ii) caffeine; and (iii) riboflavin (vitamin B2). The molecules were selected based on their prevalence in a variety of common food sources and drinks, and were added in excess (10 mM). Note, the average concentration of caffeine in coffee is found to be 3 mM,[43] with typical concentrations of 3 mM and 0.3 mM for L-ascorbic acid[44] and riboflavin[45] in orange juice, respectively.

CVs were conducted for 10 mM concentration of each electroactive species, in order to determine the electrochemical signature. At this high concentration, any potential surface fouling effects would be exacerbated. For L-ascorbic acid, the CV (**Figure 3.12**) shows no reductive peak at pH 3 (scanning from 0 V negatively) as the molecule is fully protonated, and therefore cannot be reduced.[46]

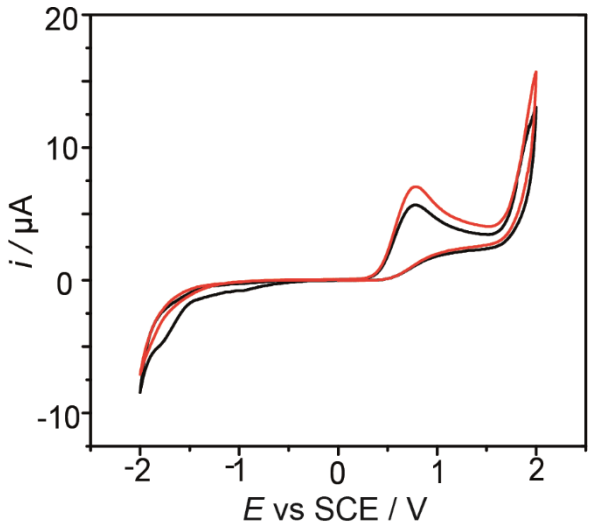

Figure 3.12: *CV of 10 mM L-ascorbic acid in 0.2 M KNO_3 (pH 3) using a 1 mm BDD electrode in stationary solution, at 0.1 V s^{-1}; first scan (red) and second scan (black).*

Upon oxidation, L-ascorbic acid is converted to dehydro-L-ascorbic acid, which undergoes irreversible hydration to the electroinactive species 2,3-diketo-L-gulonic acid (EC mechanism).[47] A small reduction peak ($E_{1/2}$= −0.91 V) is observed, on the second scan, which is likely due to the conversion of any remaining dehydro-L-ascorbic acid back to L-ascorbic acid.[48] A drop in the anodic i_p in the second scan is observed,[47] which could be due to the product of L-ascorbic acid oxidation fouling the electrode surface.[49]

For caffeine (**Figure 3.13**), no reduction peak is observed in the first scan, with a small peak visible in the second scan ($E_{1/2}$= −0.95 V).

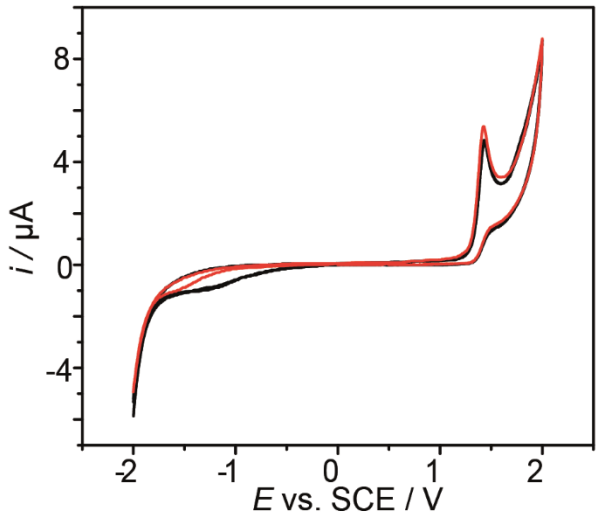

Figure 3.13*: *CV of 10 mM caffeine in 0.2 M KNO_3 (pH 3) using a 1 mm BDD electrode in stationary solution, at 0.1 V s^{-1}; first scan (red) and second scan (black).

The overall oxidation of caffeine is a four-electron, four-proton oxidation reaction to a bis-imine product,[50] which also hydrates to an electroinactive product (EC mechanism).[51] Therefore, as for L-ascorbic acid, the small reductive peak could be due to the reduction of not yet hydrated bis-imine.[51]

In contrast, riboflavin does undergoes reduction (two-electron, two-proton) converting from a quinone to hydroquinone species, with a reductive peak current clearly observed in the first scan at −0.68 V vs. SCE (**Figure 3.14**).[52] The repeat scan cathodically shows a reduction in the peak current (by 26 %), suggesting there may be some surface fouling.

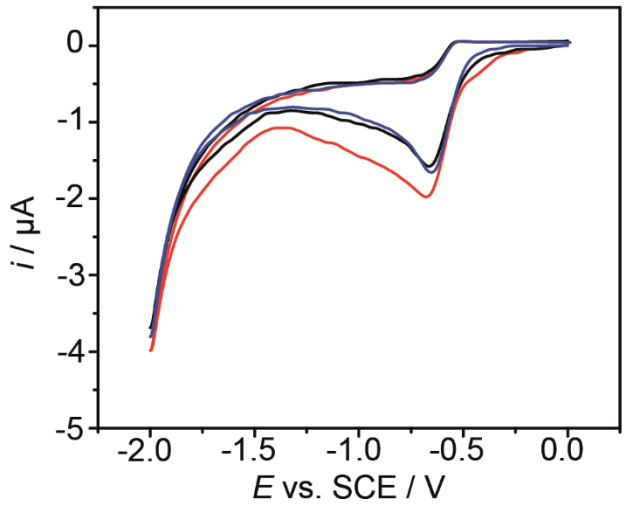

Figure 3.14*: *CV of 10 mM riboflavin in 0.2 M KNO_3 (pH 3) using a 1 mm BDD electrode in stationary solution, at 0.1 V s^{-1}; first scan (red) and second scan (black). Blue scan recorded immediately after holding the electrode at −1.5 V for 325 s in 10 mM riboflavin in 0.2 M KNO_3 (pH 3).

EC-XRF was conducted at E_{dep} = −1.5 V in a solution containing 1.1 μM Pd^{2+} and 10 mM of either (a) L-ascorbic acid; (b) caffeine or (c) riboflavin (pH 3) in 0.2 M KNO_3 at f = 20 Hz and a t_{dep} of 325 s, as shown in **Figure 3.15**. The expected detection signal (including error) under these conditions for this concentration of Pd, assuming no impediment of the electrodeposition process (taken from **Figure 3.9**) is illustrated by the dotted lines in **Figure 3.15**. As shown, all three molecules, within error, return the correct XRF_{max} signal, even for detection in the presence of riboflavin where evidence of surface fouling was observed (**Figure 3.14**).

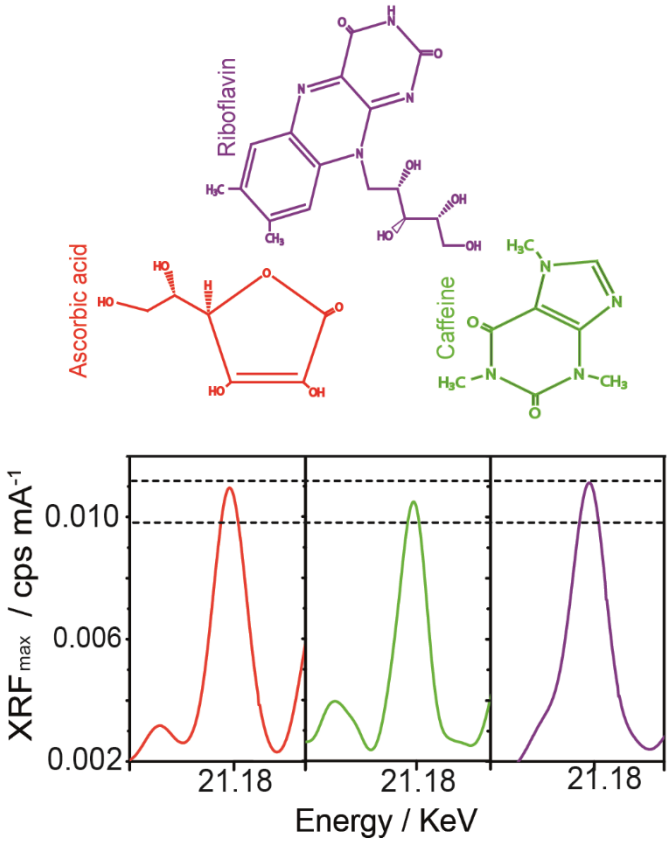

Figure 3.15*: *EC-XRF spectra for L-ascorbic acid (red) caffeine (green) and riboflavin (purple) in the presence of 1.1 µM Pd^{2+} at pH 3, (f = 20 Hz) deposited at −1.5 V for 325 s. Dotted lines indicate the expected XRF signal range for 1.1 µM Pd^{2+} (from* Figure 3.9*).

Further electrochemical studies with riboflavin showed that when holding the electrode at −1.5 V for 325 s, and then immediately running a CV (**Figure 3.14**, blue line), the same CV response is observed as for the second scan in **Figure 3.14** (black line). This indicates that the electrode does not completely block the surface even with the electrode held under prolonged potential control. Riboflavin has been previously shown to absorb weakly at a high purity BDD electrode (similar to the type adopted here).[53] Thus sufficient surface sites are available for Pd deposition, as evidenced by the data in **Figure 3.15**, suggesting the two processes are non-competing, under these conditions.

3.3.8 XRF detection of other metal contaminants

In EC-XRF any metal that can be electrodeposited on the BDD surface can be detected by XRF (in the range Na^{11} to U^{92}) opening up the possibility of trace metal detection of a variety of metal-based impurities. To explore this further, a multi-metal solution containing 1.1 µM of each of the environmentally relevant metals Fe^{3+} (Kα = 6.40 keV) Cu^{2+} (Kα = 8.04 keV), Zn^{2+} (Kα = 8.63 keV), Pb^{2+} (Lα = 10.55 keV), Cd^{2+} (Kα = 23.17 keV) and Pd^{2+} (Kα = 21.18 keV) was analysed using EC-XRF. The keV values in brackets represent the strongest fluorescent emission line for the different metals. Deposition took place for t_{dep} = 325 s, at E_{dep} = −1.5 V, in 0.2 M KNO_3 (acidified to pH 3 with HCl) at *f*=20 Hz, displayed in **Figure 3.16**. The E_{dep} employed represents a significantly high deposition overpotential for all dissolved metal ions in the solution.[23b]

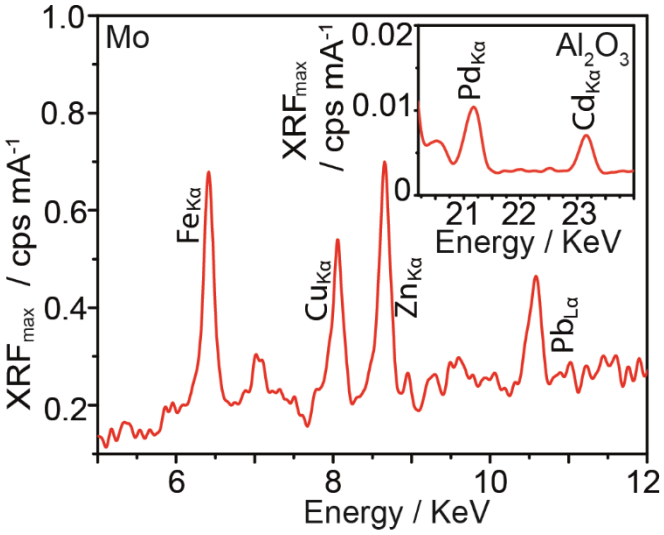

***Figure 3.16**: EC-XRF signal intensities for 1.1 µM of a range of environmentally relevant metals, at pH 3, (f = 20 Hz) deposited at −1.5 V for 325 s using the Mo secondary target (Fe, Cu, Zn and Pb), and inset: using the AlO_3 secondary target (Pd, Cd).*

In XRF, optimal excitation is achieved when the energy of the X-rays irradiating the sample is just above the energy of the absorption edge of the element,[54] hence different metals will emit stronger or weaker fluorescent signatures dependent on the secondary target used and their atomic number (*Z*). For this reason, the Mo secondary target (17.45 keV) was selected, over the AlO_3 target, in order to obtain optimal XRF signatures for Fe^{3+} (*Z* = 26), Cu^{2+} (*Z* = 29), Zn^{2+} (*Z* = 30), and Pb^{2+} (*Z* = 82). For Pd^{2+} (*Z* = 46) and Cd^{2+} (*Z* = 48), excitation via the Mo target is not possible and therefore the Al_2O_3 target was employed. Given the high keV values associated with Pd^{2+} and Cd^{2+}, and the high energies required for excitation, their fluorescent intensities are the weakest. However, importantly, the data shows that even in the presence of five other co-depositing metals, Pd deposition has neither been impeded or enhanced, as the XRF_{max} returned (0.010 cps mA^{-1}: **Figure 3.16**, inset) is as expected based on Figure 3.9 for the E_{dep} and t_{dep} employed, falling within the expected error range (**Figure 3.15**). **Figure 3.16** thus highlights the potential for using this technique to detect a wide variety of trace metals, in both single and multi-metal containing solutions. Significantly lower XRF signals were observed using the Ultra Carry™ evaporative methodology to pre-concentrate the metals (**Figure 3.17**).

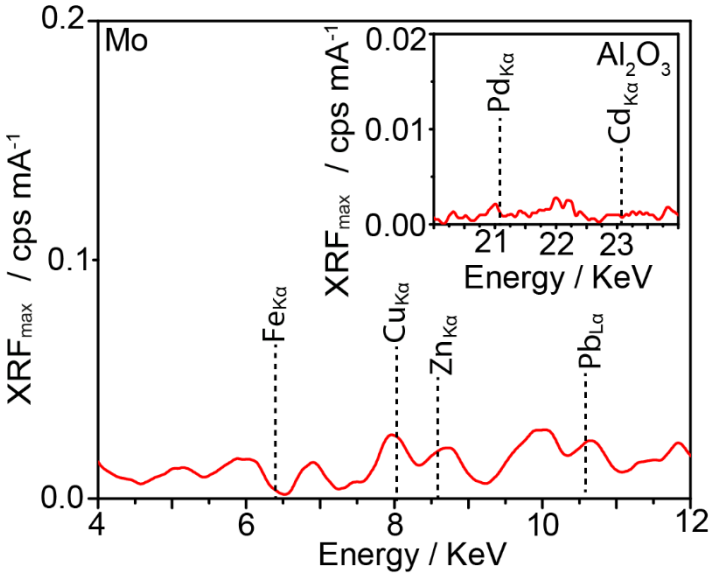

Figure 3.17*: *XRF signal intensities for 1.1 µM Fe^{3+}, Cu^{2+}, Zn^{2+}, Pb^{2+}, Pd^{2+} and Cd^{2+}, evaporatively pre-concentrated onto the Ultra Carry™ for ~1 hour. Note, lines indicate energy of most intense X-ray transmissions.

In fact, as **Figure 3.17** shows, the XRF responses of the different heavy metals are indiscernible from background noise; evidenced by the fact the observed XRF_{max} do not correlate with where the peak maxima are expected based on the known keV values for the transmission lines.

This method also comes with the additional caveat that evaporative pre-concentration takes ~60 minutes to complete. This data (and above) thus clearly demonstrates the power of electrochemical deposition as a versatile quantitative method of pre-concentration, where by simply tuning t_{dep} it is possible to achieve the required limit of detection.

Finally, there is significant opportunity to reduce both EC-XRF analysis times and concentration limits further by optimising the XRF instrumentation specifically for Pd

detection. The sources available on the commercial system employed here are far from ideal for Pd. Bespoke systems have been designed especially for Pd detection using monochromatic secondary targets such as Rh (20.22 keV) and Ag (22.16 keV),[54-55] which would enable us to significantly improve detection sensitivity or reduce deposition times.

3.4 Conclusions

Quantitative detection of Pd^{2+} in the presence of a variety of different electrochemically active compounds (present in excess), relevant to pharmaceutical, food and environmental applications, has been achieved using EC-XRF. Here the EC component is used to pre-concentrate metal (Pd) on the electrode (BDD) surface, under controlled mass transport conditions, whilst XRF is employed to both chemically identify and quantify the amount of metal on the surface (which in turn quantitatively correlates with the metal ion concentration in solution). The same, linear dependence of the XRF signal on [Pd^{2+}], for a fixed E_{dep} = −1.5 V and t_{dep} = 900 s, was determined in the presence and absence of ACM. For a fixed [Pd^{2+}] and E_{dep} = −1.5 V the XRF signal was also found to vary linearly with t_{dep} enabling electrochemical pre-concentration times to be predictably reduced to ≤ 100 s for quantitative analysis of 1.1 μM Pd = 10 ppm Pd with respect to 12g/L ACM; the maximum concentration allowed in pharmaceutical products for oral consumption. To facilitate lower concentration detection required simply increasing t_{dep}. A LOD of 34 nM was calculated (0.36 ppm with respect to 12 g/L ACM) for t_{dep} = 900 s. Lower values are possible by increasing t_{dep} further and/or changing the XRF secondary target to one which provides a great intensity signal for Pd. Pd^{2+} quantitative detection was also

possible in the presence of a large excess (1 mM) of other relevant electrochemically active compounds, such as L-ascorbic acid, caffeine and riboflavin. For 1.1 μM Pd^{2+} detection the same signal intensity was returned in both the presence and absence of these molecules (and for 12 g/L of ACM), for a fixed E_{dep} –1.5 V and t_{dep} = 325 s. Although riboflavin did appear to foul the electrode surface slightly during electrochemical pre-concentration, the high quality BDD electrode employed (minimal sp^2) helped to prevent significant fouling such that no impediment on the Pd reduction process was observed. Furthermore, even in the presence of other dissolved metal ions ($Fe^{3+,}$ Cu^{2+}, Zn^{2+}, Pb^{2+} and Cd^{2+}) the same signal intensity for 1.1 μM Pd^{2+} was also returned. This indicates that once calibrated the EC-XRF can be used quantitatively for the detection of Pd in a wide variety of solutions, containing other electrochemically active molecules. Moreover, the data also provided signal intensities for the five other metals in solution, proving that provided the metal could be electrodeposited on the surface it can be analysed. Note using conventional energy-dispersive XRF for 1.1 μM concentrations the XRF signals for all six metals were within the noise of the technique.

Finally this study paves the way for the use of *in-situ* EC-XRF trace metal identification and detection,[23] *i.e.* where EC metal deposition and XRF interrogation take place simultaneously in the measurement solution, negating the need to remove the electrode from solution to the XRF system. With advances in XRF instrumentation such that portable systems are now common place, EC-XRF analysis measurements at the source are a distinct possibility, unlike conventional ICP based techniques where the sample must be taken to the laboratory for analysis. It also should be noted that the

EC-XRF technique not only serves to quantify heavy metals but is also a method of recovery, adding to the appeal of the technique.

3.5 References

(1) Fu, F.;Wang, Q. *Journal of Environmental Management*, **2011**, *92*, 407–418.
(2) Fowler, S. W. *Marine Environmental Research*, **1990**, *29*, 1–64.
(3) Mahaffey, K. R.;Corneliussen, P. E.;Jelinek, C. F.;Fiorino, J. A. *Environmental Health Perspectives*, **1975**, *12*, 63–69.
(4) Järup, L. *British Medical Bulletin*, **2003**, *68*, 167–182.
(5) Fewtrell, L.;Kaufmann, R.;Prüss-Üstün, A. *Lead: Assessing the environmental burden of disease at national and local levels*;World Health Organisation, **2003**.
(6) Guideline on the specification limits for residues of metal catalysts or metal reagents. http://www.ema.europa.eu/docs/en_GB/document_library/Scientific _guideline/2009/09/WC500003586.pdf [Accessed 04/01/2016].
(7) Nageswara Rao, R.;Kumar Talluri, M. V. N. *Journal of Pharmaceutical and Biomedical Analysis*, **2007**, *43*, 1–13.
(8) Totland, M.;Jarvis, I.;Jarvis, K. E. *Chemical Geology*, **1992**, *95*, 35–62.
(9) Jagner, D. *Analyst*, **1982**, *107*, 593–599.
(10) Buffle, J.;Tercier-Waeber, M. L. *TrAC Trends in Analytical Chemistry*, **2005**, *24*, 172–191.
(11) Ross, J. W.;DeMars, R. D.;Shain, I. *Anal. Chem.*, **1956**, *28*, 1768–1771.
(12) Economou, A.;Fielden, P. R. *Analyst*, **2003**, *128*, 205–213.
(13) McGaw, E. A.;Swain, G. M. *Anal. Chim. Acta.*, **2006**, *575*, 180–189.
(14) Hull, E.;Piech, R.;Kubiak, W. W. *Electroanalysis*, **2008**, *20*, 2070–2075.
(15) Hutton, L. A.;Newton, M. E.;Unwin, P. R.;Macpherson, J. V. *Anal. Chem.*, **2011**, *83*, 735–745.
(16) Elkassabany, M.;Hoseney, R. *Cereal Chem*, *57*, 88–91.
(17) Pisoschi, A. M.;Pop, A.;Serban, A. I.;Fafaneata, C. *Electrochim. Acta.*, **2014**, *121*, 443–460.
(18) Channon, R. B.;Joseph, M. B.;Bitziou, E.;Bristow, A. W. T.;Ray, A. D.;Macpherson, J. V. *Anal. Chem.*, **2015**, *87*, 1006–10071.
(19) Skoog, D. A.;West, D. M. *Principles of instrumental analysis*;Saunders College Philadelphia, **1980**.
(20) Kanrar, B.;Sanyal, K.;Misra, N. L.;Aggarwal, S. K. *Spectrochimica Acta Part B: Atomic Spectroscopy*, **2014**, *101*, 130–133.
(21) Daher, R. T. *Anal. Chem.*, **1995**, *67*, 405–410.
(22) Marguí, E.;Van Grieken, R.;Fontàs, C.;Hidalgo, M.;Queralt, I. *Applied Spectroscopy Reviews*, **2010**, *45*, 179–205.
(23) Hutton, L. A.;O'Neil, G. D.;Read, T. L.;Ayres, Z. J.;Newton, M. E.;Macpherson, J. V. *Anal. Chem.*, **2014**, *86*, 4566–4572.
(24) Macpherson, J. V. *Phys. Chem. Chem. Phys.*, **2015**, *17*, 2935–2949.
(25) Streli, C.;Aiginoer, H.;Wobrauschek, P. *Spectrochimica Acta Part B: Atomic Spectroscopy*, **1989**, *44*, 491–497.
(26) Görög, S. *TrAC Trends in Analytical Chemistry*, **2006**, *25*, 755–757.
(27) Ahuja, S.;Alsante, K. M. *Handbook of isolation and characterization of impurities in pharmaceuticals*;Academic press, **2003**.
(28) Roy, J. *AAPS PharmSciTech*, **2002**, *3*, 1–8.
(29) Ahuja, S. *Advanced Drug Delivery Reviews*, **2007**, *59*, 3–11.
(30) Garrett, C. E.;Prasad, K. *Advanced Synthesis & Catalysis*, **2004**, *346*, 889–900.
(31) Nicolaou, K. C.;Bulger, P. G.;Sarlah, D. *Angewandte Chemie International Edition*, **2005**, *44*, 4442–4489.

(32) Torborg, C.;Beller, M. *Advanced Synthesis & Catalysis*, **2009**, *351*, 3027–3043.
(33) Bard, A. J.;Faulkner, L. R. *Electrochemical methods: fundamentals and applications*;Wiley New York, **1980**.
(34) Hutton, L.;Newton, M. E.;Unwin, P. R.;Macpherson, J. V. *Anal. Chem.*, **2009**, *81*, 1023–1032.
(35) Diculescu, V.;Chiorcea-Paquim, A.-M.;Corduneanu, O.;Oliveira-Brett, A. *J. Solid. State. Electr.*, **2007**, *11*, 887–898.
(36) Van Grieken, R.;Markowicz, A. *Handbook of X-ray Spectrometry*;CRC Press, **2001**.
(37) Heckel, J.;Schramm, R. **1996**,
(38) Savitzky, A.;Golay, M. J. *Anal. Chem.*, **1964**, *36*, 1627–1639.
(39) Granberg, R. A.;Rasmuson, Å. C. *Journal of Chemical & Engineering Data*, **1999**, *44*, 1391–1395.
(40) Aboul-Enein, H. *Chromatographia*, **2012**, *75*, 810–811.
(41) Miner, D. J.;Rice, J. R.;Riggin, R. M.;Kissinger, P. T. *Anal. Chem.*, **1981**, *53*, 2258–2263.
(42) Batchelor-McAuley, C.;Banks, C. E.;Simm, A. O.;Jones, T. G. J.;Compton, R. G. *ChemPhysChem*, **2006**, *7*, 1081–1085.
(43) Barone, J. J.;Roberts, H. R. *Food and Chemical Toxicology*, **1996**, *34*, 119–129.
(44) Bertotti, M.;Vaz, J. M.;Telles, R. *Journal of Chemical Education*, **1995**, *72*, 445.
(45) Bailey, M. I.;Thomas, A. W. *The Journal of Nutrition*, **1942**, *24*, 85–92.
(46) Crans, D. C.;Baruah, B.;Gaidamauskas, E.;Lemons, B. G.;Lorenz, B. B.;Johnson, M. D. *Journal of Inorganic Biochemistry*, **2008**, *102*, 1334-1347.
(47) Skrovankova, S.;Mlcek, J.;Sochor, J.;Baron, M.;Kynicky, J.;Jurikova, T. *Int. J. Electrochem. Sci*, **2015**, *10*, 2421–2431.
(48) Dutton, G. *Glucuronic Acid Free and Combined: Chemistry, Biochemistry, Pharmacology, and Medicine*;Elsevier, **2012**.
(49) Safavi, A.;Maleki, N.;Moradlou, O.;Tajabadi, F. *Analytical Biochemistry*, **2006**, *359*, 224–229.
(50) Švorc, L. *International Journal of Electrochemical Science*, **2013**, *8*, 5755–5773.
(51) Spãtaru, N.;Sarada, B. V.;Tryk, D. A.;Fujishima, A. *Electroanalysis*, **2002**, *14*, 721–728.
(52) Tan, S. L. J.;Webster, R. D. *J. Am. Chem. Soc.*, **2012**, *134*, 5954–5964.
(53) Chatterjee, A.;Foord, J. S. *Diamond. Relat. Mater.*, **2009**, *18*, 899–903.
(54) Van Meel, K.;Smekens, A.;Behets, M.;Kazandjian, P.;Van Grieken, R. *Anal. Chem.*, **2007**, *79*, 6383–6389.
(55) Uo, M.;Wada, T.;Sugiyama, T. *Japanese Dental Science Review*, **2015**, *51*, 2–9.

Chapter 4

Quinone electrochemistry for the comparative assessment of sp^2 surface content of boron doped diamond electrodes

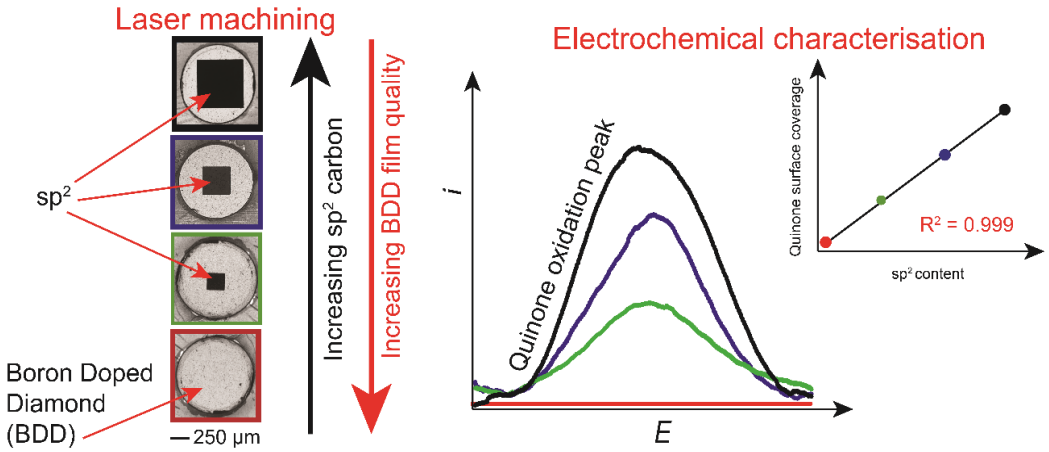

In this chapter, surface coverage measurements of electroactive quinone groups only present on sp^2 carbon sites, are used to inform on the sp^2 surface content of boron doped diamond (BDD) electrodes. Laser micromachining of a BDD electrode surface is used to systematically increase the amount of sp^2 carbon present by increasing the area machined. A linear relationship (R^2 = 0.9999) between quinone surface coverage and surface area laser micromachined is determined. Quinone surface coverage (Γ) measurements are also compared to other approaches of investigating sp^2 content, including solvent window and capacitance electrochemical methods as well as Raman spectroscopy. It was also considered important to prove that Γ measurements are applicable to native BDD, not just a laser micromachined surface. Thus comparative Γ assessment of electrodes containing different amounts of surface sp^2 carbon due to differences in the growth process is demonstrated.

4.1 Introduction

Polycrystalline boron doped diamond (BDD) has emerged as a popular material for the electrochemist in recent years[1,2] due to its exciting electroanalytical properties compared to more conventional electrode materials including: an extended solvent window (SW), low background currents, high chemical inertness and mechanical robustness, as well as increased resistance to fouling. For this reason, BDD electrodes have found use in a wide range of applications, such as electroanalysis,[3] biosensing,[4] wastewater processing[5] and spectroelectrochemistry.[6] Many of these properties arise from the sp^3 bonded carbon structure. However, achieving a pure sp^3 material during diamond synthesis especially in combination with high boron dopant levels, is challenging and almost impossible for nano- and smaller sized grain material.[7,8] Increasing sp^2 content has disadvantages e.g. increased background current, reduced SW, increased susceptibility to corrosion etc., but can also be advantageous[9] e.g. enhanced electrocatalytic properties[10] and provision of pH active functional groups.[11] Thus for each electrochemical application sp^2 surface presence needs to be carefully considered and controlled if possible.

Raman spectroscopy is widely used to assess sp^2 content in BDD electrodes[12] (discussed in detail in **Chapter 1.6.1**) often by comparing the ratio of the sp^3 (1332 cm^{-1}) peak to the G (1550 cm^{-1}) peak.[13] This method is however qualitative,[14] works best when comparing electrodes of the same dopant density and samples only a small area per measurement (~μm^2 – tens of μm^2 depending on magnification), which is especially problematic when sp^2 content is spatially heterogeneous.[15] Often neglected is the fact Raman also penetrates up to several microns[16] into the surface, returning information over this depth range, which is non-ideal for the electrochemist, who cares

only about surface sp^2 content. It is therefore imperative that *surface sensitive* characterisation methods are employed when assessing BDD material quality for electrochemical applications. To this end X-ray photoelectron spectroscopy has been explored,[17] but the method is relatively expensive, time-consuming and requires trained operators. It is also difficult to resolve the sp^2 and sp^3 signatures with peak deconvolution required,[18] leading to variations in peak assignments throughout the literature.[19,20]

In contrast electrochemistry represents a low cost, rapid characterisation technique providing information about charge transfer processes occurring at the electrode-solution interface. The presence of sp^2 carbon at the electrode surface has been shown previously to modify the SW and capacitance (*C*) of BDD electrodes[2,21] and result in surface bound quinone groups, which show a pH dependent redox signature, when suitably activated.[11] However, to date, no attempt has been made to correlate these observations with sp^2 surface content. In this chapter the use of the quinone redox signature to provide information on BDD sp^2 surface coverage is demonstrated. Direct comparisons with SW and *C* are also made.

4.2 Experimental

4.2.1 Materials

All solutions were prepared from Milli-Q water (Millipore Corp.), resistivity 18.2 MΩ cm at 25 °C. Four different BDD electrodes, numbered 1–4, were grown under different microwave chemical vapour deposition (CVD) conditions, in order to deliberately vary the sp^2 content of the electrodes. Electrodes 1–3 (Element Six, UK) contained ~3×10^{20} boron atoms cm^{-3}, and were grown thick (~250–500 µm) so that

they could be removed from the growth substrate and polished to ~ nm roughness. Due to the thickness of the material, large grain sizes of μm's to tens of μm's result. Electrode 1 was used as the baseline material for all laser machining studies and was considered to contain minimal sp^2 carbon (Element Six Diafilm EA grade material).[21] Electrode 4 (Advanced Diamond Technologies Inc., USA) was ultrananocrystalline (UNC) BDD and 2 μm thick (1.6×10^{21} boron atoms cm^{-3})[21] with the surface was left as-grown (surface roughness 9.3 ± 0.4 nm) with the electrode still attached to its niobium growth substrate.

C and SW measurements were run in 0.1 M potassium nitrate (KNO_3, Fisher Scientific). For quinone surface coverage (Γ) measurements, a pH 2 Carmody buffer was prepared,[22] with solution pH measured using a commercial pH meter (SevenEasy, Mettler Toledo).

4.2.2 Electrode preparation

Electrode 1 was laser machined using a 532 nm Nd:YAG nanosecond laser micromachiner (A-532 system, Oxford Lasers Ltd). Laser micromachining of BDD is known to result in sp^2 formation on the surface.[23] To systematically increase sp^2 content, six squares (n=3 for each i.e. 18 squares in total) of increasing size (length dimension 200 μm increasing to 700 μm) were machined into 18 individual electrodes of uniform geometric diameter, as shown in **Figure 4.1**.

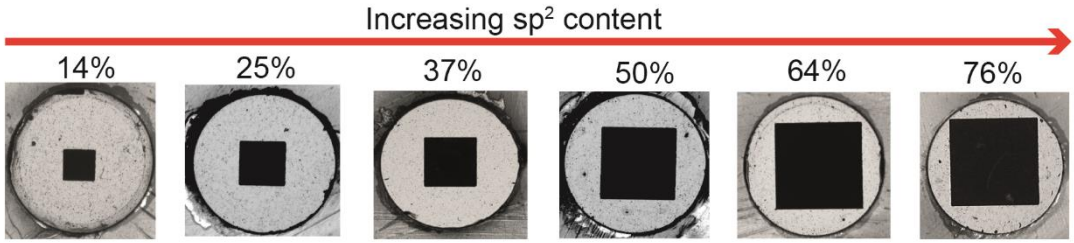

***Figure 4.1**: Optical images of the squares of increasing size (side length: left to right) 200, 300, 400, 500, 600 to 700 µm, laser micromachined into BDD.*

Identical laser parameters were employed (1000 Hz / 0.195 W with a machining speed of 0.3 mm s^{-1}) optimised to maximise sp^2 production.[24] Once machined, the electrodes were acid treated in boiling concentrated H_2SO_4 (98%) saturated with KNO_3 to oxygen terminate the surface and remove any loosely contacted sp^2 introduced during machining.[11] To provide a reliable ohmic contact, Ti (10 nm) / Au (300 nm) was sputtered (MiniLab 060 Platform, Moorfield Nanotechnology Ltd.) onto the back face of Electrodes 1–3 and top face of Electrode 4, and annealed at 400 °C for 5 h.[21]

For comparative electrode measurements (*vide infra*), all electrodes were acid treated in the same way prior to experiment. This involved running cyclic voltammetry (CV) experiments in 0.1 M H_2SO_4, from 0 V to −2 V and then 2 V, before returning to 0 V for 20 cycles.

4.2.3 Electrochemical setup

All electrochemical measurements were performed using a platinum counter and a saturated calomel reference electrode (SCE). The BDD electrodes were mounted onto a Ti/Au sputtered glass slide, using silver epoxy (RS Components Ltd.). To restrict the electrode area, Kapton tape (RS Components Ltd.) was laser machined to create 1 mm

diameter holes and positioned on the electrodes accordingly (**Figure 4.1**). All potentials are quoted versus SCE, with all experiments conducted at room temperature (25±2°C). SW values are calculated using a *i* density threshold of ±0.4 mA cm^{-2} using the second full CV scan[21] and C measurements were made as detailed in **Chapter 2.5.1**.

4.2.4 *Γ* measurements

For each electrode, CVs in pH 2 buffer, to maximise current signal, [11] were carried out (scan rate of 0.1 V s^{-1}), cycling from 0 to 0.7 V. The quinone peaks were integrated to obtain the charge passed, *Q*, and converted to *Γ* (mol cm^{-2}) using **Equation 4.1**:[25]

$$Q = nAF\Gamma \qquad (4.1)$$

where *n* = the number of electrons transferred = 2;[11,26] *A* = total electrode surface area (cm^2); calculated from WLI and *F* = Faraday's constant (96485 C mol^{-1}).

4.2.5 White Light Laser Interferometry (WLI)

A Bruker ContourGT (Bruker Nano Inc., USA) was used to record WLI profiles. 3D rendering of interferometry data was performed and the increase in electrode area after machining calculated using Gwyddion 2.42.

4.3 Results and Discussion

4.3.1 Characterisation of laser micromachined electrodes

4.3.1.1 Interferometry

To investigate the uniformity of the laser micromachining process, interferometry line scan data was collected for each of the laser micromachined BDD samples, shown in **Figure 4.2**.

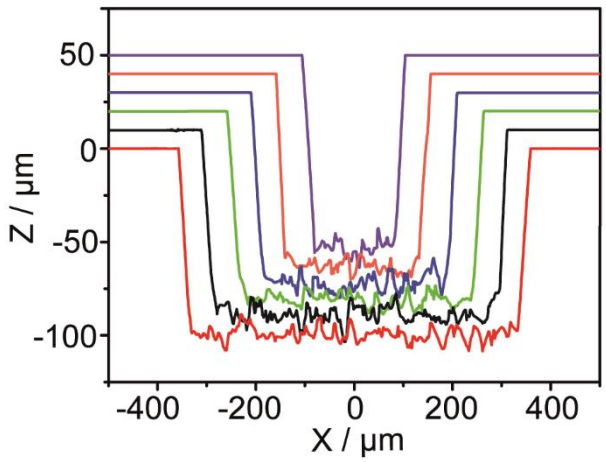

Figure 4.2*: *Interferometry data for the laser micromachined pits 200, 300, 400, 500, 600, 700 µm, corresponding to purple, orange, blue, green, black and red respectively, offset in the Z axis for clarity.

The laser micromachining was found to be consistent with pit depths of 101.2 ± 1.9 µm and a root mean squared (rms) roughness of 3.89 ± 0.18 µm across all samples. The average rms roughness values and pit depths for each of the samples (n=3) are summarised in **Table 4.1**.

Table 4.1: Summary of average rms and pit depth for laser features using WLI.

Laser feature side length / µm	Average rms / µm	Average pit depth / µm
700	3.67±0.06	98.63±0.06
600	3.77±0.15	99.53±0.15
500	3.83±0.15	100.43±0.12
400	4.13±0.06	101.8±0.35
300	3.97±0.15	102.5±0.74
200	3.97±0.06	104.2±1.79

4.3.1.2 Surface Area Calculations

The total surface area for each sample was calculated using Gwyddion 2.42 (Czech Metrology Institute, CZE) based on the topographical information collected by WLI. The surface area data collected by WLI was then used to calculate the percentage of the 1 mm masked area which had been exposed to laser ablation, including both the base of the pits and the sidewalls. Samples were processed by Laplace interpolation using Gwyddion 2.42 (Czech Metrology Institute, CZE) and a three-point level was applied to the bare diamond surface to set the data zero point. A mask was applied fully covering the laser feature. The surface area increase was then calculated by subtracting the projected mask area from the mask surface area (incorporating the laser feature and corresponding roughness from WLI). The calculated surface area increase (laser pit) was added to the area of the 1 mm^2 Kapton mask to give the total area of the electrode. These areas are summarised in **Table 4.2**.

Table 4.2: Total electrode area including laser features, calculated by WLI.

Laser feature side length / µm	700	600	500	400	300	200
Average electrode area / cm^2	0.0123± 7.4×10^{-6}	0.0117± 8.0×10^{-6}	0.0109± 1.1×10^{-4}	0.0099± 4.9×10^{-5}	0.0092± 2.9×10^{-5}	0.0086± 1.1×10^{-5}

The process was repeated, with the projected area restricted to the size of the laser features. WLI data was then used to calculate the total area of the laser feature. The ratio of the full laser area to the laser micromachined area was then calculated. The percentage area of the laser feature with respect to the total area of the electrode is referred to from hereon as the area laser micromachined (%). This can be summarised in **Equation 4.2**:

$$\text{Machined surface area (\%)} = \frac{\text{machined surface area}}{\text{total electrode surface area}} \times 100 \quad (4.2)$$

For the laser features machined into the BDD surface (side lengths = 200, 300, 400, 500, 600 and 700 µm) this equates to 14, 25, 37, 50, 64 and 76 % respectively, as shown in **Figure 4.1**.

4.3.2 Quinone group identification

The electrochemical response of the laser micromachined BDD was investigated in order to identify possible electroactive quinone peaks that had been introduced into the electrode surface. Three possible quinone-like groups were identified, labelled (i)-(iii) shown on **Figure 4.3**, occurring at ~ −0.2 V, +0.17 V and +0.45 vs. SCE respectively (for a scan rate of 0.1 V s^{-1}) under degassed conditions. Note, just the oxidative peaks

are labelled for clarity. These oxidation peaks are likely to be associated with surface bound quinone groups due to the presence of reduction peaks at a similar potential.

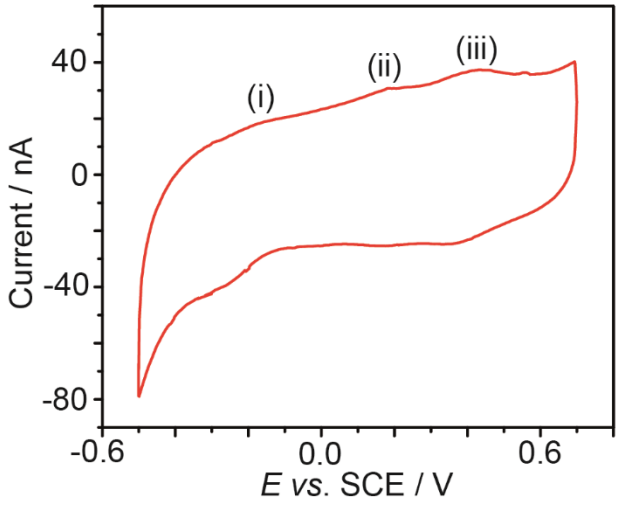

Figure 4.3**:** *CV in pH 2 Carmody buffer of the 50% laser micromachined sample, run at 0.1 V* s^{-1}*, degassed with* N_2 *for 30 minutes, showing the positions three possible quinone oxidation peaks (i)–(iii).*

In order for Γ measurements of quinone-like groups on the surface, to be established as an electroanalytical method for the comparative assessment of sp^2 content in BDD, the technique must be simple and rapid. For this reason, peak (i) was discounted as the peak is not easily discernible without degassing of the solution, due to the onset of oxygen evolution on such a heavily laser ablated (high sp^2) surface.

The response of peak (ii) in aerated solution for the laser micromachined electrodes is shown in **Figure 4.4**.

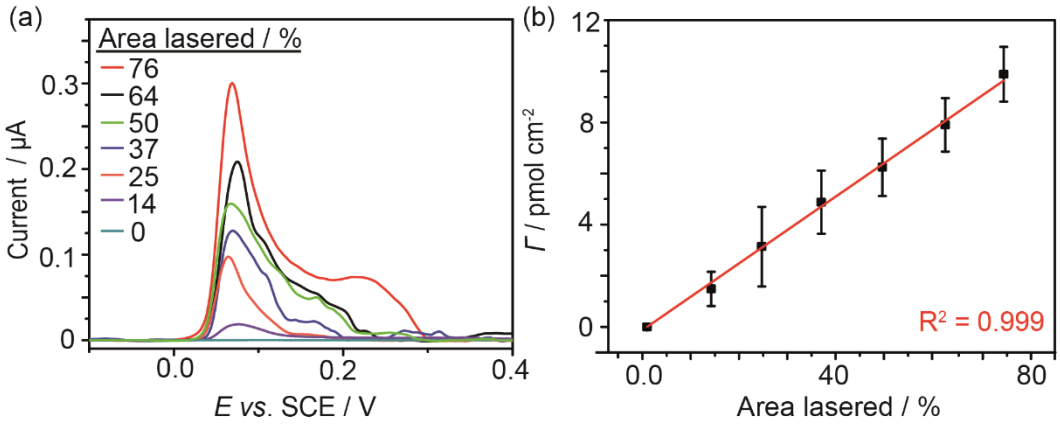

***Figure 4.4**: (a) Representative (ii) quinone oxidation peaks for the six machined electrodes and a blank (n=3), in pH 2 buffer, at a scan rate of 0.1 V s^{-1} (b) Plot of machined surface area (%) versus Γ.*

The observed response is more complex than observed for the degassed experiment (**Figure 4.3**) appearing to show a convolution of several peaks. Integration of the peak (from +0.0 to +0.3 V vs. SCE) and subsequent calculation of Γ, results in a linear correlation (R^2 = 0.999) between the % area laser micromachined and the amount of quinone molecules present on the laser micromachined BDD electrode surfaces. However, there is a large amount of variability in the Γ value observed, with Γ measurements for the laser micromachined electrodes overlapping due to large error bars, despite the laser ablated area increasing dramatically by > 10% from electrode to electrode. The response of peak (iii) for the laser micromachined electrodes was thus investigated (shown in **Figure 4.5**).

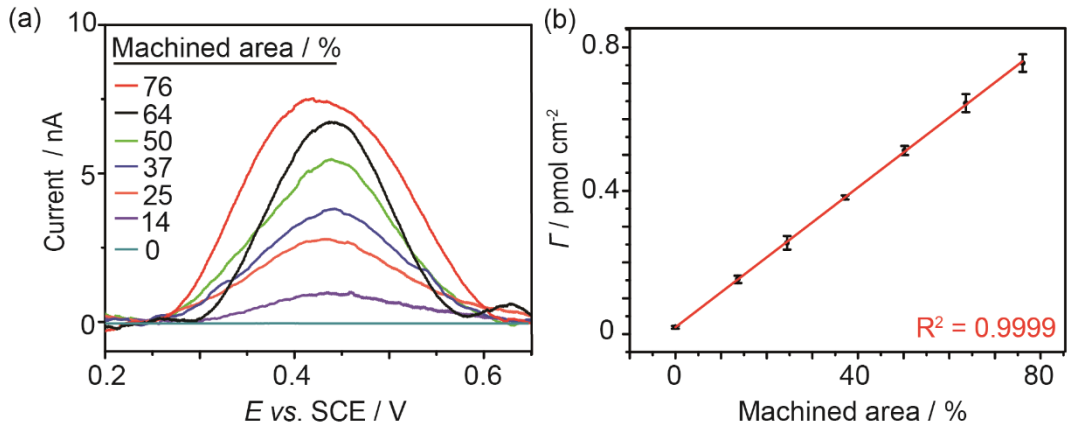

Figure 4.5**:** *(b) Representative (iii) quinone oxidation peaks for the six machined electrodes and a blank (n=3), in pH 2 buffer, at a scan rate of 0.1 V* s^{-1}*. (b) Plot of machined surface area (%) versus Γ.*

The peaks were integrated (from +0.25 to +0.62 V vs. SCE) and the *Γ* calculated. **Figure 4.5b** shows *Γ* vs. % machined surface area. As the area machined increases *Γ* also increases linearly (R^2 = 0.9999) indicating a very strong correlation between the quinone surface coverage and the amount of sp^2 created due to the laser ablation process. The sensitivity is also vastly increased compared to that of peak (ii), with significant differences between the *Γ* values obtained for the laser micromachined electrodes (0–76% laser machined areas). Furthermore, compared to peak (ii) (**Figure 4.4a**) the peak is Gaussian in shape, and was stable after cycling for repeat cycles (*n*=20). This suggests that *Γ* can be effectively used to inform on sp^2 carbon present at the electrode surface.

4.3.3 Comparison with SW and C

C and SW measurements (**Figure 4.6a** and **Figure 4.6b** respectively) were also made with the same 18 electrodes (6 laser micromachining conditions, to *n*=3), and

subsequently compared to Γ data, shown in **Figure 4.6c**. It is apparent that C also follows a similar trend to Γ, with % machined surface area, with a linear response observed (R^2 = 0.9992). This is supported by literature, with quinone groups shown to increase the total C observed.[31,32] We define the SW as the potential window in which a current of no more than of ±0.4 mA cm^{-2} is passed.[21] This is defined as the threshold current and is marked by a dotted line in **Figure 4.6b**. From **Figure 4.6c**, the SW data does not follow the same trend as Γ and C and plateaus for machined areas ≥ 64%. This is due to the complexity of the SW's observed when sp^2 carbon is present, especially as levels increase (**Figure 4.6b**).

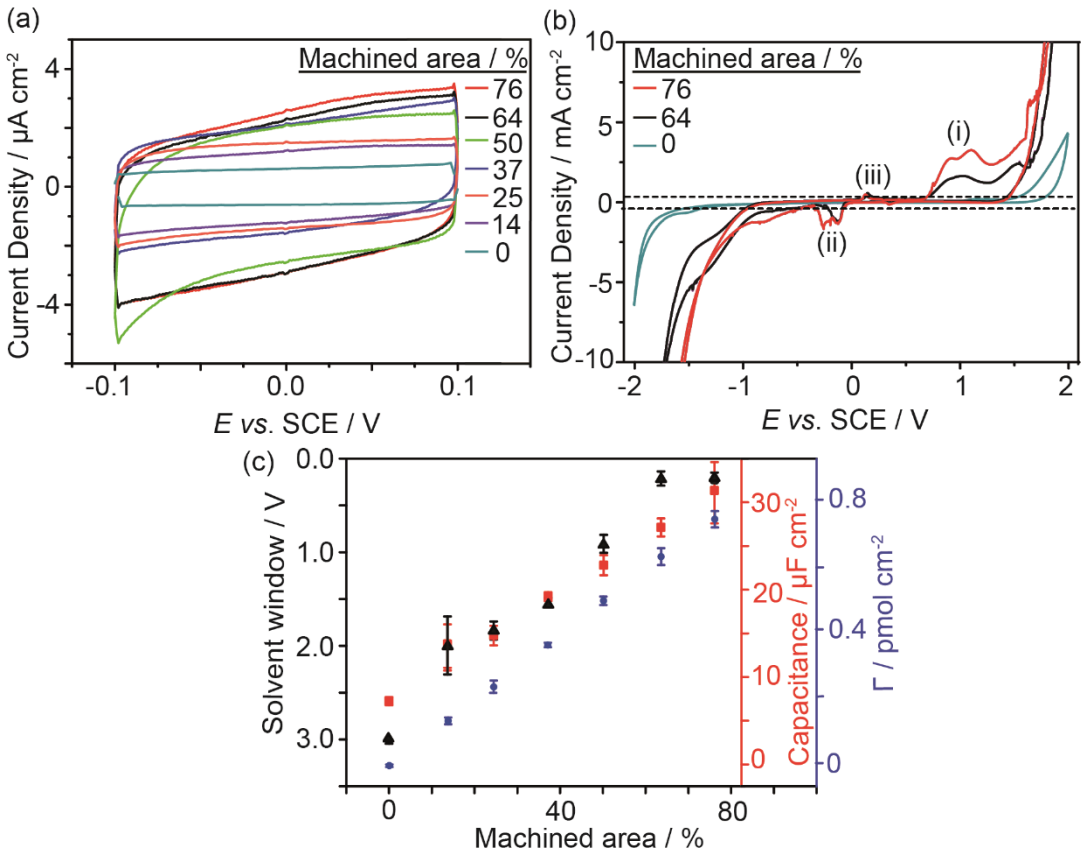

***Figure 4.6**: Electrochemical measurements (scan rate of 0.1 V s^{-1}) for six BDD electrodes with increasing machined area (0–76%) including: (a) C data, (b) selected SW data for clarity, showing the ±0.4 mA cm^{-2} threshold (dotted lines) and (c) comparison of SW, C and Γ with % machined surface area.*

At high sp^2 levels, significant oxidation features close to the anodic solvent window (labelled i) are observed. The features labelled (ii) and (iii) we ascribe to the reduction and oxidation of reactive oxygen species, respectively, such as hydrogen peroxide electrogenerated in the presence of quinone groups. Although there are clear differences the current magnitude of the SW features, especially anodically for 64% and 76% machined electrodes, there is little variation in the SW values recorded. Furthermore, no threshold current could be found which enabled a linear response between SW and % machined surface area.

4.3.4 Γ Assessment of BDD films

It is also important to demonstrate whether the approach advocated in **Figure 4.5** for Γ could be used to distinguish between electrodes that have naturally present sp^2 from the growth process. Thus BDD electrodes 1–4, grown using procedures which should result in an increasing sp^2 content (and are both thin film and thick freestanding) were analysed, with SW and C values summarised in **Table 4.3.** Care was taken to subject the BDD electrodes to the same pre-treatment conditions before analysis to ensure comparable surfaces.

***Table 4.3**: SW and C values for Electrodes 1–4.*

Electrode	SW / V	Capacitance / μF cm^{-2}
1	3.375	6.2 ± 0.5
2	3.116	6.5 ± 0.4
3	3.065	6.8 ± 0.6
4	1.352	20.8 ± 0.4

The SW and *C* data confirm that the sp^2 content of the electrodes increases from 1–4. Whilst the SW values fall within the linear region of **Figure 4.6c**, electrode 4 has a SW value close to the edge of the linear range. It is therefore possible that for some low quality BDD films, SW measurements will not provide appropriate assessment of sp^2 content. It is also important to note that *C* can also be affected by other factors such as contact resistance, therefore may not always exclusively represent the sp^2 component.

Changes in the synthesis conditions and resulting thickness of electrodes 1–4 are also reflected optically (**Figure 4.7a**) in the resulting grain structures observed. **Figure 4.7** shows the quinone oxidation response for the four electrodes.

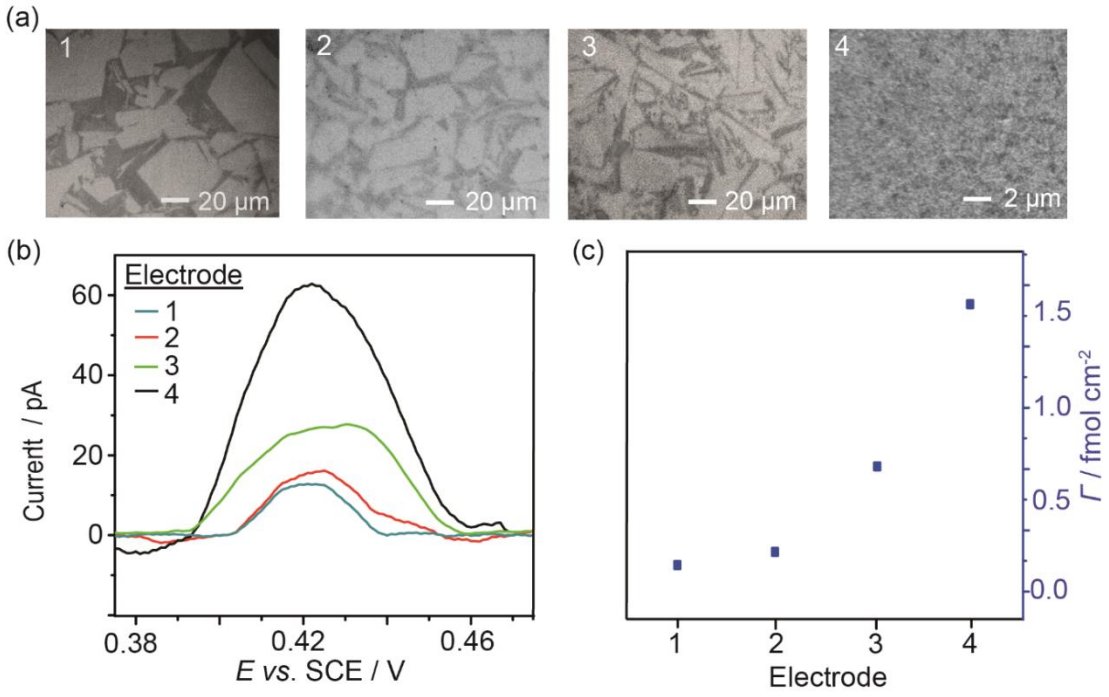

***Figure 4.7**: Investigation of BDD electrodes 1–4 including (a) optical images (×50 and ×100 objective for 1–3 and 4 respectively) showing grain structures and (b) the quinone oxidation responses at a scan rate of 0.1 V s^{-1} and (c) Γ measurements.*

A clear increase in quinone oxidation peak, i.e. increasing Γ is observed for electrodes 1–4, with Γ values of $1.8 \times 10^{-16} \pm 1.6 \times 10^{-17}$, $2.9 \times 10^{-16} \pm 1.9 \times 10^{-17}$, $7.0 \times 10^{-16} \pm 3.2 \times 10^{-17}$ and $1.6 \times 10^{-15} \pm 5.6 \times 10^{-17}$ mol cm^{-2} recorded, respectively (**Figure 4.7c**). Note the data recorded on the UNC electrode 4 suggests electrochemically active sp^2 coverages almost an order of magnitude higher than the minimal sp^2 content electrode 1.

4.3.5 Raman Spectroscopy

For comparison, Raman analysis was conducted on samples 1–4, shown in **Figure 4.8**.

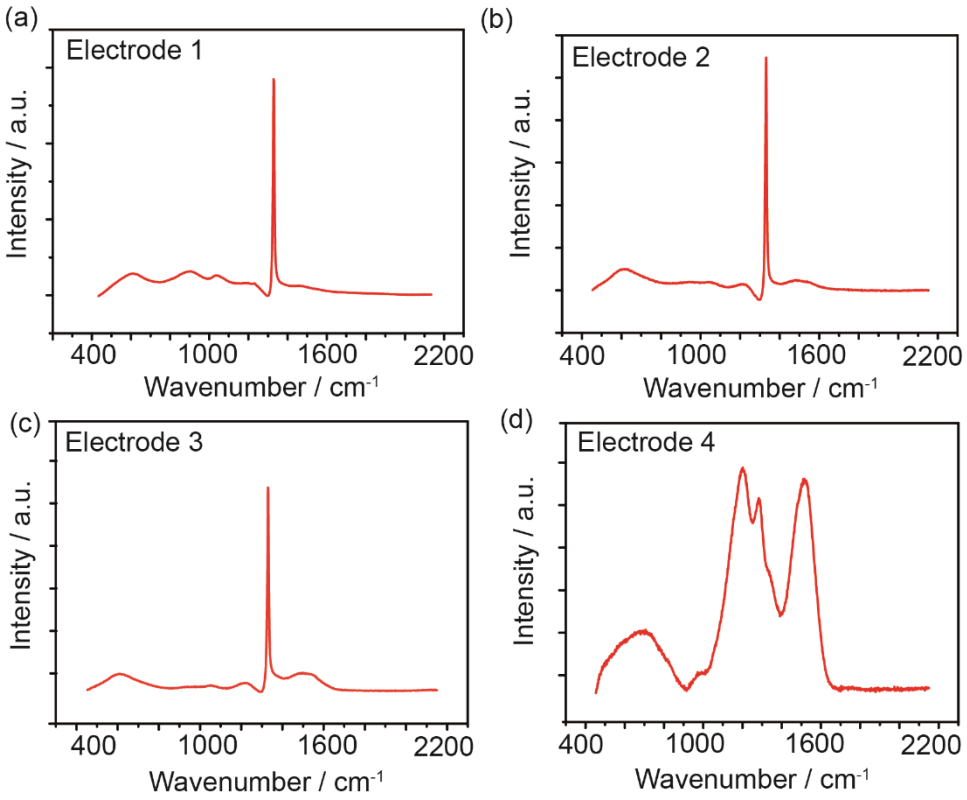

***Figure 4.8**: Example Raman spectra for electrodes 1–4 (a–d respectively) at 532 nm, ×50 objective using a Renishaw inVia Raman microscope.*

For Electrode 4 an sp^2 signal was observed at all random locations investigated (n=20) by Raman spot measurements (532 nm, ×50 objective, Renishaw inVia Raman microscope), whilst Electrodes 1–3 all showed spatial variations, with a fraction of spots (per electrode) showing minimal sp^2 signal, if at all. This is illustrated in **Figure 4.9**, showing the ratio of the G peak (1550 cm^{-1}, attributed to sp^2 carbon – see **Chapter 1.6.1**) compared to the 1332 cm^{-1} peak (sp^3 carbon). It is apparent that there are regions containing considerably more sp^2 carbon.

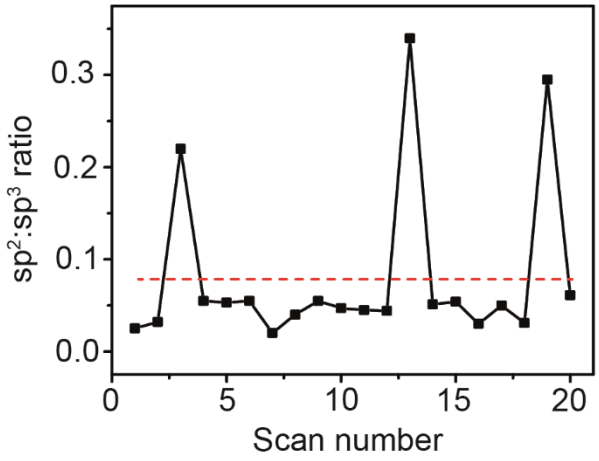

***Figure 4.9*: *Raman measurements at randomised locations on Electrode 4*.**

Furthermore, it has been shown that with increasing B concentration, the intensity of the 1332 cm^{-1} peak decreases. As the boron concentration is higher in Electrode 4 (1.6×10^{21} boron atoms cm^{-3}) than Electrodes 1–3, the D peak was reduced in intensity (due to strain, discussed in **Chapter 1.6.1**) compared to electrodes 1–3, making D/G ratio comparisons between electrodes inappropriate.

4.4 Conclusions

In this chapter, a new method for comparatively assessing the sp^2 surface content of different BDD electrodes is introduced. A laser machining process is used to systematically increase the sp^2 content of a BDD electrode by ablating progressively larger squares of graphitised carbon into the surface of a minimal sp^2 content BDD electrode. The graphitised surface contains quinone groups which can be oxidised. The area under the oxidation peak which equates to Γ scales linearly (R^2 = 0.9999) with sp^2 surface content (under acidic conditions) expressed as % of machined surface area compared to total electrode area. We show this approach is also applicable to BDD electrodes which contain inherent sp^2 resulting from the growth process. Γ measurements were able to clearly distinguish between four different electrodes and place them in order of increasing sp^2 surface content. Γ values as low as 0.18 fmol cm^{-2} were recorded on the minimal content BDD electrode rising to 1.6 fmol cm^{-2} for the UNC material, demonstrating both excellent sensitivity and selectivity for BDD electrode characterisation. We suggest Γ measurements as a preferred method, compared to Raman microscopy, for comparing sp^2 content in electrode surfaces, as the latter is unfortunately not purely surface sensitive and requires the same doping levels in electrodes.

4.5 References

(1) Einaga, Y.;Foord, J. S.;Swain, G. M. *MRS Bulletin*, **2014**, *39*, 525–532.
(2) Macpherson, J. V. *Phys. Chem. Chem. Phys.*, **2015**, *17*, 2935–2949.
(3) Compton, R. G.;Foord, J. S.;Marken, F. *Electroanalysis*, **2003**, *15*, 1349–1363.
(4) Zhou, Y.;Zhi, J. *Talanta*, **2009**, *79*, 1189–1196.
(5) Gandini, D.;Mahé, E.;Michaud, P. A.;Haenni, W.;Perret, A.;Comninellis, C. *Journal of Applied Electrochemistry*, **2000**, *30*, 1345–1350.
(6) Hutton, L. A.;O'Neil, G. D.;Read, T. L.;Ayres, Z. J.;Newton, M. E.;Macpherson, J. V. *Anal. Chem.*, **2014**, *86*, 4566–4572.
(7) Watanabe, T.;Honda, Y.;Kanda, K.;Einaga, Y. *physica status solidi (a)*, **2014**, *211*, 2709–2717.
(8) Williams, O. A.;Nesladek, M.;Daenen, M.;Michaelson, S.;Hoffman, A.;Osawa, E.;Haenen, K.;Jackman, R. B. *Diamond. Relat. Mater.*, **2008**, *17*, 1080–1088.
(9) Bennett, J. A.;Wang, J.;Show, Y.;Swain, G. M. *J. Electrochem. Soc.*, **2004**, *151*, 306–313.
(10) Garcia-Segura, S.;dos Santos, E. V.;Martínez-Huitle, C. A. *Electrochem. Commun.*, **2015**, *59*, 52–55.
(11) Ayres, Z. J.;Borrill, A. J.;Newland, J. C.;Newton, M. E.;Macpherson, J. V. *Anal. Chem.*, **2016**, *88*, 974–980.
(12) Ferrari, A. C.;Robertson, J. *Philosophical Transactions of the Royal Society of London A: Mathematical, Physical and Engineering Sciences*, **2004**, *362*, 2477–2512.
(13) Prawer, S.;Nemanich, R. J. *Philosophical Transactions of the Royal Society of London A: Mathematical, Physical and Engineering Sciences*, **2004**, *362*, 2537–2565.
(14) Cuesta, A.;Dhamelincourt, P.;Laureyns, J.;Martínez-Alonso, A.;Tascón, J. M. D. *Carbon*, **1994**, *32*, 1523–1532.
(15) Patten, H. V.;Hutton, L. A.;Webb, J. R.;Newton, M. E.;Unwin, P. R.;Macpherson, J. V. *Chemical Communications*, **2015**, *51*, 164–167.
(16) Ferreira, N. G.;Abramof, E.;Corat, E. J.;Trava-Airoldi, V. J. *Carbon*, **2003**, *41*, 1301–1308.
(17) Briggs, D.;Seah, M. P. *Practical surface analysis by Auger and X-ray photoelectron spectroscopy*;John Wiley & Sons, **1983**. 105–125
(18) Calliari, L. *Diamond. Relat. Mater.*, **2005**, *14*, 1232–1240.
(19) Jackson, S. T.;Nuzzo, R. G. *Applied Surface Science*, **1995**, *90*, 195–203.
(20) Mérel, P.;Tabbal, M.;Chaker, M.;Moisa, S.;Margot, J. *Applied Surface Science*, **1998**, *136*, 105–110.
(21) Hutton, L. A.;Iacobini, J. G.;Bitziou, E.;Channon, R. B.;Newton, M. E.;Macpherson, J. V. *Anal. Chem.*, **2013**, *85*, 7230–7240.
(22) Carmody, W. R. *Journal of Chemical Education*, **1961**, *38*, 559.
(23) Butler-Smith, P. W.;Axinte, D. A.;Pacella, M.;Fay, M. W. *Journal of Materials Processing Technology*, **2013**, *213*, 194–200.
(24) Wang, C. Z.;Ho, K. M.;Shirk, M. D.;Molian, P. A. *Physical Review Letters*, **2000**, *85*, 4092–4095.
(25) Bard, A. J.;Faulkner, L. R. *Electrochemical methods: fundamentals and applications*;Wiley New York, **1980**. 626–634.
(26) Lu, M.;Compton, R. G. *Analyst*, **2014**, *139*, 4599–4605.
(27) Lobyntseva, E.;Kallio, T.;Alexeyeva, N.;Tammeveski, K.;Kontturi, K. *Electrochim. Acta.*, **2007**, *52*, 7262–7269.

(28) Santacesaria, E.;Di Serio, M.;Russo, A.;Leone, U.;Velotti, R. *Chemical Engineering Science*, **1999**, *54*, 2799–2806.
(29) Liu, T.;Meng, X.;Wang, Y.;Liang, X.;Mi, Z.;Qi, X.;Li, S.;Wu, W.;Min, E.;Fu, S. *Industrial & engineering chemistry research*, **2004**, *43*, 166–172.
(30) Song, C.;Zhang, J. *PEM fuel cell electrocatalysts and catalyst layers*; Springer. 2008.
(31) Algharaibeh, Z.;Pickup, P. G. *Electrochem. Commun.*, **2011**, *13*, 147–149.
(32) Le Comte, A.;Chhin, D.;Gagnon, A.;Retoux, R.;Brousse, T.;Belanger, D. *Journal of Materials Chemistry A*, **2015**, *3*, 6146–6156.

Chapter 5

Impact of multimode chemical vapour deposition growth under low pressure conditions on the spatial variation of sp^2 carbon in boron doped diamond electrodes

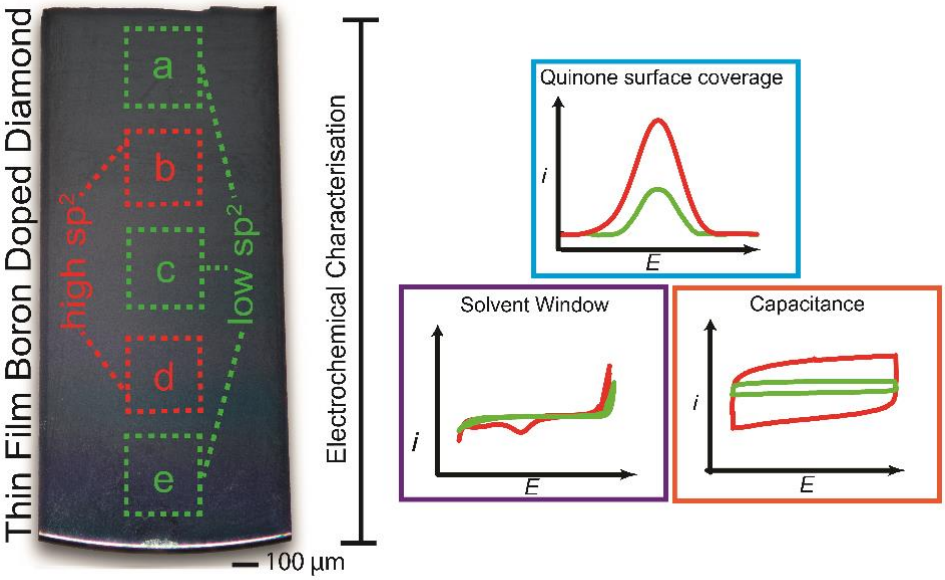

The impact of low pressure growth in a multi-mode microwave chemical vapour deposition (MW-CVD) reactor on the sp^2 content of thin film (~ micron) boron doped diamond (BDD), under different methane (CH_4) concentrations (1% and 5%), is investigated. The boron is doped at a concentration suitable for electrochemical studies and the sp^2 *surface* content is comparatively assessed using a variety of electrochemical measurements: capacitance; solvent window analysis and quinone surface coverage. Distinctive regions, across both growth wafers, containing appreciably differing amounts of sp^2 carbon are identified. For example, on the 1% CH_4 wafer, some areas exhibit electrochemical signatures indicative of high quality, minimal sp^2 content BDD, whereas others show regions comprising significant sp^2 carbon. Note Raman microscopy was unable to identify these variations. On the 5% CH_4 wafer, no region was found to contain minimal levels of sp^2 carbon. Changes in

sp^2 content across the BDD films indicates spatial variations in parameters such as temperature, methane and atomic hydrogen concentrations during growth. This is linked directly to the use of a multi-moded chamber for MW-CVD BDD synthesis under low pressure conditions. Varying sp^2 levels can have significant impact on the resulting electrochemical behaviour of the BDD.

5.1 Introduction

Boron-doped diamond (BDD) electrodes exhibit many exceptional properties compared to other conventional electrodes due to its sp^3 carbon structure, making it a desirable material for the electrochemist.[1] These properties include: low capacitance (*C*), a wide solvent window (SW), as well as resistance to fouling and mechanical wear.[2] However, growing BDD in the phase pure sp^3 form, without contamination from sp^2 bonded carbon, is challenging especially as boron concentration increases.[3] It is thus very important, especially when interpreting the material performance properties, to evaluate and account for the presence of sp^2 non diamond carbon impurities introduced during growth.[4,5,6] Interestingly, these can impact the electrochemical response both negatively e.g. reduced SW, increased background currents, increased susceptibility to corrosion,[7] and positively e.g. increased electrocatalytic activity,[8] introduction of pH sensitive functional groups,[9] stronger adsorption sites for electrosynthesis.[10]

A common technique to produce BDD at suitable dopant levels for electrochemical use ($> 10^{20}$ B atoms cm^{-3}) is microwave chemical vapour deposition (MW-CVD). However, the reactor conditions employed, such as: (i) substrate temperature; (ii) methane concentration; (iii) deposition pressure; (iv) microwave power and (v) hydrogen concentration,[11,12] can greatly impact on sp^2 incorporation. For example, higher quality (low sp^2 content) BDD films are often grown using low CH_4 concentrations (≤ 1%) allowing the hydrogen in the reactor to preferentially etch away the majority of the sp^2 present.[13] By increasing CH_4 concentration (to > 5%) higher sp^2 content ‘nanocrystalline’ BDD is produced which can be considered an aggregate of disordered graphite and diamond nanocrystals.[14] In some applications, higher CH_4

concentrations may be preferred as growth is significantly faster and results in smoother films, despite the increase in sp^2 carbon.[15] Unfortunately, regulating growth parameters is not straight forward as each of the above parameters (i–vi) all influence each other.

The design of the MW-CVD reactor can also impact the quality and uniformity of the BDD films produced. For example, to increase deposition areas and make synthetic diamond production more economical, multi-mode (overmoded) MW-CVD systems are often utilised, where the reactor is designed to facilitate the overlap of transverse magnetic resonant modes to create a larger plasma.[16,17] Coupled with a low pressure growth regime (<80 Torr), deposition areas > 10 cm have been achieved.[18] However, recent numerical simulations have shown that overmoded reactors run at these low pressures can result in non-uniform microwave power distributions close to the substrate surface.[19] This in turn will result in variations of the concentration of species (*i.e.* CH_4 and H) in the plasma, which in turn affects growth and etch rates within the CVD reactor.[13]

A vast amount of research has been conducted to produce thin film i.e. < 20 μm (and still attached to the growth substrate) diamond with compositional uniformity that is cost effective.[16,20,21] To date this still presents both a scientific and technical challenge, with the only option to move to higher power densities or lower CH_4 concentrations resulting in significantly higher production costs.[13] For this reason some manufacturers and research groups still opt to grow diamond using overmoded MW-CVD systems at low pressures, often outside recommended conditions for uniform growth.[22,23,24]

In this study, we investigate the effect of operating an overmoded MW-CVD reactor under low pressure conditions (40 Torr) and varying methane concentrations (1% and 5%), on thin film BDD growth, and explore the suitability of the resulting material for electrochemical use. In particular, we assess spatial variations in film quality, focusing primarily on sp^2 incorporation and its effect on the resulting electrochemical response. To the best of our knowledge, we present, for the first time, experimental confirmation of variations in growth conditions on the same wafer (via electrochemical characterisation techniques) in an overmoded MW-CVD reactor under low pressure conditions, supporting previous simulation work.[19,25]

5.2 Experimental

5.2.1 Diamond Growth

The BDD films utilised in this study were grown on 500 µm thick, 2-inch diameter (5.08 cm) silicon (100) p-type wafers by MW-CVD, using a Seki 6500 series MP reactor, which was overmoded (multi-mode cavity), allowing for larger discharge areas.[25] The silicon substrates were cleaned using a standard cleaning process (SC-1) using hydrogen peroxide (30% H_2O_2 in H_2O, Sigma Aldrich), ammonium hydroxide (30% in H_2O, Sigma Aldrich) and ultrapure Milli-Q water (Millipore Corp., resistivity 18.2 MΩ cm at 25 °C) in a 1:1:5 ratio at 75°C for 10 minutes, followed by sonication in ultrapure water for 10 minutes and subsequently spinning dry.[26] In order to facilitate growth on the non-diamond substrate, the Si surface was seeded with small (~5 nm) diamond nanoparticles (NP: PL-D-G01 diamond powder; PlasmaChem GmbH, Germany) by sonicating in a nanodiamond (4 ± 2 nm)/H_2O colloid for 10 minutes.[26]

Before use the NPs were subject to a cleaning procedure to remove sp^2 carbon contamination.[27] This type of seeding results in a nucleation density in excess of 10^{11} NP's cm^{-2}.[28] The seeded wafers were then rinsed with DI water, spun dry at 3000 rpm and immediately placed in the MW-CVD reactor for diamond growth.

Two films were grown under 1% and 5% CH_4 conditions (in the presence of 99% and 95% H_2 respectively) at 40 Torr and 3.5 kW microwave power, for 825 mins (1%) and 180 mins (5%). The thickness of the films was ~ 1 μm as determined by pyrometric interferometry during the growth process (one spot measurement in the centre of the wafer). The BDD films were doped using trimethylboron in hydrogen, at a B to C ratio in the gas phase of ~6400 ppm (~1.5×10^{21} B atoms cm^{-3})[29] ensuring the material was sufficiently doped to function as an electrode. The substrate temperature at the centre of the film was ~800 ^{o}C as determined by dual wavelength pyrometry.

5.2.2 Electrode preparation

To ensure the electrodes were oxygen (O-)-terminated and to ensure a comparative surface chemistry prior to electrochemical measurements, all electrodes were acid treated by running cyclic voltammetry (CV) experiments in 0.1 M H_2SO_4, from 0 V to -2 V and then to + 2 V, before returning to 0 V, for 20 cycles.[30]

5.2.3 Electrochemical measurements

For all electrochemical measurements, a three-electrode configuration was utilised with a platinum wire as a counter electrode and a saturated calomel electrode (SCE) as the reference electrode. To create the working electrodes, segments (width = 1 cm, length = 2 cm) were laser micromachined (A-532 system, Oxford Lasers Ltd) from the 2 inch (5.08 cm diameter) BDD wafer, *vide infra*. To create a reliable ohmic contact for electroanalysis, Ti (10 nm) / Au (300 nm) was sputtered (MiniLab 060 Platform, Moorfield Nanotechnology Ltd.) on the top face of the BDD segment and annealed at 400 °C for 5 h.[30] The electrode area for each measurement was defined by a Kapton tape mask (RS Components Ltd.), laser micromachined (A-532 system, Oxford Lasers Ltd) to create a 1 mm exposed area of the BDD for electroanalysis (**Figure 5.1**). A new mask was applied for each region to be analysed. For each segment, five electrochemical measurements were made in different areas across the segment.

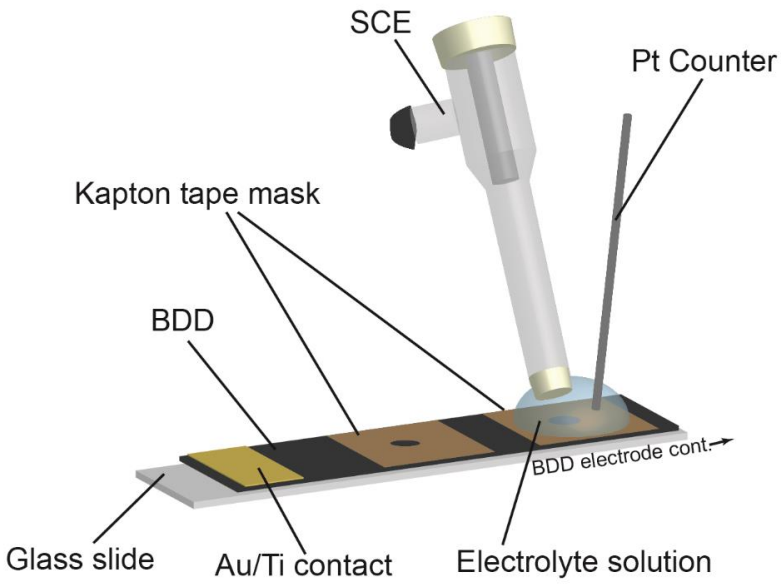

***Figure 5.1**: Setup utilised to investigate the electrochemical response across a wafer segment.*

All solutions were prepared from Milli-Q water (Millipore Corp.), resistivity 18.2 MΩ cm at 25 °C. A solution containing 1 mM hexaaminеruthenium (III) chloride ($Ru(NH_3)_6^{3+}$: >99%, Strem Chemicals) with 0.1 M potassium nitrate (KNO_3: 99.9%, Puratronic) as the supporting electrolyte was prepared, along with a background electrolyte solution of 0.1 M KNO_3 for solvent window (SW) and capacitance (*C*) measurements. The solution (~500 µL) was introduced to the surface of the electrode using a micropipette, utilising the hydrophobic nature of Kapton tape to form a droplet.[31] For all electrochemical measurements the second scan is displayed. *C* measurements were determined from cyclic voltammetry (CV) data, discussed in detail in **Chapter 2.5.1**.

For quinone surface coverage measurements, a pH 2 Carmody buffer was prepared using boric acid (99.97%, Sigma Aldrich), citric acid (≥99.5%, Sigma Aldrich) and tertiary sodium phosphate (≥95%, Sigma Aldrich). The quinone oxidation peak was recorded by running CV measurements from 0 V to 0.7 V and back to 0 V at 0.1 V s^{-1} and then integrating (from +0.37 to +0.47 V vs. SCE i.e. the region of quinone oxidation) to obtain the charge passed, *Q*, which was converted to a surface coverage, Γ (mol cm^{-2}), using **Equation 4.1** in **Chapter 4.2.4**.

5.2.4 Micro-Raman Spectroscopy

Micro-Raman was conducted on a Renishaw inVia Raman microscope at room temperature, with a laser wavelength of 532 nm, a ×50 objective and a spot size of ~ 10 µm.

5.2.5 White Light Laser Interferometry (WLI)

A Bruker ContourGT (Bruker Nano Inc., USA) was used to record WLI profiles. After electrochemical measurements, WLI of the analysis area was conducted, with the Kapton tape mask still in place for each electrode (n=3 to obtain a mean averaged image). 3D rendering of the interferometry data was performed using Gwyddion 2.42 to calculate the electrode area, in the area defined by the Kapton tape. Surface roughness (R_{rms}) was determined using the Gwyddion 2.42 software. The areas calculated using WLI were found to be in good agreement with the area determined electrochemically, *vide infra*.

5.2.6 Field Emission-Scanning Electron Microscopy (FE-SEM)

FE-SEM images were recorded using a high-resolution Zeiss GeminiSEM instrument. An in-lens detector was used at a 10 kV accelerating voltage operated at a working distance of 10 mm.

5.3 Results and Discussion

The two, 2" BDD wafers grown in this study showed concentric interference bands (illustrated schematically in **Figure 5.2** using the colours purple and blue to indicate the colours seen by eye). These arise most likely due to variation in thickness across the wafer. The distinctive bands were used to define five regions across the wafer (labelled 1–5 for 1% CH_4 growth and a–e for 5 % CH_4 growth, **Figure 5.2**) for further

investigation. The white dotted line (**Figure 5.2**) represents the segment cut from the wafer.

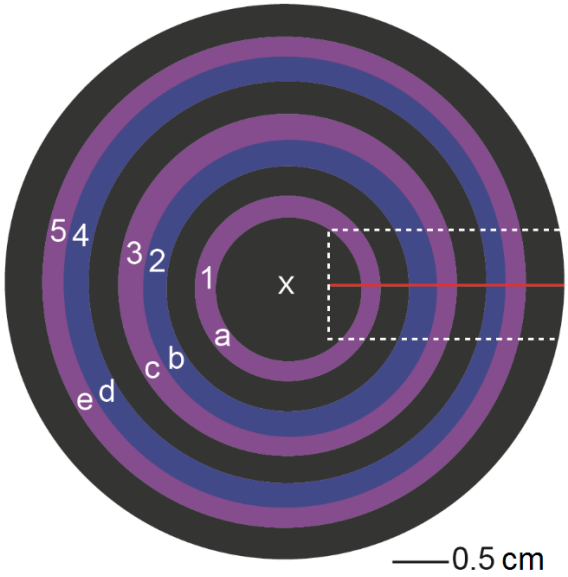

Figure 5.2: *Schematic showing the different regions of the BDD wafer under investigation. The segment laser micromachined out for analysis is indicated by the white dotted line and the red line indicates the WLI line scan conducted (vide infra).*

5.3.1 WLI

In order to determine R_{rms} and crystallite size for each of the regions selected for analysis, WLI was utilised. It is well known that silicon-thin film BDD wafers can bow when the substrate is cooled from growth temperature (~800 °C) to ambient (25 °C) due to the mismatch in the coefficients of thermal expansion between the BDD and silicon.[32] This is evident in the WLI line scans (beam thickness ~1 mm), recorded across the centre position of a segment for both growth conditions, **Figure 5.3a**. The red line in Figure 2 indicates the position of the WLI line scan. The interference bands selected for analysis are visible as 'peaks' and 'troughs', exacerbated more on the 5% CH_4 wafer due most likely to the faster growth rate. Each region was then investigated

using ×100 magnification over a 47 × 62 µm area, and the scan recorded *n*=3 times, to obtain a mean-averaged image.

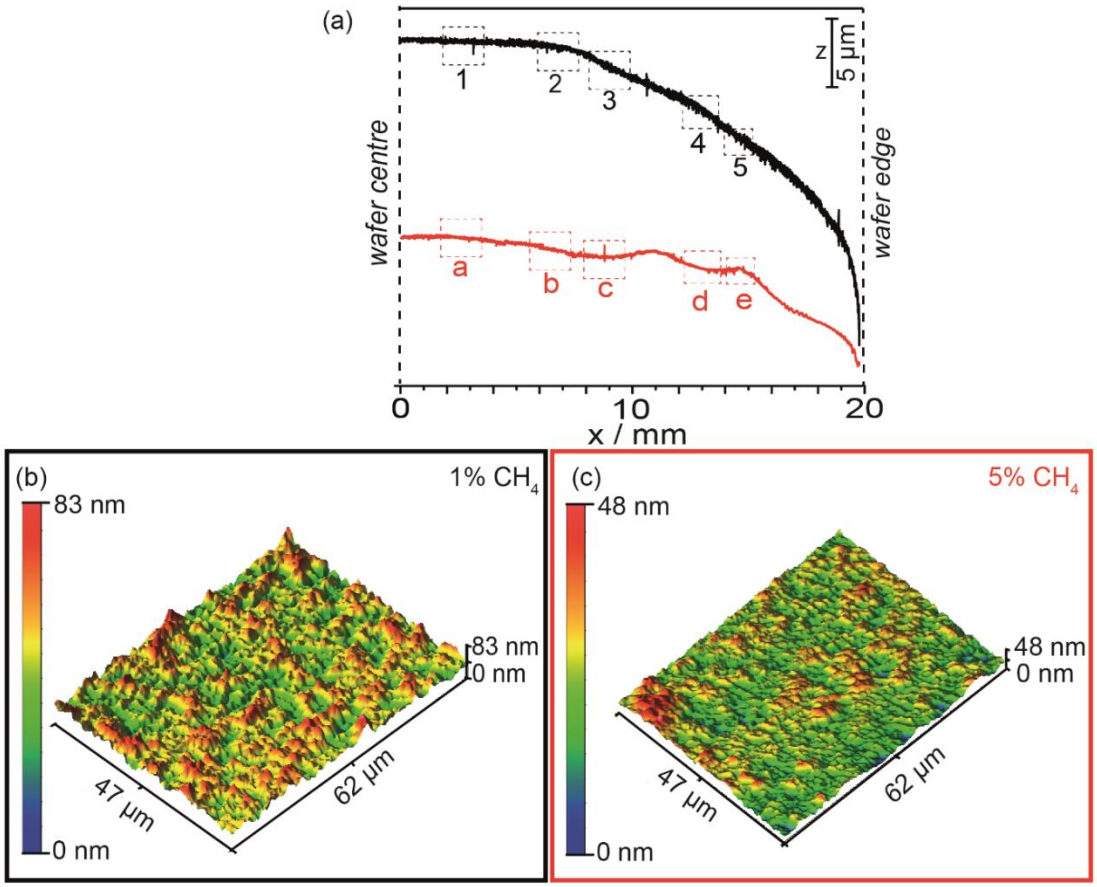

Figure 5.3**:** *(a) Mean averaged WLI line scans (n=3) across the 1% CH_4 (black line) and 5% CH_4 (red line) BDD thin film segments (offset for clarity). Representative 3D renders of WLI profiles for (b) 1% CH_4, (c) 5% CH_4 electrodes at regions 1 and a respectively.*

Whilst a clear difference in roughness and BDD crystallite size was observed between the 1% and 5% CH_4 samples (**Figure 5.3b** and **Figure 5.3c** respectively), little variation was observed within the individual segment, with R_{rms} for 1% and 5% CH_4 regions (1–5 and a–e respectively, measured to *n*=3) determined as 10.3 ± 0.4 nm and 6.7 ± 0.6 nm respectively. The average grain size was found to be 1.1 ± 0.1 µm for 1% CH_4, compared to that of 0.5 ± 0.3 µm for the 5% CH_4 segment. The reduced R_{rms} and

smaller grain sizes of the 5% CH_4 electrode is indicative of 'renucleation/twinning' of the diamond crystals, often seen under higher CH_4 conditions.[33]

5.3.2 Raman Spectroscopy

For comparison against the electrochemical approach to assessing sp^2 carbon content, Raman spectroscopy (n=3) was conducted in each of the different regions of the segment for both (a) 1% CH_4 (regions 1–5) and (b) 5% CH_4 (regions a–e), **Figure 5.4**.

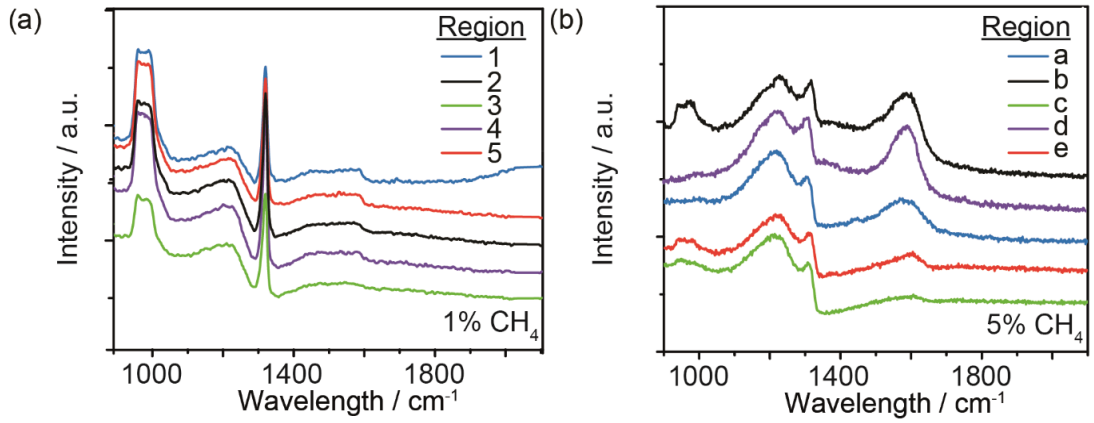

***Figure 5.4**: Representative micro-Raman spectra for the different regions on the (a) 1% and (b) 5% BDD samples at 532 nm, offset for clarity.*

For all regions on the 1% wafer a sharp peak at 1332 cm^{-1} is visible, corresponding to diamond (sp^3 carbon). The full width at half maximum (FWHM) of the diamond peak at 1332 cm^{-1} provides a qualitative indication of film quality, with peak broadening indicative of defects due to a shorter phonon lifetime.[34] However, as both wafers show "bowing" (> 5 μm in the z direction over 20 mm, **Figure 5.3a**) the effect of strain must also be taken into account as it acts to reduce the intensity and shift and broaden the 1332 cm^{-1} peak.[35] For all of the 1% CH_4 regions probed, the FWHM is similar 17 ± 2 cm^{-1}, suggesting that crystallite quality/strain effects are consistent across the wafer.

For the 5% CH_4 sample, for all regions investigated a much broader, less intense diamond peak at 1313 cm^{-1} is observed[36,37] with FWHM values of a= 29 ± 1 cm^{-1}, b = 29 ± 3 cm^{-1}, c = 23 ± 1 cm^{-1}, d = 27 ± 2 cm^{-1} and e = 24 ± 1 cm^{-1}. This could indicate that the film quality of the 5% CH_4 is: (i) much lower than that of the 1%; (ii) strain is more significant in this film compared to that grown with 1% CH_4.[38]

The G-peak, corresponding to the presence of amorphous carbon at 1550 cm^{-1} is also much more prominent in the 5% CH_4 segment than the 1% CH_4 segment, indicating again a lower quality film. For the 1% CH_4 film, the G peak contribution is minimal and little difference can be seen across all of the five regions investigated. However, there is a clear variation in the 5% film, with the smallest G-peak observed for region c, followed by e, a, b and d (largest peak). For the 5% film, comparatively assessing the sp^2 content by ratioing the 1332 cm^{-1} peak to the G-peak is not viable, unless we can be sure for all the regions investigated the boron concentration is the same as is the strain.

The peaks observed at 950 cm^{-1} originate from the Si support (second order peak), supporting the fact that the Raman laser is capable of penetrating through the ~ micron thick BDD film to the underlying Si substrate. Furthermore, the range of different Si signal intensities also suggests that there is a variation in BDD film thickness across the wafers.

5.3.3 Electrochemical Characterisation

Before conducting any electrochemical experiments, the BDD segments were electrochemically cycled in 0.1 M H_2SO_4 to ensure oxygen termination of the surface.[30] To investigate if each of the five regions on the two segments were suitably doped for electrochemical measurements and to ensure that a reliable contact had been made, cyclic voltammograms (CVs) were recorded in 1 mM $Ru(NH_3)_6^{3+}$ (fast one electron transfer outer sphere redox species)[39] and 0.1 M KNO_3 at a scan rate of 0.1 V s^{-1}. As summarised in **Table 5.1** (and shown in **Figure 5.5**), the peak-to-peak separation (ΔE_p) was investigated.

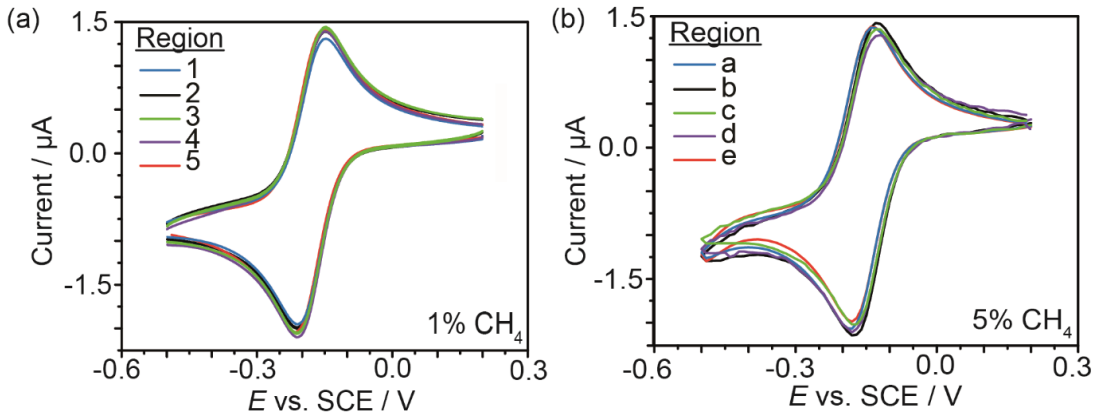

***Figure 5.5**: Electrochemical characterisation for the reduction of 1 mM $Ru(NH_3)_6^{3+}$ in 0.1 M KNO_3 at a scan rate of 0.1 V s^{-1} for each region on the (a) 1% and (b) 5% CH_4 segments.*

For a temperature of 25 °C, an ΔE_p close to 59 mV is expected for this redox couple. As can be seen from **Table 5.1**, the experimentally recorded ΔE_p are sufficiently close to the expected value,[2,40] for us to assume we have an ohmically contacted, suitably doped BDD electrode in all regions of the two segments.

Table 5.1: *Material and Electrochemical Characteristics of the 1% and 5% CH_4 BDD segments at regions specified in Figure 5.2, along with high pressure MW-CVD data collected elsewhere.*[4,30]

BDD Segment	Analysis region	ΔE_p / mV	SW / V	C / µF cm^{-2}	Γ / mol cm^{-2}
1% CH_4	1	60	3.31 ± 0.10	5.46 ± 0.10	$2.6 \times 10^{-16} \pm 1.7 \times 10^{-17}$
	2	67	1.69 ± 0.11	12.54 ± 0.13	$4.2 \times 10^{-16} \pm 2.3 \times 10^{-17}$
	3	65	3.49 ± 0.09	3.18 ± 0.17	$1.9 \times 10^{-16} \pm 1.3 \times 10^{-17}$
	4	62	1.23 ± 0.10	17.99 ± 0.08	$4.9 \times 10^{-16} \pm 1.4 \times 10^{-17}$
	5	69	3.21 ± 0.10	7.84 ± 0.09	$2.7 \times 10^{-16} \pm 1.5 \times 10^{-17}$
5% CH_4	a	68	2.10 ± 0.12	7.27 ± 0.18	$6.3 \times 10^{-16} \pm 1.3 \times 10^{-17}$
	b	67	1.76 ± 0.11	15.57 ± 0.14	$6.0 \times 10^{-15} \pm 1.2 \times 10^{-17}$
	c	63	2.14 ± 0.11	5.45 ± 0.13	$4.0 \times 10^{-16} \pm 1.5 \times 10^{-17}$
	d	67	1.42 ± 0.10	25.34 ± 0.08	$8.5 \times 10^{-15} \pm 1.1 \times 10^{-17}$
	e	60	1.91 ± 0.10	9.08 ± 0.06	$3.0 \times 10^{-15} \pm 2.5 \times 10^{-17}$
High pressure MW-CVD BDD[4,30]	n/a	65	3.60	6.5 ±0.4	$1.8 \times 10^{-16} \pm 1.6 \times 10^{-17}$

The electrode area was also determined through use of the Randles-Sevcik equation (see **Chapter 1.4.3**) which assumes planar diffusion dominates, summarised in **Table 5.2** alongside the areas calculated by WLI for the same electrode (n=3 measurements). The WLI and electrochemical data show good agreement. Given the surface of the thin film electrodes are relatively smooth (rms roughness determined as 10.3 ± 0.4 nm and 6.7 ± 0.6 nm for the 1% and 5% CH_4 grown films respectively), the closeness of the two sets of data is not surprising and indicates under these conditions, electrochemistry alone would be suitable for determining the electrode area.

Table 5.2: *Electrode areas calculated by WLI and electrochemical data ($Ru(NH_3)_6^{3+/2+}$).*

		Calculated Area / cm^2	
BDD Sample	**Analysis region**	**WLI**	**Electrochemistry (Randles-Sevcik)**
1% CH_4	1	0.0073 ± 0.0001	0.0076
	2	0.0077 ± 0.0001	0.0077
	3	0.0080 ±0.0001	0.0080
	4	0.0081 ±0.0002	0.0083
	5	0.0077 ±0.0002	0.0079
5% CH_4	a	0.0083 ±0.0002	0.0085
	b	0.0086 ±0.0001	0.0086
	c	0.0080 ±0.0001	0.0080
	d	0.0084 ±0.0002	0.0085
	e	0.0076 ±0.0002	0.0079

Although Raman spectroscopy[36] (**Figure 5.4**) provides an indication of the presence of sp^2 carbon (showing variations on the 5% CH_4 segment and indicating minimal sp^2 on the 1% CH_4 segment), the technique is not only qualitative, but is relatively surface insensitive providing information about the sp^2 content within a laser penetration depth of up to several microns.[41] Thus for electrode applications, where all charge transfer processes take place at the electrode/electrolyte interface, Raman spectroscopy does not necessarily provide the required information on surface sp^2 content. Furthermore, unless, Raman mapping is utilised, information is obtained in localised spots (limited by the resolution of the laser beam, typically microns in size) and thus does not provide a view of the entire surface.

In contrast, electrochemical methods[30] for characterising sp^2 surface content provide a rapid, cost effective alternative for the whole electrode. It has been previously shown that both the surface double layer capacitance and the electroactive quinone response

associated with sp^2 carbon on the surface of BDD directly correlate with sp^2 surface carbon content.[30,4] Furthermore, features close to the oxygen evolution wave in aqueous solution and the presence of an oxygen reduction wave, become apparent in the solvent window as the sp^2 carbon content increases.[2, 4] Three electrochemical characterisation techniques were thus employed to assess for the presence of sp^2 carbon across both BDD segments including: (1) *C*; (2) SW and (3) quinone surface coverage measurements (Γ).

5.3.4 Capacitance

Higher *C* values than an sp^3 only BDD electrode (<< 10 μF cm^{-2})[30] are attributed to the incorporation of sp^2 and in part due to the presence of quinone-like groups on the BDD surface.[2] To determine *C* values CV measurements were conducted in 0.1 M KNO_3 at a scan rate of 0.1 V s^{-1}, starting from 0 V cycling from -0.1 to 0.1 V and then back to 0 V, presented in **Figure 5.6**. *C* was calculated using **Equation 2.2** detailed in **Chapter 2.5.1** and summarised in **Table 5.1**.

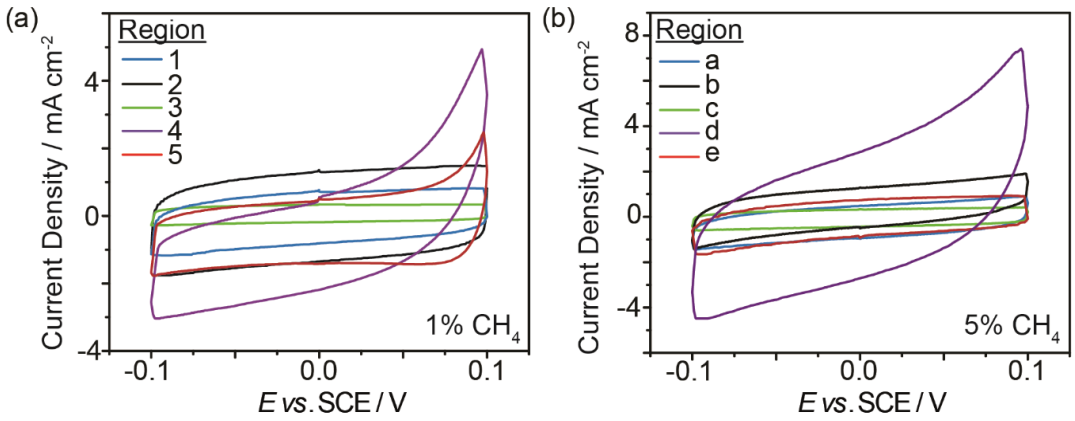

***Figure 5.6**: Comparison of representative C measurements for the (a) 1% and (b) 5% CH_4 BDD samples, run in 0.1 M KNO_3 at a scan rate of 0.1 V s^{-1}.*

Overall, the 5% CH_4 wafer has higher *C* values compared to that of the 1% CH_4 wafer, suggesting more sp^2 carbon sites on the surface. This is expected due to the reduced grain size, resulting in more grain boundaries. Localised variations in B dopant density may also contribute to increased capacitance due to changes in the density of states.[30] There are also significant variations in the *C* across the segment, as indicated by the *C* values recorded for the five different regions, with *C* varying from highest in regions 4 (and d), followed by 2 (and b), 5 (and e), 1 (and a) to lowest in region 3 (and c), for the 1% and 5% wafers respectively. Interestingly, for the 1% CH_4 wafer, Raman is unable to distinguish variations in the sp^2 content across the segment, the signal intensity for the sp^2 band is too low.

5.3.5 Solvent Window

The SW is defined by the electrochemical process of water decomposition, where oxygen and hydrogen evolution takes place at anodic and cathodic extremes respectively. In order to compare SW ranges, the anodic and cathodic potential limits were defined as the potential at which a current density of 0.4 mA cm^{-2} is passed for water electrolysis.[2] For high quality BDD, with little sp^2 content, the SW is typically wide (>3 V) due to the inert nature of the sp^3 diamond surface.[2] In contrast, when sp^2 is present, the SW value reduces due to increased catalytic activity facilitates water electrolysis, and the cathodic window exhibits a signal (within the range -0.5 to -1.5 V) indicative of oxygen reduction reaction (ORR).[42] Furthermore, due to the presence of sp^2, features are observed in the anodic window from ~0.6 to 1.5 V, attributed to the oxidation of sp^2 containing surface species.[7] Figure 6 a and b shows SW scans for both

1% and 5% CH_4 electrodes respectively, recorded in 0.1 M KNO_3 (pH = 6.5) at a scan rate of 0.1 V s^{-1}, starting at 0 V scanning to −2 V, up to 2 V before returning to 0 V.

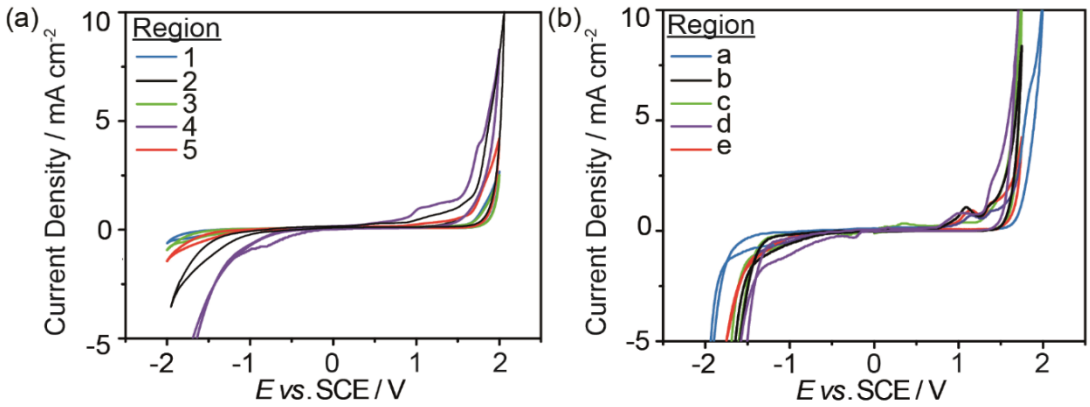

Figure 5.7*: *Representative SW measurements made in 0.1 M KNO_3 (pH = 6.5) at a scan rate of 0.1 V^{-1} for the (a) 1% and (b) 5% CH_4 BDD samples.

Qualitatively, for all regions of the 5% CH_4 wafer, features attributed to sp^2 are observed in the SW. However, for the 1% CH_4 wafer, regions 1, 3 and 5 appear to indicate negligible sp^2 content, as no sp^2 oxidation features are evident nor an obvious ORR wave. Overall, larger SW values are recorded on the 1% CH_4 electrode, which is expected, as the slower growth rate has resulted in larger grain sizes, resulting in fewer grain boundaries (where sp^2 often resides). Some regions of the 1% wafer (b and d) do show SW values similar to that of the 5% wafer (2 and 4), indicative of an sp^2 presence, and for both wafers, the SW values vary across the wafer, as summarised in **Table 5.1**.

5.3.6 Quinone surface coverage

Electrochemically active quinone groups are absent on a fully hybridised sp^3 carbon surface, yet readily form on sp^2 carbon, therefore Γ can be analysed to comparatively assess sp^2 content. For each region, CVs in pH 2 buffer, to maximise current signal,[4]

were carried out (scan rate of 0.1 V s^{-1}), cycling from 0 to 0.7 V. **Figure 5.8a** and **Figure 5.8b** shows representative quinone oxidation peaks scans both the 1% and 5% CH_4 segments respectively at the defined regions. Γ was calculated using **Equation 4.1** detailed in **Chapter 4.2.4** and summarised in **Table 5.1**.

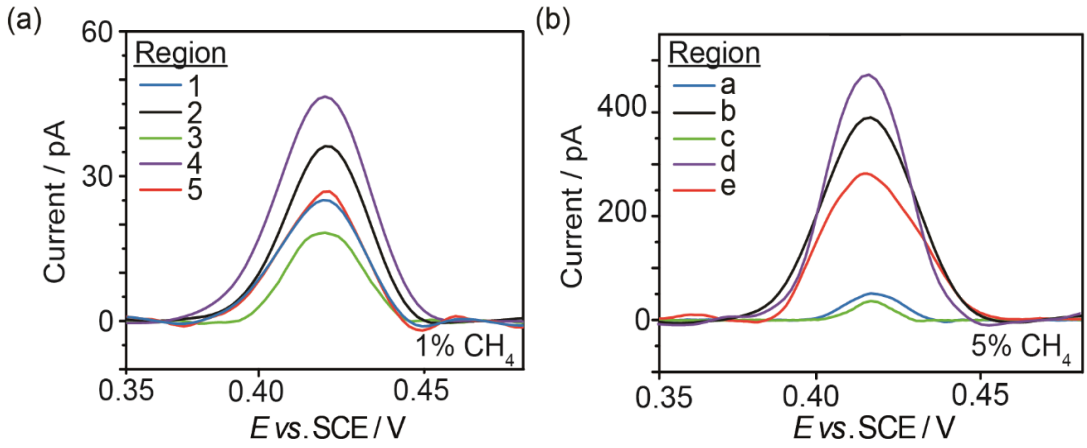

Figure 5.8*: *Representative quinone peaks for each of the regions on (a) 1% and (b) 5% CH_4 BDD samples.

Much higher Γ values are observed, on the 5% CH_4 wafer, especially in regions where C and SW have shown sp^2 content to be high. Again this technique identifies significant variations in Γ across each wafer (summarised in **Table 5.1**), supporting the growing evidence that the sp^2 content varies spatially across both segments (wafers). It is important to note that the quinone content (which directly correlates with sp^2) varies over nearly two orders of magnitude when considering both the 1% and 5% CH_4 segments. For example, region 3 on the 1% CH_4 wafer, which also shows the largest SW and lowest C values, has a Γ of 1.9×10^{-16} mol cm^{-2}, similar to that of freestanding, high quality BDD ($\Gamma = 1.8 \times 10^{-16}$ mol cm^{-2}), grown using MW-CVD under conditions especially optimised to minimise sp^2 content.[30] However, region d on the 5% wafer, which shows the smallest SW and highest C values returns a Γ value of

8.5×10^{-15} mol cm^{-2}, nearly two orders of magnitude greater, indicative of electrode material containing considerable sp^2.

5.3.7 Comparison of electrochemical techniques and Raman

In order to visualise the trends in sp^2 surface content across both wafers, the electrochemical measurements for *C*, SW and Γ are presented in **Figure 5.9**, along with the corresponding regions where measurements were taken. **Figure 5.9** shows that both segments show a similar profile of varying sp^2 content (inferred from the electrochemical measurements) with regions 1, 3 and 5 of the 1% CH_4 segment containing minimal sp^2 concentrations i.e. displaying wide SWs, low *C* and low Γ of similar values to that found with high quality BDD.[30] Regions 2 and 4 however, exhibit a measurable sp^2 carbon presence. For the 5% CH_4 segment, sp^2 carbon is observed over all regions, with regions b and d displaying the highest levels. Note whilst Raman was able to map the variations adequately on the 5% CH_4 segment, this was not possible on the 1% CH_4 segment. **Figure 5.9c** shows the Raman G peak baseline corrected signal intensity for both the 5% CH_4 segment and the 1% CH_4 segment. The Raman data clearly shows the same trend to that of the electrochemical data for the 5% CH_4 wafer, but fails to differentiate each region for the 1% CH_4, showing no significant difference across the electrode. However, electrochemically clear differences are observed on the 1% CH_4 segment with regions 2 and 4 showing an electrochemically appreciable sp^2 content. This in turn could influence the resulting electrochemical response towards surface sensitive analytes and produce differing electrochemical behaviour compared to electrodes from regions 1, 3 and 5 of the segment.

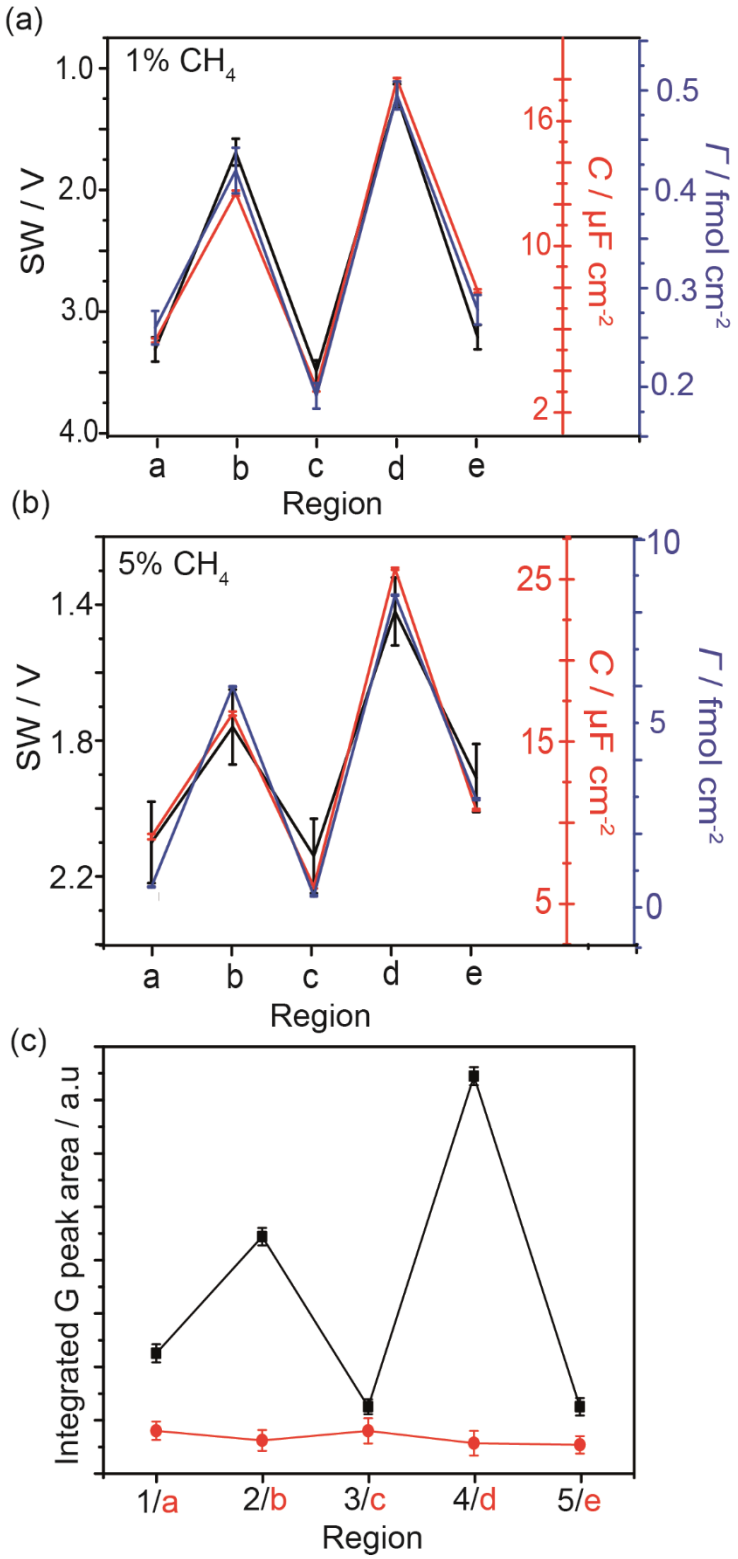

***Figure 5.9**: Comparison of C, SW and Γ measurements (n=3) for the (a) 1% and (b) 5% CH_4 BDD segments. (c) Plot of the integrated G peak area for each region on the 1% CH_4 (black line) and 5% CH_4 (red line) CH_4 BDD wafers.*

The spatially varying sp^2 content, in a consistent manner across both wafers, supports previous simulation work that at low power densities a 'doughnut' shaped plasma can be formed, resulting in fluctuations in microwave power in the CVD reactor.[19] Each wafer was positioned in very similar locations in the reactor during separate growth runs. This in turn impacts the concentrations of reactor species at the BDD surface, which effects the growth and etch rates and ultimately the quality (defined as amount of sp^2 present) of the final BDD wafer at different locations. The regions containing low sp^2 are likely to have been exposed to conditions that facilitate higher quality BDD growth such as higher atomic H and lower CH_4 concentrations, compared to that of the regions containing significantly more sp^2. To verify whether the data was consistent with segments cut from other areas of the wafer, illustrated in **Figure 5.10**.

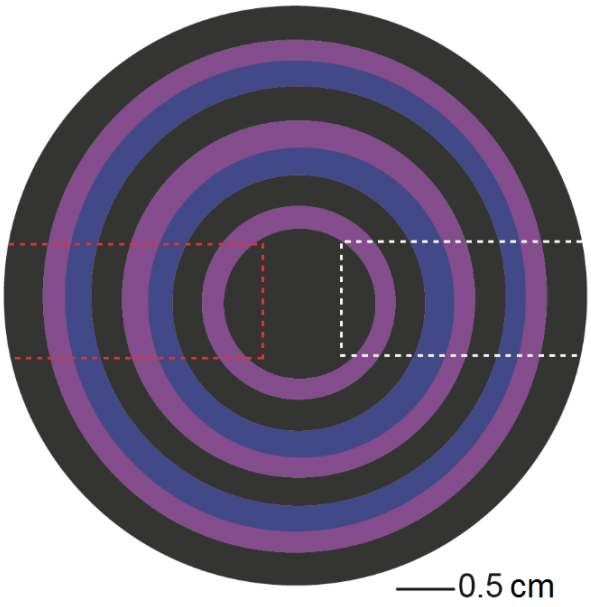

Figure 5.10*: *Diagram illustrating the segment of the BDD wafer selected for analysis in discussed in detail in this Chapter (white dotted line) and (2) opposite segment (red dotted line).

Table 5.3 shows the electrochemical data recorded from all five regions for both the 1% and 5% CH_4 wafers, but taken from segments cut from the opposite side of the wafer (red dotted lines). The similarity between the data suggests that the electrochemical properties are consistent across the whole region of a concentric interference band, which runs around the wafer.

***Table 5.3**: Electrochemical characteristics of the 1% and 5% CH_4 BDD regions on segment sections 1 (white) and section 2 (red).*

BDD Sample	Analysis region	SW / V		C / µF cm^{-2}		Γ / mol cm^{-2}	
1% CH_4	1	3.31	3.24	5.46	5.34	2.60×10^{-16}	2.57×10^{-16}
	2	1.69	1.75	12.54	12.45	4.19×10^{-16}	4.10×10^{-16}
	3	3.49	3.42	3.18	4.05	1.91×10^{-16}	1.91×10^{-16}
	4	1.23	1.22	17.99	18.05	4.95×10^{-16}	4.96×10^{-16}
	5	3.21	3.15	7.84	7.83	2.78×10^{-16}	2.73×10^{-16}
5% CH_4	A	2.10	2.11	7.27	7.02	6.37×10^{-16}	6.37×10^{-16}
	B	1.76	1.74	15.57	15.45	6.04×10^{-15}	6.04×10^{-15}
	C	2.14	2.01	5.45	5.34	4.01×10^{-16}	4.01×10^{-16}
	D	1.42	1.34	25.34	26.32	8.51×10^{-15}	8.51×10^{-15}
	E	1.91	1.87	9.08	9.11	3.01×10^{-15}	3.01×10^{-15}

5.3.8 FE-SEM images

To view the thickness of the wafers at the distinctive regions along the wafer (1% CH_4: 1–5 and 5% CH_4: a–e) the laser micromachined edge was positioned in the FE-SEM perpendicular to the electron beam. This allowed both the Si support and the BDD grains to be imaged. **Figure 5.11** shows the regions that displayed the least (3/c) and most (4/d) sp^2 carbon for the 1% CH_4 wafer (images a and b respectively) and the 5% CH_4 wafer (images c and d respectively).

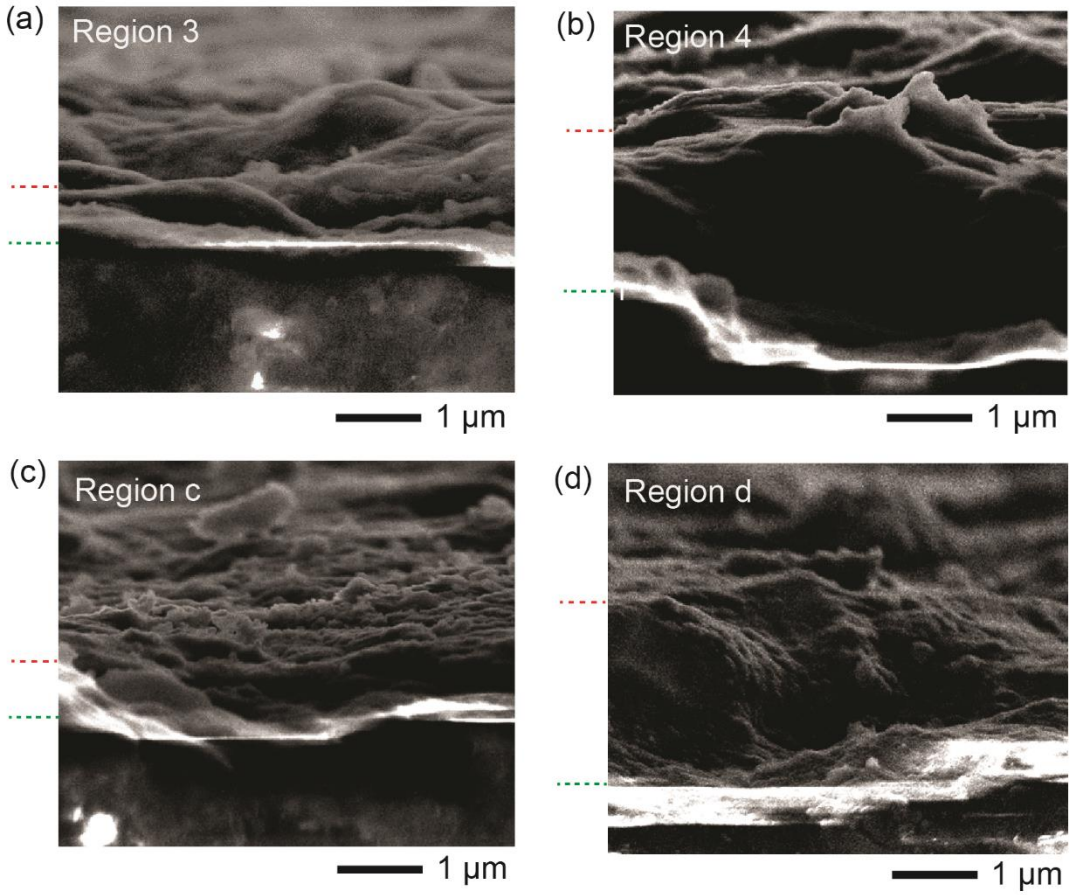

Figure 5.11*: *FE-SEM image comparison of regions 3 and 4 on the 1% CH_4 wafer (images a and b respectively) and regions c and d on the 5% CH_4 wafer (images c and d respectively). The edge of Si substrate is illustrated by the green dotted line and the top of a BDD grain indicated by the red dotted line.

Given the fact that the BDD grains do not grow perfectly perpendicular to the Si substrate, it is not possible to quantitatively determine the grain sizes at the locations. Qualitatively the BDD thickness is larger at the regions that displayed higher sp^2 contents (2/b,4/d) compared to the regions that showed lower sp^2 contents (1/a, 3/c, 5/e). This supports the concept that the regions are exposed to different growth conditions that effect sp^2 incorporation. It can be postulated that for regions (1/a, 3/c and 5/e) a slower growth rate occurs, resulting in the more efficient etching of sp^2 carbon by $H^{\bullet}$, resulting in a higher quality (lower sp^2) film.

5.4 Conclusions

The variation in sp^2 surface content for thin film BDD grown under low power density conditions in an overmoded CVD reactor has been characterised using electrochemical methods. The material is grown using boron dopant densities which make it applicable for electrochemical use. Clear differences in the electrochemical response are observed at defined regions across the same wafer (segment), due to a varying sp^2 carbon incorporation during synthesis. The variation is thought to be due to localised variations in growth conditions throughout the MW-CVD reactor, due to the formation of a non-uniform plasma, which results in a non-uniform power density, when using a multi-mode system at low pressure.[19,25] The same trend in sp^2 variation across the five different regions of the segment was seen for both the 1% and 5% CH_4 growth wafers, except the 5% CH_4 wafer showed an overall higher sp^2 surface content. Interestingly, even though Raman spectroscopy is often the characterisation method of choice for thin film diamond, it was found that the technique does not have the sensitivity to distinguish the variation in surface sp^2 carbon especially at the lower sp^2 levels (1% CH_4 wafer growth). Raman showed the sp^2 content to be essentially minimal and unvarying for the 1% CH_4 BDD wafer, whilst electrochemical assessment revealed at least two of the regions to have electrochemically appreciable levels of sp^2. For this reason, we also advocate using electrochemical characterisation of BDD when looking to utilise the material for electroanalytical applications.

It is also important to note that the variation in sp^2 content is significant across each wafer. For example, some areas on the 1% CH_4 wafer showed electrochemical signatures akin to minimal sp^2 content BDD, grown at much higher microwave power densities.[4,30] These features include wide SWs (> 3V), low *C*'s (<<10 μF cm^{-2}), and

very low levels ($< 3 \times 10^{-16}$ mol cm^{-2}) of surface quinone groups, making the electrode ideal for high detection sensitivity electroanalysis work. On the 5% CH_4 wafer, all regions showed high sp^2 content, with two of the regions showing especially high levels; such electrodes are useful when an increased electrocatalytic efficiency is required from the BDD electrode.

This study has clearly shown that BDD grown under the more economical, multi-mode (overmoded) MW-CVD conditions does not result in wafers which show a consistent and minimal level of sp^2 carbon, even under 1% CH_4 conditions. Therefore, for electrochemical use, depending on where the electrode measurement is taken, even on the same wafer, differing results may be seen if sp^2 carbon plays a role in the electrochemical response. Thus, caution should be exercised by the electrochemist in using material grown using an overmoded source under low power density conditions, without a complete characterisation of the material properties first. The incorporation of sp^2 carbon can also influence the mechanical properties of diamond including hardness and the materials Young's modulus,[41] which is an important consideration for applications which exploit the mechanical properties of the BDD.

This study also shows that both high quality BDD (minimal content sp^2 BDD) is possible in select regions and this overmoded growth process provides route for varying sp^2 levels over the same wafer in a controllable way. Thus for electrochemical studies which wish to explore the effect of sp^2 carbon on the electrochemical response of the BDD electrode, one wafer alone opens up a combinatorial approach to addressing this question.

5.5 References

(1) Pleskov, Y. V. *Russian Journal of Electrochemistry*, **2002**, *38*, 1275–1291.
(2) Macpherson, J. V. *Phys. Chem. Chem. Phys.*, **2015**, *17*, 2935–2949.
(3) Polo, M. C.;Cifre, J.;Esteve, J. *Vacuum*, **1994**, *45*, 1013–1014.
(4) Ayres, Z. J.;Cobb, S. J.;Newton, M. E.;Macpherson, J. V. *Electrochem. Commun.*, **2016**, *72*, 59–63.
(5) Watanabe, T.;Honda, Y.;Kanda, K.;Einaga, Y. *physica status solidi (a)*, **2014**, *211*, 2709–2717.
(6) Cinková, K.;Batchelor-McAuley, C.;Marton, M.;Vojs, M.;Švorc, Ľ.;Compton, R. G. *Carbon*, **2016**, *110*, 148–154.
(7) Bennett, J. A.;Wang, J.;Show, Y.;Swain, G. M. *J. Electrochem. Soc.*, **2004**, *151*, 306–313.
(8) Garcia-Segura, S.;Vieira dos Santos, E.;Martínez-Huitle, C. A. *Electrochem. Commun.*, **2015**, *59*, 52–55.
(9) Ayres, Z. J.;Borrill, A. J.;Newland, J. C.;Newton, M. E.;Macpherson, J. V. *Anal. Chem.*, **2015**, 974–980.
(10) de Paiva Barreto, J. P.;de Freitas Araújo, K. C.;de Araújo, D. M.;Martínez-Huitle, C. A. *ECS Electrochemistry Letters*, **2015**, *4*, E9–E11.
(11) Zuo, S. S.;Yaran, M. K.;Grotjohn, T. A.;Reinhard, D. K.;Asmussen, J. *Diamond. Relat. Mater.*, **2008**, *17*, 300–305.
(12) Tachibana, T.;Ando, Y.;Watanabe, A.;Nishibayashi, Y.;Kobashi, K.;Hirao, T.;Oura, K. *Diamond. Relat. Mater.*, **2001**, *10*, 1569–1572.
(13) Williams, O. A. *Diamond. Relat. Mater.*, **2011**, *20*, 621–640.
(14) May, P. W. *Philosophical Transactions of the Royal Society of London A: Mathematical, Physical and Engineering Sciences*, **2000**, *358*, 473–495.
(15) Brillas, E.;Huitle, C. A. M. *Synthetic diamond films: preparation, electrochemistry, characterization and applications*;John Wiley & Sons, **2011**. 133–143.
(16) Weng, J.;Xiong, L. W.;Wang, J. H.;Dai, S. Y.;Man, W. D.;Liu, F. *Diamond. Relat. Mater.*, **2012**, *30*, 15–19.
(17) Dischler, B.;Wild, C. *Low-pressure synthetic diamond: manufacturing and applications*;Springer Science & Business Media, **2013**.
(18) Piret, G.;Hébert, C.;Mazellier, J.-P.;Rousseau, L.;Scorsone, E.;Cottance, M.;Lissorgues, G.;Heuschkel, M. O.;Picaud, S.;Bergonzo, P.;Yvert, B. *Biomaterials*, **2015**, *53*, 173–183.
(19) Yamada, H.;Chayahara, A.;Mokuno, Y.;Shikata, S. *Diamond. Relat. Mater.*, **2015**, *54*, 9–14.
(20) Huang, W. S.;Tran, D. T.;Asmussen, J.;Grotjohn, T. A.;Reinhard, D. *Diamond. Relat. Mater.*, **2006**, *15*, 341-344.
(21) Mallik, A. K.;Pal, K. S.;Dandapat, N.;Guha, B. K.;Datta, S.;Basu, D. *Diamond. Relat. Mater.*, **2012**, *30*, 53–61.
(22) Scorsone, E.;Saada, S.;Arnault, J.;Bergonzo, P. *Journal of Applied Physics*, **2009**, *106*, 014908.
(23) Achatz, P.;Garrido, J. A.;Williams, O. A.;Bruno, P.;Gruen, D. M.;Kromka, A.;Steinmüller, D.;Stutzmann, M. *physica status solidi (a)*, **2007**, *204*, 2874–2880.
(24) Kromka, A.;Rezek, B.;Remes, Z.;Michalka, M.;Ledinsky, M.;Zemek, J.;Potmesil, J.;Vanecek, M. *Chemical Vapor Deposition*, **2008**, *14*, 181–186.

(25) Silva, F.;Hassouni, K.;Bonnin, X.;Gicquel, A. *Journal of Physics: Condensed Matter*, **2009**, *21*, 364202.
(26) Hees, J.;Kriele, A.;Williams, O. A. *Chemical Physics Letters*, **2011**, *509*, 12-15.
(27) Williams, O. A.;Hees, J.;Dieker, C.;Jäger, W.;Kirste, L.;Nebel, C. E. *ACS nano*, **2010**, *4*, 4824–4830.
(28) Williams, O. A.;Douhéret, O.;Daenen, M.;Haenen, K.;Ōsawa, E.;Takahashi, M. *Chemical Physics Letters*, **2007**, *445*, 255–258.
(29) Gajewski, W.;Achatz, P.;Williams, O. A.;Haenen, K.;Bustarret, E.;Stutzmann, M.;Garrido, J. A. *Physical Review B*, **2009**, *79*, 045206.
(30) Hutton, L. A.;Iacobini, J. G.;Bitziou, E.;Channon, R. B.;Newton, M. E.;Macpherson, J. V. *Anal. Chem.*, **2013**, *85*, 7230–7240.
(31) Mohammad, F. *Specialty polymers: materials and applications*;IK International Pvt Ltd, **2007**. 435–437.
(32) Edwards, M. J.;Bowen, C. R.;Allsopp, D. W. E.;Dent, A. C. E. *Journal of Physics D: Applied Physics*, **2010**, *43*, 385502.
(33) Bühlmann, S.;Blank, E.;Haubner, R.;Lux, B. *Diamond. Relat. Mater.*, **1999**, *8*, 194-201.
(34) Neves, A.;Nazaré, M. H. *Properties, growth and applications of diamond*;IET, **2001**. 67–69.
(35) Pandey, M.;D'Cunha, R.;Tyagi, A. K. *Journal of Alloys and Compounds*, **2002**, *333*, 260–265.
(36) Prawer, S.;Nemanich, R. J. *Philosophical Transactions of the Royal Society of London A: Mathematical, Physical and Engineering Sciences*, **2004**, *362*, 2537–2565.
(37) Orwa, J. O.;Nugent, K. W.;Jamieson, D. N.;Prawer, S. *Physical Review B*, **2000**, *62*, 5461–5472.
(38) May, P.;Ludlow, W.;Hannaway, M.;Heard, P.;Smith, J.;Rosser, K. *Diamond. Relat. Mater.*, **2008**, *17*, 105–117.
(39) Endicott, J. F.;Taube, H. *J. Am. Chem. Soc.*, **1964**, *86*, 1686–1691.
(40) Simonov, A. N.;Morris, G. P.;Mashkina, E. A.;Bethwaite, B.;Gillow, K.;Baker, R. E.;Gavaghan, D. J.;Bond, A. M. *Anal. Chem.*, **2014**, *86*, 8408–8417.
(41) Ferreira, N. G.;Abramof, E.;Corat, E. J.;Trava-Airoldi, V. J. *Carbon*, **2003**, *41*, 1301–1308.
(42) Martin, H. B.;Argoitia, A.;Landau, U.;Anderson, A. B.;Angus, J. C. *J. Electrochem. Soc.*, **1996**, *143*, 133–136.

Chapter 6

Controlled sp^2 functionalization of boron doped diamond as a route for the fabrication of robust and Nernstian pH electrodes

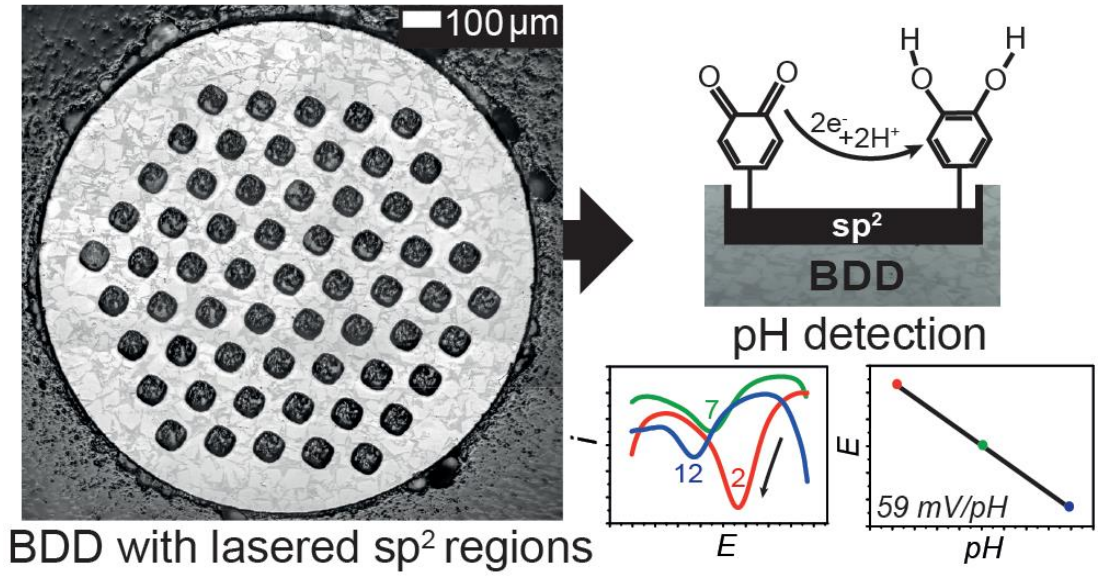

In this chapter, the development of a robust boron doped diamond (BDD) pH sensor is described. To obtain pH sensitivity, laser micromachining is utilised to introduce controlled regions of sp^2 carbon into a high quality polycrystalline BDD electrode. The resulting sp^2 carbon is then activated to produce electrochemically active quinone groups using a high temperature acid treatment, followed by anodic polarisation. Once activated, no further treatment is required for all measurements. The quinone groups show a linear (R^2 = 0.999) pH dependent and Nernstian (59 mV/pH unit) current-voltage response over a large analysable pH range, from pH 2–12 in buffered solutions. Using the laser approach, it is possible to optimise sp^2 coverage on the BDD surface, such that a measurable pH response is recorded, whilst minimising background currents arising from oxygen reduction reactions on sp^2 carbon in the potential region of interest. This enables the sensor to be used in aerated solutions, boding well for *in*

situ analysis. The BDD voltammetric pH electrode response is also uncompromised by the presence of excess metal ions such as Pb^{2+}, Cd^{2+}, Fe^{3+}, Cu^{2+} and Zn^{2+}. The BDD pH sensor is stable over a three-month period (the time period of testing), can be stored in air in between measurements, requires no re-activation of the surface between measurements and can be reproducibly fabricated using the proposed approach. The efficacy of this pH sensor in a real-world sample is demonstrated with pH measurements in UK seawater.

6.1 Introduction

The ability to sense pH in aqueous solutions is fundamental to the study of many different chemical environments and is therefore prevalent in many industries including healthcare,[1] waste management,[2] water and environmental monitoring.[3,4] The most common pH sensor to date is the potentiometric glass pH electrode, due to its high sensitivity to protons, large analysable pH range from pH 0 to pH 12 and fairly rapid response time of < 60 s, as well as its commercial availability.[5,6] It is however associated with several limitations including: 'alkali errors' where interfering ions such as Na^+ and Li^+ affect the pH response at high pH values;[7] fragility due to the very thin glass membrane and potential drift over time, resulting in the need to re-calibrate regularly.[8] It is for this reason that the development of robust and reliable pH sensors has received significant interest from the scientific community over recent years.[9] This is especially true for applications requiring long term placement or environments which challenge the fragility of the thin glass membrane.

Carbon electrodes are currently finding favour for pH measurements due to their wide availability, potential low cost and biocompatibility, making them ideal for biological and environmental applications.[10,11] Many studies have investigated a range of carbon materials including single-walled carbon nanotubes,[12] glassy carbon (GC),[13] graphene,[14] edge plane pyrolytic graphite (EPPG)[15] and screen printed carbon (SPE).[16] pH sensing with carbon electrodes is typically carried out using voltammetry, where the surface is chemically functionalized with pH sensitive molecules, which undergo proton assisted electron transfer.[17,18] These tend to be quinone in nature where the peak current position for electrolysis of the surface bound quinone groups, shows a Nernstian dependence on proton concentration. Whilst this has resulted in the

production of robust pH sensors, the derivatization procedures can be time consuming, complex and costly due to the number of reagents required.[17]

To reduce preparation times, it has also been shown that the electro-reduction of naturally present quinone groups on the surface of sp^2 containing carbon electrodes such as GC, EPPG and SPE also show a Nernstian pH dependent current-voltage response.[13,15,16] The electrodes all required some form of activation prior to use. For GC[13] and EPPG,[15] surface mechanical polishing was found to be important, whilst for SPE, the surface required chemical oxidation. For all electrodes solution degassing was required,[16] to avoid oxygen reduction reaction (ORR) interferences. This makes measurements at the source, when oxygen is naturally present, challenging.

There have also been limited studies with boron doped diamond (BDD), an electrode which has many interesting material properties compared to other common electrodes such as GC, platinum and gold, due to its sp^3 nature. These include: high chemical inertness; mechanical robustness; oxygen insensitivity; wide solvent window; low background currents and reduced fouling.[19,20] As such, BDD electrodes have been employed in innovative ways to measure pH. For example, due to the extended solvent window, chronopotentiometry was employed to monitor the potential dependent pH response for a fixed negative current.[21,22] However, this approach is affected by redox species in solution which can also be reduced at the applied current.[22] Chronopotentiometry has also been investigated under zero current conditions, with oxygen (O-)terminated BDD.[23] Here an oxygen plasma was used to activate the BDD surface. However, a linear sub-Nernstian (50.8 mV pH^{-1}) voltage response towards pH was observed, stable only for two days.

This work develops a robust approach for the measurement of pH based on BDD electrodes. Minimal sp^2 content conducting BDD electrodes are utilised as the starting material with sp^2 carbon controllably added to defined regions of the BDD surface using laser (ablation) micromachining. Activation of the sp^2 regions of the surface prior to use, results in a sufficient number of quinone groups, which undergo reversible proton dependent voltammetry. sp^2 carbon coverage is optimised on the electrode surface such that a Nernstian response to pH based on current-voltage measurements, is observed, whilst maintaining minimal background currents from ORR, in the potential region of interest. Importantly, once activated the electrode does not need reactivating in between measurements, is long-lasting (electrode has so far been used for 3 months without fail) and the pH measurements can be made in aerated solutions, both boding well for long-term use *in-situ*.

6.2 Experimental

6.2.1 Laser micromachined electrode fabrication and pretreatment

1 mm BDD glass sealed electrodes were fabricated as discussed in detail in **Chapter 2.3.1**. Laser micromachining or ablation of BDD proceeds via the vaporisation of carbon and the subsequent graphitization of the exposed surface.[24] The resulting residual graphitic layer on the BDD surface is formed by the transition of metastable diamond to stable graphite under laser induced thermal exposure.[25] Studies have found that laser ablation with longer pulse durations *i.e.* ns compared to fs, result in a greater extent of graphitisation.[26] A 34 ns, 355 nm YAG laser (5.102 W at 10 kHz) was therefore used to create circular pits by manipulation of a computer numerical control

stage holding the sample, relative to a fixed beam. A hexagonal array of sixty-one pits, ~45 µm diameter and 25 µm deep, spaced 100 µm centre-centre, was laser machined into the BDD surface. The stage traversing speed and laser repetition rate was predetermined so that the BDD surface was exposed to one laser pulse every 3 µm. Due to uncompensated stage acceleration/deceleration issues, some areas of the machined surface within a laser micromachined pit were exposed to more pulses than others.

After laser micromachining, in order to "*activate*" the sp^2 carbon to produce the necessary pH sensitive redox active quinone groups and remove loosely bound sp^2 carbon the electrode was first heated at ~200 °C for 15 minutes in concentrated H_2SO_4 (98%) saturated with KNO_3. Anodic polarisation of the laser micromachined BDD electrode was then conducted under constant current conditions (+0.1 mA for 60 s) in 0.1 M room temperature H_2SO_4, similar to procedures utilised to produce acidic surface oxides on "activated" carbon materials.[27] It was noted that not carrying out this procedure post laser ablation, results in unstable electrode response towards pH, with the pH response varying with time. This is postulated to be due to the anodic polarisation removing any loose sp^2 carbon present within the roughened laser features that were not removed by the acid cleaning step. The constant current of +0.1 mA was selected in order to encourage oxygen evolution at the electrode surface as well as the formation of high order oxygen-containing functional groups such as quinones on the electrode surface. Furthermore, at such extreme anodic potentials, during polarisation, production of oxidants such as ozone and hydroxyl radicals have been noted to occur, which may help to further oxidise/clean the electrode surface.

6.2.2 Electrochemical set-up

For the electrochemical measurements a three electrode configuration was utilized with BDD as the working electrode, a platinum wire as a counter electrode and a saturated calomel electrode (SCE) as the reference electrode. For anodic polarization a galvanostat was utilized (Keithley 6220 Precision Current Source). For both solvent window (SW) and capacitance measurements (*C*) a 0.1 M KNO_3 solution was employed at a scan rate of 0.1 V s^{-1}. *C* measurements were determined from CV data as detailed in **Chapter 2.5.1**. Square wave voltammetry (SWV) was conducted at a frequency of 150 Hz, amplitude of 200 mV and step potential of 2 mV. SWV was utilised over linear sweep voltammetry in order to improve the signal-to-noise ratio.

6.2.3 X-ray photoelectron spectroscopy (XPS)

XPS analysis was conducted using a Kratos Axis Ultra DLD photoelectron spectrometer, with a monochromated Al kα X-ray source (1486.69 eV) operating at 150 W. All measurements were performed under ultra-high vacuum (UHV) conditions with a spectrometer base pressure of 2×10^{-10} mbar. Core level XPS spectra were collected using a pass energy of 20 eV (resolution ~0.4 eV) with a 1 mm spot size. In order to investigate the different carbon chemical environments at the electrode surface all data, collected was fitted using Lorentzian-Gaussian peaks after a Shirley background subtraction. The C 1s peak was calibrated to 285 eV for charge correction.[28]

6.2.4 Raman Spectroscopy

Micro-Raman was conducted on a Renishaw inVia Raman microscope at room temperature, with a laser wavelength of 514 nm, a ×50 objective and a spot size of ~10 μm.

6.2.5 Field Emission Scanning Electron Microscopy (FE-SEM)

FE-SEM images were collected using a high-resolution Zeiss Supra VP. An in-lens detector was utilized at accelerating voltages between 2 and 15 kV, with a working distance of 4 mm.

6.2.6 White Light Laser Interferometry (WLI)

WLI images were recorded using a Bruker ContourGT (Bruker Nano Inc., USA). 3D rendering of interferometry data was performed and the increase in electrode area after laser ablation quantified using Gwyddion 2.41 (Czech Metrology Institute, CZE).

6.3 Results and Discussion

6.3.1 Polarisation Time Optimisation

The inner-sphere redox couple $Fe^{2+/3+}$ was utilised to aid optimisation of the time required to anodically polarise the laser micromachined BDD electrode. Work by McCreery et al.,[29] has shown that $Fe^{2+/3+}$ is particularly sensitive to carbonyl groups (C=O), with the increased presence of C=O on an electrode surface resulting in a smaller peak-to-peak (ΔE_p) separation, indicative of faster electron transfer (ET) kinetics. It was therefore considered that ΔE_p could be used to qualitatively indicate an increase in the number of C=O groups on the electrode surface with respect to the anodic treatment applied. From this data, it may also be possible to indirectly infer an increase in quinone groups on the electrode surface. **Figure 6.1a** shows the $Fe^{2+/3+}$ CV responses for a range of anodic polarisation times under constant current conditions (+0.1 mA), with **Figure 6.1b** illustrating the trend observed (n=3).

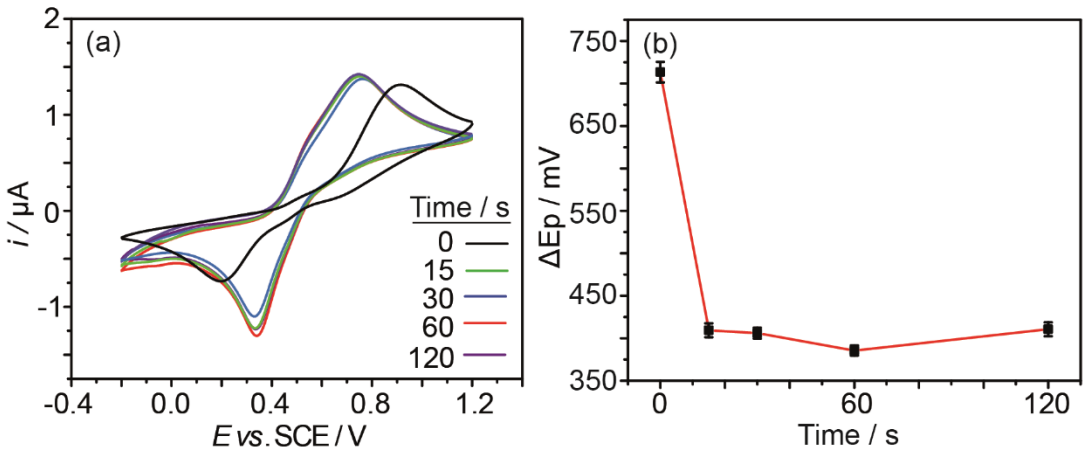

Figure 6.1: (a) The CV response 1 mM $Fe^{2+/3+}$ in 0.1 M $HClO_4$ at 0.1 V s^{-1} for the laser micromachined BDD electrode at varying polarisation times (0–120 s), held at constant current (+ 0.1 mA) in 0.1 M H_2SO_4.

As Figure 6.1 shows, anodic polarisation of the surface results in a significant change in the ΔE_p, even after just 60 s, ΔE_p has reduced from 715 mV ± 9 mV (no polarisation)

to 385 ± 6 mV. Longer treatments did not result in significant changes to the ΔE_p observed. 60 s resulted in the smallest ΔE_p recorded and thus anodic polarisation was conducted for 60 s throughout this study.

6.3.2 Electrode Characterisation

6.3.2.1 Imaging the electrode surface

Prior to use, it was extremely important to characterise the BDD electrode before and after laser micromachining. In order to understand the extent of surface damage induced by the laser micromachining, the laser micromachined BDD electrode was visualised with various imaging techniques, including optical microscopy, FE-SEM and WLI. **Figure 6.2a** shows a typical optical image of a laser micromachined 1 mm diameter glass-sealed BDD electrode.

Clearly visible are sixty-one laser pits of diameter ~45 ± 2 µm, with a pit to pit spacing of ~100 µm, as confirmed by interferometry (**Figure 6.2b**). Cross-sectional data **(Figure 6.2c**) obtained from **Figure 6.2b** (red line) indicates that the pits have a typical depth of 25 ± 5 µm, with a surface roughness of ~5 µm (**Figure 6.2c**) compared to the surrounding lapped surface, ~ nm roughness.[20] **Figure 6.2d** shows a typical FE-SEM image of a laser pit. Whilst BDD grains (light and dark regions) are still visible in the surrounding area, surface damage induced by the laser micromachining process is apparent within the laser micromachined pit. It is also important to note that there may be contribution of quinone functionalities from this exposed laser micromachined side wall, due to the imperfect glass seal around the 1 mm BDD. This is particularly evident in the interferometry image displayed in **Figure 6.2b**.

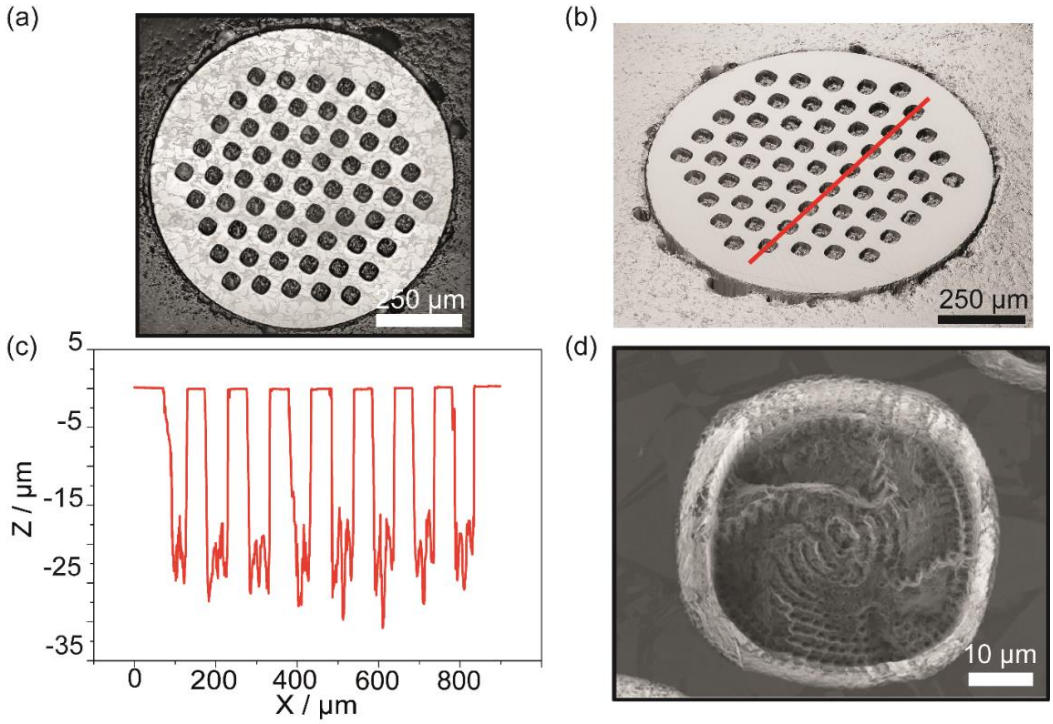

Figure 6.2*: *Images of the 1 mm laser micromachined BDD electrode including (a) an optical image showing the full laser array; (b) a 3D rendering of the electrode surface from interferometry; (c) a cross-section of the WLI data collected (position indicated by the red line in Figure 1b) showing the laser pit depths, widths and spacings and (d) an FE-SEM image of an individual laser pit.

6.3.2.2 Electrochemical characterisation

The BDD electrode employed in this study was electrochemically characterised using the fast one electron transfer outer sphere redox couple (1 mM) $Ru(NH_3)_6^{3+}$ in 0.1 M KNO_3. **Figure 6.3** shows the CVs recorded at 0.1 V s^{-1} for the 1 mm BDD electrode before and after laser micromachining of the surface to produce an array of sixty-one pits, ~50 µm in diameter, ~25 µm in depth, 100 µm separation centre-centre.

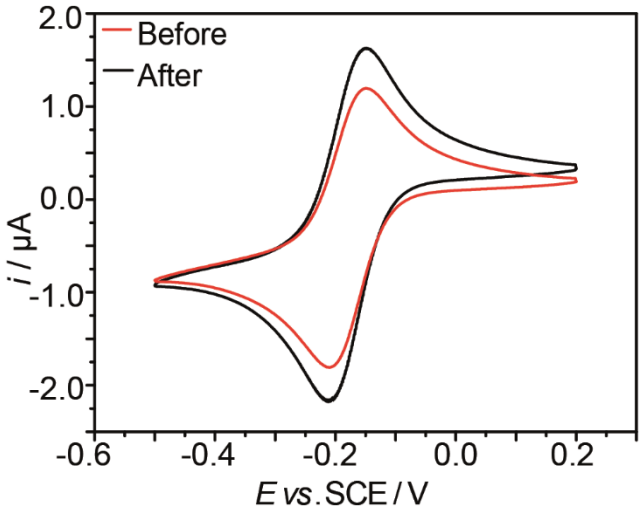

Figure 6.3*: *CVs of 1 mM $Ru(NH_3)_6^{3+}$ in 0.1 M KNO_3 at 0.1 V s^{-1} for the 1 mm BDD electrode before (red) and after (black) laser micromachining.

$Ru(NH_3)_6^{3+/2+}$, an outer sphere redox couple should be insensitive to changes in the surface chemistry, provided the availability of surface charge carriers has not been impaired during the laser process. Possible damage to the surface in terms of producing a sufficient number of defect states to trap charge significantly to impact on the ET kinetics was not observed, with reversible behaviour was observed for T = 298 K, with a peak-to-peak separation (ΔE_p) of 59 mV obtained both before and after laser micromachining.

6.3.2.3 Calculating electrode area after laser ablation

Three methods: (1) Interferometry (detailed in Section 6.2.6), (2) Randles-Sevcik analysis and (3) a 2D finite element simulation were employed to calculate an effective increase in electrode area due to laser ablation.

From the experimental data collected in **Figure 6.3** the increase in area was approximated through use of the Randles-Sevcik equation (Equation 1.7). Where i_p is the peak current, n is the number of electrons transferred per redox event (n = 1), A is the electrode area, D is the diffusion coefficient (8.16×10^{-6} cm^2 s^{-1} determined experimentally using an Au ultramicroelectrode (UME) of radius = 14.5 µm), C is the analyte concentration (8.5×10^{-7} mol cm^{-3}) and v is the scan rate (0.1 V s^{-1}), assuming a temperature of 298 K. For the i_p measured (1.196 µA) before laser micromachining, the area of the electrode was determined as 5.80×10^{-3} cm^2 (diameter = 0.859 mm) which was confirmed optically (diameter = 0.9 mm). After laser machining i_p increased to 1.629 µA, equating to an area of 7.89×10^{-3} cm^2 using Equation X.1, suggesting an increase in area by 36 %. Note, Randles Sevcik serves only as an approximation as it assumes linear diffusion profiles contribute to the current, which is true for large (> 50 µm) planar surfaces. Of three electrodes tested, the CV characteristics post-laser ablation/activation consistently displayed an increased current compared to the bare electrode, at this scan speed (35% — shown in **Figure 6.3**, 23% and 18% — data not shown).

As scan speed effects diffusional length scales, which in turn effects whether surface "roughness" is seen in the current response or not, a simple 2D finite element simulation was implemented. The pitted surface was modelled as a series of square-shaped trench structures of diameter 50 µm and depth 25 µm, separated centre to centre by 100 µm, as shown in **Figure 6.4**.

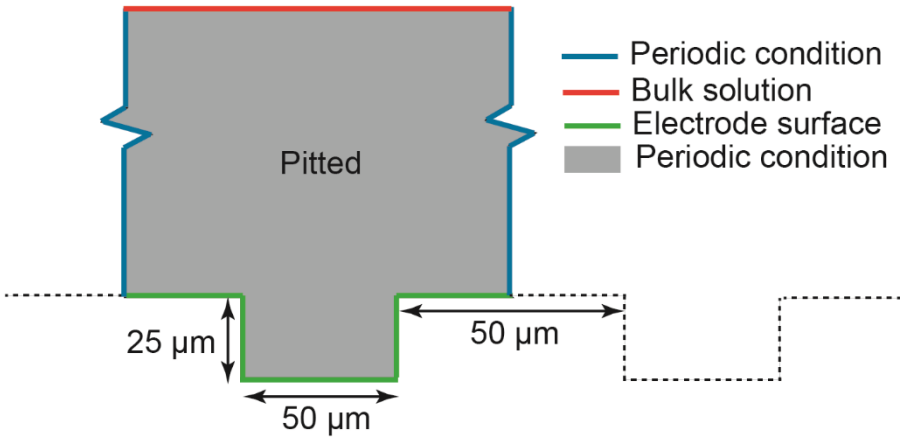

Figure 6.4*: *Schematic of the simulated domain for the 2D finite element model approximating a slice through the centre of a single pit (simulated by Dr. Maxim Joseph). A tall rectangular domain (grey) is bounded on the long vertical edges by a periodic condition (blue), on the top edge by a bulk solution (red) and on the bottom by the working electrode (green). A single pit is represented in the centre of the working electrode surface as a simple rectangle.

Fick's diffusion was applied in the grey domain, whilst the Nernst equation was used to describe the electrode boundary conditions (*i.e.* electron transfer is much faster than diffusional transport which is a reasonable assumption for the fast electron transfer outer sphere redox couple employed) and a periodic boundary condition applied at the blue boundary i.e. what leaves one boundary enters the other. Meshing was set to 1 element per 100 nm at the electrode surface, which was allowed to grow at a rate of 1.01. The total number of mesh elements employed was 387,334. The model predicted an increase in peak current of 21% compared to the bare surface at 0.1 V s^{-1}. The experimental observed increased peak current, after laser micromachining, is thus attributed to both an increase in the surface area due to the introduction of laser micromachined pits and possible etching of the glass which seals the BDD, exposing the laser micromachined side walls, during the high temperature acid treatment.

6.3.2.4 Solvent Window

The changes to the solvent window due to the laser micromachining process was also explored. **Figure 6.5** shows solvent windows recorded in 0.1 M KNO_3 (starting from 0 V cycling from −2 V to 2 V and then back to 0 V) at a scan rate of 0.1 V s^{-1} for the BDD electrode pre- and post-laser ablation. A GC electrode (3 mm diameter) solvent window is shown for comparison, mechanically polished to a glass finish in between measurements.[13]

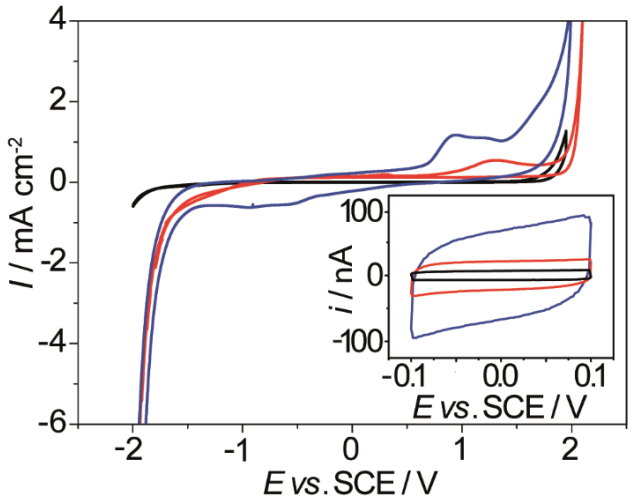

***Figure 6.5**: Comparison of solvent windows and capacitance (inset) for BDD (black), laser micromachined BDD (red) and GC (blue), collected in 0.1 M KNO_3 (scan rate of 0.1 V s^{-1}).*

In order to compare solvent windows sizes, the anodic and cathodic potential limits have been defined as the potential at which a current density (*I*) of 0.4 mA cm^{-2} is passed for water electrolysis.[20] The bare BDD electrode exhibits a wide solvent window of 3.7 V, low capacitive currents (6.8 µF cm^{-2} at 0 V) and no evidence of an oxygen reduction signal (ORR) indicative of sp^2-free BDD, which is electrocatalytically inert.[30,20]

In contrast, GC, which contains significant sp^2 carbon,[31] is much more catalytically active, with a smaller solvent window (1.0 V) and higher capacitance currents (23.8 μF cm^{-2} at 0 V). Also evident in the cathodic potential range, −0.2 to −1.5 V, is an increased background current most likely due to ORR at the GC electrode. In the anodic window, over the range +0.6 to +1.5 V, features are observed most likely due to oxidation of sp^2 containing surface species.[32]

For the laser micromachined "activated" BDD electrode, where "activated" refers to the boiling acid and electrochemical anodic treatment applied post laser micromachining, the solvent window at 2.5 V is smaller than that of the bare BDD surface but significantly larger than for GC. Anodic signatures associated with sp^2 carbon are seen at +1.2 V, which are smaller than observed for GC. Cathodically, a current is recorded at −1.5 V which could be due to a catalytically pushed out ORR signature. The capacitance at 0 V is 10.8 μF cm^{-2}. Overall, the data suggests that the laser activated BDD electrode is more catalytically active than bare BDD, due to incorporation of sp^2 functionality, but significantly less than that of GC. This was further explored by running CV experiments using 1 mM $Fe^{2+/3+}$ in 0.1 M H_2SO_4. A change in ET kinetics was observed (shown in **Table 6.1**) after laser ablation and surface pretreatment, indicating that the catalytic activity of the laser micromachined BDD material is between that of bare BDD and GC.

***Table 6.1**: ΔE_p values for bare BDD, laser micromachined BDD and GC for the $Fe^{2+/3+}$ redox couple.*

Electrode	Surface treatment	ΔE_p (Fe^{2+}/Fe^{3+}) / mV
Glassy Carbon	Alumina polish	150 ± 5
Laser Micromachined BDD	Acid clean, Anodic polarisation	385 ± 6
Bare BDD	Alumina polish	715 ± 9

Importantly, the ability to pattern sp^2 carbon in defined regions means that sp^2 incorporation can be controlled so the advantages of BDD such as low background currents, wide solvent window and catalytically hindered ORR response, are retained as much as possible. This contrasts with sp^2 carbon incorporation during the growth process, as is typical with ultrananocrystalline and nanocrystalline BDD,[33] where sp^2 carbon is now present across the whole surface, likely residing at grain boundaries.[34] A further twenty repeat solvent window scans were conducted with no obvious change in currents or sp^2 features observed, suggesting that the sp^2 carbon introduced into the BDD electrode after laser micromachining/activation is stable.

6.3.2.5 XPS Analysis

To further investigate the change in surface chemistry during laser micromachining, XPS was performed. The technique is particularly useful for determining surface chemistry, allowing the top few nanometers of the sample surface to be characterized.[28] In order to accurately analyse the laser micromachined/activated BDD surface using a 1 mm XPS spot size a 3 mm diameter pit was machined into BDD using the parameters outlined in Experimental for the 45 µm diameter features machined previously. XPS survey spectra (**Figure 6.6**) were collected for both the

laser micromachined/activated and bare BDD electrodes in order to identify peaks of interest and ensure there was no contamination of the BDD surface during sample preparation and loading.

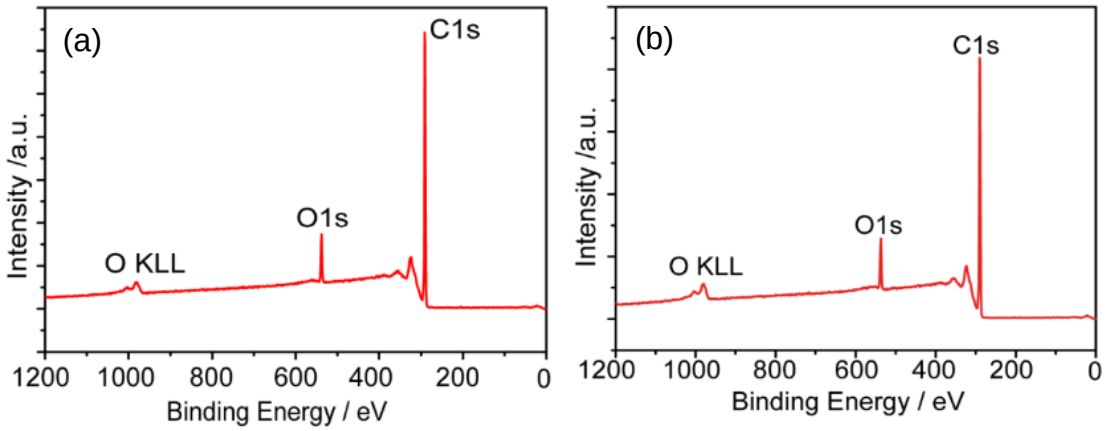

***Figure 6.6**: XPS survey spectrum of (a) the bare BDD surface and (b) a laser micromachined/activated region of the BDD surface.*

The analysis was conducted using a Kratos Axis Ultra DLD instrument, with a monochromatic Al source (1486.69 eV) with a 1 mm spot size. In both spectra the expected Auger electron peaks (O KLL) are present as well as O 1s and C 1s,[35] with no obvious contamination from other elements observed.

Figure 6.7 shows typical XPS spectra for the BDD surface (a) before and (b) after laser micromachining/activation.

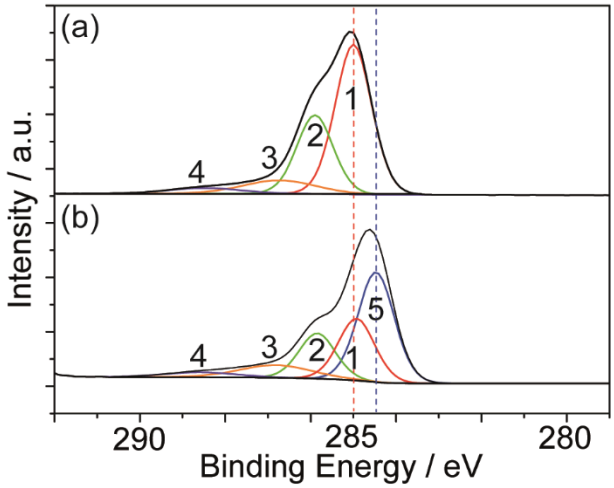

Figure 6.7: C1s XPS spectra of the (a) bare BDD and (b) laser micromachined BDD electrode surface.

The background XPS spectrum of BDD, shown in **Figure 6.7a**, exhibits a prominent signature (peak 1) at 285 eV attributed to sp^3 carbon (C-C). All peaks are referenced with respect to this peak. There is no obvious sp^2 peak (−0.4 eV from the central C-C peak) indicating negligible sp^2 carbon content BDD, in agreement with the electrochemical data shown in **Figure 6.5**.[36]

The peaks present in **Figure 6.7a** at higher binding energies can be assigned to different oxygen environments present on the BDD surface.[30] Peak 2 (+1 eV) corresponds to the presence of alcohol (C-OH) groups on the electrode surface, with peak 3 due to ether (C-O-C) groups at ~ +1.7 eV.[37] Peak 4 can be attributed to carbonyl groups (C=O) reported to fall between +2.9 to +3.9 eV of sp^3 carbon.[30] There may also be a small contribution at ~ +4 eV, which is associated with the presence of carboxyl (COOH) groups at the BDD surface.[38]

Figure 6.7b shows the change in the XPS spectra after laser micromachining the BDD electrode and subsequent activation. With the XPS beam now focussed at the bottom of a laser pit, a drop in signal intensity is observed which is likely due to the increased surface roughness as a result of laser micromachining. Immediately obvious is the emergence of peak 5 at −0.4 eV attributed to the production of graphitic sp^2 carbon (C=C), formed during the laser micromachining process. An increase in surface carbonyl groups (peak 4) is also observed, with the peak area increasing by approximately 15% after laser micromachining.

Angle resolved XPS was also employed to help establish the assignment of the sp^2 carbon peak in the XPS spectra and confirm the location of the sp^2 carbon in the 3 mm laser micromachined/activated BDD electrode, machined specifically for 1 mm XPS spot size. By tilting the sample of interest away from the analyser the XPS spectra collected can make the spectra more sensitive to the outermost atomic layers. Angles of 0^o and 70^o were employed, rotating the sample when appropriate, as illustrated in **Figure 6.8** for obtaining spectra of the laser micromachined surface.

By angling the sample to 70^o a greater proportion of the upper most layers of the BDD laser pit.[39] **Figure 6.8** shows the XPS spectra collected at (a) 0^o and (b) 70^o of the laser micromachined/activated surface.

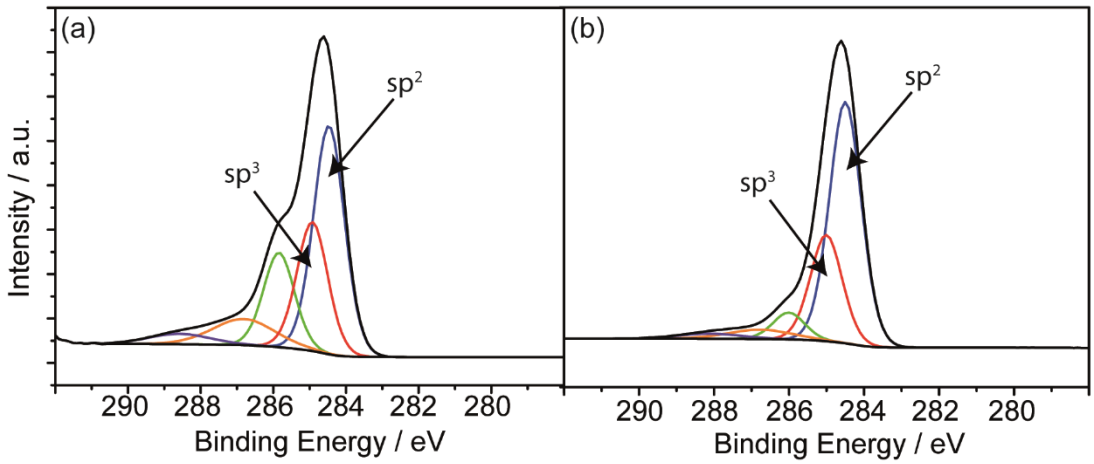

***Figure 6.8*:** C *1s XPS spectra of the laser micromachined/activated BDD surface pit at an angle of (a) 0° and (b) 70°. The green, orange and purple peaks are assigned to various oxygen-containing functional groups (vide supra).*

By moving from 0° to 70° angle, the sp^2/sp^3 ratio increases from 1.68 to 2.4, suggesting more sp^2 carbon is located in the upper surface.

6.3.2.6 Raman Microscopy

Micro-Raman spectroscopy was used to investigate the change in the sp^3-sp^2 content of the electrodes before and after laser machining. The 514 nm laser spot size at the sample was approximately 10 µm in diameter (with a ×50 objective). The small spot size enabled Raman spectra to be collected from both the laser micromachined/activated (red line) and bare/activated (black line) regions of the surface, with multiple measurements (n = 7) collected and mean averaged to ensure the data collected was representative (**Figure 6.9**).

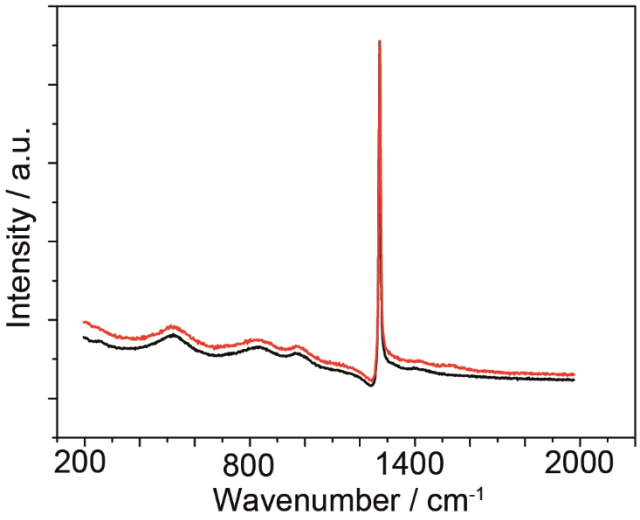

Figure 6.9: Micro-Raman spectra of the bare BDD sample (black) and within a laser pit (red).

Both Raman spectra in Figure 6.9 show the characteristic peak associated with sp^3 carbon, at 1332 cm^{-1}, with peak asymmetry attributed to a Fano resonance, as expected for heavily doped BDD.[40] In the region 1400–1600 cm^{-1}, which corresponds to graphite or amorphous carbon (sp^2 carbon),[41] there is only a very slight indication that sp^2 carbon is present after laser micromachining/activation of the surface (as indicated on Figure 6.9). However, for the heavily BDD employed here, although the Raman signal originates from close to the electrode surface, it is not truly surface sensitive, as with XPS (and electrochemical analysis).[42] This data therefore suggests that the laser ablation procedure has not impacted significantly on the material quality, sub-surface.

6.3.3 pH Detection

6.3.3.1 Background response

A SWV experiment to investigate the background response of a bare BDD electrode in pH 2 solution was conducted, as shown in **Figure 6.10**. The surface of the electrode was activated using the same procedure as for the laser micromachined electrode. In

Figure 6.10, there is evidence of a very small peak at +0.41 V, with a peak height of 5 nA (background corrected). This peak occurs in the same position on the laser micromachined surface at pH 2, but is significantly smaller, 5 nA compared with 0.6 µA on the laser micromachined/activated electrode. Furthermore, given it is very difficult to produce a perfect glass-sealed electrode as shown in the interferometric image in the insert to **Figure 6.2b**, there will be laser-cut BDD edges and sidewalls exposed to solution which also contain sp^2 carbon as a direct result of the laser ablation process. It is likely this contributes to the signal observed.

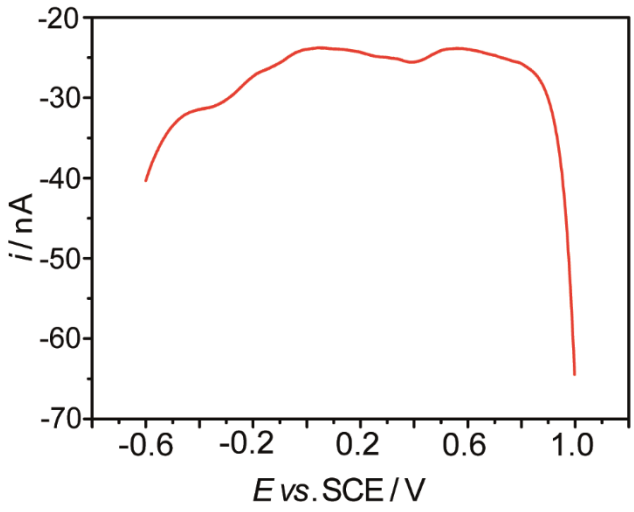

Figure 6.10*: *SWV (frequency= 150 Hz, step potential = 2 mV, amplitude = 200 mV) recorded in pH 2 solution with a bare BDD electrode.

6.3.3.2 Calculating quinone surface coverage

To calculate the quinone surface coverage, cyclic voltammograms were recorded in pH 2 solution on the laser micromachined/activated BDD electrode at a scan rate of 0.1 V s^{-1} (shown in **Figure 6.11**).

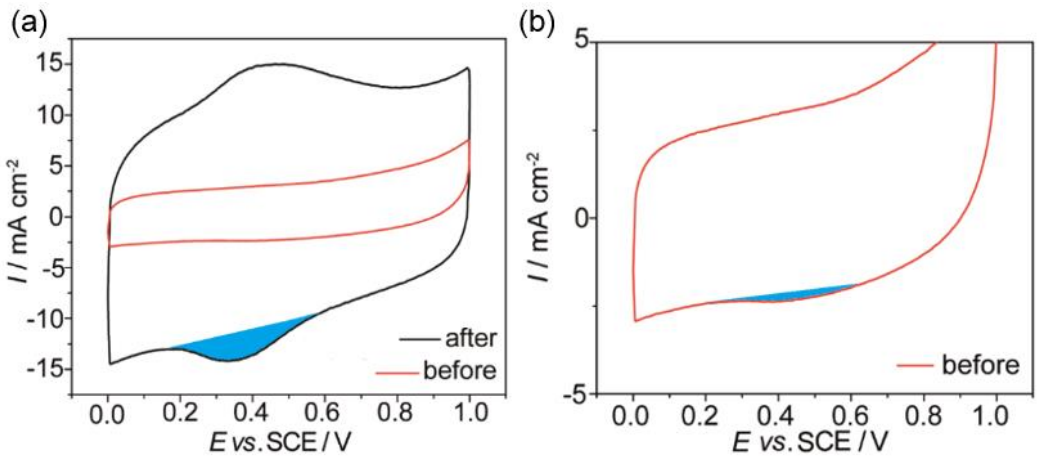

***Figure 6.11**: (a) CVs of laser micromachined/activated BDD electrode (black) and bare BDD electrode (red) in pH 2 solution at a scan rate of 0.1 V s^{-1}, with the integrated areas highlighted in blue, as well as (b) the bare BDD electrode data scaled in order to display the quinone reduction peak.*

The peaks were background subtracted (2 point linear function) integrated (from 0.55 to 0.17 V vs. SCE) to obtain the charge passed, Q, and converted to Γ (mol cm^{-2}) using Equation 6.2:[43]

$$Q = nAF\Gamma \qquad (6.2)$$

where n = the number of electrons transferred = 2;[44],[13] A = total electrode surface area (cm^2); calculated from WLI and F = Faraday's constant (96485 C mol^{-1}).

The quinone surface coverage was calculated to be 1.9×10^{-11} mol cm^{-2}. This value is unsurprisingly lower than that calculated for an sp^2 carbon electrode, EPPG, (5.9×10^{-11} mol cm^{-2}), activated by mechanical polishing.[13]

6.3.3.3 pH response of quinone reduction reaction

The pH dependence of the electrochemical response of surface bound quinones on the laser micromachined/activated BDD electrode was investigated using SWV across a wide pH range (2–12), **Figure 6.12a**. As shown, as the pH is increased the reduction

peak position shifts towards more negative potentials. This corresponds well with previous studies with sp^2 activated GC and EPPG electrodes materials.[13, 15] Note, for pH 2, at −0.4 V, the current begins to increase, most likely due to proton reduction. As this current response does not fall within the quinone reduction potential region of −0.2 to +0.4 V vs. SCE, it is not problematic. **Figure 6.12b** shows a plot of the reduction peak potential vs. pH for three laser micromachined/activated BDD electrodes. Identical laser conditions/activation procedures were employed for each electrode.

Not only does **Figure 6.12b** shows an excellent linear response (R^2 = 0.999 for each electrode) across the analysed pH range 2–12, but also demonstrates the reproducibility of the pH sensor fabrication procedure. Each electrode exhibits a gradient close to that theoretically expected, 59 mV per pH unit (for T=298 K); 59 ± 1 mV pH^{-1}, 59 mV ± 1 pH^{-1} and 58 ± 1 mV pH^{-1}. This is expected for a two proton, two electron process, which has also been found with intrinsically occurring quinones on GC and EPPG electrodes.[13,15]

Importantly, no appreciable ORR wave is observed within the quinone reduction potential window, resulting in well-defined peaks and a large signal-to-noise ratio. This contrasts with other carbon-based electrodes that have used intrinsic quinone groups for pH detection, and require degassing of the solution to make accurate measurements, especially at the lower pH values.[13,15] This study highlights the benefit of using BDD as the bulk electrode material as degassing is not necessary, making the sensor ideal for *in-situ* applications.

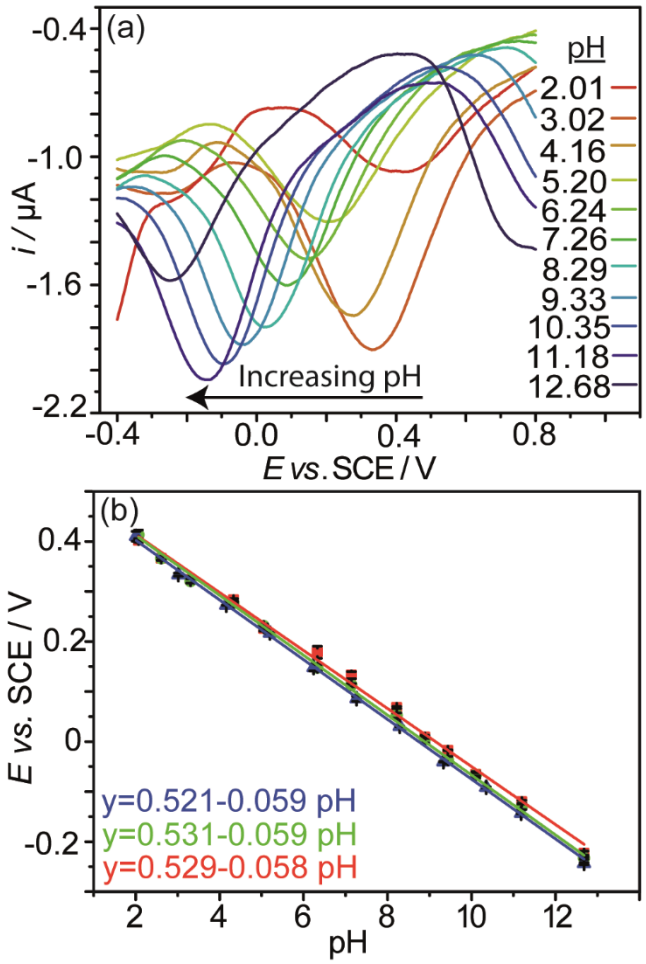

***Figure 6.12**: (a) Quinone reduction peaks using SWV (frequency= 150 Hz, step potential = 2 mV, amplitude = 200 mV) across the pH range of 2–12 in buffered solution and subsequent calibration graphs (b) for 3 independently fabricated BDD pH sensors all exhibiting an R^2 value of 0.999.*

Furthermore, obtaining a linear response across the entire analysed pH region (2.01 – 12.68) indicates that the acid dissociation constant (pK_a) of the surface-bound quinone species produced by laser micromachining is much higher than the typical pK_a's of quinone molecules in bulk solution.[15,45,46] For example, for ortho-benzoquinone in solution at 25 °C pK_{a1} and pK_{a2} are reported to be 9.25 and 13 respectively,[15,45] with the majority of quinone species exhibiting similar pK_a values.[46] If this was not the case, a Nernstian response would not be observed across the entire pH range analysed, with

a change in gradient observed as pK_{a1} is reached (i.e., 30 mV / pH unit indicating a two electron, one proton regime), discussed in detail in **Chapter 1.7.2.4**. It can therefore be assumed that the quinone groups on the laser micromachined BDD surface remain protonated, resulting in a Nernstian response even at high pH values (> pH 12). Similar observations have previously been reported elsewhere, indicating quinone groups immobilised on electrode surfaces can exhibit vastly larger pK_a values (shifts > 3 pK_a units) than their solution-based counterparts.[47,48]

6.3.4 Electrode Stability

The electrochemical stability of the laser micromachined/activated BDD electrode was also considered. In particular, using the same electrode, repeat measurements were made once a week in a pH 2.58 solution, over a period of three months. In between measurements the electrode was stored dry. The SWV's and corresponding peak potential versus time (in days) are displayed in **Figure 6.13**. As shown, over this period, the peak potential data does not fall outside a ± 0.02 pH unit error range. Furthermore, once laser micromachined and then activated no further electrode treatment was required in between measurements and no storage solution for the electrode was necessary. We believe that the initial stage of the activation process in boiling oxidising concentrated acid (15 minutes at ≥ 200 °C) removes unstable sp^2 fragments from the electrode, leaving behind a very stable, robust surface.

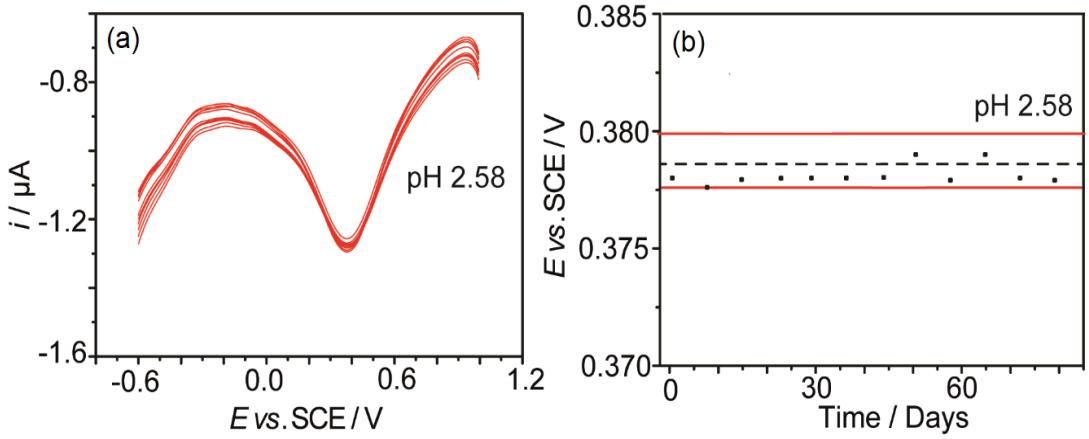

***Figure 6.13**: (a) Quinone reduction peaks using SWV (frequency= 150 Hz, step potential = 2 mV, amplitude = 200 mV) in pH 2.58 solution using the same laser micromachined/activated BDD electrode (y=0.531–0.059 pH) over a twelve-week period (measured weekly). (b) Plot of peak potential per week (n = expected range from the calibration data and the red lines indicating ± 0.02 pH units from the mean value. 3), with dashed black line showing the mean potential value for pH 2.58, falling within the expected range from the calibration data and the red lines indicating ± 0.02 pH units from the mean value.*

6.3.5 Interferences

In any analytical measurement, interferences need to be considered. Given the voltage range for quinone reduction for pH 2−12 spans from ~ −0.2 to +0.4 V vs. SCE it is only species present within this potential range that are likely to cause problems. Furthermore, they would need to be present at concentrations sufficient to mask the signal, with currents in the µA range, for a 1 mm diameter disk electrode. Therefore, in order to investigate possible interferences that may mask the voltammetric pH signal several common heavy metal contaminants were investigated. Three pH buffer solutions were selected to represent acidic, neutral and alkaline conditions (pH 2.6, 6.3 and 9.4). 1 mM of each metal salt was added to the three solutions (one metal salt only per solution) and the pH recorded using SWV, using both the (a) laser micromachined/activated BDD electrode and (b) mechanically polished GC electrode.

The heavy metals investigated included Pb^{2+}, Cd^{2+}, Zn^{2+} and Cu^{2+}, **Figure 6.14–Figure 6.18** respectively.

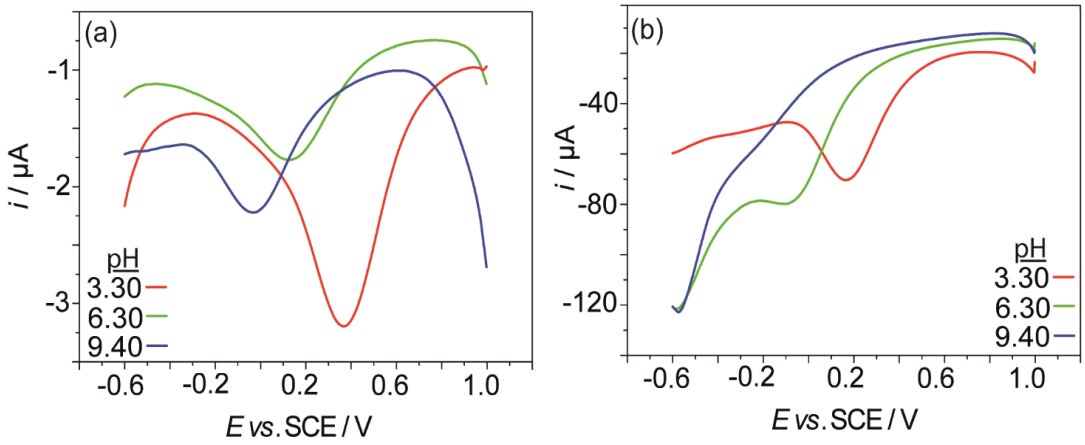

***Figure 6.14**: SWV in pH 2.6 (red), 6.3 (green) and 9.4 (blue) buffer solutions in the presence of 1mM Pb^{2+} for (a) the laser machined BDD electrode and (b) a 3 mm GC electrode.*

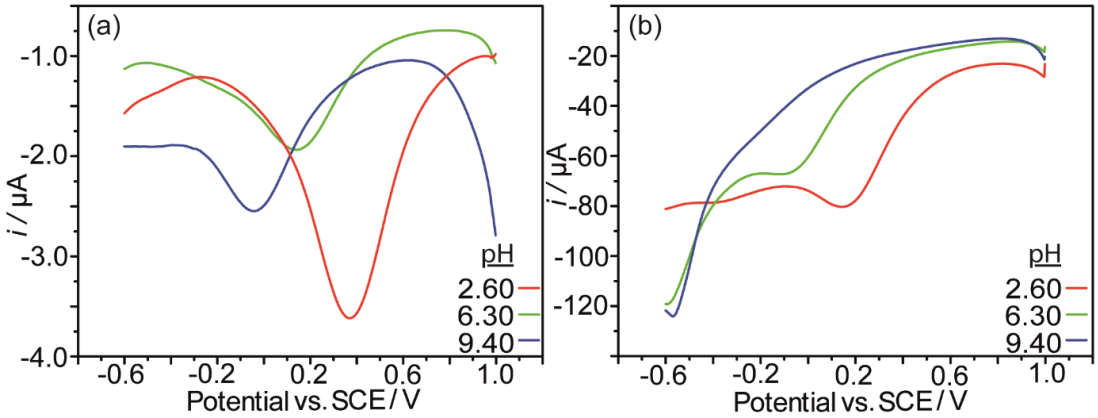

***Figure 6.15**: SWV in pH 2.6 (red), 6.3 (green) and 9.4 (blue) buffer solutions in the presence of 1mM Cd^{2+} for (a) the laser micromachined/activated BDD electrode and (b) a 3 mm GC electrode.*

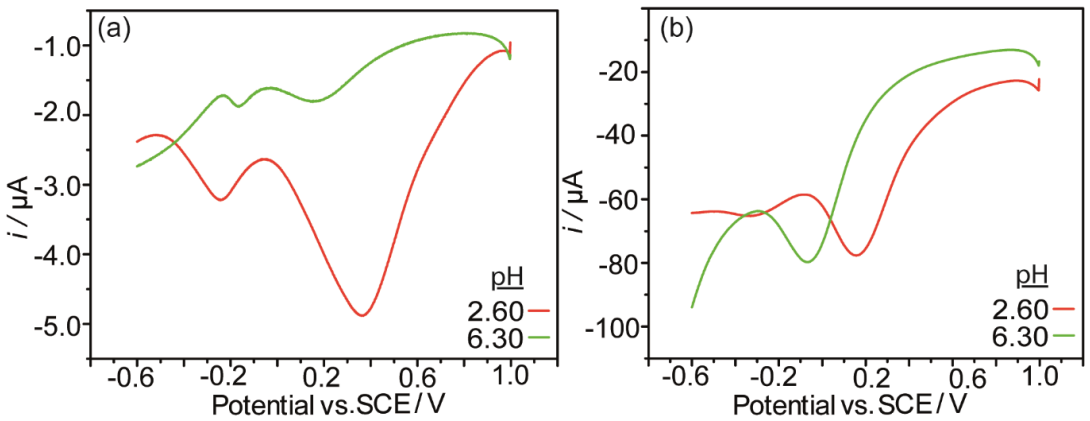

***Figure 6.16**: SWV in pH 2.6 (red) and pH 6.3 (green) buffer solutions in the presence of 1 mM Fe^{3+} for (a) the laser micromachined/activated BDD electrode and (b) a GC electrode.*

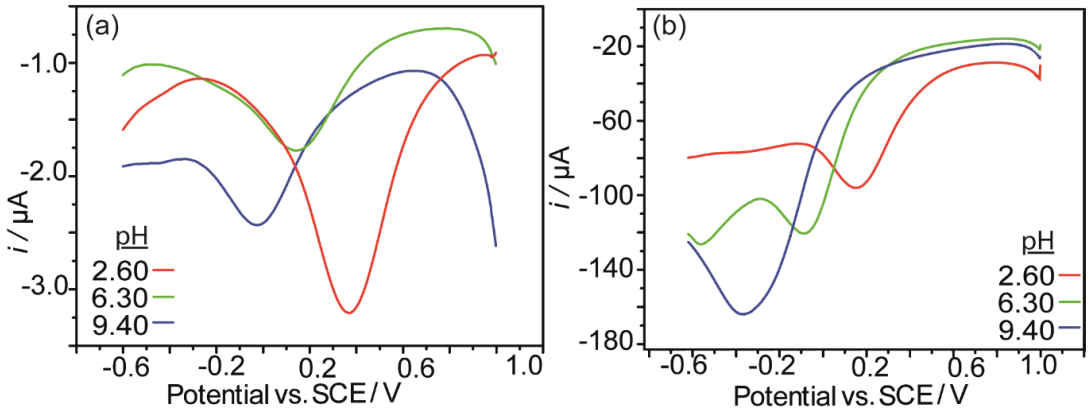

***Figure 6.17**: SWV in pH 2.6 (red), 6.3 (green) and 9.4 (blue) buffer solutions in the presence of 1 mM Zn^{2+} for (i) the laser micromachined/activated BDD electrode and (ii) a GC electrode.*

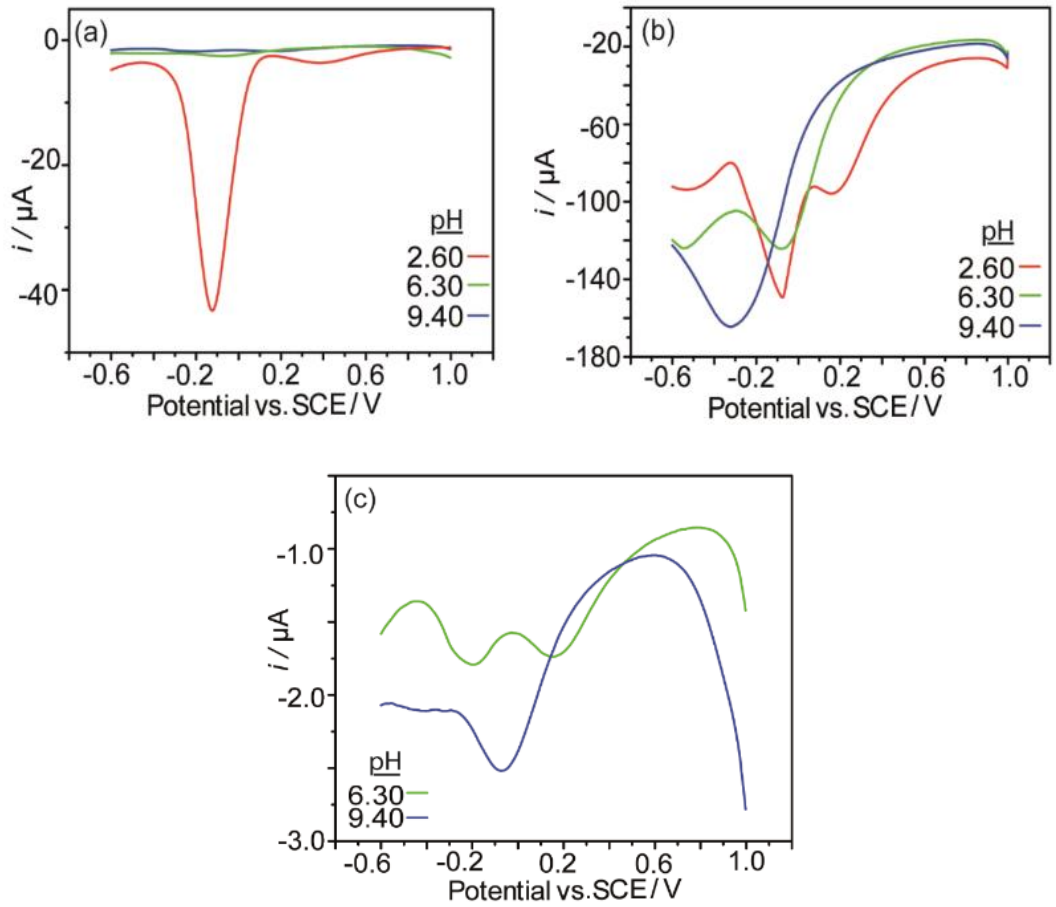

***Figure 6.18**: SWV in pH 3.3 (red), 6.3 (green) and 9.4 (blue) in the presence of 1 mM Cu^{2+} for (a) the laser micromachined/activated BDD electrode and (b) a GC electrode. (c) provides a zoomed in view of the BDD SWV signal for pH 2.6 and 6.3 for clarity.*

Whilst the ORR background currents begin to mask the quinone reduction response on GC, the laser micromachined BDD electrode exhibits a pH response that is still clearly distinguishable due to low background currents and catalytically hindered ORR. Note for Fe^{3+}, only pH 2.6 and 6.3 solutions were used due to insolubility in high pH solutions.[49] For Fe^{3+}, a second peak is observed (far left) in both pH solutions, which is occurs outside of the pH 2–12 potential range.

For Cu^{2+} (pH 2.6) a large Cu^{2+} reduction peak occurs at ~ −0.1 V, but the quinone reduction peak is still clear. Furthermore, the peaks for Cu^{2+} and quinone reduction are

sufficiently well separated on BDD, whereas they overlap on GC (vide supra), due to the different electroactivities of the two electrodes. However, at environmentally relevant concentrations, particularly around 1 ppm, the difference in current alone cannot be used to identify the quinone peak in **Figure 6.19**. Thus for environmental samples where the pH of the solution is unknown this may present difficulties.

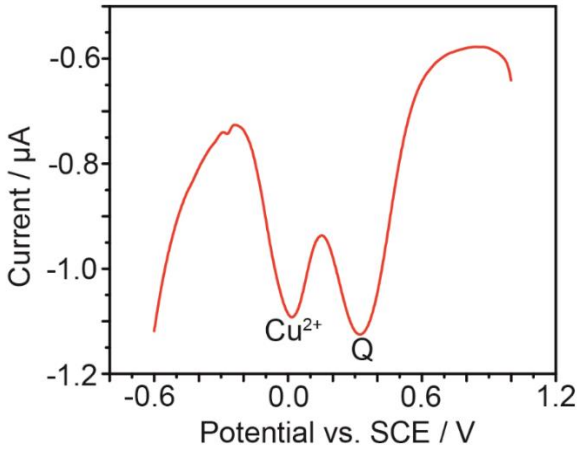

***Figure 6.19**: SWV in pH 2 (red), in the presence of 1 ppm Cu^{2+} for the laser micromachined/activated BDD electrode showing the quinone peak (Q) and the Cu2+ peak.*

To mitigate this issue, two methods were explored. First, shown in **Figure 6.20**, is the CV response. Due to the surface bound nature of the quinone peak, the ΔE_p is 40 mV (theoretically 0 mV for a surface bound molecule) compared to that of the Cu^{2+} peak (117 mV). It is considered that the reduced ΔE_p of the quinone could be used to identify the pH peak.

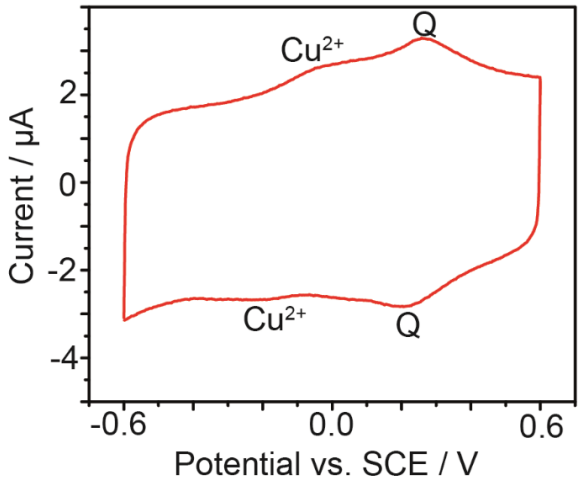

Figure 6.20*: *CV in pH 1 buffer solution ran at 0.1 V s^{-1} in the presence of 1 ppm Cu^{2+}.

Unfortunately, this mitigation route involves running a second electrochemical technique (CV), in addition to the SWV response to identify the two peaks. Therefore, manipulation of the frequency (Hz) of the SWV was also explored (**Figure 6.21**). It was found that by increasing the SWV Hz the the Cu^{2+} signal decreases relative to the quinone peak. This is likely due to the fact the Cu^{2+} diffusion layer is reduced due to a quicker scan time, resulting in a reduced Cu^{2+} signal, whilst the capacitive contribution of quinone response increases, resulting in a larger quinone signal overall (see **Chapter 1.4.5**). For this reason, operating at high Hz is advocated when running pH measurements in solutions containing Cu^{2+} to mitigate interference.

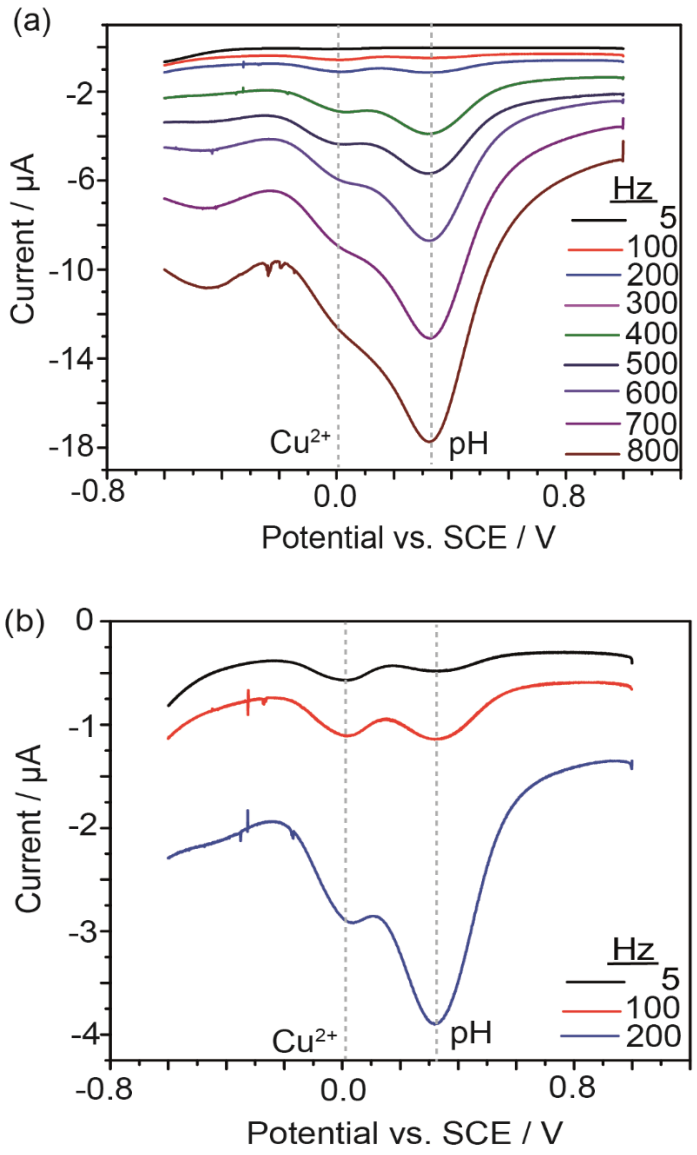

Figure 6.21: *SWV in pH 1 buffer solution (step potential = 2 mV, amplitude = 200 mV) in the presence of 1 ppm Cu^{2+} at different frequencies.*

6.3.6 Real-world analysis

The pH of seawater collected from Poldhu Beach, Mullion, Cornwall, UK was analysed (at T = 25 °C) in order to test the capabilities of the BDD pH sensor in a complex sample matrix. The SWV response of the laser micromachined/activated

BDD electrode in seawater (unfiltered and with no additional salts added) is shown in **Figure 6.22**.

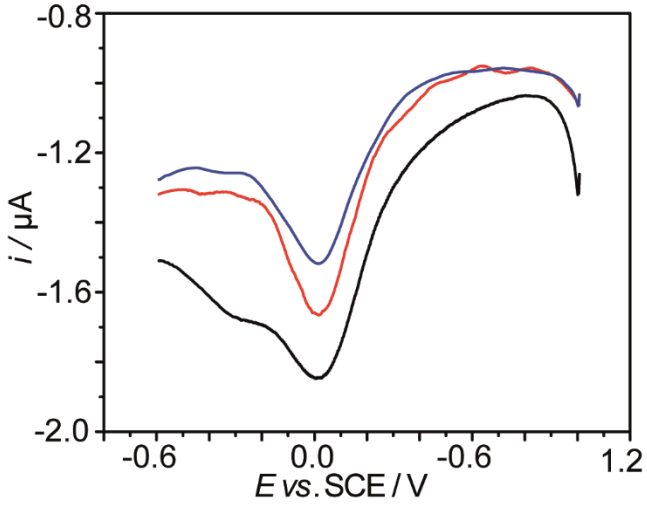

***Figure 6.22**: Replicate SWV's corresponding to the first (black), second (blue) and third (red) repeat scans recorded in seawater using a laser micromachined/activated BDD electrode.*

The seawater had a measured solution conductivity of 54.3 mS cm^{-1}. The electrode recorded three consecutive SWV's, returning peak potentials of 0.023 V, 0.019 V and 0.019 V respectively. The electrode had been previously calibrated, as shown in **Figure 6.11**, recording a calibration line of y = 0.521–0.059 pH (R^2 = 0.999). Using the measured peak potentials, this corresponded to a measured pH of 8.40 ± 0.04 pH units. The seawater pH was independently measured using a commercially available glass pH electrode, and found to be 8.39 ± 0.02 pH units, comparing well with that determined using the BDD electrode.

6.3.7 Temperature

Understanding the temperature dependence of the BDD pH electrode is fundamental to the operation of the sensor for a wide range of applications, including making measurements in seawater (temperature can range from –2°C to 35°C), the human body (37°C) and down oil wells (up to 200°C at suitably high pressures). The glass pH electrode exhibits a Nernstian temperature dependence, which is well defined (increase in gradient slope by 0.199 mV per °C), and thus a 'temperature correction factor' is applied during operation of the sensor to improve accuracy.[50] To explore the pH response of the BDD electrode over a range of temperatures, the pH responses of two BDD pH electrodes were explored at 5, 15, 25, 40, 60 and 75°C using a temperature controlled water bath. The gradients recorded experimentally are summarised in **Table 6.2**, across the pH range 2–12 (buffered pH solutions 2, 4, 7, 10 and 12 were utilised), along with the theoretical gradients predicted by the Nernst equation at 298 K.

Table 6.2: *Summary of BDD pH responses at elevated temperatures.*

		Electrode			
		1		**2**	
T / °C	**Theoretical gradient / mV pH^{-1}**	**Experimental gradient / mV pH^{-1}**	**R^2**	**Experimental gradient / mV pH^{-1}**	**R^2**
5	55	54± 0.8	0.999	54± 1.0	0.997
10	56	55 ± 0.8	0.997	56 ± 1.0	0.998
25	59	58 ± 0.8	0.998	59 ± 0.62	0.999
40	62	62 ± 1.0	0.998	63 ± 0.72	0.999
60	66	66 ± 1.6	0.995	68 ± 0.89	0.998
75	69	74 ± 1.5	0.997	72 ± 1.2	0.997

It is clear that the BDD pH electrode exhibits a Nernstian dependence at both elevated temperatures and those below room temperature, with the experimental values obtained similar to those predicted theoretically.[50] Furthermore, the fact that as part of the fabrication procedure the BDD pH electrode is elevated to temperatures ~ 200°C indicates that the quinone groups incorporated into the surface due to laser ablation are inherently stable, boding well for the operation of the sensor in more extreme environments.

6.3.8 Blood Analysis

Electrochemically monitoring blood pH is difficult as the glass pH electrode cannot be used *in-vivo* due to its fragility and adsorption of amino-acids, peptides and proteins onto electrode surfaces, which is well documented.[51] pH measurements in blood (sheep blood, TCS biosciences, UK) were therefore conducted to test the robustness of the BDD pH sensor (**Figure 6.23**).

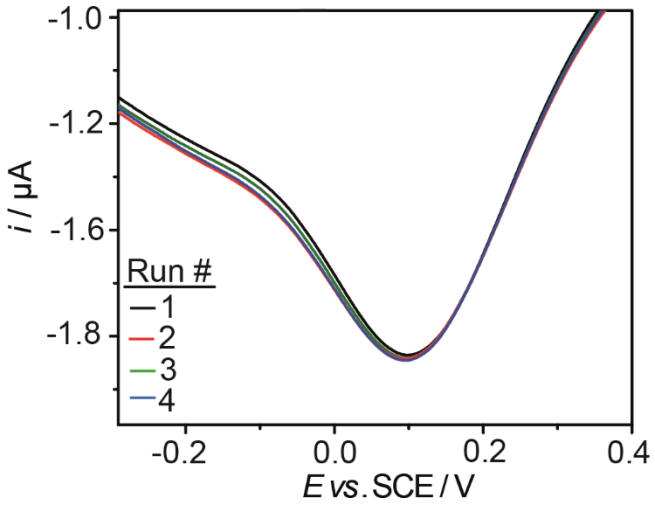

***Figure 6.23**: Replicate SWV's corresponding to the first (black), second (red), third (green) and fourth (blue) repeat scans recorded in sheep blood using a laser micromachined/activated BDD electrode.*

The pH response was found to be 7.10 ± 0.02 for the BDD pH electrode, comparing well to the glass pH electrode (pH 7.06). Furthermore, no interferences in the potential window are observed, along with no significant fouling. This indicates that the BDD pH electrode exhibits the anti-fouling properties of BDD. In the future, BDD pH sensor may find use in a wide range of biological applications.

6.4 Conclusion

A voltammetric pH sensor has been fabricated via the controlled incorporation of sp^2 into a BDD electrode using laser micromachining (ablation) followed by activation of the sp^2 carbon, using high temperature treatment (> 200 $^{\circ}$C) in boiling, concentrated acid, followed by anodic oxidation. Specifically, a laser is employed to produce a defined number of sp^2 regions in the BDD surface. The subsequent activation process of the sp^2 carbon results in a highly stable surface, containing pH dependent, redox-active quinone groups, the SWV response of which can be utilised to measure solution pH. As sp^2 carbon in BDD acts to increase background currents, reduce solvent windows and electrochemically reduce oxygen, the ability to controllably add sp^2 carbon regions into BDD means it is possible to optimize the amount of sp^2 required to produce the required signal, whilst keeping background and ORR currents reduced in the potential region of interest.

The fabrication process is shown to be highly reproducible with the BDD pH sensor exhibiting excellent linearity (R^2 = 0.999) over the pH range 2–12 as well as good sensitivity (59 ± 1 mV pH^{-1}), achieving a Nernstian response, as expected for a two electron, two proton process. By optimising sp^2 coverage of the surface, degassing of

the solution to remove oxygen is not necessary, due to the fact that the ORR signal is reduced and shifted to more negative potentials, compared to high content sp^2 electrodes such as GC or EPPG. This indicates the BDD pH sensor is viable for *in-situ* applications. Furthermore, the sensor can be stored dry and once activated does not require further activation between measurements. The pH response was found to be unaffected by the presence of many different metal ions, deliberately added at high concentration to challenge the electrochemical response. Current electrodes have been used over a time period of three months (and are still functioning), producing consistent and Nernstian calibration lines. The BDD electrode was also found to replicate the pH measurement made in complex real-world matrices including seawater and blood using a conventional glass electrode. The sensor also operates in a Nernstian manner at elevated temperatures.

Having developed a BDD pH sensor, we envisage future investigations to determine if the sensor to be suitable for scenarios which exploit the material properties of diamond such as high-temperature, high-pressure or corrosive environments. The fact that the BDD electrode is still functional after exposure to high temperature acids (> 200 °C) bodes well for high temperature applications. Furthermore, the sensor shows promise for *in-vivo* measurements. Integration of this pH electrode into all-diamond electrochemical devices[52] is also possible.

6.5 References

(1) Helmlinger, G.;Yuan, F.;Dellian, M.;Jain, R. K. *Nat. Med.*, **1997**, *3*, 177–182.
(2) Komonweeraket, K.;Cetin, B.;Benson, C. H.;Aydilek, A. H.;Edil, T. B. *Waste. Manage.*, **2015**, *38*, 174–184.
(3) Hanrahan, G.;Patil, D. G.;Wang, J. *J. Environ. Monitor.*, **2004**, *6*, 657–664.
(4) Banna, M. H.;Najjaran, H.;Sadiq, R.;Imran, S. A.;Rodriguez, M. J.;Hoorfar, M. *Sensor. Actuat. B-Chem.*, **2014**, *193*, 434–441.
(5) Boyes, W. *Instrumentation Reference Book* ;Butterworth-Heinemann: Boston, **2010**. 374–395
(6) Pungor, E.;Toth, K. *Analyst*, **1970**, *95*, 625–648.
(7) Baucke, F. *Fresen. J. Anal. Chem.*, **1994**, *349*, 582–596.
(8) Farinato, R. S.;Tomkins, R. P. T.;Turner, P. J. *Anal. Chim. Acta.*, **1974**, *70*, 245–247.
(9) Cheng, C.;Tian, X.;Guo, Y.;Li, Y.;Yuan, H.;Xiao, D. *Electrochim. Acta.*, **2011**, *56*, 9883–9886.
(10) Chłopek, J.;Czajkowska, B.;Szaraniec, B.;Frackowiak, E.;Szostak, K.;Béguin, F. *Carbon*, **2006**, *44*, 1106–1111.
(11) Grill, A. *Diamond. Relat. Mater.*, **2003**, *12*, 166–170.
(12) Wang, D.;Chen, L. *Nano. Lett.*, **2007**, *7*, 1480–1484.
(13) Lu, M.;Compton, R. G. *Analyst*, **2014**, *139*, 4599–4605.
(14) Ang, P. K.;Chen, W.;Wee, A. T. S.;Loh, K. P. *J. Am. Chem. Soc.*, **2008**, *130*, 14392–14393.
(15) Lu, M.;Compton, R. G. *Analyst*, **2014**, *139*, 2397–2403.
(16) Galdino, F. E.;Smith, J. P.;Kwamou, S. I.;Kampouris, D. K.;Iniesta, J.;Smith, G. C.;Bonacin, J. A.;Banks, C. E. *Anal. Chem.*, **2015**, 14–17.
(17) Kahlert, H. *J. Solid. State. Electr.*, **2008**, *12*, 1255–1266.
(18) Xiong, L.;Batchelor-McAuley, C.;Compton, R. G. *Sensor. Actuat. B-Chem.*, **2011**, *159*, 251–255.
(19) Fujishima, A. *Diamond electrochemistry*;Elsevier, **2005**.
(20) Macpherson, J. V. *Phys. Chem. Chem. Phys.*, **2015**, *17*, 2935–2949.
(21) Fierro, S.;Seishima, R.;Nagano, O.;Saya, H.;Einaga, Y. *Sci. Rep.*, **2013**, *3*, 1–10.
(22) Fierro, S.;Mitani, N.;Comninellis, C.;Einaga, Y. *Phys. Chem. Chem. Phys.*, **2011**, *13*, 16795–16799.
(23) Silva, E. L.;Bastos, A. C.;Neto, M. A.;Silva, R. F.;Ferreira, M. G. S.;Zheludkevich, M. L.;Oliveira, F. J. *Electrochem. Commun.*, **2014**, *40*, 31–34.
(24) Rothschild, M.;Arnone, C.;Ehrlich, D. J. *Journal of Vacuum Science & Technology B*, **1986**, *4*, 310–314.
(25) Butler-Smith, P. W.;Axinte, D. A.;Pacella, M.;Fay, M. W. *Journal of Materials Processing Technology*, **2013**, *213*, 194–200.
(26) Wang, C. Z.;Ho, K. M.;Shirk, M. D.;Molian, P. A. *Physical Review Letters*, **2000**, *85*, 4092–4095.
(27) Moreno-Castilla, C.;Ferro-Garcia, M. A.;Joly, J. P.;Bautista-Toledo, I.;Carrasco-Marin, F.;Rivera-Utrilla, J. *Langmuir*, **1995**, *11*, 4386–4392.
(28) Geng, S.;Zhang, S.;Onishi, H. *Materials Technology*, **2002**, *17*, 234–235.
(29) Chen, P.;McCreery, R. L. *Anal. Chem.*, **1996**, *68*, 3958–3965.
(30) Hutton, L. A.;Iacobini, J. G.;Bitziou, E.;Channon, R. B.;Newton, M. E.;Macpherson, J. V. *Anal. Chem.*, **2013**, *85*, 7230–7240.

(31) Ferrari, A. C.;Robertson, J. *Philosophical Transactions of the Royal Society of London A: Mathematical, Physical and Engineering Sciences*, **2004**, *362*, 2477–2512.
(32) McCreery, R. L. *Chem. Rev*, **2008**, *108*, 2646–2687.
(33) Show, Y.;Witek, M. A.;Sonthalia, P.;Swain, G. M. *Chemistry of Materials*, **2003**, *15*, 879–888.
(34) Williams, O. A. *Diamond. Relat. Mater.*, **2011**, *20*, 621–640.
(35) Yumitori, S. *Journal of Materials Science*, **2000**, *35*, 139–146.
(36) Dementjev, A. P.;de Graaf, A.;van de Sanden, M. C. M.;Maslakov, K. I.;Naumkin, A. V.;Serov, A. A. *Diamond. Relat. Mater.*, **2000**, *9*, 1904–1907.
(37) Torrengo, S.;Canteri, R.;Dell'Anna, R.;Minati, L.;Pasquarelli, A.;Speranza, G. *Applied Surface Science*, **2013**, *276*, 101–111.
(38) McEvoy, J. P.;Foord, J. S. *Electrochim. Acta.*, **2005**, *50*, 2933–2941.
(39) Cumpson, P. J. *Applied Surface Science*, **1999**, *144*, 16–20.
(40) Locher, R.;Wagner, J.;Fuchs, F.;Wild, C.;Hiesinger, P.;Gonon, P.;Koidl, P. *Materials Science and Engineering: B*, **1995**, *29*, 211–215.
(41) Živcová, Z. V.;Frank, O.;Petrák, V.;Tarábková, H.;Vacík, J.;Nesládek, M.;Kavan, L. *Electrochim. Acta.*, **2013**, *87*, 518–525.
(42) Amer, M. S.;Busbee, J.;Leclair, S. R.;Maguire, J. F.;Johns, J.;Voevodin, A. *Journal of Raman Spectroscopy*, **1999**, *30*, 947–950.
(43) Bard, A. J.;Faulkner, L. R. *Electrochemical methods: fundamentals and applications*;Wiley New York, **1980**. 626–634.
(44) Ayres, Z. J.;Borrill, A. J.;Newland, J. C.;Newton, M. E.;Macpherson, J. V. *Anal. Chem.*, **2016**, *88*, 974–980.
(45) Schweigert, N.;Zehnder, A. J. B.;Eggen, R. I. L. *Environmental Microbiology*, **2001**, *3*, 81–91.
(46) Wang, D.;Yang, G.;Song, X. *Electrophoresis*, **2001**, *22*, 464-469.
(47) Lee, P. T.;Harfield, J. C.;Crossley, A.;Pilgrim, B. S.;Compton, R. G. *RSC Advances*, **2013**, *3*, 7347–7354.
(48) Masheter, A. T.;Abiman, P.;Wildgoose, G. G.;Wong, E.;Xiao, L.;Rees, N. V.;Taylor, R.;Attard, G. A.;Baron, R.;Crossley, A.;Jones, J. H.;Compton, R. G. *Journal of Materials Chemistry*, **2007**, *17*, 2616–2626.
(49) García-Casal, M. N.;Layrisse, M. *Archivos latinoamericanos de nutricion*, **2001**, *51*, 35–36.
(50) Bard, A. J.;Faulkner, L. R.;Leddy, J.;Zoski, C. G. *Electrochemical methods: fundamentals and applications*;Wiley New York, **1980**.
(51) Srinivasan, S.;Duic, L.;Ramasamy, N.;Sawyer, P. N.;Stoner, G. E. *Berichte der Bunsengesellschaft für physikalische Chemie*, **1973**, *77*, 798–804.
(52) Joseph, M. B.;Bitziou, E.;Read, T. L.;Meng, L.;Palmer, N. L.;Mollart, T. P.;Newton, M. E.;Macpherson, J. V. *Anal. Chem.*, **2014**, *86*, 5238–5244.

Chapter 7

Boron doped diamond pH electrode optimisation: Solving the unbuffered problem

Thus far, a novel boron doped diamond (BDD) pH electrode was shown to operate across a large pH range (pH 2–12) in buffered aqueous solutions under a Nernstian 2 $H^+/2e^-$ regime. However, one of the main issues with quinone-based technologies is deviation from the well-defined Nernstian response when moving to unbuffered aqueous solutions. This chapter explores the BDD pH response, finding that in unbuffered media, the BDD pH sensor exhibits a pH insensitive mid-region (approximately pH 4–10). To mitigate this, two interdependent avenues are explored: (1) lowering the quinone surface coverage and (2) changing the mass transport to the electrode surface. This is achieved by manipulation of the laser micromachining parameters to create lower quinone surface coverages (Γ) and reduced pit sizes. It is found that by reducing the laser fluence (the energy delivered per area, J cm^{-2}) Γ can be decreased by approximately an order of magnitude compared to the original laser machining parameters used in **Chapter 6**. The resulting sensor operates under a Nernstian $2H^+$, $2e^-$ (linear) regime across the pH range 1–13. A major contributing factor appears to be control over the number of quinone groups on the electrode surface; imperfect sealing of the laser ablated BDD sidewalls results in an uncontrolled increase in Γ which results in deviation in the unbuffered pH dependence with measured electrode voltage. We therefore advocate the use of co-planar all-diamond devices for the production of reproducible BDD pH sensors capable of operating across the whole pH range in both buffered and unbuffered solutions.

7.1 Introduction

It is widely reported in literature that in aqueous unbuffered solutions, quinone-based electrochemical pH sensors no longer show a Nernstian response across the entire pH range. Precise understanding of why this occurs is subject to debate within the scientific community.[1,2] It is postulated that this deviation is due to the fact that by making the electrochemical measurement, the local pH in proximity to the electrode surface (interfacial pH) is perturbed due to the consumption or generation of H^+ during reduction or oxidation respectively, resulting in the measured pH being different to that of the bulk solution.[3] It has been shown previously that the interfacial pH can change by up to 5–6 pH units compared to the bulk and that for solution-phase quinone groups in neutral solution.[4]

As a consequence of perturbing the local pH, the mechanism of reduction / oxidation is also thought to switch.[1] It has been shown that as the system starts to run out of available protons, more evident when the pH is increased, then in unbuffered solution, two peaks are observed in the response. One for the original $2H^+$, $2e^-$ pathway and a second which represents a proton independent route i.e. $2e^-$ only.[5,6] As the pH increases further and proton depletion affects become more prominent, then the process switches to one peak only which reflects only the $2e^-$ route. Although it is also important to take into account the p*K*a's of the quinone molecule.[5] The product of this reaction i.e. Q_2^-, is thought to exist in a variety of states depending on its basicity and hydrogen bonding interaction with water ($Q_2^-(H_2O)_{2n}$).[1] Thus the conclusion was made that quinone moieties will only respond similarly to that of buffered solution if $[H^+] > [Q]$.[1] To date, this still presents a major scientific challenge for quinone-based pH sensing technologies as most pH measurements are made in unbuffered media.

Much of the investigation into the unbuffered quinone problem is performed with quinone species in solution, with some limited studies tethering quinone moieties to electrode surfaces.[7] The main difference between working with the molecule in free solution and on the electrode surface is the pK_a associated with surface bound species are likely to be greater than in free solution.[4] This is attributed to changes in the local environment when the quinone is tethered to an electrode surface, where entropic changes can be significantly different to the bulk solution.[4,8] It has also been found that the hydrophobicity/hydrophilicity of the electrode surface may also play a role, affecting solvent molecules in close proximity to the electrode surface.[9]

Recent work by Dai *et al.*, has shown that a linear, Nernstian response can be obtained in unbuffered solution if the quinone group used for surface functionalisation is a dihydroxyanthraquinone derivative, designed specifically to facilitate inter- and intra-hydrogen bonding between water and the quinone moiety, leaving the interfacial pH unperturbed.[10] However, not only is the synthesis of the quinone complex, the dihydroxyanthraquinone also suffers from nucleophilic attack at high pH due to hydroxide ions.[10] Furthermore, the solubility of the quinone moieties at high pH also leads to a reduction in peak current over time, meaning the sensors only have a finite lifetime.[11] To inhibit nucleophilic attack and address the solubility issues, recent work has coated alizarin (a dihydroxyanthraquinone) with a Nafion membrane, improving the stability of the electrode.[11] However, this adds to the steps required to produce the device. It is also known that the proton conductivity of the Nafion film varies strongly with both temperature and humidity, potentially inadvertently effecting the accuracy of the sensor.[12]

In this chapter, the pH response of the original design BDD pH sensor (**Chapter 6**) is explored in unbuffered solution. In buffered solution, this sensor shows a $2H^+$, $2e^-$ response over the pH range 1–13, suggesting a high pK_{a1} (see **Chapter 1.7.2.4** for more detailed discussion of p*K*a). In unbuffered solution, the sensor deviates from a Nernstian response in the pH range ~4–10, with a linear response shown at pH values < pH 4 and > pH 10. To mitigate this, two interdependent avenues are explored: (1) lowering the Γ and (2) changing the mass transport to the electrode surface, achieved by manipulation of the laser micromachining parameters to create lower quinone surface coverages and reduced pit sizes. Note, this work is still ongoing.

7.2 Experimental

7.2.1 Electrode Fabrication and Pretreatment

1 mm BDD glass sealed electrodes were fabricated as discussed in detail in **Chapter 2.3.1**. A 34 ns, 355 nm YAG laser was used to create circular pits by manipulation of a computer numerical control stage holding the sample, relative to a fixed beam changing the fluence (F, energy delivered per area J cm^{-2}) as required. Three different pH arrays were introduced into the BDD electrodes, denoted as Generation 1 (used in **Chapter 6**), Generation 2 (a microarray) and Generation 3 (the Generation 1 pH pattern but recorded using a reduced F, which also results in shallower pits but a similar diameter).

For Generation 1 and 3, the hexagonal pattern constituted sixty-one pits (see **Chapter 6.3.2.1** for optical image), spaced 100 µm centre-centre and ~45 µm in diameter machined. For Generation 1 (F = 870 J cm^{-2}) this resulted in pits ~25 µm deep, compared to ~10 µm deep for Generation 3 (F = 14.5 J cm^{-2}). Generation 2 constituted

of nineteen pits, also machined in a hexagonal array, spaced 200 µm centre-centre, ~10 µm in diameter and ~5 µm deep. The laser array patterns are illustrated in **Figure 7.1** and the parameters for each Generation are summarised in **Table 7.1.**

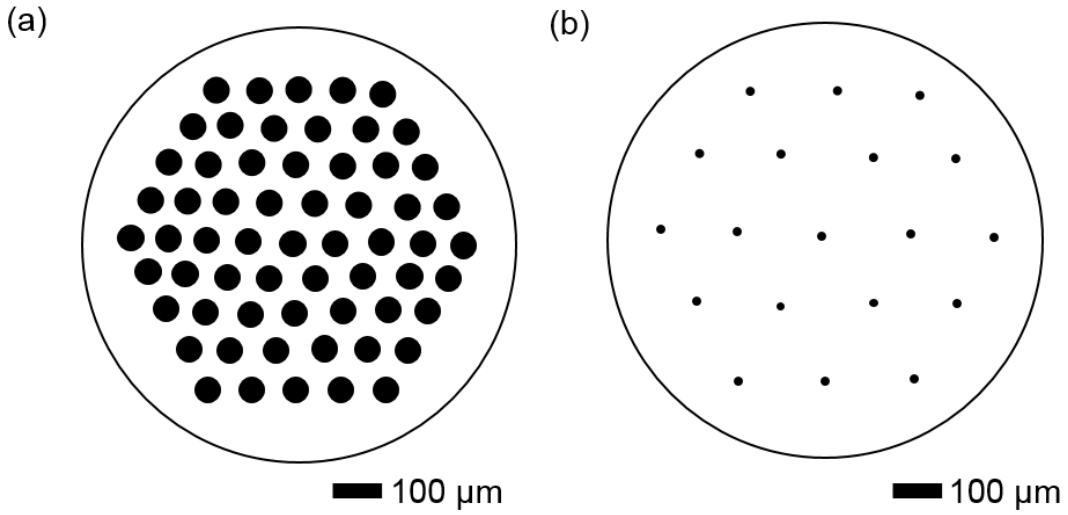

Figure 7.1: *Schematic of the laser array machined into 1mm BDD electrodes for (a) Generation 1 and Generation 3 and (b) Generation 2.*

Table 7.1: *Summary of key laser micromachining parameters for Generation 1–3.*

Generation	F/ J cm^{-2}	Pulse overlap	Pit size / µm	Interferometric laser ablated area / cm^2
1	870	0.5	50 (depth) × 45 (wide)	9.92×10^{-3}
2	14.5	0	5 (depth) × 10 (wide)	2.12×10^{-5}
3	14.5	0.5	10 (depth) × 45 (wide)	2.74×10^{-3}

It is important to note that Generation 1 and 3 are subject to pulse overlap where each laser pulse crosses over with the previous illustrated in **Figure 7.2**. Note the laser pulse is ~3 µm but the overall pit size made per pulse is ~5 µm diameter due to the heat affected zone (HAZ) discussed in detail in **Chapter 2.5.3**.

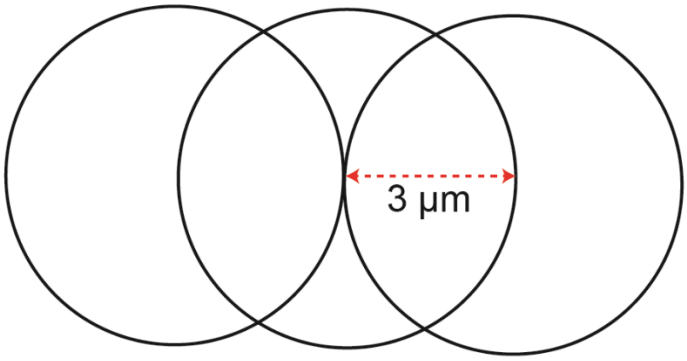

Figure 7.2*: *Illustration of the half pitch overlap utilised to create the pH laser array for Generation 1 and Generation 3 for each laser pulse.

After laser micromachining, in order to "*activate*" the sp^2 carbon to produce the necessary pH sensitive redox active quinone groups and remove loosely bound sp^2 carbon the electrode was first heated at ~200 °C for 15 minutes in concentrated H_2SO_4 (98%) saturated with KNO_3.[13] Anodic polarisation of the laser micromachined BDD electrode was then conducted under constant current conditions (+0.1 mA for 60 s) in 0.1 M room temperature H_2SO_4, as discussed in **Chapter 6.2.1**. For anodic polarization a galvanostat was utilized (Keithley 6220 Precision Current Source). Note, this electrode pretreatment is only required once.[14]

7.2.2 Electrochemical set-up

For the electrochemical measurements a three-electrode configuration was utilized with BDD as the working electrode, a platinum wire as a counter electrode and a saturated calomel electrode (SCE) as the reference electrode. Quinone surface

coverage was calculated using the method described in **Chapter 4**.[15] Square wave voltammetry (SWV) was conducted at a frequency of 150 Hz, amplitude of 200 mV and step potential of 2 mV. For buffered solutions Carmody buffers were utilised,[16] and unbuffered solutions were prepared with ultrapure Milli-Q water (Millipore Corp., resistivity 18.2 MΩ cm at 25 °C) with the addition of 0.1 KNO_3 and the pH adjusted with 1 M HNO_3 and 1 M KOH accordingly.

7.2.3 White Light Laser Interferometry (WLI)

WLI images were recorded using a Bruker ContourGT interferometer (Bruker Nano Inc., USA). 3D rendering of interferometry data was performed and the increase in electrode area after laser ablation quantified using Gwyddion 2.41 (Czech Metrology Institute, CZE).

7.3 Results

7.3.1 Unbuffered Response

Initially, the pH response of the BDD pH sensor was investigated across a wide pH range in both buffered and unbuffered solutions, shown in **Figure 7.3**, using SWV.

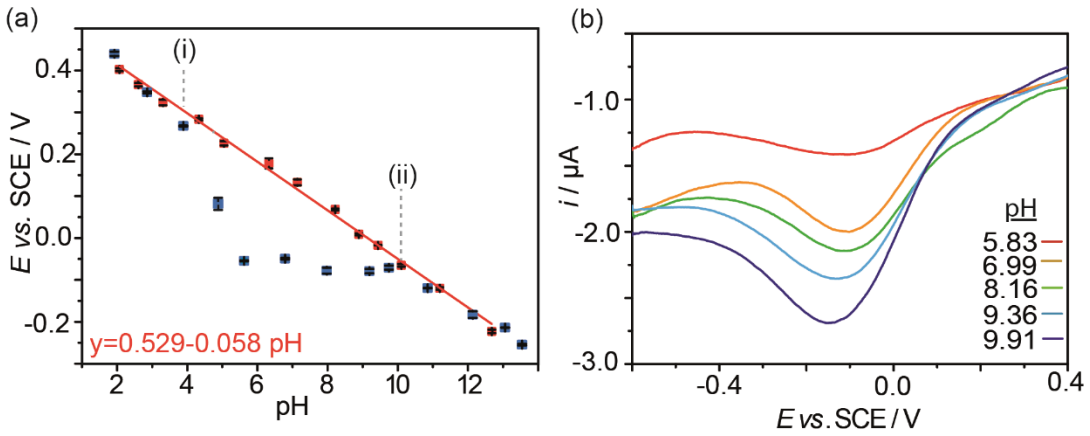

***Figure 7.3**: Glass sealed Generation 1 BDD electrode (a) pH plot showing the buffered (red) and unbuffered (blue) response and (b) the SWV response ((frequency= 150 Hz, step potential = 2 mV, amplitude = 200 mV) for the pH independent mid-region in unbuffered solution shown in (a).*

Note, whilst the BDD pH electrode operates as expected in buffered solution, a pH independent mid-region is observed under unbuffered conditions, with linear pH dependent (59 mV per pH unit) regions observed at pH values ~ < 4 pH and > pH 10. It is considered that the pH independent mid-region is caused by changes to the interfacial pH induced by making the pH measurement (consumption of protons). Interestingly this region occurs around pH 7 (neutral), with the sensor switching back to a 59 mV per pH unit dependence ~ 3 pH units either side of pH 7 (~ pH 4 and pH 10 respectively), shown as (i) and (ii) on **Figure 7.3a**.

Although we are still working towards a comprehensive understanding, one possible reason can be formulated by considering the equilibrium concentrations of H^+ and OH^- that exist in water under neutral pH 7 (1×10^{-7} and 1×10^{-7} mol L^{-1}) and representative acidic and alkaline conditions respectively, (pH 4 = 1×10^{-4} and 1×10^{-10} mol L^{-1}) and (pH 10 = 1×10^{-10} and 1×10^{-4} mol L^{-1}). We postulate that the magnitude of the pH change is more significant in and around neutral pH, as even a small change in H^+ concentration could lead to a large change in interfacial pH. Once points (i) and (ii) are reached, the local pH change is no longer significant compared to the bulk pH and thus has no observable effect. This is supported by the theory that if $[H^+] > [Q]$ a 59 mV per pH unit dependence will be observed, shown in **Figure 7.3a** at a pH ≤ 4.

However, there is very little literature precedent[17] for the sensor regaining a $2H^+$, $2e^-$ proton dependence after deviating; most literature suggests that the quinone response remains insensitive to pH, after switching, for the remainder of the pH scale.[1,2 ,18] We propose that this simply arises due to the very high surface pK_{a1} of our quinone on the BDD surface, which exceeds pH 12. For the vast amount of other studies, especially those in solution, the pK_{a1} and pK_{a2} of the quinone is reached prior to pH 10 (from buffered solution measurements) resulting in a pH independent response after the (ii) deviation point.[1] Therefore it is difficult to say whether in these studies the quinone functionalised electrode is deviating at all pH's when $[Q] > [H^+]$ or it has switched back at higher pH to its expected response based on the p*K*a's of the quinone. We propose our surface functionalised BDD pH sensor a Nernstian response will be observed for either $[H^+] > [Q]$ or $[OH^-] > [Q]$.

Another possibility, discussed by Quan *et al.*, is that the equilibrium position of the quinone reaction is unaffected when the [Q] > H^+ or OH^-, resulting in the pH independent mid-region.[1] At low pH values, where the [H^+] > [Q], the quinone undergoes a $2H^+$, $2e^-$ reaction, resulting in a 59 mV dependence at pH values < pH 4. At the other end of the scale at pH values > pH 10, where the [OH^-] > [Q], due to the basicity of the quinone, the reaction route favoured is such that the main reaction product is QH_2, resulting in a 59 mV dependence, even though proton concentrations are low.[1] This supports the idea that for the BDD pH sensor a Nernstian response will be observed for either [H^+] > [Q] or [OH^-] > [Q], with the switch back on of the pH dependence observable at pH values > pH 10 due to the high pK_{a1} of the quinone that is integrally part of the BDD surface.

There is one study in the literature which shows a similar response to ours by Sato *et al.*[7] where they immobilised a 2-mercaptohydroquinone monolayer onto a gold surface. In buffered solutions the quinone was found to have a pK_{a1} in excess of 12.7. In unbuffered solutions for a surface concentration of 2.8×10^{-10} mol cm^{-2}, they saw a $2H^+$, $2e^-$ response in both the acidic (pH < 5) and alkali regions (pH > 9) but observed deviations from this behaviour in the region 5–9. They did not comment on the response under alkali conditions and attributed the deviation to a local pH change or the possible involvement of $Q^{\bullet -}$ due to the hydrophobic nature of the 2-mercaptohydroquinone.

Interestingly, work by Galdino *et al.* claim that they have successfully fabricated a graphite screen printed pH electrode that operates under a Nernstian $2H^+$, $2e^-$ regime in unbuffered solution. However, they only provide data in unbuffered solutions at the

pH extremes (pH 2.86 and 10.43).[19] Hence if they too have a deviation in the neutral region it will not be picked up with these limited measurements. We thus advocate that in order for researchers to truly show that their quinone-based sensors are operating linearly in unbuffered solution, the neutral region should be probed, with a sufficient number of pH readings.

To mitigate the mid-region effect observed in unbuffered solution, two methods were explored: (1) reducing the number of quinone moieties on the electrode surface and (2) changing the pit size and distribution increase the diffusional flux of protons to and away from the electrode surface.[20] Note, in (1) by decreasing the number of essentially "active sites" the flux per site is also effectively increasing.[21]

7.3.2 Effect of laser parameters on quinone surface coverage

To address (1), the effect of the most critical laser micromachining parameter i.e. laser fluence directly related to laser power, was explored on quinone surface coverage, as shown in **Figure 7.4**. The laser array pattern (sixty-one pits) was kept the same, but the laser power altered. Note, laser power varies from system to system and can decrease with time (for example due to degradation of the laser optics), thus laser power has been converted to fluence (power delivered per area, J cm^{-2}). A range of different F values were explored from just above the experimentally calculated ablation threshold of BDD (~12 J cm^{-2}) to the F used for the original pH laser array (870 J cm^{-2}).

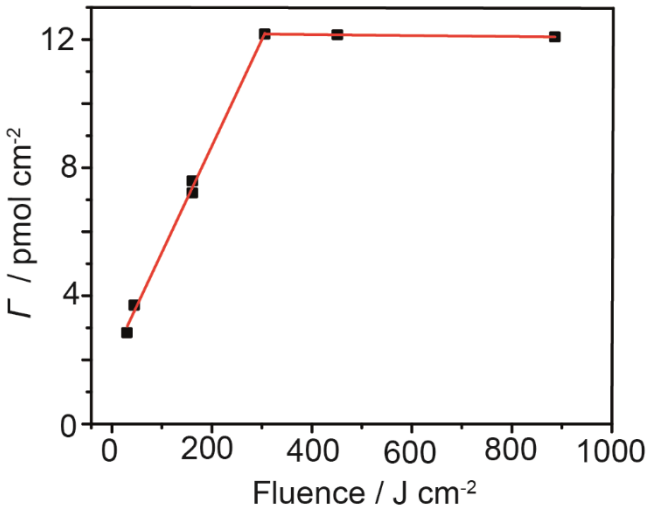

Figure 7.4*: *Laser fluence vs Γ (collected in pH 2 solution at 0.1 V s^{-1}).

For these measurements it is important to note that Γ has been calculated by considering only the area machined and not the area of the total electrode; we assume with the quinone surface coverage of the high quality BDD employed is minimal in the non-machined areas ($1.8 \times 10^{-16} \pm 1.6 \times 10^{-17}$ mol cm^{-2}).[15] A linear dependence between $_F$ and Γ was observed from 14.5–300 J cm^{-2}. Increasing $_F$ beyond ~ 300 J cm^{-2} was found to have no significant effect on further increasing the number of quinones on the electrode surface. Note, the maximum Γ (~ 1.21×10^{-11} mol cm^{-2}) reached using laser ablation is less than the Γ reported on edge plane pyrolytic graphite (5.9 × 10^{-11} mol cm^{-2}).[22] This suggests that the surface of the electrode is not fully converted to sp^2 carbon. Note, for BDD the high temperature acid treatment (200 °C in concentrated (98%) H_2SO_4) and subsequent anodic polarisation likely plays a factor in this, acting to remove any loosely bound sp^2 carbon at the electrode surface.[14]

Given that the $_F$ used for the Generation 1 design BDD pH electrode (Chapter 6) is at the far end of the $_F$ scale (870 J cm^{-2}) it is clear that by decreasing $_F$, Γ can be reduced by nearly an order of magnitude. The degree of control over sp^2 carbon incorporation

highlights the advantage of using laser ablation as a functionalisation route. It should also be noted that very small Γ can be obtained using this procedure (2.98×10^{-12} to 1.2×10^{-11} mol cm^{-2}). This is compared to standard electrode functionalisation routes, such as the gold-thiol self-assembled monolayer methods and alumina polishing of carbon surfaces where typical surface coverages are in the range 10^{-10}– 10^{-9} mol cm^{-2} and even higher due to the fact that multilayers can form.[4,23]

7.3.3 Laser array redesign

Having established that changing $_F$ results in a change in Γ, the pH laser array was redesigned. It should be noted that by reducing $_F$ the depth of the pits laser micromachined is also effected (the less energy per area, the less material removed). Thus by changing the laser design the diffusion profile of H^+ towards and away from the pits is also altered. Fortunately, this combination is harmonious, resulting in both a reduced quinone surface coverage and increased H^+ diffusion.

Figure 7.5a, shows the original pH laser array (Generation 1) along with two additional designs: Generation 2, a microarray and Generation 3, which utilises the same inter-pit spacing as Generation 1, but is laser micromachined at a reduced fluence (14.5 J cm^{-2}). Generation 2 is also laser micromachined at this reduced fluence 14.5 J cm^{-2} but constitutes one laser pulse per pit to create a 10 µm wide and 5 µm deep feature. The WLI data for a pit in each Generation is shown in **Figure 7.5b**.

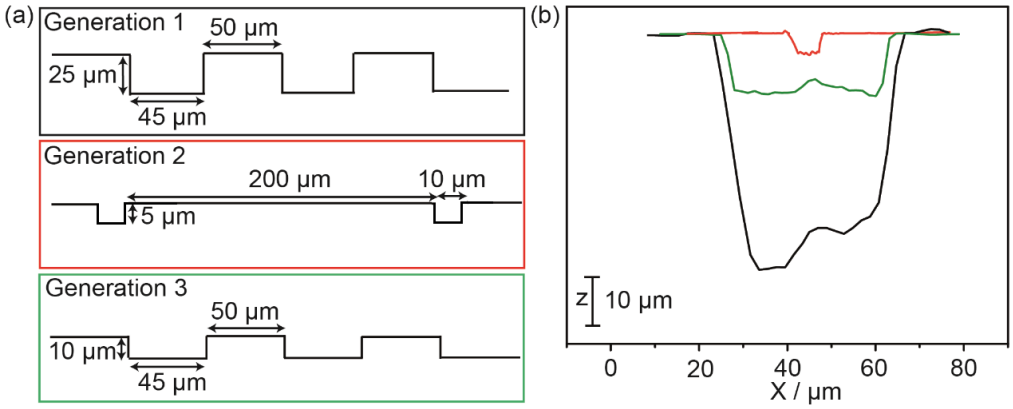

Figure 7.5**:** *(a) schematic of Generation 1,2 and 3 laser micromachining designs and (b) Representative WLI data of a pit for each Generation.*

To comparatively assess the sp^2 carbon introduced into the surface of the BDD electrodes for the three Generations, Γ was assessed (n=3), using the method established in **Chapter 4,** except as stated above Γ is calculated using the WLI area of the laser micromachined area rather than the whole electrode area. For this measurement the Generation 1 and 3 electrodes were in an all diamond format,[24] whereas the Generation 2 electrode was glass sealed. This is where the BDD is encased in an insulating diamond surround, [24] eliminating any quinone contribution from the laser ablated side walls that often arises on the glass sealed counterparts (see **Chapter 2.3.2** for fabrication information).

Γ was found to be $1.20 \times 10^{-11} \pm 1.2 \times 10^{-15}$(Generation 1), $2.86 \times 10^{-12} \pm 1.5 \times 10^{-15}$ (Generation 2) and $2.98 \times 10^{-12} \pm 1.3 \times 10^{-15}$ mol cm^{-2} (Generation 3). Note, in Chapter 6 the Generation 1 electrode employed was glass sealed, with the Γ found for Generation 1 (all-diamond) is significantly smaller than previously reported in **Chapter 6 (**6.7×10^{-9} mol cm^{-2}, converted to Γ only for the laser ablated area). This

indicates that the side walls of the BDD round were significantly exposed in **Chapter 6**.

There is only a small decrease in Γ for the Generation 2 electrode (glass sealed) compared to the Generation 3 electrode (all diamond), even though the machined pattern area is much smaller for Generation 2 than Generation 3 (2.12×10^{-5} cm^2 versus 2.74×10^{-3} cm^2 respectively). We attribute this to the co-planar arrangement of BDD and insulating diamond in the all diamond BDD electrode. In contrast with the glass sealed electrode due to the fabrication approach, BDD protrudes from the glass capillary exposing the laser ablated sidewalls, which will also contribute to the Γ observed. The effect of sidewall exposure on the pH response is discussed in detail *vide infra.*

7.3.4 Generation 2 - Microarray

The pH response for Generation 2 (glass sealed) was explored in both buffered and unbuffered solution (**Figure 7.6**) using SWV across the pH range 2–12.

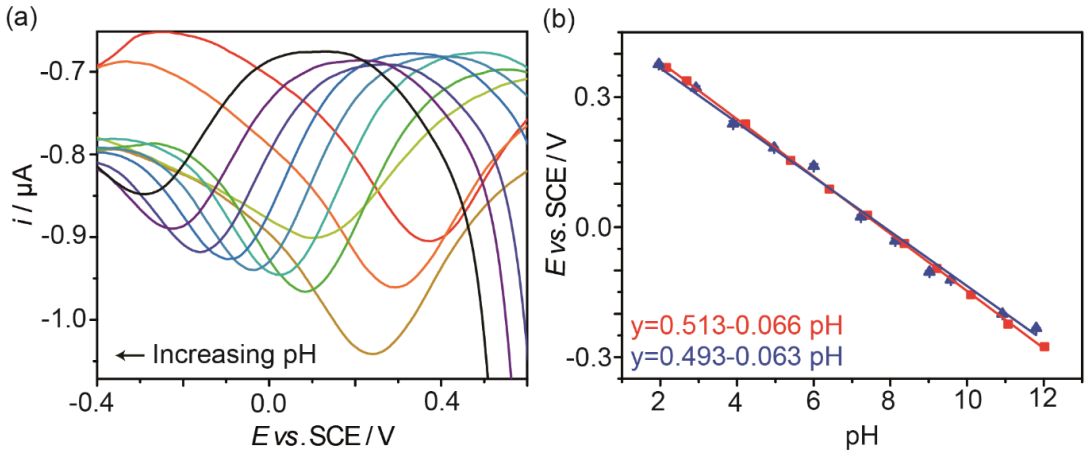

Figure 7.6*: *Glass sealed Generation 2 BDD electrode (a) Quinone reduction peaks using SWV (frequency= 150 Hz, step potential = 2 mV, amplitude = 200 mV) across the pH range of 2–12 in unbuffered solution and subsequent calibration graphs (b) both buffered (blue) and unbuffered (red) solutions exhibiting an R^2 value of 0.999 and 0.998 respectively.

It was found that the Generation 2 BDD pH electrode shows an excellent linear response (R^2 = 0.999 for each electrode) across the analysed pH range 2–12 and exhibits a similar response in unbuffered to that of buffered solutions. Note, both the buffered and unbuffered responses show a slight super-Nernstian response (66 mV and 63 mV per pH unit respectively at 298 K).

The current magnitudes observed are smaller than those observed for the Generation 1 electrode as is expected given the reduced number of quinone moieties on the electrode surface. Note, given the microarray design, this electrode may be useful for assessing pH under high flow conditions due to the likely increased flux to the sp^2 sites

compared to that of Generation 1. This highlights that by changing the laser ablation pattern the pH BDD sensor could be tuned for different applications.

7.3.5 Generation 3

The response of a glass sealed Generation 3 BDD electrode was also explored (**Figure 7.7**) in both unbuffered and buffered conditions.

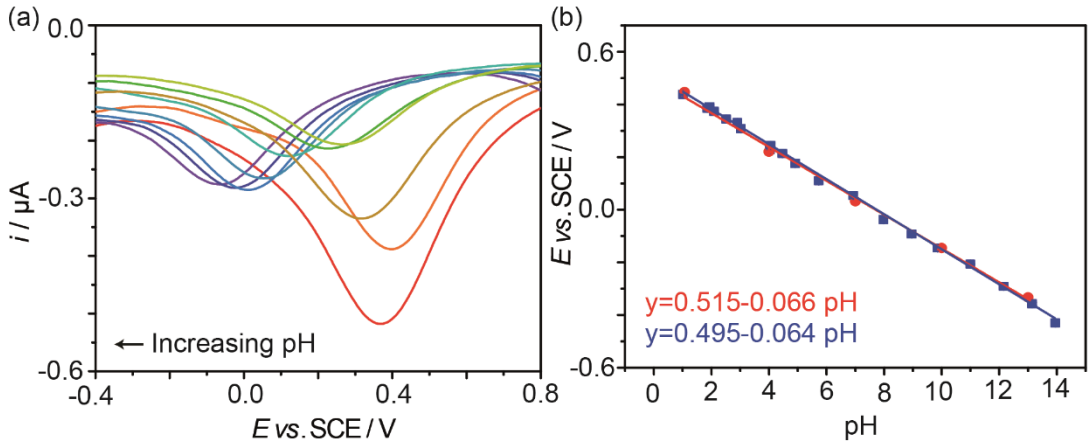

***Figure 7.7**: Glass sealed Generation 3 (a) Quinone reduction peaks using SWV (frequency= 150 Hz, step potential = 2 mV, amplitude = 200 mV) across the pH range of 2–12 in unbuffered solution and subsequent calibration graphs (b) both buffered (blue) and unbuffered (red) solutions exhibiting an R^2 value of 0.999 and 0.999 respectively.*

Similarly to the Generation 2 electrode, the sensor was found to operate under a slightly super-Nernstian regime across the whole pH range and does not suffer from a pH independent mid-region. Given that the current signal is increased for Generation 3 compared to Generation 2, as expected given the higher surface coverage of quinone moieties, further studies were conducted using the Generation 3 electrode.

7.3.5.1 Glass sealed versus all diamond electrode

For Generation 3 electrodes sealed in glass, it was noted that inter-electrode variability was poor, with the pH independent mid-region re-emerging if the BDD protruded from the glass seal or if the seal became damaged. **Figure 7.8** shows data recorded with two different Generation 3 glass sealed BDD electrodes which protrude from the glass sheath by different amounts (assessed by optical microscopy) ~12 and 45 µm (red triangles and blue squares respectively).

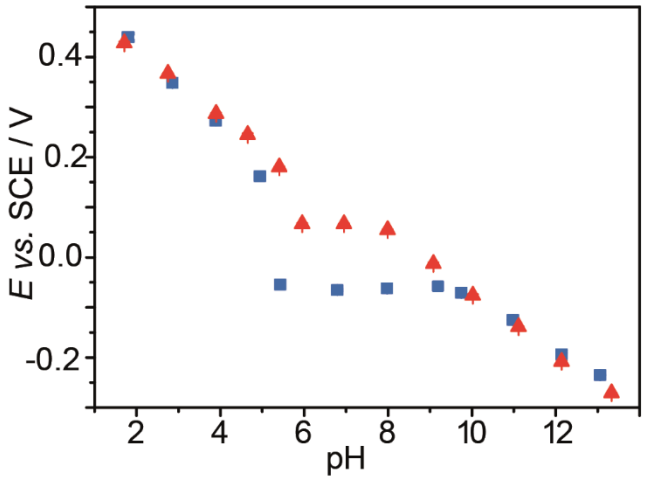

Figure 7.8: Plot of peak potential (E_{pc}) vs pH for an electrode showing slight exposure of the sidewall (~12 µm red) and more pronounced exposure (~45 µm, blue).

Figure 7.8 shows that as more of the side wall is exposed, the range of the pH independent mid-region expands from ~ pH 6–8 to ~ pH 4.5–9.5. Note, the sidewall is ablated using a higher $_F$ ~ 1200 J cm^{-2} in order to cut the 1 mm diameter BDD from the ~470 µm thick BDD wafer. The cutting angle also means that the resulting sidewall of the BDD round is exposed parallel to the laser beam rather than perpendicular (the latter is used for all generation patterns).

In order to understand how this laser cutting process influences Γ for the BDD, a piece of BDD was appropriately orientated in the laser micromachiner so that the top surface would be glanced with the laser beam (shown schematically in **Figure 7.9**), mimicking the parallel exposure of the sidewall. Laser ablation was undertaken to generate a larger sidewall area that could easily be handled.

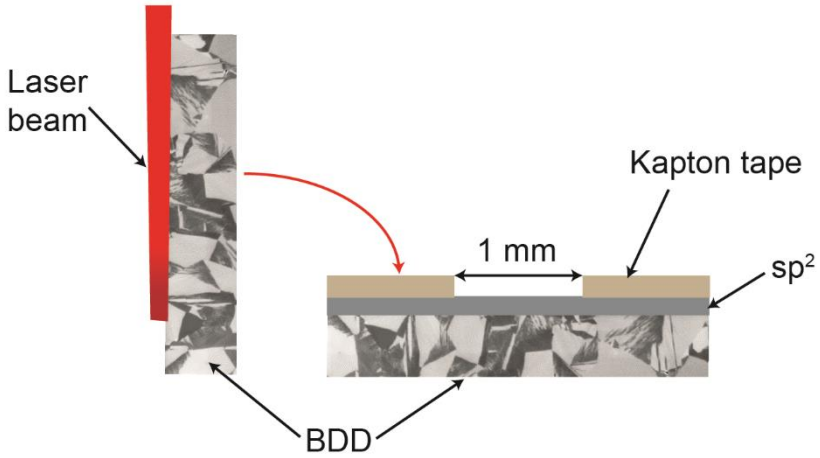

***Figure 7.9**: Illustration of the side glancing experiment where the BDD is positioned parallel with the laser beam to laser ablate surface. The BDD is then rotated and electrochemical analysis performed using 1 mm Kapton tape mask.*[15]

Γ was calculated using the method outlined in **Chapter 4** (utilising only the machined electrode area) and found to be 1.78×10^{-12} mol cm^{-2} $\pm$ 5.3×10^{-15} mol cm^{-2}. This is slightly less than that found for Generation 3 ($2.98 \times 10^{-12} \pm 1.3 \times 10^{-15}$ mol cm^{-2}; all diamond) despite the higher $_F$, indicating that the parallel lasering regime may be different to perpendicular micromachining with regards the relationship between $_F$ and Γ. The role of the exposed sidewall and its effect on the E versus pH response is clearly one that will warrant further work. Exposing the sidewall exposes more quinone molecules to solution in a ring-like geometry. However, whether the response is simply due to the increased number of molecules over the entire electrode area or related to the geometrical arrangement of the exposed molecules[25] is still not fully understood.

Unfortunately at the time of data collection Γ measurements were not collected for the electrodes shown in **Figure 7.8**. Therefore, further work is needed to establish the exact relationship between the deviation region in the pH-potential plot, Γ and geometry.

7.3.6 All diamond pH sensor

To prevent sidewall exposure, movement to all-diamond devices[24] (fabrication discussed in detail in **Chapter 2.3.3**) was conducted. An example of the exposed BDD sidewall is shown in **Figure 7.10a**, alongside an optical image of an all-diamond device where BDD is surrounded by insulating, intrinsic diamond (shown in **Figure 7.10b**).

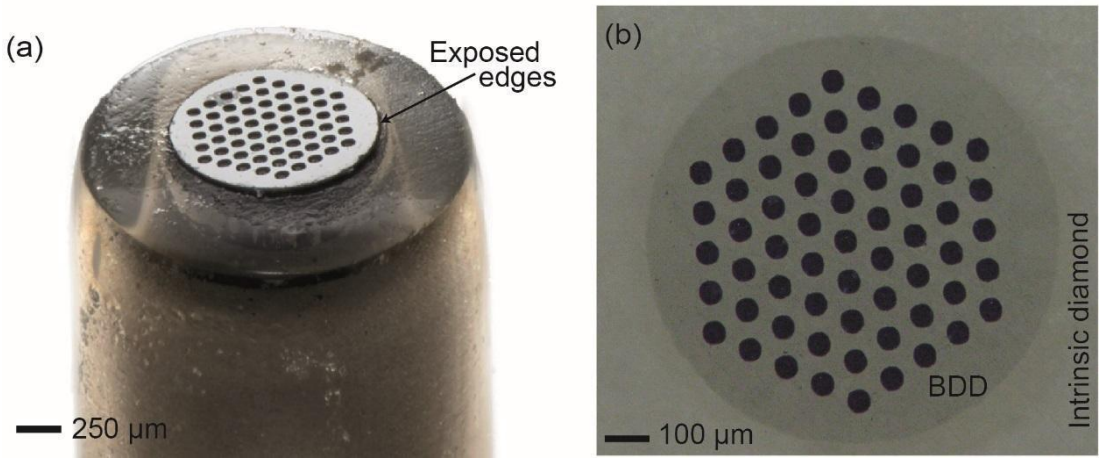

Figure 7.10: *(a) Glass sealed BDD pH electrode showing the protruding BDD round and the exposed laser ablated edge and (b) an optical image showing a coplanar all-diamond pH device; a BDD 1 mm electrode surrounded by insulating, intrinsic diamond.*

Given that the edges appear to play a role in the unbuffered response, both Generation 1 and Generation 3 were translated to all-diamond devices, with the buffered and unbuffered pH responses shown in **Figure 7.11**.

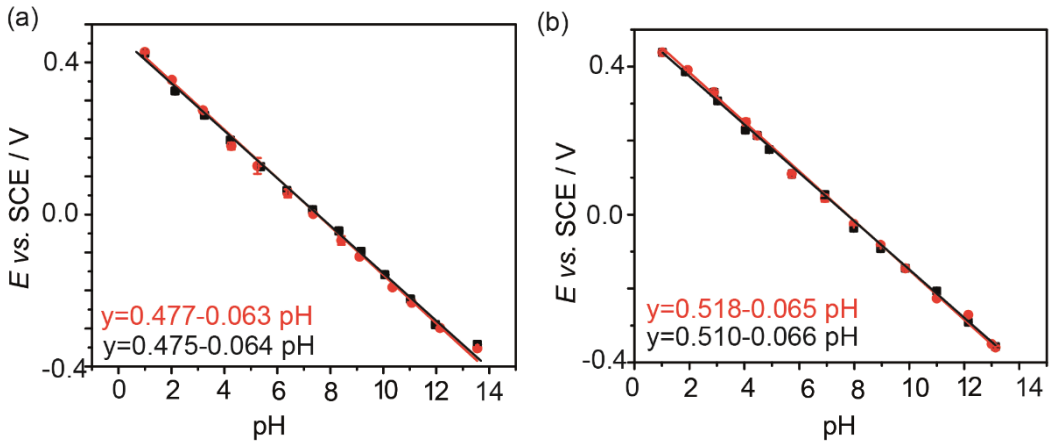

Figure 7.11*: *Comparison of the buffered response for Generation 1 (a) and Generation 3 (b), overlaid with the response for each in buffered and unbuffered solutions (red and black respectively).

Interestingly, both Generations 1 and 3 show a Nernstian response across the pH range in the all-diamond format, following their buffered counterparts. This supports the finding that sidewall exposure is a significant contributor to deviation in unbuffered solutions, increasing the number of quinone groups and thus the consumption of protons. Note, for pH 13.5 (Generation 1, **Figure 7.11a**), slight deviation is observed indicating that pK_{a1} of the quinone is around pH 13, and that there may be a slight difference in the pK_{a1} between Generation 1 and Generation 3.

7.4 Conclusion

This chapter demonstrates the successful fabrication of a voltammetric BDD pH sensor that operates under a Nernstian ($2H^+/2e^-$) regime across a large dynamic pH range (1–13) in both buffered and unbuffered solutions. This overcomes issues with the original BDD pH sensor described in **Chapter 6**, which shows a pH insensitive neutral region in unbuffered solutions. Fabrication of a fully functional BDD pH microarray is also demonstrated which may be useful for certain applications including high flow conditions.

We show that for the original BDD pH array, a pH independent region ranging from ~ pH 4–10 is observed caused by the consumption of protons during the 2 $H^+/2e^-$ quinone reduction reaction. At the pH extremes < pH 4 and > pH 10, a Nernstian response is observed. This is attributed to the local pH change being more effective at neutral pH where the concentrations of H^+ and OH^- are equivalent. We therefore extend work by Quan *et al.*,[1] stating that not only will a Nernstian response be observed for either $[H^+] > [Q]$ but also for $[OH^-] > [Q]$. We postulate that many studies do not observe the regaining of a Nernstian response > pH 10 due to reaching pK_{a2} of their quinone species prior to pH 10. We therefore advocate that future researchers must demonstrate their quinone based technology operating in the neutral unbuffered region – where deviation from a Nernstian regime occurs.

Both improving mass transport and reducing the Γ was explored by simple manipulation of laser parameters. It was found that by reducing the $_F$ smaller pit sizes (5 µm) could be achieved and that Γ can be altered by nearly an order of magnitude. Applying these conditions to the BDD pH sensor resulted in a linear pH response in

unbuffered solutions. Unfortunately, it was found that if the glass seal was damaged, or the electrode protruded, despite the reduction in both pit size and Γ, a deviation in unbuffered solution was still observed. It can therefore be concluded that the BDD sidewall exposure plays a significant role in the response observed, contributing a large number of quinones and resulting in a significant local pH change. Furthermore, it is shown that the more sidewall is exposed, the larger the pH insensitive region. Translation of the BDD pH sensors to all-diamond devices was thus conducted, resulting in reproducible BDD pH sensor that can operate in both buffered and unbuffered solutions.

Although moving towards an all-diamond format has resulted in the production of a sensor capable of operating in unbuffered solution, a more definitive study must now be conducted to form a comprehensive understanding.

7.5 References

(1) Quan, M.;Sanchez, D.;Wasylkiw, M. F.;Smith, D. K. *J. Am. Chem. Soc.*, **2007**, *129*, 12847–12856.
(2) Guin, P. S.;Das, S.;Mandal, P. C. *International Journal of Electrochemistry*, **2011**, *1*, 22.
(3) Kim, R. S.;Chung, T. D. *Bulletin of the Korean Chemical Society*, **2014**, *35*, 3143–3155.
(4) Batchelor-McAuley, C.;Kozub, B. R.;Menshykau, D.;Compton, R. G. *The Journal of Physical Chemistry C*, **2011**, *115*, 714-718.
(5) Chambers, J. Q. *The Quinonoid Compounds (1988)*; John Wiley & Sons, Inc. 2010.
(6) Forster, R. J.;O'Kelly, J. P. *J. Electroanal. Chem.*, **2001**, *498*, 127–135.
(7) Sato, Y.;Fujita, M.;Mizutani, F.;Uosaki, K. *J. Electroanal. Chem.*, **1996**, *409*, 145–154.
(8) Abiman, P.;Wildgoose, G. G.;Crossley, A.;Jones, J. H.;Compton, R. G. *Chemistry – A European Journal*, **2007**, *13*, 9663–9667.
(9) Masheter, A. T.;Abiman, P.;Wildgoose, G. G.;Wong, E.;Xiao, L.;Rees, N. V.;Taylor, R.;Attard, G. A.;Baron, R.;Crossley, A.;Jones, J. H.;Compton, R. G. *Journal of Materials Chemistry*, **2007**, *17*, 2616–2626.
(10) Dai, C.;Crawford, L. P.;Song, P.;Fisher, A. C.;Lawrence, N. S. *RSC Advances*, **2015**, *5*, 104048–104053.
(11) Dai, C.;Song, P.;Wadhawan, J. D.;Fisher, A. C.;Lawrence, N. S. *Electroanalysis*, **2015**, *27*, 917–923.
(12) Sone, Y.;Ekdunge, P.;Simonsson, D. *J. Electrochem. Soc.*, **1996**, *143*, 1254–1259.
(13) Hutton, L.;Newton, M. E.;Unwin, P. R.;Macpherson, J. V. *Anal. Chem.*, **2009**, *81*, 1023–1032.
(14) Ayres, Z. J.;Borrill, A. J.;Newland, J. C.;Newton, M. E.;Macpherson, J. V. *Anal. Chem.*, **2016**, *88*, 974–980.
(15) Ayres, Z. J.;Cobb, S. J.;Newton, M. E.;Macpherson, J. V. *Electrochem. Commun.*, **2016**, *72*, 59–63.
(16) Carmody, W. R. *Journal of Chemical Education*, **1961**, *38*, 559.
(17) Sato, Y.;Fujita, M.;Mizutani, F.;Uosaki, K. *J. Electroanal. Chem.*, **1996**, *409*, 145-154.
(18) Bailey, S. I.;Ritchie, I. M. *Electrochim. Acta.*, **1985**, *30*, 3–12.
(19) Galdino, F. E.;Smith, J. P.;Kwamou, S. I.;Kampouris, D. K.;Iniesta, J.;Smith, G. C.;Bonacin, J. A.;Banks, C. E. *Anal. Chem.*, **2015**, *87*, 11666–11672.
(20) Bard, A. J.;Faulkner, L. R. *Electrochemical methods: fundamentals and applications*;Wiley New York, **1980**. 626–634.
(21) Amatore, C.;Savéant, J. M.;Tessier, D. *Journal of Electroanalytical Chemistry and Interfacial Electrochemistry*, **1983**, *147*, 39–51.
(22) Lu, M.;Compton, R. G. *Analyst*, **2014**, *139*, 2397–2403.
(23) McDermott, M. T.;McCreery, R. L. *Langmuir*, **1994**, *10*, 4307–4314.
(24) Joseph, M. B.;Bitziou, E.;Read, T. L.;Meng, L.;Palmer, N. L.;Mollart, T. P.;Newton, M. E.;Macpherson, J. V. *Anal. Chem.*, **2014**, *86*, 5238–5244.
(25) Read, T. L.;Bitziou, E.;Joseph, M. B.;Macpherson, J. V. *Anal. Chem.*, **2014**, *86*, 367–371.

Chapter 8

Conclusions and future work

8.1 Overview

The use of boron doped diamond (BDD) as an electrode material has increased rapidly in recent years due to the material having many of the useful properties of diamond as well as exhibiting advantageous electrochemical properties, including a wide solvent window (SW), low background (capacitive) currents and higher resistance to fouling compared to other traditional electrode surfaces (discussed in detail in **Chapter 1**).[1] In this thesis, these advantageous properties are exploited for a range of electroanalytical applications.

Initial studies explore the quantitative detection of the heavy metal palladium (in Pd^{2+} form in solution) in the presence of pharmaceutically active compounds, using the newly developed technique Electrochemical X-ray Fluorescence (EC-XRF).[2] For context, a main challenge often encountered when conducting electroanalysis of heavy metals is that stripping peak assignment to individual metals is ambiguous.[3] Furthermore, conventional XRF analysis is not typically capable of reaching the parts-per-billion (ppb) detection limits required.[4] By utilising EC-XRF, where electrochemical pre-concentration of metals onto an electrode surface is coupled with XRF analysis, these issues are mitigated, with XRF providing unique chemical identification and electrochemical preconcentration improving the detection limits of energy dispersive XRF by over four orders of magnitude.[5]

Unfortunately, in previous studies EC-XRF run times have been over 1 hour in order to achieve ppb detection limits thus **Chapter 3** explores time optimisation of EC-XRF towards the application of interest. By considering the intended application — detection of Pd^{2+} residues in pharmaceutical products — as well as the required detection limits stipulated by international pharmacopeia guidelines, EC-XRF analysis times are reduced to 300 s. Quantification of [Pd^{2+}] is also demonstrated in the presence of acetaminophen (ACM), L-ascorbic acid, caffeine and riboflavin showing that Pd^{2+} detection can be conducted even in the presence of excess redox active compounds, often present in a wide range of pharmaceutical products and foodstuffs.[2] Furthermore, given that [Pd^{2+}] scales linearly with electrochemical deposition time, to improve detection limits the length of deposition can simply be extended, allowing EC-XRF to be tuned to particular applications. It is also noted that EC-XRF not only quantifies the amount of Pd^{2+} present but also has the potential to recover it from solution (by conversion to metallic Pd), making EC-XRF a powerful analytical technique.

Thorough characterisation of the material surface properties of BDD is important in electrochemistry for electroanalytical application as sp^2 carbon can impact the results observed. For example, high sp^2 content leads to increased capacitance, reduced SWs and increased electrocatalytic activity. For this reason, **Chapter 4** explores a new characterisation method for the comparative assessment of BDD quality (in terms of sp^2 content), measuring the surface coverage of quinone groups(Γ) associated with sp^2 carbon presence.[6] It is found that Γ may be a more effective way of assessing sp^2 content compared to Raman spectroscopy as the technique is truly surface sensitive. This method was used to assess the sp^2 carbon content of a variety of different BDD

electrodes including those with increasing amounts of sp^2 carbon added in from laser micromachining and those grown under different chemical vapour deposition (CVD) conditions.

Chapter 5 goes on to utilise this technique to characterise BDD thin film electrodes (grown under 1% and 5% CH_4 conditions) in an overmoded i.e. multi-mode microwave CVD reactor at low pressure (40 Torr) — often utilised by researchers and commercial suppliers alike to reduce production costs.[7,8,9] Significant variability in the electrochemical response (Γ, SW and capacitance) across the wafers are observed with some areas exhibiting electrochemical signatures indicative of high quality, minimal sp^2 content BDD, with others showing regions comprising significant sp^2 carbon. These changes in sp^2 content across the BDD films are attributed to spatial variations in parameters such as temperature, methane and atomic hydrogen concentrations during growth[10] due to the operation of the multi-moded CVD system at low pressure. Whilst Raman spectroscopy is often used as a primary characterisation method for BDD, Raman was unable to identify these variations for the 1% CH_4 wafer. This highlights the importance of using surface sensitive characterisation methods such as Γ to assess BDD films before use in electrochemical measurements.

In **Chapter 6**, a novel BDD based pH electrode is demonstrated which overcomes several limitations of the commercial glass pH electrode including fragility and alkali errors.[11] This is achieved by the introduction of pH sensitive quinone groups into the BDD electrode surface via laser ablation. The BDD pH sensor is demonstrated to operate under a Nernstian (59 mV/pH unit) regime over a wide pH range in buffered aqueous solution (2–12) and can accurately determine solution pH, even in the

presence of heavy metals such as Pb^{2+}, Cd^{2+} and Cu^{2+}. Unfortunately one of the main limitations of quinone technology is that deviation from the well-defined Nernstian response in unbuffered solutions, due to perturbation of the local pH caused by making the measurement. **Chapter 7** therefore explores optimisation of the BDD pH sensor for operation in both buffered and unbuffered solutions. Redesign of the pH array is explored, reducing the size of the pits as well as the effect of laser fluence (energy delivered per area, J cm^{-2}) in order to change the mass transport of H^+ to/from the electrode surface and manipulate Γ. By altering the laser fluence, and consequently reducing the number of quinones on the electrode surface as well as moving to an all-diamond format, a BDD pH electrode capable of operating in a Nernstian manner across a large pH range (1–13) in both buffered and unbuffered media was successfully fabricated.

8.2 Future Directions

Several different BDD based technologies have been explored in this thesis providing much scope for further work. It is considered that the optimisation of EC-XRF in Chapter 3 will provide foundation for future work using the technique, particularly ensuring fast analysis times (≤ 300 s). Future work could also involve using the technique on-line in a pharmaceutical process to quantitatively assess the palladium content as well as recover it.

Furthermore, utilising quinone surface coverage for the comparative assessment of BDD has the potential to become a steadfast BDD characterisation method in the electrochemical community. The BDD pH sensor, given its stability and the fact in can operate in both buffered and unbuffered solutions, opens the door to accurate pH

sensing in a whole host of extreme environments. Thus the remainder of this chapter discusses potential future applications of the BDD pH sensor.

8.2.1 All-diamond devices for a combinatorial sensor approach

Recent research has shown that a range of all-diamond devices can be fabricated with the desired geometry, using laser ablation to produce the electrode template structure — the only limitation being the resolution of the laser system (10 μm).[12,13] Work has previously explored all-diamond band arrays for conductivity measurements as well as ring-disc arrangements for pH generation-collection experiments.[12,13,14] In environmental systems, conductivity and solution pH are often both required. A natural step forward would be to create a combined all-diamond conductivity and pH sensor. The advantage would be that this sensor could survive in extreme environments, such as ocean monitoring, where due to the pressures and corrosive (high salt) environment other sensors would fail. Furthermore, as both conductivity and pH measurements show a dependence on temperature,[15] a thermocouple could be integrated onto the back face of the all-diamond device, utilising the high thermal conductivity of diamond.[16]

Additionally, work by Read *et al.*[14] recently showed the use of a ring disc electrode for heavy metal analysis, where one electrode (ring) is used to lower the local pH and force all the mercury into the Hg^{2+} form, whilst the other (disc) is used to electrochemically deposit and strip Hg from the surface.[14] To calculate the change in local pH generated by the electrode, the central disc was coated with iridium oxide (IrOx) to make it pH sensitive. This means that unfortunately the change in pH could

not be calculated at the same time as the analyte of interest. Furthermore, IrOx film stability issues were encountered. Instead, the BDD pH electrode could be utilised in a ring-disc arrangement, where the disc is laser ablated to create a functioning pH electrode, with the same disc also utilised as a detector for metal deposition and stripping. This would result in a sensor that could measure pH, generate pH and electrochemically detect a target analyte all encompassed into one robust device.

8.2.2 Towards *in-vivo* pH measurements

Given that the BDD pH sensor has been shown to operate accurately in blood and that BDD is biocompatible,[17,18] future work could entail working towards *in-vivo* measurements of pH. Measurement of pH is an extremely important as the fully-functioning, healthy human body maintains homeostasis which is reflected in the tightly regulated pH in blood (ranging from 7.36 to 7.44) and tissue (~7.20).[19] Deviation from standard conditions can be life threatening, indicating trauma, including loss of oxygen to limbs, as well as serious diseases.[20,21] For this reason, regular arterial blood gas monitoring is essential for critically ill patients.[22] Miniaturisation of the pH sensor would need to be explored reducing the size of the sensor to at least 250 μm in diameter so that the BDD pH electrode can be integrated into a hypodermic needle (or similar). To create sub-micron pH arrays focused ion beam etching could also be explored. As current, blood gas analysers used for pH can only take measurements approximately every 30 minutes,[22] something the BDD pH electrode could greatly improve upon, with the sensor capable of a 3 second temporal resolution. This could provide useful information to clinicians including whether drug administration is effective.

8.3 References

(1) Macpherson, J. V. *Phys. Chem. Chem. Phys.*, **2015**, *17*, 2935–2949.
(2) Ayres, Z. J.;Newton, M. E.;Macpherson, J. V. *Analyst*, **2016**, *141*, 3349–3357.
(3) Schonberger, E. A.;Pickering, W. F. *Talanta*, **1980**, *27*, 11–18.
(4) Kadachi, A. N.;Al-Eshaikh, M. A. *X-Ray Spectrometry*, **2012**, *41*, 350–354.
(5) Hutton, L. A.;O'Neil, G. D.;Read, T. L.;Ayres, Z. J.;Newton, M. E.;Macpherson, J. V. *Anal. Chem.*, **2014**, *86*, 4566–4572.
(6) Ayres, Z. J.;Cobb, S. J.;Newton, M. E.;Macpherson, J. V. *Electrochem. Commun.*, **2016**, *72*, 59–63.
(7) Scorsone, E.;Saada, S.;Arnault, J.;Bergonzo, P. *Journal of Applied Physics*, **2009**, *106*, 014908.
(8) Achatz, P.;Garrido, J. A.;Williams, O. A.;Bruno, P.;Gruen, D. M.;Kromka, A.;Steinmüller, D.;Stutzmann, M. *physica status solidi (a)*, **2007**, *204*, 2874–2880.
(9) Kromka, A.;Rezek, B.;Remes, Z.;Michalka, M.;Ledinsky, M.;Zemek, J.;Potmesil, J.;Vanecek, M. *Chemical Vapor Deposition*, **2008**, *14*, 181–186.
(10) May, P. W. *Philosophical Transactions of the Royal Society of London A: Mathematical, Physical and Engineering Sciences*, **2000**, *358*, 473–495.
(11) Ayres, Z. J.;Borrill, A. J.;Newland, J. C.;Newton, M. E.;Macpherson, J. V. *Anal. Chem.*, **2016**, *88*, 974–980.
(12) Joseph, M. B.;Bitziou, E.;Read, T. L.;Meng, L.;Palmer, N. L.;Mollart, T. P.;Newton, M. E.;Macpherson, J. V. *Anal. Chem.*, **2014**, *86*, 5238–5244.
(13) Joseph, M. B.;Colburn, A.;Mollart, T. P.;Palmer, N.;Newton, M. E.;Macpherson, J. V. *Sensor. Actuat. B-Chem.*, **2017**, *238*, 1128–1135.
(14) Read, T. L.;Bitziou, E.;Joseph, M. B.;Macpherson, J. V. *Anal. Chem.*, **2014**, *86*, 367–371.
(15) Kuyucak, S.;Chung, S.-H. *Biophysical Chemistry*, **1994**, *52*, 15–24.
(16) Kraft, A. *Int. J. Electrochem. Sci*, **2007**, *2*, 355–385.
(17) Alice, C. T.;Barbora, V.;Robert, E.;Clément, H.;Patrizia, F.;Philippe, B.;Richard, B. J. *Journal of Neural Engineering*, **2015**, *12*, 066016.
(18) Alcaide, M.;Taylor, A.;Fjorback, M.;Zachar, V.;Pennisi, C. P. *Frontiers in Neuroscience*, **2016**, *10*, 1–3.
(19) Hamm, L. L.;Nakhoul, N.;Hering-Smith, K. S. *Clinical Journal of the American Society of Nephrology : CJASN*, **2015**, *10*, 2232–2242.
(20) Zygun, D. A.;Steiner, L. A.;Johnston, A. J.;Hutchinson, P. J.;Al-Rawi, P. G.;Chatfield, D.;Kirkpatrick, P. J.;Menon, D. K.;Gupta, A. K. *Neurosurgery*, **2004**, *55*, 877–882.
(21) Kato, Y.;Ozawa, S.;Miyamoto, C.;Maehata, Y.;Suzuki, A.;Maeda, T.;Baba, Y. *Cancer Cell International*, **2013**, *13*, 89.
(22) Singh, V.;Khatana, S.;Gupta, P. *National Journal of Maxillofacial Surgery*, **2013**, *4*, 136–141.